École polytechnique
Laboratoire d'Hydrodynamique
Palaiseau, France

Thèse présentée pour obtenir le grade de

DOCTEUR DE L'ÉCOLE POLYTECHNIQUE

Spécialité : Mécanique

par

Eunok YIM

STABILITY OF COLUMNAR AND PANCAKE VORTICES IN STRATIFIED-ROTATING FLUIDS

Thése soutenue le 7 décembre 2015 devant le jury composé de

Paul BILLANT	Directeur de thèse	LadHyX, Palaiseau
Xavier CARTON	Rapporteur	UBO, Brest
François GALLAIRE	Examinateur	EPFL, Lausanne, Swiss
Michael LE BARS	Rapporteur	IRPHE, Marseille
Claire MÉNESGUEN	Examinatrice	IFREMER, Plouzané
Alexandre STEGNER	Examinateur	LMD, Palaiseau
Vladimir ZEITLIN	Examinateur	LMD-UPMC, Paris

Abstract

The stability of vortices in a stratified and rotating fluid is studied numerically and theoretically in order to better understand the dynamics of vortices in the oceans and atmosphere. In the first part, the stability of a columnar vertical axisymmetric vortex is analysed. For strong stratification and rapid background rotation and some vortex profiles such as a Gaussian angular velocity, the dominant instability is a special instability, called "Gent-McWilliams instability", which bends and slices the vortex into pancake-shaped vortices. Numerical and asymptotic stability analyses for long-wavelength show that this instability originates from a destabilization of the long-wavelength bending mode by a critical layer at the radius where the frequency of the mode is equal to the angular velocity of the vortex. A necessary condition for instability is that the base vorticity gradient is positive at the critical radius. In the second part, the stability of an axisymmetric pancake-shape vortex with a Gaussian angular velocity in both radial and vertical directions is analyzed depending on the intensity of the stratification, the rotation of the fluid, the aspect ratio α of the vortex and the Reynolds number Re. In the case of a strongly stratified non-rotating fluid, centrifugal and shear instabilities are shown to have similar characteristics as for columnar vortices. The centrifugal instability occurs when the buoyancy Reynolds number ReF_h^2 (where F_h is the Froude number) is above a threshold and can be non-axisymmetric close to the threshold. The shear instability develops only when the vertical Froude number F_h/α is low such that the vortex thickness is larger than the cutoff wavelength for a columnar vortex for the same parameters. Gravitational and baroclinic instabilities are also observed, respectively, above and just below the threshold $F_h/\alpha = 1.5$ which corresponds to a zero maximum total density gradient. A simple model predicts the characteristics of the baroclinic instability. Strongly stratified rotating fluids are next considered. The centrifugal instability becomes stabilized for small Rossby number Ro, in agreement with the generalized Rayleigh criterion. An instability similar to the Gent-McWilliams instability of a columnar vortex occurs for small Froude and Rossby numbers. The occurrence of the shear instability continues to be governed by confinement effects. Mixed shear-baroclinic and baroclinic-Gent-McWilliams instabilities are also observed when the isopycnals are strongly deformed in the vortex core. The baroclinic instability develops when $F_h/\alpha(1 + 1/|Ro|) > 1.46$, i.e. when the Burger number based on the absolute angular velocity is below a threshold.

Keywords: instability, columnar vortex, pancake vortex, stratified fluid, rotating fluid

Résumé

La stabilité de tourbillons dans un fluide stratifié en rotation est étudiée numériquement et théoriquement afin de mieux comprendre la dynamique des tourbillons dans les océans et l'atmosphère. Dans la première partie, la stabilité d'un tourbillon colonnaire vertical est analysée. Pour des fortes stratifications et des rotations rapides, certains tourbillons comme ceux ayant une vitesse angulaire gaussienne présente une instabilité particulière, appelée "instabilité de Gent-McWilliams", qui courbe et découpe le tourbillon en couches. Des analyses numériques et asymptotiques pour de grandes longueurs d'onde montrent que cette instabilité provient d'une déstabilisation du mode de déplacement de grande longueur d'onde par une couche critique au niveau du rayon où la fréquence du mode est égale à la vitesse angulaire du tourbillon. Une condition nécessaire d'instabilité est que le gradient de vorticité de base soit positif au niveau du rayon critique. Dans la deuxième partie, la stabilité d'un tourbillon axisymétrique en forme de crêpe avec une vitesse angulaire gaussienne dans les directions radiale et verticale est analysée en fonction de l'intensité de la stratification, de la rotation du fluide, du rapport d'aspect α du tourbillon et du nombre de Reynolds Re. Dans le cas d'un fluide fortement stratifié non-tournant, les instabilités centrifuges et de cisaillement ont les mêmes caractéristiques que celles des tourbillons colonnaires. L'instabilité centrifuge se produit lorsque le nombre de Reynolds de flottabilité ReF_h^2 (où F_h est le nombre de Froude) est supérieur à un seuil et est non-axisymétrique près du seuil. L'instabilité de cisaillement ne se développe que lorsque le nombre de Froude vertical F_h/α est faible de sorte que l'épaisseur du tourbillon est plus grande que la longueur d'onde de coupure d'un vortex colonnaire pour les mêmes paramètres. Des instabilités gravitationnelles et baroclines sont également observées, respectivement, au dessus et juste en dessous du seuil $F_h/\alpha = 1.5$ qui correspond à un gradient de densité total maximum nul. Un modèle simplifié prédit les caractéristiques de l'instabilité barocline. Le cas des fluides fortement stratifiés-tournants est ensuite considéré. L'instabilité centrifuge disparaît pour les nombres de Rossby Ro petits, en accord avec le critère de Rayleigh généralisé. Une instabilité semblable à l'instabilité de Gent-McWilliams d'un tourbillon colonnaire se produit pour les faibles nombres de Froude et Rossby. L'existence de l'instabilité de cisaillement continue d'être régie par des effets de confinement. Des instabilités mixtes, Gent-McWilliams-barocline et cisaillement-barocline, sont également observées quand les iso-densités sont fortement déformées dans le coeur du tourbillon. L'instabilité barocline se développe lorsque $F_h/\alpha(1 + 1/|Ro|) > 1.46$, c'est à dire lorsque le nombre de Burger basé sur la vitesse angulaire absolue est inférieure à un seuil.

Mots clés: instabilité, tourbillon colonnaire, tourbillon crêpe ou lenticulaire, fluide stratifié, fluide tournant

Acknowledgment

I would like to first express my sincere appreciation to my advisor Paul Billant. I really thank to his patience, motivation and support during my PhD. I learned so many things from him and he helped me all the time of my research. Whenever I was depressed or stuck during the study, he has always been there to encourage me to continue and guide me to find solutions. I not only admire his infinite knowledge and insights but also his modesty and endless passion for knowledge. Having him as my PhD advisor was one of the luckiest thing I ever had. One day, I wish to become an amazing person like him.

I wish to thank to my juries Xavier Carton, François Gallaire, Michael le Bars, Claire Ménesguen, Alexandre Stegner and Vladimir Zeitlin, for reading my thesis carefully and giving me wise comments as well as a lot of encouragements. Also I should not forget to thank their tough questions during the defense which widen my research from various aspects.

I also thank to faculties in LadHyX. Thank you Jean-Marc for many brilliant idea and art & science experiences. Thank you Patrick, Peter, Caroline M., Camille, Lutz, Charles, Sabine, Avin, Christophe, Sébastien, Emmanuel de L., Abdul, Antoine S., Julien H., Caroline F., Antoine G., Daniel, toaï, Delphine, Sandrine and Thérèse. I also want to thank to professor Jeong-guon Ih at KAIST for his thoughtful advises during the master courses both in research and life.

I want to thank to my friends and lab-mates who welcomed me with their all hearts. Thanks to them, I was one of the happiest person. I appreciate for all the time we have spent together, for serious discussions on science and being my french teachers. Thank you Junho for introducing me to Paul and plenty advises not only in research but also in administrative works in France. Thank you Xavier for your code and teaching me with patient. Marine, grâce a toi, j'ai pu améliorer mon francais et merci pour tout! Davide, thank you for all 'apéro's we had. Gaétan, thank to you for discussions, conference trips and drinks. Mathieu, just to have you in our office, it was like to have encyclopedia not only for research but also all the administrative stuffs. Mannu, I specially thank you for being my marathon trainer and also for the activities like hiking and very clean lake swimming. Jeremy, I miss discussing with you for many different stuffs and I never get bored when I am with you! Caroline, thank you for your kindness and many jokes although I almost break your nose! P'tite Eline merci pour les soirées! Tilili Ocean! I am really happy that I met you and thank you for many picnics and the hiking and swimming. Thank you Yifan for all your help on the foreign issue! Onofrio, thanks for your advise on 'working hard'! Thank you Anna for your artist energy! I also thank to Nicolas for the coffee last summer, Timothée for discussions on Korean food, Chakri for spicy food alliance, Baptist for sports, Jerome and Cyprien for running, Raphaël for the swag cap, Tristan for starbucks coffee, Lionel, Romain, Guillaume, Philippe, Jean-Philippe, Julien B., Johann, Irma and Hanneke for coffee room discussions, Loïc for enigma, Francesco and Vlado for conference discussions and super awesome spirits and Gordon for English. Thank you Luc, for your immense supports and care.

My thank continues to my friends and family who supported in Korea. 현진언니, 명현언니, 재석오빠, 효식오빠, 상만오빠. 항상 잘 챙겨주어서 너무 고마워요. 언제나 자랑스

러운 기계과 동기들! 지인이, 혜정이, 동영이, 준선이 외국에서 만나서 반가웠다! 하나야! 네가 가까운 곳에 있어서 정말 힘이 되었고, 또 함께 여행 다닐 수 있어서 너무 좋았어. 발표 보러 와주어서 고마워. 현진이, 나경이, 정화, 정민이, 주호, 명현이, 경록이, 형준이, 상협이, 광필이, 창욱오빠, 영록이, 동규, 광연이 다들 한국 갈 때 마다 바쁜 데도 만나주어서 너무 고마워. 그리고 우리 MCZD 윤화, 상임이, 다영이, 소지 너무 사랑하고 언제나 응원해주고 또 내 친구여서 고마워. 삼촌, 숙모, 이모부, 이모 항상 관심과 사랑주셔서 너무 감사해요. 고모부, 고모, 작은아빠, 작은엄마 감사합니다. 그리고 우리 형부 윤선생, 용섭오빠! 친동생처럼 아껴주어서 너무 고마워요! 언니, 오빠가 프랑스까지 찾아와 주어서 너무 행복했어. 나의 반쪽, 용녀, 예옥 언니! 알지? 내가 얼마나 고마워하는지. 언니가 없었다면 지금의 나는 없었을거야. 엄마, 아빠, 고맙고 사랑한다는 말 밖에는 더 할 수 있는 말이 없어요. 우리를 위해서 항상 희생하고 애써주어서 감사하고 또 감사해요.

I thank again to all the people that I have met in LadHyX, Polytechnique and France for unforgettable memories and I am sure that they will continue. Thank you very much, merci beaucoup, 감사합니다.

18 Feb. 2016

Palaiseau, France

Eunok YIM

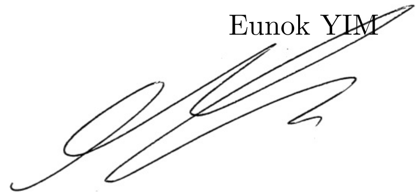

Contents

1

Background and motivations

In this chapter, the general motivations and the basics are discussed. The stability of columnar and pancake vortices in stratified and rotating fluids are briefly introduced. For an isolated columnar vortex, centrifugal, shear, radiative and Gent-McWilliams instabilities are presented. For pancake vortices, the density structures and some stability results are shown. The goals of the thesis are to generalize the stability conditions of the Gent-McWilliams instability for columnar vortices and to characterize the stability of pancake vortices in terms of control parameters.

Contents

1.1 General motivations

The main interests in geophysical fluids dynamics are to better understand the motions of the atmosphere and oceans to improve the earth system modelings, forecast of various natural phenomena, environmental protection and further extension to other planets. However, it is not so easy to study the atmosphere and oceans because they are highly complex involving many physical processes and a huge range of spatial and temporal scales.

The two distinguishing attributes of such fluids are the presence of the Coriolis force due to the planetary rotation and density variations along the vertical. The density stratification is generally stable: the light fluid being above the heavy fluid.

The importance of the stratification and rotation effects depends on the typical scales of the motions. For large scale ($>$ 100km in the atmosphere, $>$ 10km in the ocean), both stratification and rotation are strong. Weather patterns, large eddies, fronts and the major currents are examples. In contrast, at intermediate scales (mesoscales:1-100km in the atmosphere, submesoscales $\sim$ 10km in the oceans), the effect of the planetary rotation is comparably weak whereas stratification effects are still strong. Sea breeze, mountain waves, internal waves, submesoscale eddies and coastal upwellings are examples. The planetary rotation and stratification are weak for small scales ($< O(1)$km). Tornadoes, whirlpools, mixing and dispersion of pollutants are at these small scales. However, each scale can exchange with the others or one phenomenon can lie on a wide range of scales as can be seen in figure 1.1 (Kantha & Clayson, 2000). All different scales should be collectively considered: the accuracy of long-term climate predictions depends largely on the processes at small scales that are not resolved but only parameterised empirically in numerical climate models.

The stratification and rotation effects can be measured by dimensionless parameters: Rossby (Ro) and Froude (F_h) numbers:

$$Ro = \frac{\text{inertia}}{\text{background rotation}} = \frac{V}{fL}, \qquad F_h = \frac{\text{inertia}}{\text{background stratification}} = \frac{V}{NL}, \tag{1.1}$$

where V is the characteristic velocity, L the typical horizontal length scale of the motion, f the Coriolis parameter defined as $f = 2\Omega_E \sin\varphi$ where Ω_E is rotation rate of the Earth (or a planet), φ the latitude and N the Brunt-Väisälä frequency defined as

$$N = \sqrt{\frac{-g}{\rho_0}\frac{\partial \rho}{\partial z}}, \tag{1.2}$$

where g is the gravity, $\partial\rho/\partial z$ the vertical density gradient and ρ_0 a reference density. The smaller F_h and Ro are, the stronger influences of stratification and rotation on the motions. When $Ro \ll 1$ and $F_h \ll 1$, the equation of motions can be simplified to the quasi-geostrophic equation and when $Ro \geq 1$, they are ageostrophic. Densities in the atmosphere and oceans are generally function of temperature, pressure and also salinity for the ocean. Figure 1.2 shows the typical density distributions in the oceans (Pedlosky, 1992). The density changes with the depth but the variations of the density are very small. The differences between minimum and maximum density are only about 0.004(g/cm^3). Hence, the Boussinesq approximations can be applied to the equations of motion since the density variations ρ' are much smaller than the reference density $\rho' \ll \rho_0$. The Earth's rotation varies with the latitude φ. The f-plane approximation is when f is assumed to be constant and the β-plane approximation takes into account small meridional y variation as $f \simeq f_0 + \beta y$. Generally, the stable stratification inhibits vertical motions. The ambient rotation tends to

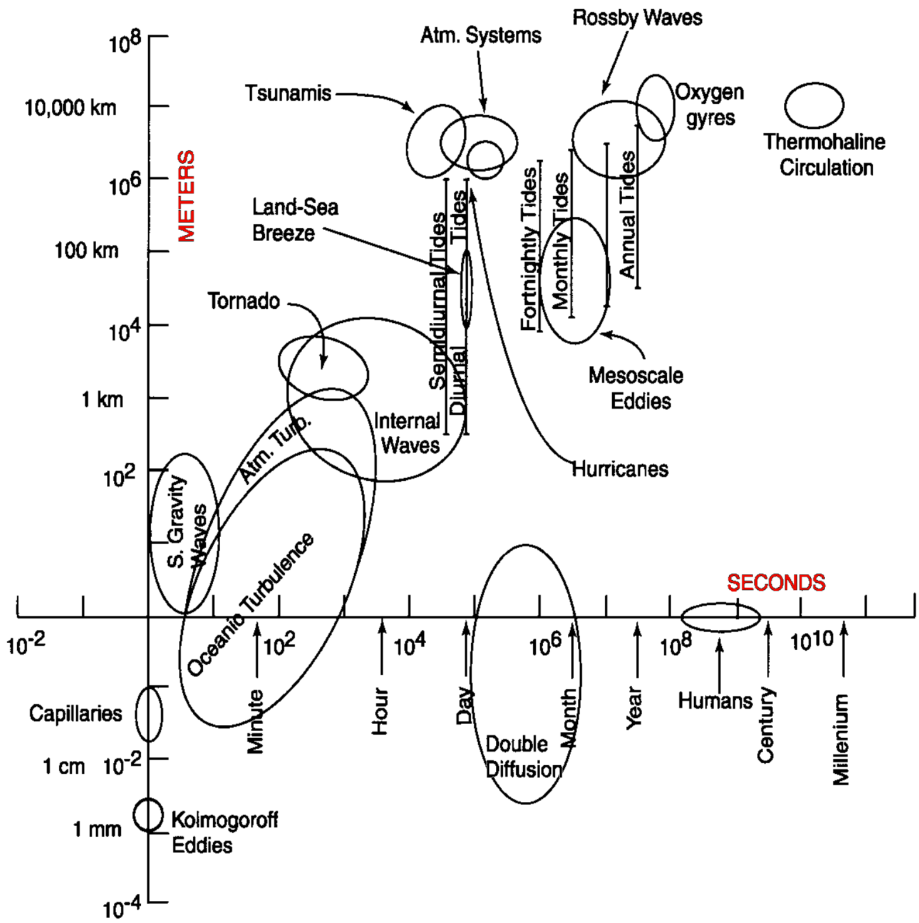

Figure 1.1: The spatial and temporal scales of motions in the atmosphere and the oceans. Image from Kantha & Clayson (2000).

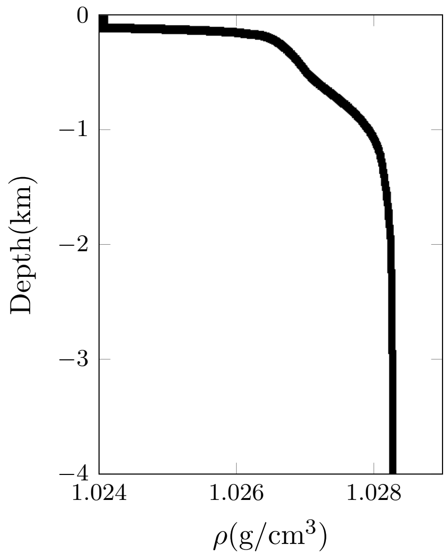

Figure 1.2: Typical density distribution of the ocean. Image is reproduced from Pedlosky (1992).

impart vertical coherence to the motions. In the thesis, we use the Boussinesq and f-plane approximations.

Among all the important geophysical phenomena, we are particularly interested in vortices or eddies. Vortices in the atmosphere are important because they can be natural hazards confronting humans. Tropical cyclones are examples of the atmospheric vortices (typhoons for western North Pacific Ocean and hurricanes otherwise). Because they are accompanied with strong winds, rain and damaging storm surges, they have been an important subject in meteorology. Figure 1.3a shows two typhoons observed in August 2015 near Korea and Japan: Goni and Atsani. Their typical radii are 100km and 200km and the maximum speed observed is 204km/h and 120km/h, respectively on 24 August 2015 (NASA Earth Observatory, UNISYS). Hence, their Rossby numbers are

$$Ro_{\text{Goni}} = \frac{V}{L2\Omega_0 \sin\varphi} = \frac{204\text{km/h}}{100\text{km} \times 2 \times \frac{2\pi}{24\text{h}} \sin 30^\circ} \simeq 77, \qquad Ro_{\text{Atsani}} \simeq \frac{120}{200\frac{4\pi}{24}\sin 35^\circ} \simeq 1.2, \tag{1.3}$$

respectively. Since the Rossby number for Atsani is much smaller than the one for Goni, it is more affected by the planetary rotation. Nevertheless, the trajectories of the two typhoons are mostly influenced by the trade winds (northeasterly) around $\varphi = 10^\circ - 25^\circ$ and by the westerlies around $\varphi = 25^\circ - 40^\circ$ as seen in figure 1.3b.

Vortices are also found in the oceans. The circular structure in the middle of figure 1.4 is a vertical cross-section of an anticyclone, called Mediterranean eddy (Meddy) which is formed by the salty water flowing from Mediterranean sea to Atlantic ocean. The image has been obtained by seismic reflection. The quantity displayed is the acoustic reflectivity which is a measure of temperature variations. Meddies are generally observed in mid-Atlantic ocean (see bottom left map in figure 1.4). The horizontal extension of these eddies is around 50–100km long and the thickness is about 1km (Richardson *et al.*, 2000). Their lifetime is up to 2 years (Armi *et al.*, 1989; Hobbs, 2007). The Rossby number of this Meddy is about $0.3 - 0.7$ (Hua *et al.*, 2013). Figure 1.5 shows another example of eddy in East/Japan sea. The velocity distribution of warm core Ulleung eddy is depicted in figure 1.5a on April 1993 (Shin *et al.*, 2005). This eddy is formed by the encounter of the warm (from south) and

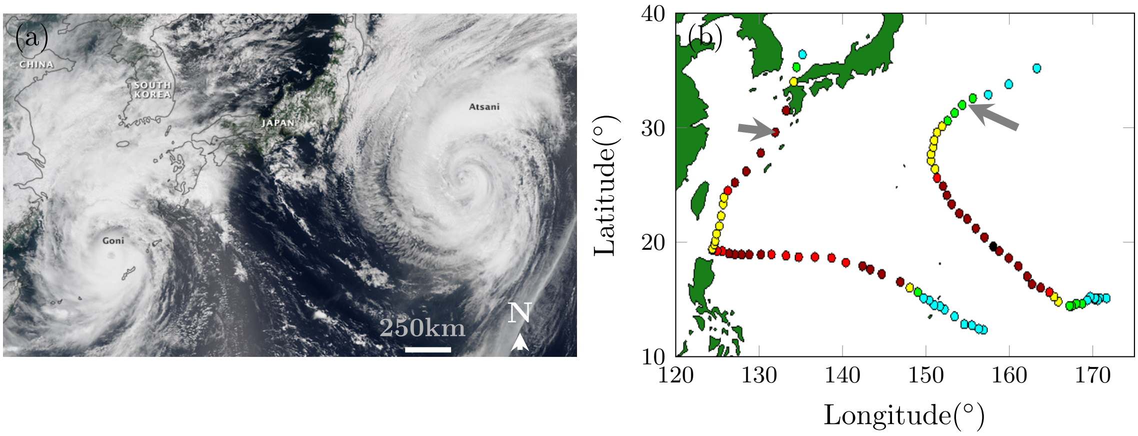

Figure 1.3: (a) Satellite images of the fifteenth (Goni) and sixteenth (Atsani) typhoons on 24 August 2015. Images from NASA Earth Observatory. (b) Trajectories of the typhoons. Left one is for Goni and the color indicates the strength of the velocity. The arrows indicate 24 August. The trajectories are reproduced from the latitude and longitude data from UNISYS.

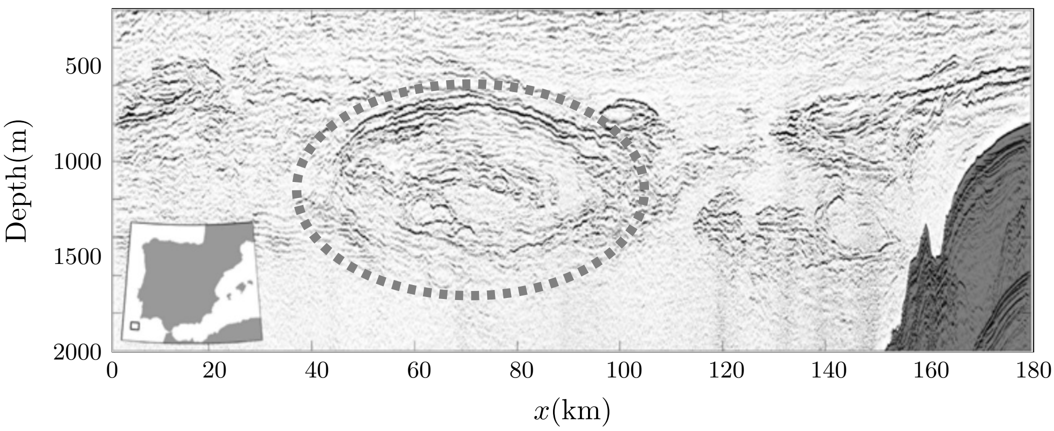

Figure 1.4: Vertical seismic image of Meddy on April–May 2007. Images from Hua *et al.* (2013).

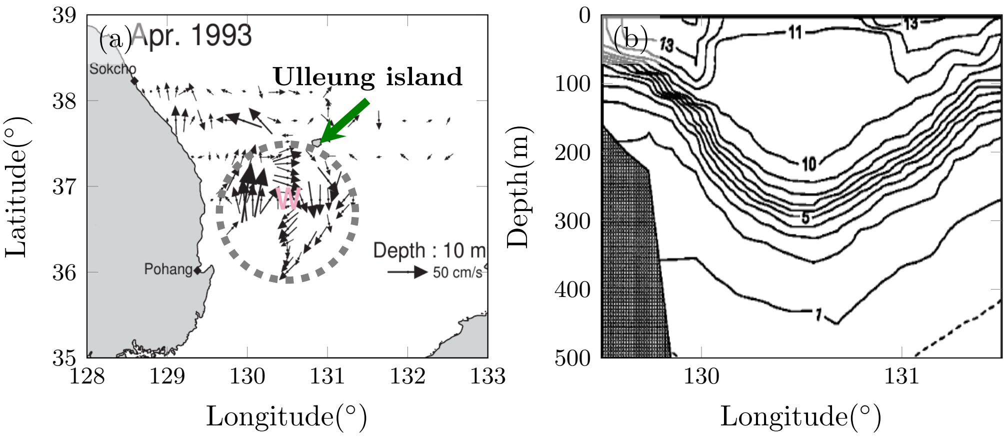

Figure 1.5: (a) Horizontal current velocities (cm/s) and (b) vertical temperature (°C) distributions of East/Japan sea on April 1993. Images from Shin *et al.* (2005).

cold (from north) currents flowing along the Korea peninsula. Both warm and cold core eddies can be generated. Once generated, they are trapped in Ulleung basin just below the Ulleung island. Figure 1.5b shows the temperature distribution in a vertical cross-section of the Ulleung eddy at lattitude 37°. The diameter of this eddy is 150−170km and its maximum depth is about 300m. They can live up to 3 years (Shin *et al.*, 2005). Compared to Meddies, this eddy exists near the surface of the ocean. The Rossby number of this Ulleung eddy is about 0.2. Studying the dynamics of these eddies are also very important because they can transport energy, pollutant and mix the oceans. As these eddies stir the oceans, they sometimes draw nutrients up from the deep, fertilizing the surface waters to promote blooms of phytoplankton in the open ocean (McGillicuddy *et al.*, 2007; Lehahn *et al.*, 2011; Kim *et al.*, 2012). Figure 1.6 shows an anticyclonic eddy found under South Africa. This eddy is detached from Agulhas current, which flows along the south eastern coast of Africa and around the tip of South Africa. Agulhas eddies are known to transport warm, salty water from the Indian Ocean to the South Atlantic (Bryden *et al.*, 2005). Due to its different properties from the surrounding water, the phytoplankton blooms inside the eddy make the eddy visible by the satellite.

As we saw from the examples, vortices in the atmosphere and ocean can exist over large ranges of Rossby numbers. Their regimes of existence are summarized in figure 1.7 as functions of Ro and F_v. F_v is the vertical Froude number $F_v = U/NL_v$, where L_v is the typical height of the vortices. As seen in figure 1.7, F_v varies only in a small range from $O(10^{-1})$ to $O(10)$.

1.2 Stability of vortices in stratified-rotating fluids

Because there are too many variables/parameters at play in the motions of atmosphere and oceans, it is difficult to describe the mechanisms and physics involved in typhoons and eddies. Hence, laboratory experiments and numerical simulations for simpler models are developed to describe better these geophysical vortices. Instabilities are understood as one of the key feature which materializes the emergence and disappearance of such vortices. In this section, instabilities of vortices in stratified-rotating fluids are described. The vortices are categorized as columnar and pancake vortices. Columnar vortex is a vortex whose angular velocity only varies in radial direction while the one for pancake vortex varies both in radial and vertical directions.

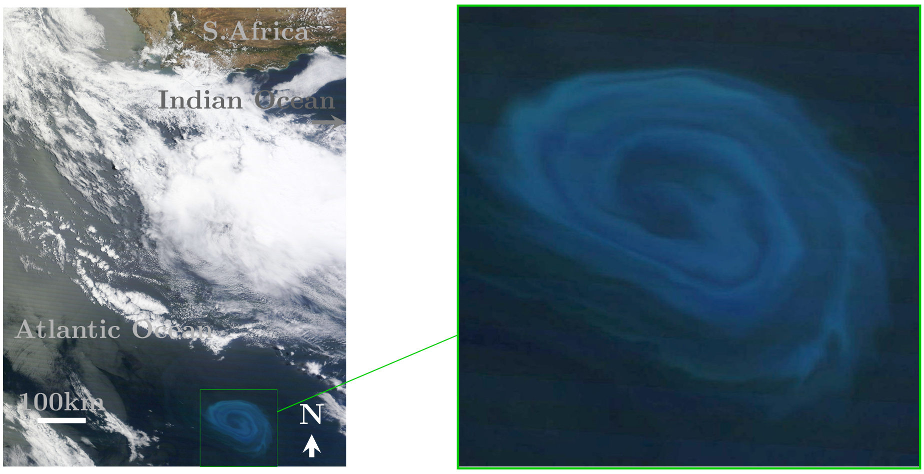

Figure 1.6: Blooms of phytoplankton inside an anti-cyclonic (counter-clockwise) eddy peeled off from the Agulhas Current, which flows along the southeastern coast of Africa and around the tip of South Africa. Images from NASA Earth Observatory.

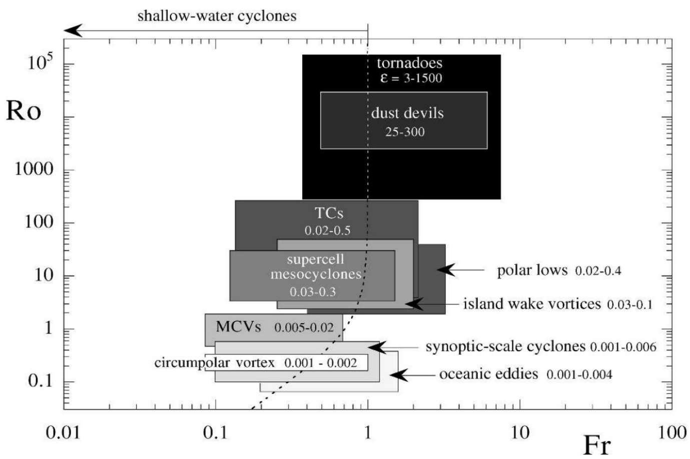

Figure 1.7: Parameter regimes for atmospheric vortices and mesoscale oceanic eddies as functions of Ro and F_v. TS means tropical cyclones (Typhoons and hurricanes) and MCV is for mesoscale convective vortices. Images from Schecter & Montgomery (2006).

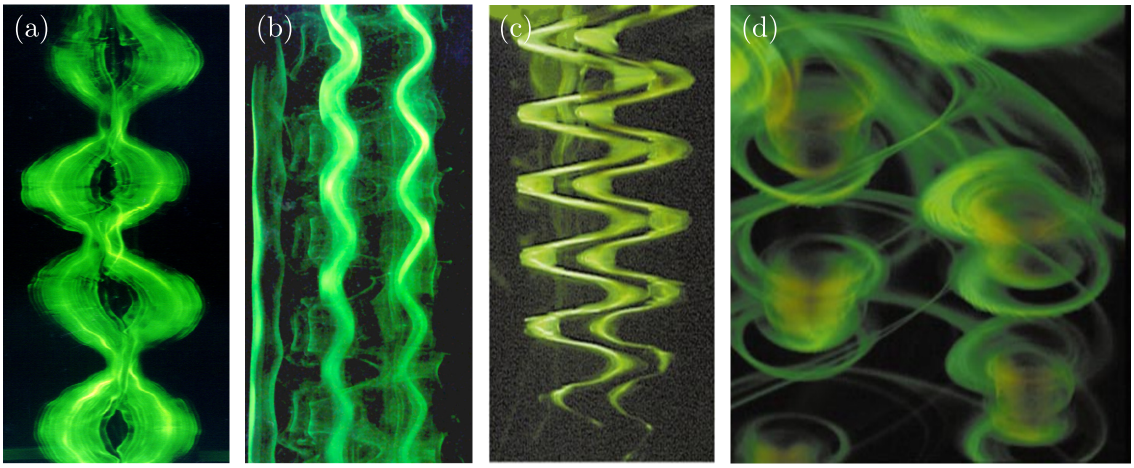

Figure 1.8: Instabilities on vortex pairs: side view of (a) Crow, (b) elliptic and (c) zig-zag instabilities, and (d) oblique view of pancake vortices generated by the zig-zag instability. Images are reproduced from Leweke & Williamson (2011), Meunier & Leweke (2001) and Billant & Chomaz (2000), respectively.

1.2.1 Columnar vortices

The stability of a single columnar vortex has a long history and it can be unstable to various instabilities such as centrifugal, shear, radiative and Gent-McWilliams instabilities. When two columnar vortices are close from each other: Crow, elliptic and zig-zag instabilities are found. In this section, a brief introduction and the instability criteria for different instabilities occurring in columnar vortices are discussed.

For an interacting vortex pair, Crow and elliptic instabilities are found for homogeneous fluids (see figure 1.8a,b) (Leweke *et al.*, 2016). Crow instability is a long-wavelength instability which occurs in aircraft wakes (Crow, 1970; Widnall *et al.*, 1971; Leweke *et al.*, 2016). This instability only exists for a counter-rotating vortex pair (Jimenez, 1975; Klein *et al.*, 1995; Leweke *et al.*, 2016). In contrast, elliptic instability is a short-wavelength instability and it develops for both counter- and co-rotating pairs (Leweke & Williamson, 1998; Meunier & Leweke, 2005; Leweke *et al.*, 2016). An example of elliptic instability on a co-rotating vortex pair is shown in figure 1.8b (Meunier & Leweke, 2001). Streamlines are elliptic due to the strain exerted by the neighboring vortex. The resonance of Kelvin waves with the strain destabilizes the vortex (Moore & Saffman, 1975; Tsai & Widnall, 1976; Kerswell, 2002; Le Dizès & Laporte, 2002; Leweke *et al.*, 2016). When the flow is stratified, Crow and elliptic instabilities only exist in weakly stratified fluids and are stabilized in strongly stratified fluids (Billant & Chomaz, 2000; Otheguy *et al.*, 2006; Billant *et al.*, 2010; Leweke *et al.*, 2016). Instead, Billant & Chomaz (2000, 2001), Otheguy *et al.* (2006), Billant (2010) and Billant *et al.* (2010) have shown that co- and counter-rotating vortex pairs in stratified and stratified-rotating fluids can be unstable to the zig-zag instability (see figure 1.8c,d). The zig-zag instability is triggered in stratified fluids because the self-induction is positive while it is negative in homogeneous fluids. As a result, the columnar vortex pair is sliced into thin pancake vortices (see figure 1.8d).

For an isolated vortex, centrifugal instability occurs when the balance between the centrifugal force and the pressure gradient is disrupted: when the angular momentum of the fluids decreases with radius r in inviscid fluids (Rayleigh, 1917). This condition has been generalized to rotating fluids by Kloosterziel & van Heijst (1991) as

$$\Phi = (f/2 + V_\theta/r)(f + \zeta) < 0, \tag{1.4}$$

where V_θ is the velocity of the vortex and $\zeta = 1/r\partial(rV_\theta)/\partial r$ the vertical vorticity. Figure 1.9 shows example of the centrifugal instability in lab experiments (Fontane, 2002) and numerical simulations (Smyth & McWilliams, 1998). As can be seen, the centrifugal instability is 3D instability with a large vertical wavenumber k. The criterion (1.4) has been

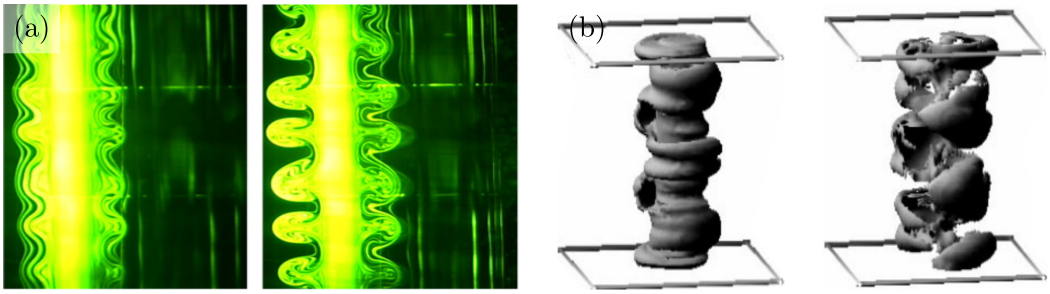

Figure 1.9: Vertical side view of the centrifugal instability in (a) laboratory experiment (Fontane, 2002) and (b) numerical (DNS) simulation (Smyth & McWilliams, 1998).

extended to stratified fluids by Billant & Gallaire (2005). They found that the growth rate ω_i of the centrifugal instability is proportional to $\sqrt{-\Phi}$ and the stratification stabilizes only small vertical wavenumbers. In the case of baroclinic vortices, further generalizations of the Rayleigh criterion are discussed by Solberg (1936) and Eliassen & Kleinschmidt (1957) by considering the energy difference when two particles at two density levels are exchanged. Let us consider a particle at radius r_1 and height z_1 with density ρ_1 and velocity V_1, and a particle with density ρ_2 and velocity V_2 at (r_2, z_2) in a rotating frame with a uniform angular velocity $f/2$. The initial total energy E_i of the two particles are the sum of kinetic KE and potential PE energies

$$E_i = KE + PE = \frac{1}{2}\rho_0(V_1^2 + V_2^2) + g(\rho_1 z_1 + \rho_2 z_2). \tag{1.5}$$

Because we are under the Boussinesq approximation, the reference density ρ_0 is used for kinetic energy but not for potential energy which is associated with the gravity term. After the exchange, the velocity of each particles are changed to $V_1 \to V_{1f}$ and $V_2 \to V_{2f}$ and the total energy E_f is

$$E_f = KE + PE = \frac{1}{2}\rho_0(V_{1f}^2 + V_{2f}^2) + g(\rho_1 z_2 + \rho_2 z_1). \tag{1.6}$$

The conservation of total angular momentum gives $U_{1f} = r_1/r_2 U_1$ and $U_{2f} = r_2/r_1 U_2$ where $U_1 = V_1 + r_1 f/2$, $U_2 = V_2 + r_2 f/2$, $U_{1f} = V_{1f} + r_2 f/2$ and $U_{2f} = V_{2f} + r_1 f/2$. The flow is unstable if the energy after the exchange is smaller than initially: $E_f - E_i < 0$. Assuming that $\Delta r = r_2 - r_1 \ll 1$ and $\Delta z = z_2 - z_1 \ll 1$,

$$\rho_2 - \rho_1 = \frac{\partial \rho}{\partial r}\Delta r + \frac{\partial \rho}{\partial z}\Delta z, \tag{1.7}$$

$$r_2^2 U_2^2 - r_1^2 U_1^2 = \frac{\partial (r^2 U^2)}{\partial r}\Delta r + \frac{\partial (r^2 U^2)}{\partial z}\Delta z. \tag{1.8}$$

Hence, the total energy difference $\Delta E = E_f - E_i$ is

$$\Delta E = \left[\frac{1}{r^3}\frac{\partial(rU)^2}{\partial r} - 2\frac{g}{\rho_0}\frac{\partial\rho}{\partial r}x - \frac{g}{\rho_0}\frac{\partial\rho}{\partial z}x^2\right]\rho_0\Delta r^2, \tag{1.9}$$

where $x = \Delta z/\Delta r$ and the thermal wind relation has been used: $1/r\partial U^2/\partial z = -g/\rho_0\partial\rho/\partial r$. When $x = 0$, we recover Rayleigh criterion (1.4) and when $x \to \infty$ the condition for gravitational (static) instability. Even if these two criteria are not satisfied, i.e. $1/r^3\partial(rU)^2/\partial r > 0$ and $\partial\rho/\partial z < 0$, (1.9) can be negative for some value of x when

$$\frac{1}{r^3}\frac{\partial(rU)^2}{\partial r} - \frac{1}{r^3}\frac{\partial(rU)^2}{\partial z}\frac{\frac{\partial\rho}{\partial r}}{\frac{\partial\rho}{\partial z}} = \left(\frac{2V}{r}+f\right)(\zeta+f) - \left(\frac{2V}{r}+f\right)\frac{\partial V}{\partial z}\frac{\frac{\partial\rho}{\partial r}}{\frac{\partial\rho}{\partial z}} < 0. \tag{1.10}$$

This condition can also be expressed in terms of the potential vorticity Π as (Hoskins, 1974),

$$\Phi = \frac{1}{r^3}\frac{\partial(r(V+rf/2))^2}{\partial r}\bigg|_\rho = \left(\frac{2V}{r}+f\right)\frac{\Pi}{\frac{\partial\rho}{\partial z}} < 0, \tag{1.11}$$

where

$$\Pi = (\mathbf{Z} + f\boldsymbol{e}_z)\cdot\nabla\rho, \tag{1.12}$$

where $\mathbf{Z}$ is the relative vorticity. Hence, the centrifugal instability is expected when the absolute circulation decreases with the radius along isopycnal surfaces for some radius.

Shear instability is a 2D Kelvin-Helmholtz instability developing because of the radial shear. The necessary condition for the shear instability is the existence of an inflection point r_I (Rayleigh, 1880):

$$\frac{\mathrm{d}\zeta(r_I)}{\mathrm{d}r} = 0. \tag{1.13}$$

Figure 1.10 shows the example of the shear instability view from top (Chomaz *et al.*, 1988) and the numerical result (Carton & Legras, 1994). The radius where sharp changes occur corresponds to inflection radius r_I. Gent & McWilliams (1986), Carton & McWilliams (1989), Carnevale & Kloosterziel (1994) and Orlandi & Carnevale (1999) showed that the minimum azimuthal wavenumber m for the shear instability is $m = 2$ and when the steepness of the base flow increased, the shear instability destabilizes at larger azimuthal wavenumbers m. Also, the growth rate for the shear instability is maximum when the vertical wavenumber k is zero. Deloncle *et al.* (2007) found for parallel flow that the growth rate depends on kF_h in the presence of stratification.

Recent studies have shown that columnar vortices can also be unstable to a radiative instability in stratified rotating fluids (Smyth & McWilliams, 1998; Schecter & Montgomery, 2004; Billant & Le Dizès, 2009; Le Dizès & Billant, 2009; Riedinger *et al.*, 2010, 2011; Park & Billant, 2012, 2013). This instability is specific to stratified fluids and occurs due to the over-reflection of inertia-gravity waves, coming from the vortex core, at the critical radius r_c where $m\Omega(r_c) = \omega$ with Ω the angular velocity and ω the frequency of the wave. When the incident wave reaches the critical radius, some portions of the wave are reflected back and other portions are transmitted. The transmitted waves have negative momentum so that the reflected waves have larger momentum than the incident one in order that the total momentum is conserved. As a result, the waves grow with time (Takehiro & Hayashi, 1992; Park, 2012). The necessary conditions for the radiative instability are: there exist two turning points r_t where $\omega(r_{t1,2}) = \omega_{ep\pm}$ where $\omega_{ep\pm}$ are epicyclic frequencies defined as

$$\omega_{ep\pm} = m\Omega \pm \sqrt{(f+\zeta)(f+2\Omega)}. \tag{1.14}$$

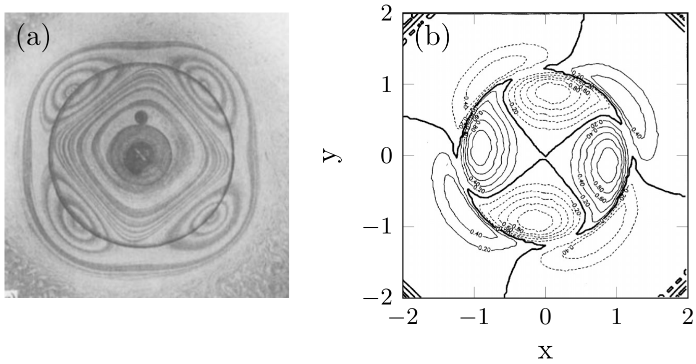

Figure 1.10: Horizontal view of the shear instability in (a) laboratory experiment of a soap film (Chomaz *et al.*, 1988) and (b) numerical simulation of an isolated vortex (Carton & Legras, 1994).

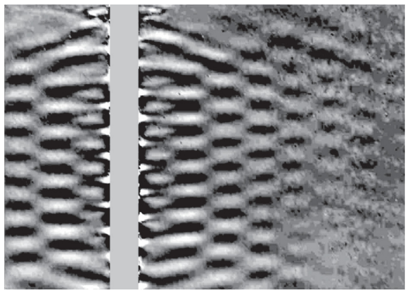

Figure 1.11: Vertical side view of experimental results of the radiative instability from a rotating cylinder in stratified fluids. Image from Riedinger *et al.* (2011).

Also, the critical radius r_c should lie between the two turning points $r_{t1} < r_c < r_{t2}$ (Le Dizès & Billant, 2009; Park & Billant, 2012, 2013). The radiative instability is most unstable when the fluid is strongly stratified and non-rotating. As the background rotation increases, its growth rate decreases and vanishes for strongly stratified and rapidly rotating fluids. Figure 1.11 shows an example of the radiative instability observed in the flow around a rotating cylinder in stratified fluids (Riedinger *et al.*, 2011).

Finally, Gent & McWilliams (1986) evidenced that a columnar vortex in stratified-rotating fluids can be unstable to an internal instability (here we call it Gent-McWilliams instability) which bends the vortex with finite axial wavenumber k for azimuthal wavenumber $m = 1$ (see figure 1.12 (Smyth & McWilliams, 1998)). Gent & McWilliams (1986) have shown that in the quasi-geostrophic limit, when the steepness of the base flow is as steep as the Carton & McWilliams (1989) vortex with the angular velocity profile $\Omega = \Omega_0 \exp(-r^2)$, the Gent-McWilliams instability dominates the shear instability. A necessary condition for the Gent-McWilliams instability in quasi-geostrophic fluids is the Rayleigh $\zeta'(r) > 0$ and Fjortoft criteria. Smyth & McWilliams (1998) have shown the effect of F_h and Ro on this instability for some ratios of F_h and Ro: $F_h/Ro = \infty, 0.5, 0.005$ and 0. When Ro is in the centrifugally stable regime, the Gent-McWilliams instability is the most unstable. Flierl (1988) has explained the mechanism of the Gent-McWilliams instability by considering a vortex with piecewise vorticities in quasi-geostrophic fluids. The behaviour of such vortex can be fully described analytically as shown by Flierl (1988). Here, we provide extended explanations of the work of Flierl (1988) on the mechanism of the Gent-McWilliams instability. The vortex is composed with three levels of vorticity in radial direction: for $r \leq 1$, the potential

1

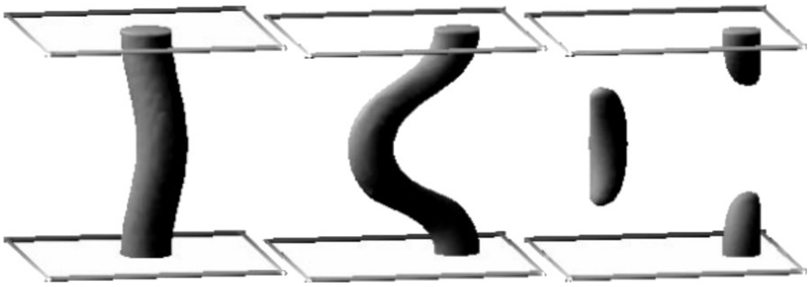

Figure 1.12: Vertical side view of numerical (DNS) simulation of the Gent-McWilliams instability. Image is reproduced from Smyth & McWilliams (1998).

vorticity is q_1+q_2; for $1<r<b$, the potential vorticity is q_2; for $r>b$ the potential vorticity is zero. Since the sign of two vorticities (q_1 and q_2) should be opposite for instability, the sign of outer vorticity is considered negative $q_2<0$. The base velocities at $r=1$ and b are $\bar{V}(1)$ and $\bar{V}(b)$, respectively. By looking at the perturbationa of the two boundaries ($r=1$ and $r=b$), we can explain the instability. In Flierl (1988), the small perturbations are represented as η in the vicinity of $r=1$ and τ near $r=b$. The dynamic and kinematic boundary conditions give in quasi-geostrophic fluids

$$\left.\begin{aligned} \frac{\partial\eta}{\partial t}+\bar{V}(1)\frac{\partial\eta}{\partial\theta} &= \mathrm{I}_1(k)\mathrm{K}_1(k)q_1\frac{\partial\eta}{\partial\theta}+b\mathrm{I}_1(k)\mathrm{K}_1(kb)q_2\frac{\partial\tau}{\partial\theta},\\ \frac{\partial\tau}{\partial t}+\frac{\bar{V}(b)}{b}\frac{\partial\tau}{\partial\theta} &= \frac{1}{b}\mathrm{I}_1(k)\mathrm{K}_1(kb)q_1\frac{\partial\eta}{\partial\theta}+\mathrm{I}_1(kb)\mathrm{K}_1(kb)q_2\frac{\partial\tau}{\partial\theta}, \end{aligned}\right\} \tag{1.15}$$

where I_1 and K_1 are modified Bessel functions of first and second kind of order 1, respectively. Since perturbations are proportional to $\exp(\mathrm{i}\theta-\mathrm{i}\omega t)+c.c.$, we can express η and τ in terms of displacements in the x and y directions in the form

$$\left.\begin{aligned} \eta &= \Delta x_1\cos\theta+\Delta y_1\sin\theta,\\ \tau &= \Delta x_2\cos\theta+\Delta y_2\sin\theta, \end{aligned}\right\} \tag{1.16}$$

where the time dependence is contained in $(\Delta x_i,\,\Delta y_i)$. Because the vorticities are constant, the velocities are $\bar{V}=(q_2+q_1)r/2$ for $r\leq 1$ and $\bar{V}=q_2r/2+q_1/(2r)$ for $1\leq r\leq b$. If we non-dimensionalize time such that $q_1+q_2=2$, i.e. $\bar{V}(1)=1$, the velocity at $r=b$ becomes $\bar{V}(b)=q_2b/2+(1-q_2/2)/b$. Substituting (1.16) into (1.15) gives

$$\frac{\partial\Delta x_1}{\partial t}+(1-\mathrm{I}_1(k)\mathrm{K}_1(k)(2-q_2))\Delta y_1=b\mathrm{I}_1(k)\mathrm{K}_1(kb)q_2\Delta y_2, \tag{1.17}$$

$$\frac{\partial\Delta y_1}{\partial t}-(1-\mathrm{I}_1(k)\mathrm{K}_1(k)(2-q_2))\Delta x_1=-b\mathrm{I}_1(k)\mathrm{K}_1(kb)q_2\Delta x_2, \tag{1.18}$$

$$\frac{\partial\Delta x_2}{\partial t}+\left(\frac{1}{b^2}-\frac{q_2}{2b^2}+\frac{q_2}{2}-\mathrm{I}_1(kb)\mathrm{K}_1(kb)q_2\right)\Delta y_2=\frac{1}{b}\mathrm{I}_1(k)\mathrm{K}_1(kb)(2-q_2)\Delta y_1, \tag{1.19}$$

$$\frac{\partial\Delta y_2}{\partial t}-\left(\frac{1}{b^2}-\frac{q_2}{2b^2}+\frac{q_2}{2}-\mathrm{I}_1(kb)\mathrm{K}_1(kb)q_2\right)\Delta x_2=-\frac{1}{b}\mathrm{I}_1(k)\mathrm{K}_1(kb)(2-q_2)\Delta x_1. \tag{1.20}$$

Considering the case $\bar{V}(b)=0$ corresponding to an isolated vortex then $b^2=(q_2-2)/q_2$. Expanding the Bessel functions for small k and expanding (1.17)–(1.20) in terms of mean displacements $(\Delta x_1+\Delta x_2,\Delta y_1+\Delta y_2)/2$ and relative displacements $(\Delta x_1-\Delta x_2,\Delta y_1-\Delta y_2)$

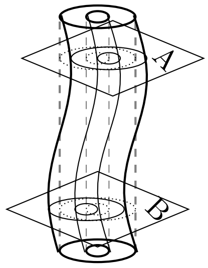

Figure 1.13: Schematic drawing of columnar vortex with piecewise vorticity.

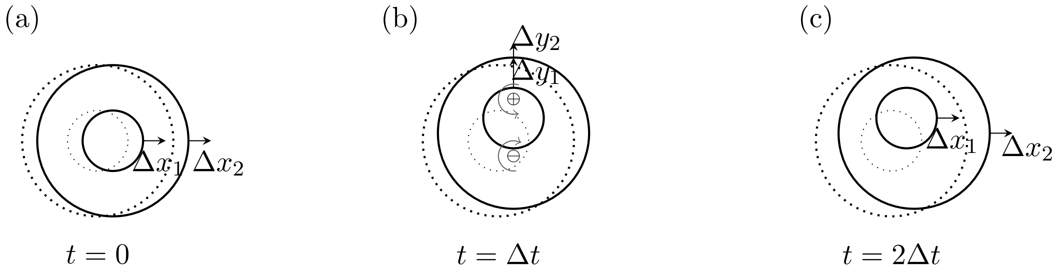

Figure 1.14: Top view of the piecewise vortex at plane A in figure 1.13. (a) The initial displacements at $t = 0$ of the inner contour is Δx_1 and the outer contour is Δx_2 in the same direction. (b) The displacements generated by the initial displacements after small time passes. (c) The resulting positive feedback on displacements in the x directions. Dotted lines indicates the vorticity contours at $t = 0$.

give

$$\frac{\partial(\Delta x_1 + \Delta x_2)}{\partial t} = -q_2(\Delta y_1 - \Delta y_2) + k^2 \left[Q_n(\Delta y_1 + \Delta y_2) + P_n(\Delta y_1 - \Delta y_2)\right], \tag{1.21}$$

$$\frac{\partial(\Delta y_1 + \Delta y_2)}{\partial t} = q_2(\Delta x_1 - \Delta x_2) - k^2 \left[Q_n(\Delta x_1 + \Delta x_2) + P_n(\Delta x_1 - \Delta x_2)\right], \tag{1.22}$$

$$\frac{\partial(\Delta x_1 - \Delta x_2)}{\partial t} = k^2 \left[\left(Q_n + \frac{1}{8}\right)(\Delta y_1 + \Delta y_2) + Q_n(\Delta y_1 - \Delta y_2)\right], \tag{1.23}$$

$$\frac{\partial(\Delta y_1 - \Delta y_2)}{\partial t} = -k^2 \left[\left(Q_n + \frac{1}{8}\right)(\Delta x_1 + \Delta x_2) + Q_n(\Delta x_1 - \Delta x_2)\right], \tag{1.24}$$

where

$$Q_n = \frac{q_2 - 2}{16} \ln\left(1 - \frac{2}{q_2}\right), \tag{1.25}$$

$$P_n = \frac{1}{8}\left[(2 - q_2)\left(\frac{3}{2}\ln\left(1 - \frac{2}{q_2}\right) + 2C_n + 1\right) - 1\right], \tag{1.26}$$

where $C_n = -1 + 2\gamma_e - 2\ln 2 + 2\ln k$.

Figures 1.13 and 1.14 show schematic drawings of the contours of the piece-wise vorticity of the columnar vortex. Dashed lines are for the vortex at rest and solid lines are when the vortex is disturbed with a small vertical wavenumber k. First, let us consider the cross-section A. Assume that we give small displacements of Δx_1 and Δx_2 in the same direction (say, $\Delta x_1 = \Delta x_2 > 0$) with $k \ll 1$ while there are no displacement in the y direction ($\Delta y_1 = \Delta y_2 = 0$) (see figure 1.14a). Equation (1.22) and (1.24) give the resulting velocity in the y direction as

$$\frac{\partial(\Delta y_1 + \Delta y_2)}{\partial t} = -k^2 Q_n (\Delta x_1 + \Delta x_2), \tag{1.27}$$

$$\frac{\partial(\Delta y_1 - \Delta y_2)}{\partial t} = -k^2 \left(Q_n + \frac{1}{8}\right) (\Delta x_1 + \Delta x_2). \tag{1.28}$$

Since q_2 is negative, Q_n defined in (1.25) is also negative and (1.27) implies a positive mean velocity in the y direction. Hence, after time Δt, the mean y displacement is positive: $(\Delta y_1 + \Delta y_2)/2 > 0$. Next, the sign of $(Q_n + 1/8)$ in (1.28) is also negative for any negative q_2. The left hand side of (1.28) is then positive meaning that $\Delta y_1 - \Delta y_2 > 0$. Since $Q_n < Q_n + 1/8$, this indicates that $\Delta y_1 > \Delta y_2 > 0$ as depicted in figure 1.14b. These two different y displacements generate vorticity anomalies in the core as marked as $\oplus$ and $\ominus$ in figure 1.14b. As indicated by (1.21), these anomalies result in positive x mean velocity $\partial(\Delta x_1 + \Delta x_2)/2/\partial t > 0$ further translating the vortex from the initial position as depicted in figure 1.14c. The same reasoning can be applied to the motions in the cross-section B in figure 1.13. Therefore the initial bending perturbations grow. In summary, for an isolated vortex in quasi-geostrophic fluids, bending perturbation with a small wavenumber grows. Although, this discussion explains qualitatively the mechanism of destabilization of the bending mode, it is limited to quasi-geostrophic fluids and the role of the criterion $\zeta'(r) > 0$ discussed by Gent & McWilliams (1986) is unclear. In contrast, Reasor & Montgomery (2001) and Reasor *et al.* (2004) found that certain type of vortices are stable to bending perturbations. A vortex whose vorticity gradient is negative $\zeta'(r_c) < 0$ at a critical radius r_c where $\Omega(r_c) = \omega$ tends to align back vertically when it is subjected to long-wavelength disturbances due to the damping at the critical radius (Briggs *et al.*, 1970; Schecter *et al.*, 2002; Schecter & Montgomery, 2003). In inviscid fluids, this stabilization process is understood from the conservation of total angular momentum (Schecter *et al.*, 2000, 2002). Although Schecter *et al.* (2002) and Schecter & Montgomery (2003) focused on the stabilization mechanism when $\zeta'(r_c) < 0$, they predicted that an instability should occur if the weak outer vorticity gradient at the critical layer is positive $\zeta'(r_c) > 0$ in strongly stratified and rotating fluids. In chapter 3, we shall prove by means of long-wavelength stability analyses of the bending mode of columnar vortices in stratified rotating fluids that the source of the Gent-McWilliams instability is a critical layer with positive vorticity gradient.

1.2.2 Pancake vortices

For vortices with finite thickness, several stability analyses have taken the pancake shape into account by means of models with several uniform layers within the shallow-water or quasi-geostrophic approximations. Baey & Carton (2002) have shown the generation of multipoles in two-layer rotating shallow water. Baroclinic instability occurs for small Burger number and cyclones turned out to be more unstable than anticyclones. Benilov (2003) studied a vortex which is confined in a thin upper layer in a quasi-geostrophic two-layer model. He found that the baroclinic instability which occurs in the lower layer and both layers is due to the positive gradient of potential vorticity at the critical layer. Lahaye & Zeitlin (2015) investigated the centrifugal instability of an anticyclone in two-layers shallow water. They have shown that the asymmetric centrifugal instability is dominant when Ro is small and $m = 2$ barotropic instability dominates for very small Ro. Saunders (1973) and Griffiths & Linden (1981) experimentally studied vortices in two-layers rotating fluids. Figure 1.15a,b show the top and side views of a cone shaped vortex and figure 1.15c shows the side view of a pancake or lenticular shaped vortex in a stratified rotating fluid. They are generated by two different methods: first, a cylinder which contains homogeneous fluids with density

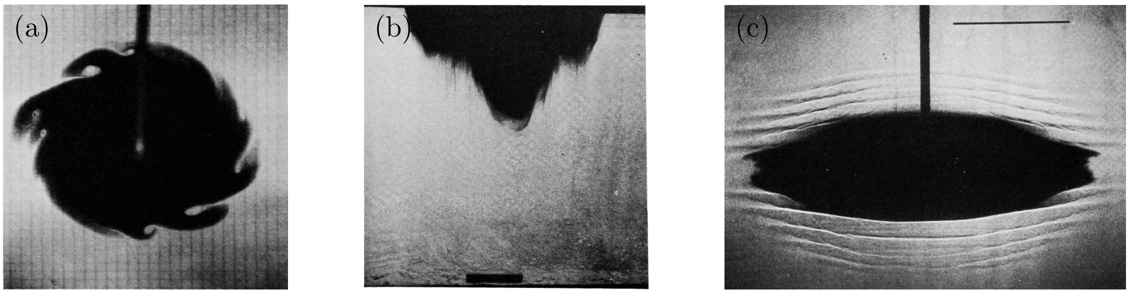

Figure 1.15: (a) Top and (b) side view of a cone-shape vortex and (c) pancake vortex. Images from Griffiths & Linden (1981).

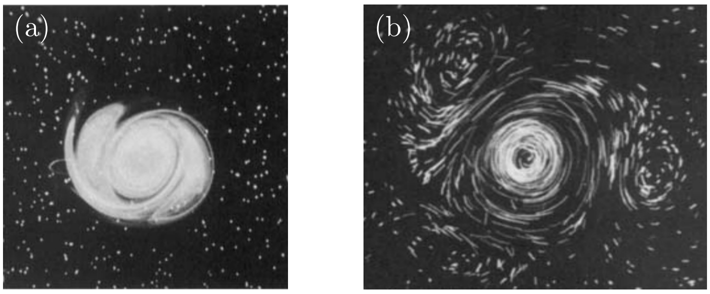

Figure 1.16: Top view of (a) tripolar and (b) triangular vortices. Images from Flór & van Heijst (1996).

ρ_1 is located in the center of a rotating tank filled with heavier fluids with density ρ_2. When the cylinder is removed, a cone shaped vortex develops with time. For the pancake shaped vortex in figure 1.15c, a uniform density fluid is injected into a linearly stratified fluid. They found that both types of vortex are unstable to finite azimuthal wavenumber disturbances. For the cone-shape vortices, the most amplified azimuthal wavenumber is inversely proportional to the square root of the Burger number which is defined as $Bu = g'h/f^2R^2$ where $g' = g|\rho_1 - \rho_2|/\rho_1$, h is the height and R the radius of the cylinder. The layering above and beneath the vortex in figure 1.15c is due to McIntyre instability caused by the differences between the diffusivity κ and the kinematic viscosity ν. Verzicco *et al.* (1997) numerically reproduced the experimental results of Griffiths & Linden (1981) and found that the initial instability is driven by baroclinic instability. Thivolle-Cazat *et al.* (2005) extended the study of Griffiths & Linden (1981) with a much larger rotating tank and observed that baroclinic instability occurs due to initial cyclogeostrophic adjustment process and re-appears later as classical baroclinic instability as found by Griffiths & Linden (1981).

Flór & van Heijst (1996) conducted an experimental study of a pancake a vortex in a linearly stratified non-rotating fluid. They found that disturbances with azimuthal wavenumber $m = 2$ or $m = 3$ are unstable when the Froude number $F = V_{\max}/NR_{\mathrm{vmax}}$ is larger than $F > 0.1$, where $V_{\max}$ is the maximum velocity, N the Brunt–Väisälä frequency, and R_{vmax} the radius of the maximum azimuthal velocity. They also showed that the nonlinear evolutions of the instabilities: formations of tripole ($m = 2$) and dipole splitting, are similar to those for two-dimensional vortices. Some differences come from the faster decay rate of the satellites compared to the core. Bonnier *et al.* (2000) and Beckers *et al.* (2001) studied the density structures in pancake vortices. Bonnier *et al.* (2000) investigated vortices in the far-wake of a towed sphere. The density field inside the vortices shows a pinching of the isopycnals in order to satisfy the hydrostatic and cyclostrophic balances. Beckers *et al.*

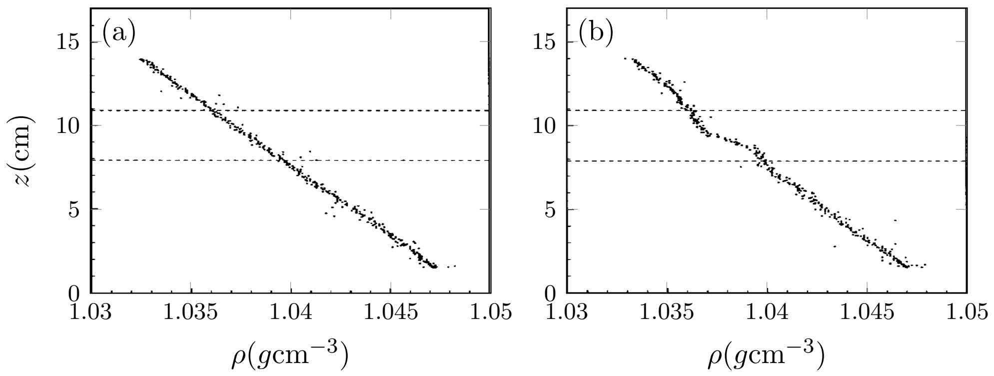

Figure 1.17: Vertical density profiles measured in the center of a monopolar vortex, (a) before the injection, (b) after the injection. Images reproduced from Beckers *et al.* (2001).

(2001) found similar isopycnal deformations experimentally and numerically. Figure 1.17 shows the vertical density profiles of the flow before (figure 1.17a) and after (figure 1.17b) generation of the pancake vortices. The density perturbation is due to the cyclostrophic and hydrostatic balances which are given as

$$\text{Cyclostrophic balance :} \quad \frac{V_\theta^2}{r} = \frac{1}{\rho_0}\frac{\partial p}{\partial r}, \tag{1.29}$$

$$\text{Hydrostatic balance :} \quad -\frac{g}{\rho_0}\rho_b = \frac{1}{\rho_0}\frac{\partial p}{\partial z}. \tag{1.30}$$

These two equations yield the thermal-wind relation

$$\frac{\partial\left(V_\theta^2/r\right)}{\partial z} = -\frac{g}{\rho_0}\frac{\partial \rho_b}{\partial r}. \tag{1.31}$$

where V_θ is the azimuthal velocity of the vortex, ρ_b the density perturbation relative to the unperturbed background linear density profile. As can be seen in (1.31), the vertical gradient of the base velocity determines the radial density gradient. Beckers *et al.* (2001) explained this balance mechanism of the vortex. When the base density is deformed without azimuthal velocity as depicted in solid lines in figure 1.18a ($\rho_b \neq 0$ and $V_\theta = 0$), the restoration of the isopycnals will induce a radially inward flow. A temporary circulation is then formed as indicated by the arrows. On the other hand, when there only exists the velocity but no density perturbations as in figure 1.18b ($\rho_b = 0$ and $V_\theta \neq 0$), the centrifugal forces result in the cyclostrophic adjustment and consequently, the isopycnals will be deformed (dashed lines) (Beckers *et al.*, 2001).

Hedstrom & Armi (1988) generated a stable pancake vortex by well controlled injection of the fluids. They showed that the aspect ratio and the velocity fields of the generated vortex are in good agreement with the prediction by Gill (1981). Recently, Aubert *et al.* (2012) and Hassanzadeh *et al.* (2012) extended the work of Gill (1981). The density gradient inside the vortex has influence on the aspect ratio of the vortex while Gill (1981) has not considered it. They found a universal law for the aspect ratio of pancake vortices: it is proportional to the square root of $(Ro(1+Ro)/(N^2 - N_c^2))$ where N_c is the Brunt–Väisälä frequency in the vortex core. They showed experimentally and numerically that this law holds not only for freely decaying pancake vortices in laboratory but also for planetary vortices (Aubert *et al.*, 2012; Hassanzadeh *et al.*, 2012). Lazar *et al.* (2013*a*,*b*) investigated the stability of

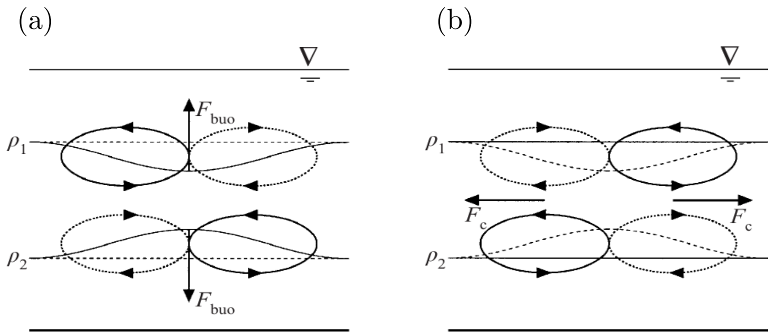

Figure 1.18: (a) Schematic drawing of the circulation pattern induced by the buoyancy force F_{buo} due to the release of a density perturbation. (b) Schematic drawing of the circulation pattern due to the centrifugal force F_{c} in a vortex that is initially not in cyclostrophic balance. Images from Beckers *et al.* (2001).

a vortex in a linearly stratified shallow layer numerically and experimentally. They showed the stabilization of the axisymmetric centrifugal instability when viscosity and stratification are present. Recently, the global stability of a pancake vortex in continuously stratified and rotating fluids has started to be investigated. The studies are either in the non-rotating limit (Beckers *et al.*, 2003; Negretti & Billant, 2013) or in the quasi-geostrophic limit (Nguyen *et al.*, 2012; Hua *et al.*, 2013). For stratified non-rotating fluids, Beckers *et al.* (2003) showed the stability of a vortex with angular velocity $\Omega = \exp(-r^q - z^2/2\alpha^2)$ in terms of q, Re and F, where q is the steepness parameter and α the aspect ratio fixed to $\alpha = 0.3$. Beckers *et al.* (2003) performed 3D nonlinear numerical simulations of azimuthally perturbed vortices using the Navier-Stokes equations under the Boussinesq approximation in order to retrieve the most unstable mode. They observed five types of nonlinear evolution of the unstable mode depending on Re, q and F: shielded monopole (no instability), weak tripolar, compact tripolar, noncompact tripolar and dipole spliting. The vortices tend to be shielded monopole when $q \leq 4$ and $Re \simeq 500$. When Re and q are increased, weak, compact and noncompact tripolar vortices are observed. For large $Re \geq 5000$ and $q \geq 5$, dipole splitting is observed. The instability is similar to the shear instability of two dimensional vortices with the most unstable azimuthal wavenumber increasing with the steepness parameter q (Carton & Legras, 1994). When $q = 2$, they found that the vortex is stable. Negretti & Billant (2013) have conducted a linear stability analysis of a pancake vortex with a Gaussian vorticity profile. They found that the vortex is unstable to gravitational instability when the aspect ratio α is small such that $\alpha/F_h < 1.1$. The gravitational instability occurs when the total vertical density gradient is positive $\partial\rho_t/\partial_z > 0$, i.e. when the isopycnals are overturned (see figure 1.19). They have not observed the shear instability as Beckers *et al.* (2003) because the vorticity gradient does not vanish for a Gaussian vorticity profile. Nguyen *et al.* (2012) have performed numerical stability analyses of a pancake vortex with a Gaussian angular velocity in a continuously quasi-geostrophic fluid. They have shown that the pancake vortex is unstable to baroclinic and barotropic instabilities depending on the Burger number. They distinguished the instabilities as symmetric (figure 1.20a,b) and anti-symmetric (figure 1.20c) modes with respect to $z = 0$ (Nguyen *et al.*, 2012). When $Bu = (\alpha Ro/2F_h)^2$ is very small as $Bu < 0.05$, the $m = 3$ baroclinic mode is dominant, when $0.05 < Bu < 1$, the $m = 2$ baroclinic mode is the most unstable and for $Bu > 1$, the $m = 1$ barotropic mode becomes the most unstable one. The potential vorticity extrema of the unstable modes are localized near the critical level where $\omega_r = m\Omega(r_c)$ when $Bu < 1$ showing that the critical layers play an important role as discussed by Benilov (2003). In

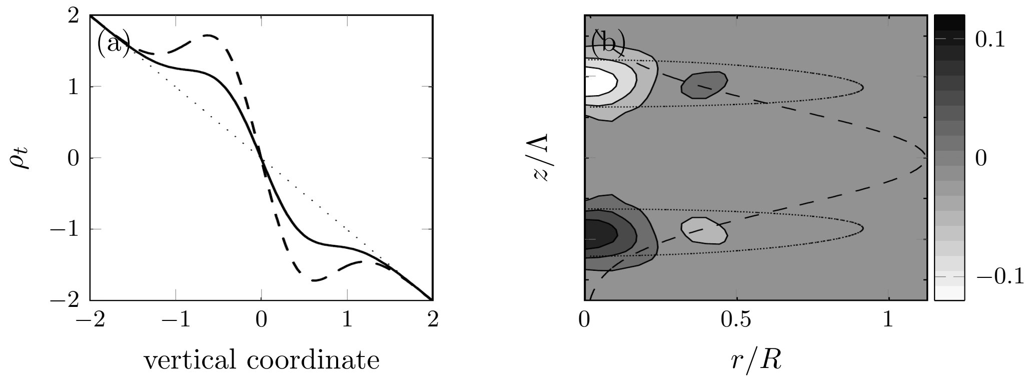

Figure 1.19: (a) Vertical profiles of the base density of gravitationally unstable (dashed line) and stable (solid line) vortices. The dotted line indicates the background density stratification N^2. (b) Vertical velocity perturbation $\mathrm{Re}(u_z)$ of the gravitational instability. The dotted lines delimit the regions where the total vertical density gradient of the base state is positive. Images from Negretti & Billant (2013).

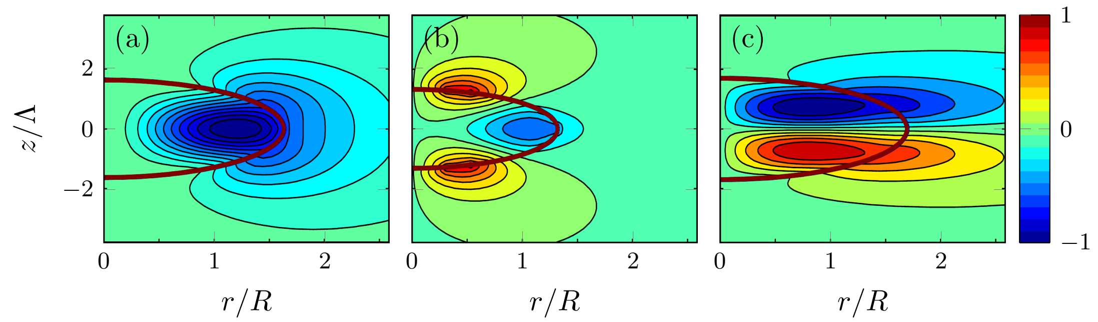

Figure 1.20: Streamfunctions of the symmetric baroclinic instability for (a) $m = 2$ and (b) $m = 1$ for $Bu = 0.3$ and (c) $m = 1$ anti-symmetric barotropic instability for $Bu = 2$. The thick solid line indicates the critical level where $\omega_r = m\Omega(r_c)$. Images from Nguyen *et al.* (2012).

contrast, when $Bu > 1$, the potential vorticity extrema are located near the vortex core (Nguyen *et al.*, 2012). Hua *et al.* (2013) performed three-dimensional numerical simulations of pancake vortices in quasi-geostrophic fluids. They found that the nonlinear evolution of the azimuthal wavenumber disturbances lead to layering near the critical layers.

Because the essential difference between columnar and pancake vortices is the baroclinicity of the vortex, the baroclinic instability is discussed briefly. The baroclinic instability has been first studied in parallel flows in the quasi-geostrophic limit (Eady, 1949; Charney, 1947; Phillips, 1954). The potential energy stored in the inclined isopycnals are converted to kinetic energy by the instability (Vallis, 2006). A necessary condition for the baroclinic instability is that the potential vorticity gradient changes sign somewhere in the flow (Charney & Stern, 1962; Vallis, 2006). For more complex flows, a generalization has been proposed (Eliassen, 1983; Hoskins *et al.*, 1985; Ménesguen *et al.*, 2012): the potential vorticity gradient along isopycnals changes sign

$$\left.\frac{\partial \Pi}{\partial r}\right|_{\rho} = \frac{\partial \Pi}{\partial r} - \frac{\partial \Pi}{\partial z}\frac{\frac{\partial \rho}{\partial r}}{\frac{\partial \rho}{\partial z}}. \tag{1.32}$$

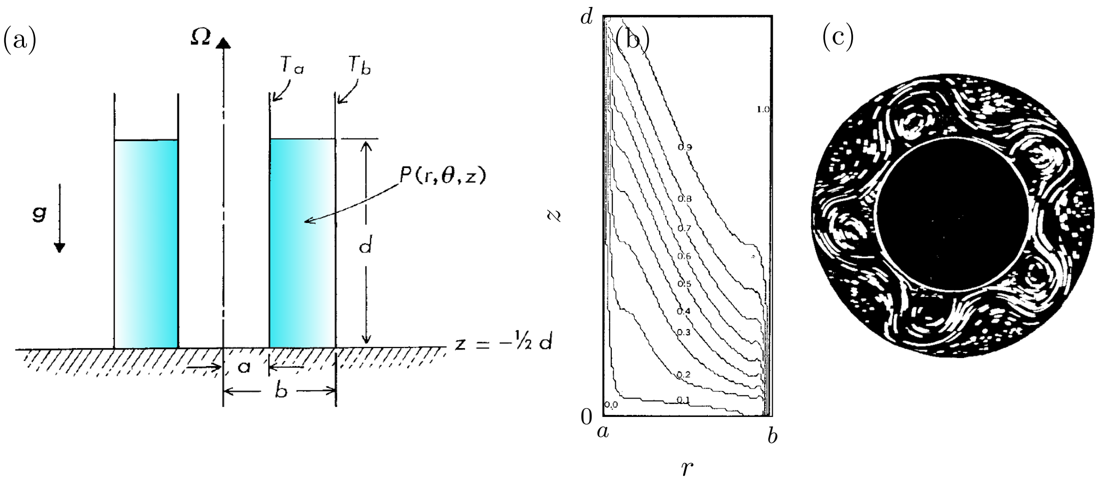

Figure 1.21: (a) Experimental setup used to study the baroclinic instability, (b) horizontal temperature distribution in vertical cross section when the tank is rotating and (c) top view of regular waves. The colors in (a) indicate the horizontal temperature gradient when the tank is at rest. Images are reproduced from Hide & Mason (1975).

Hide & Mason (1975) reviewed the experimental observations of the baroclinic instability in rotating annulus. The density gradient is created by the horizontal temperature differences between two cylinders as seen figure 1.21a. The inner cylinder has a radius a and a uniform surface temperature T_a while the outer cylinder has a radius b and a temperature T_b. An example of the temperature distribution when the tank is rotating is shown in figure 1.21b. Due to the thermal-wind relation the isopycnals (here it is only a function of temperature) are inclined. Depending on the temperature differences, the height and the radii of the cylinders, symmetric, regular and irregular waves can be observed. Figure 1.21c shows the top view of a regular wave (Hide & Mason, 1975). They have applied the Eady model to their baseflow by assuming that the radii of inner and outer cylinders are similar and that all bounding surfaces are rigid. They found that the instability only occurs for Burger number smaller than a critical Burger number: $Bu = 2gd[\rho(T_a) - \rho(T_b)]/(\rho(T_a + T_b) f^2 (b-a)^2) < Bu_{\text{crit}}$ where

$$Bu_{\text{crit}} = \left(\frac{2.4}{\pi}\right)^2 \frac{1}{m^2 + (2(b-a)/\pi(b+a))^2}. \tag{1.33}$$

The maximum value is about 0.6 when $m = 1$. Ménesguen *et al.* (2012) have studied the stability of a jet in rotating stratified fluids for small and intermediate Ro. When Ro is small, baroclinic and barotropic instabilities are found as in quasi-geostrophic fluids and when Ro is large ageostrophic instabilities occur. Legg *et al.* (1998) and Molemaker & Dijkstra (2000) observed the baroclinic instability in cold-core surface eddies. The growth rate of the baroclinic instability is maximum at finite azimuthal wavenumber m_c. It is stable for $m = 0$ and large m (Molemaker & Dijkstra, 2000).

1.3 Goals of the thesis

In this thesis, the stability of both columnar and pancake vortices will be studied. The main goals are to answer the following questions:

For columnar vortices

- What is the destabilization mechanism of the Gent-McWilliams instability when the flow is not quasi-geostrophic? Will the Rayleigh and Fjortoft necessary conditions hold for arbitrary Rossby and Froude numbers?
- What is the general condition for the Gent-McWilliams instability for different types of vortices?
- Why does this instability only exist in the presence of both stratification and rotation as shown by Smyth & McWilliams (1998)?

For pancake vortices

- Only few studies exist on the stability of pancake vortices in continuously stratified rotating fluid. Will the instabilities that are found for columnar vortices like centrifugal, shear, radiative and Gent-McWilliams instabilities also exist in pancake vortices? If so, how will they be affected by the pancake shape?
- What are the different instabilities specific to pancake vortices?
- What is the difference between the stability of pancake vortices in stratified non-rotating fluid and quasi-geostrophic fluids? Can we draw a stability map as a function of Rossby and Froude numbers to link these two limits?
- What are the critical Froude and Rossby numbers for each instability?

To answer these questions, the thesis is organized as follows. In chapter 2, the problem is defined and the numerical methods are introduced. In chapter 3, the stability of the $m = 1$ Gent-McWilliams instability is studied numerically and theoretically in terms of Ro and F_h for various types of columnar vortices. The stability of pancake vortices in stratified non-rotating fluids is presented in chapter 4 and the study of the effect of Ro is continued in chapter 5. The conclusions and the perspectives are presented in chapter 6.

2

Problem formulation

In this chapter, the governing equations and the methodology are presented. The Navier-Stokes equations under the Boussinesq approximation are linearized and the perturbations are assumed to be normal modes with azimuthal wavenumber m. For the columnar vortex, the vertical perturbations are also reduced to normal modes with vertical wavenumber k. For inviscid flows, shooting methods are used and Chebyshev spectral collocation method is used in the presence of viscosity. For the pancake vortices, the governing equations are discretized with finite element methods using FreeFEM++. The generalized eigenvalue problem is solved using external libraries such as SLEPc and PETSc. Leading eigenvalues are found by an iterative Krylov-Schur method and shift-invert spectral method. The code is validated against results obtained by different methods. The convergences are presented in terms of the meshing parameters.

Contents

2.1 Stability problem

2.1.1 The base state

We consider as base flow a vortex with only azimuthal velocity $\boldsymbol{u}_b(r,\theta,z) = [u_r, u_\theta, u_z] = [0, V_\theta(r,z), 0]$ in cylindrical coordinates (r,θ,z). The angular velocity is Gaussian in both radial and vertical directions

$$\frac{V_\theta(r,z)}{r} = \Omega(r,z) = \Omega_0 \mathrm{e}^{-\left(\frac{r^2}{R^2}+\frac{z^2}{\Lambda^2}\right)}, \tag{2.1}$$

where R is the radius, Λ the half thickness of the vortex and Ω_0 the maximum angular velocity. The total pressure and density are decomposed as follows:

$$p_t = p_0 + \bar{p}(z) + p_b(r,z), \tag{2.2}$$
$$\rho_t = \rho_0 + \bar{\rho}(z) + \rho_b(r,z), \tag{2.3}$$

where the values with the subscript 0 are reference values, those with a bar indicate the mean vertical profiles and those with a subscript b correspond to the perturbations due to the base flow. The Euler equations under the Boussinesq approximation in the radial and vertical directions are

$$r\Omega^2 + fr\Omega = \frac{1}{\rho_0}\frac{\partial p_t}{\partial r}, \tag{2.4}$$
$$-\frac{g}{\rho_0}\rho_t = \frac{1}{\rho_0}\frac{\partial p_t}{\partial z}, \tag{2.5}$$

corresponding to cyclostrophic and hydrostatic balances, where f is the Coriolis parameter (considered constant) and g the gravity. Combining (2.4) and (2.5) gives the thermal-wind relation:

$$\frac{\partial(r\Omega^2 + fr\Omega)}{\partial z} = -\frac{g}{\rho_0}\frac{\partial \rho_b}{\partial r}. \tag{2.6}$$

Hence, the base density deformation ρ_b is given by

$$\rho_b(r,z) = -z\frac{\rho_0}{\mathrm{g}}\left(\frac{R}{\Lambda}\right)^2 (\Omega + f)\,\Omega. \tag{2.7}$$

Figure 2.1 shows the base angular velocity Ω and vertical vorticity $\zeta = 1/r\partial(rV_\theta)/\partial r$. Figure 2.2 shows the isopycnals for different values of f for fixed Brunt-Vaisala frequency and aspect ratio $\alpha = \Lambda/R$. Due to the thermal-wind relation (2.6), the base density field becomes strongly deformed when $|f|$ is large.

2.1.2 Linearized equations

The vortex is perturbed by infinitesimal perturbations (denoted with prime) of velocity $\boldsymbol{u}' = [u'_r, u'_\theta, u'_z]$, pressure p', and density ρ' as

$$\boldsymbol{u}(r,\theta,z) = \boldsymbol{u_b} + \boldsymbol{u}' = (0, r\Omega(r,z), 0) + (u'_r, u'_\theta, u'_z), \tag{2.8}$$
$$p = p_t + p', \tag{2.9}$$
$$\rho = \rho_t + \rho'. \tag{2.10}$$

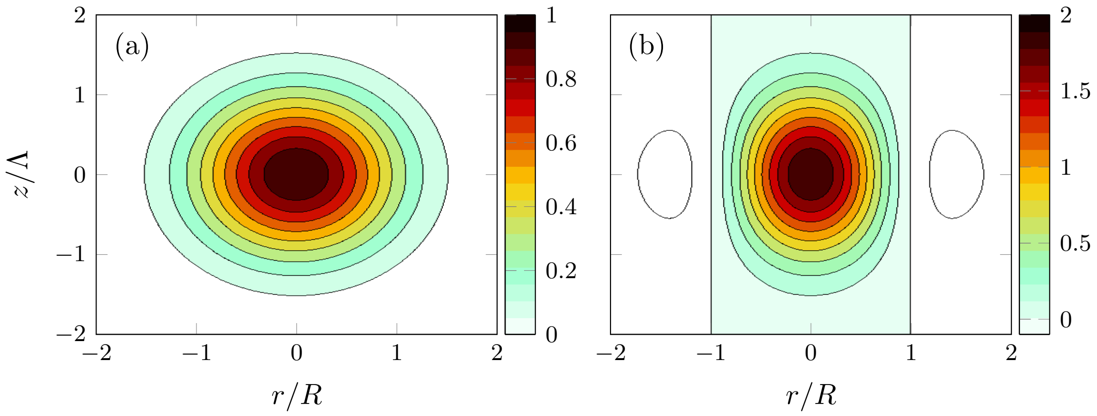

Figure 2.1: (a) Base angular velocity Ω (2.1) and (b) vertical vorticity ζ.

The perturbations are written as normal modes in the azimuthal direction

$$[u'_r, u'_\theta, u'_z, \rho', p'] = [u_r(r,z), u_\theta(r,z), u_z(r,z), \frac{\rho_0}{g}\rho(r,z), \rho_0 p(r,z)]\mathrm{e}^{-\mathrm{i}\omega t + \mathrm{i}m\theta} + \text{c.c.}, \tag{2.11}$$

where $\omega = \omega_r + \mathrm{i}\omega_i$, ω_r the frequency, ω_i the growth rate and m the azimuthal wavenumber. We consider that m is positive since negative wavenumbers can be recovered by the symmetry: $\omega(m) = \omega^*(-m)$. Under the Boussinesq approximations, the linearized Navier-Stokes equations are

$$-\mathrm{i}(\omega - m\Omega)u_r - (2\Omega + f)u_\theta = -\frac{\partial p}{\partial r} + \nu\left(\nabla^2 u_r - \frac{1}{r^2}u_r - \frac{2}{r^2}\mathrm{i}mu_\theta\right) \tag{2.12}$$

$$-\mathrm{i}(\omega - m\Omega)u_\theta + (\zeta + f)u_r + \frac{\partial r\Omega}{\partial z}u_z = -\frac{\mathrm{i}m}{r}p + \nu\left(\nabla^2 u_\theta - \frac{1}{r^2}u_\theta + \frac{2}{r^2}\mathrm{i}mu_r\right) \tag{2.13}$$

$$-\mathrm{i}(\omega - m\Omega)u_z = -\frac{\partial p}{\partial z} - \rho + \nu\nabla^2 u_z \tag{2.14}$$

$$-\mathrm{i}(\omega - m\Omega)\rho + \frac{g}{\rho_0}\frac{\partial \rho_b}{\partial r}u_r + \frac{g}{\rho_0}\frac{\partial \rho_b}{\partial z}u_z = N^2 u_z + \kappa\nabla^2\rho \tag{2.15}$$

$$\frac{1}{r}\frac{\partial r u_r}{\partial r} + \frac{1}{r}\mathrm{i}mu_\theta + \frac{\partial u_z}{\partial z} = 0 \tag{2.16}$$

where $N = \sqrt{-\mathrm{g}/\rho_0 \mathrm{d}\bar{\rho}/\mathrm{d}z}$ is the constant Brunt–Väisälä frequency, ν the viscosity and κ the diffusivity of the stratifying agent. The problem is governed by five non-dimensional numbers: aspect ratio (α), Froude number (F_h), Reynolds number (Re), Schmidt number (Sc), defined as follows:

$$\alpha = \frac{\Lambda}{R}, \qquad F_h = \frac{\Omega_0}{N}, \qquad Ro = \frac{2\Omega_0}{f}, \qquad Re = \frac{\Omega_0 R^2}{\nu}, \qquad Sc = \frac{\nu}{\kappa}. \tag{2.17}$$

In this thesis, we keep $Sc = 1$ for simplicity and to avoid the viscous-diffusive instability (McIntyre, 1970).

2.2 Numerical methods for columnar vortex

When $\alpha = \infty$, the base flow is only function of radial direction

$$\Omega = \Omega_0 \mathrm{e}^{-r^2/R^2}, \tag{2.18}$$

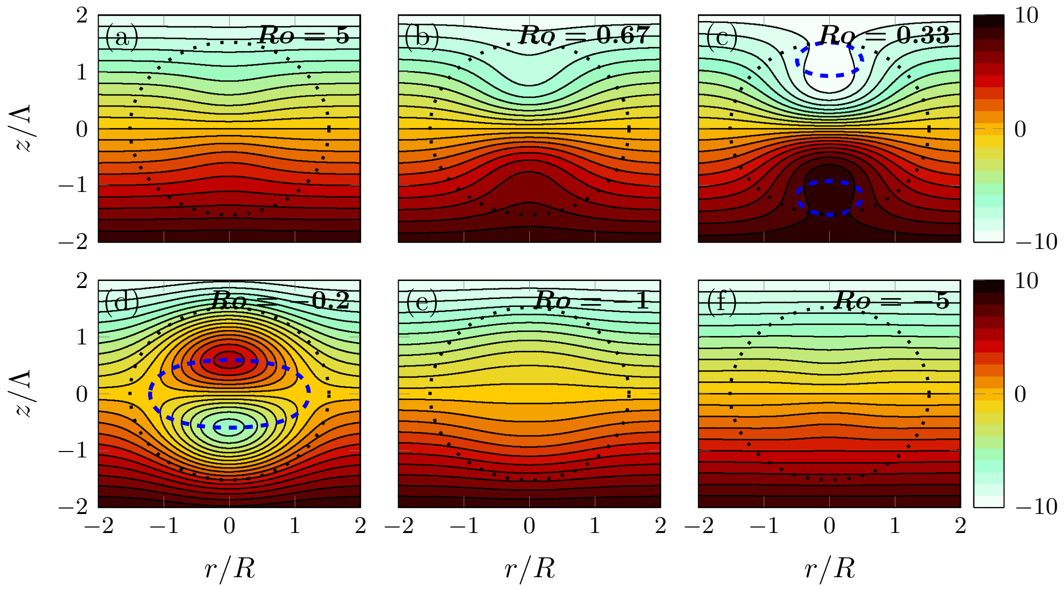

Figure 2.2: Total density contours as a function of background rotation $Ro = 2\Omega_0/f$: (a) $Ro = 5$, (b) $Ro = 0.67$, (c) $Ro = 0.33$, (d) $Ro = -0.2$, (e) $Ro = -1$ and (f) $Ro = -5$. Other parameters are fixed as $\alpha = \Lambda/R = 0.5$ and $F_h = 0.3$. The density fields (c) and (d) are gravitationally unstable $\partial\rho_t/\partial z > 0$ in the regions delimited by dashed lines. The dotted lines indicate the limits of the base vortex as $\Omega = 0.1\Omega_0$.

and the base density perturbation vanishes: $\rho_b = 0$. The perturbations are then assumed to be of the form $\xi' = \xi(r)\exp(\mathrm{i}(-\omega t + kz + m\theta))$ where k is the vertical wavenumber and ξ is any perturbation.

Inviscid flow When $\nu = 0$, (2.12) – (2.16) can be reduced to a single radial velocity equation for $\varphi = ru_r$

$$\frac{\mathrm{d}^2\varphi}{\mathrm{d}r^2} - \left[\frac{1}{r} + \frac{Q'}{Q}\right]\frac{\mathrm{d}\varphi}{\mathrm{d}r} - \left[\frac{m^2}{r^2} + k^2F_h^2\frac{\phi - s^2}{1 - s^2F_h^2} + \frac{m}{rs}\left(\zeta' - \left(\frac{2}{Ro} + \zeta\right)\left(\frac{2}{r} + \frac{Q'}{Q}\right)\right)\right]\varphi = 0, \tag{2.19}$$

where $Q = m^2/r^2 - k^2F_h^2s^2/(1 - s^2F_h^2)$, $s = m\Omega - \omega$ is the Doppler shifted frequency, $\phi = (2\Omega + 2/Ro)(\zeta + 2/Ro)$ is the Rayleigh discriminant, $\zeta = (1/r)\partial(rV_\theta)/\partial r$ is the vertical vorticity and $\Omega = V_\theta/r$ is the non-dimensional angular velocity of the basic vortex. The boundary condition at $r = 0$ is that the perturbations should be non-singular and decays or propagates outward for $r = \infty$. Hence, $\varphi \sim r^m$ for $r \to 0$ and (2.19) has solution for $r \gg 1$ as

$$\varphi = \mathrm{K}_m(\beta kr) + \frac{\omega Ro}{m(2 + \omega Ro)}\beta kr\mathrm{K}_{m-1}(\beta kr), \tag{2.20}$$

$$\varphi = \mathrm{H}_m^{(n)}(|\beta|kr) - \frac{\omega Ro}{m(2 + \omega Ro)}|\beta|kr\mathrm{H}_{m-1}^{(n)}(|\beta|kr), \tag{2.21}$$

with $\beta^2 = (4/Ro^2 - \omega^2)/(1/F_h^2 - \omega^2)$, where K_m is the modified Bessel function of order m of the second kind and $\mathrm{H}_m^{(n)}$ is the Hankel function of order m of kind n. The solution (2.20) ensures that the perturbation decays as $r \to \infty$ except when $\omega_i = 0$ and $\beta^2 < 0$. In the latter case, we use the solution (2.21) which describes an outward propagating wave, i.e.

a positive group velocity $\partial\omega/\partial\beta > 0$. Hence, $n = 1$ when $\omega_r(Ro^2/4 - F_h^2) > 0$ and $n = 2$ when $\omega_r(Ro^2/4 - F_h^2) < 0$. When $\omega_i > 0$, the asymptotic solution (2.20) corresponds also to the solution which propagates outwards.

Equation (2.19) has been solved by a shooting method. The numerical integration is started from a small radius r_1 and a large radius r_2 toward a radius r_f using the asymptotic solutions of (2.19) and an initial guess for ω. This leads to two couples of values at r_f : $[\varphi_1(r_f), \varphi_1'(r_f)]$ and $[\varphi_2(r_f), \varphi_2'(r_f)]$. The value of ω for which the Wronskian $\varphi_2(r_f)\varphi_1'(r_f) - \varphi_1(r_f)\varphi_2'(r_f)$ vanishes is then searched by an iterative scheme. The path of integration is deformed in the complex plane in order to avoid the singular radii r_c where $s = m\Omega(r_c) - \omega = 0$ or $s = \pm 1/F_h$. Since the vortex profiles studied have $\Omega'(r_c) < 0$, the path is deformed in the upper complex plane in order that the inviscid solution be the proper limit of the viscous solution (Lin, 1955; Le Dizès, 2004). Figure 2.3 shows an example a deformed integration path r which is defined as

$$r = x\left(1 - \mathrm{i}\delta m \frac{\partial\Omega}{\partial r}\left(1 - \frac{x}{r_2}\right)\right), \tag{2.22}$$

where δ is a constant and x real.

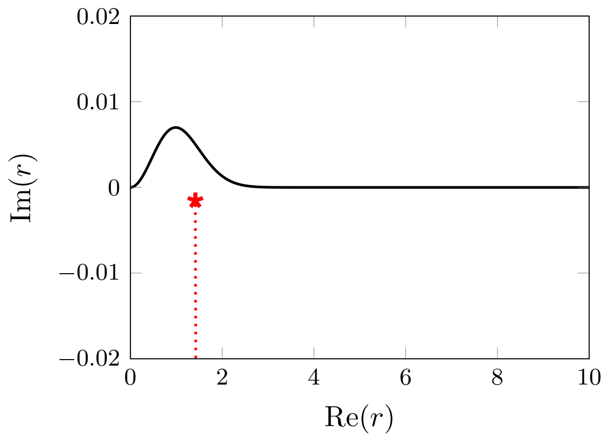

Figure 2.3: Integration path (2.22) in the complex plane (——) to avoid the critical radius r_c (······) for $r_2 = 20$ and $\delta = 0.05$.

Viscous flow The stability problem (2.12)–(2.16) in the presence of viscous and diffusive effects has been solved by a Chebyshev pseudo-spectral collocation method (Antkowiak & Brancher, 2004). This code has allowed us to check the results of the shooting code and the code for pancake vortices. The Chebyshev spectral collocation method allows to write (2.12)–(2.16) in forms of the generalized eigenvalue problem

$$-\mathrm{i}\omega\mathbf{B}\boldsymbol{v} = \mathbf{L}\boldsymbol{v}, \tag{2.23}$$

where $\boldsymbol{v} = [u_r, u_\theta, \rho]$, $\mathbf{L}$ and $\mathbf{B}$ are the differential operators. The other variables u_z and p are obtained from $\boldsymbol{v}$ afterwards. The radial direction $[-\infty, \infty]$ is mapped to the Chebyshev domain [-1, 1]. Since r is mapped to $r = \pm\infty$, no boundary conditions are needed for $r = 0$. Here, we used algebraic mapping from the Chebyshev domain to the radial domain as in Antkowiak & Brancher (2004); Fabre & Jacquin (2004).

2.3 Numerical methods for pancake vortex

2.3.1 Descriptions

For pancake vortices, only the viscous equations (2.12)–(2.16) are solved. The discretization is done by finite element method and the generalized eigenvalue problem is solved. The code has been developed by Garnaud (2012) and adapted to pancake vortices. Equations (2.12) – (2.16) are discretized with finite element method using FreeFEM++ (Hecht, 2012; Garnaud, 2012; Garnaud *et al.*, 2013). Velocity, density and pressure $(\vec{u}, \rho, p)$ are approximated with (P2, P1, P1) elements, respectively (De Vuyst, 2013). The mesh is adapted to the base state and refined around the vortex core. The domain is restricted to positive radius $r = [0, R_{\max}]$ and is set to $z = [-Z_{\max}, Z_{\max}]$ along the vertical. Figure 2.4 shows an example of a mesh adapted to the base angular velocity Ω, the vertical density gradient $\partial\rho_b/\partial z$ and the inflection point $r_I = \sqrt{2}$ where $\zeta'(r_I) = 0$. Since FreeFEM++ implements only weak

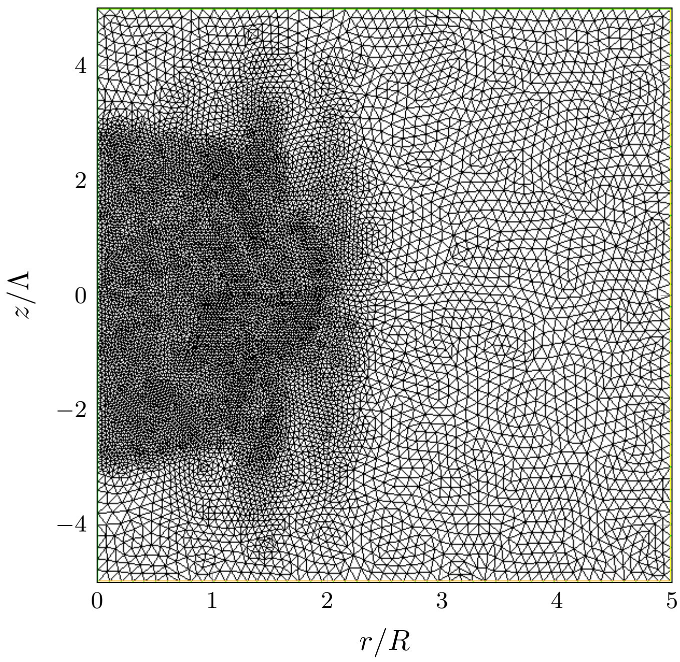

Figure 2.4: Example of a mesh adapted to the base angular velocity Ω, the vertical density gradient $\partial\rho_b/\partial z$ and the inflection point $r_I = \sqrt{2}$ where $\zeta'(r_I) = 0$. The minimum and maximum size of the elements are $S_{\min} = 0.027R$ and $S_{\max} = 0.13R$, respectively. The number of triangle is 18452.

formulations, weak forms of (2.12) – (2.16) are used. For example, weak forms of a set of partial derivative equations $A(p, q) = 0$ and $B(p, q) = 0$ are presented as

$$\int_S (A(p,q)\mathtt{v_1} + B(p,q)\mathtt{v_2}) = 0, \tag{2.24}$$

where S is the domain of interest and $\mathtt{v_1}$ and $\mathtt{v_2}$ are arbitrary vectors called test functions.

To get the weak form, (2.12) – (2.16) are first multiplied by r^2 to avoid any singularity at $r = 0$ and then by the test functions $\mathtt{v_r}, \mathtt{v}_\theta, \mathtt{v_z}, \tau$ and $\mathtt{q}$, respectively. The weak form is then found as

$$\int_S \Big[\mathrm{i}\omega u_r + \mathrm{i}m\Omega u_r (2\Omega + f) u_\theta - \frac{\partial p}{\partial r} + \nu\left(\nabla^2 u_r - \frac{1}{r^2}u_r - \frac{2}{r^2}\mathrm{i}m u_\theta\right)\Big] r^2 \mathtt{v_r}$$
$$+ \Big[\mathrm{i}\omega u_\theta + \mathrm{i}m\Omega u_\theta - (\zeta + f)u_r - \frac{\partial r\Omega}{\partial z}u_z - \frac{\mathrm{i}m}{r}p + \nu\left(\nabla^2 u_\theta - \frac{1}{r^2}u_\theta + \frac{2}{r^2}\mathrm{i}m u_r\right)\Big] r^2 \mathtt{v}_\theta$$
$$+ \Big[\mathrm{i}\omega u_z + \mathrm{i}m\Omega u_z - \frac{\partial p}{\partial z} - \rho + \nu\nabla^2 u_z\Big] r^2 \mathtt{v_z}$$
$$+ \Big[\mathrm{i}\omega\rho + \mathrm{i}m\Omega\rho - \frac{g}{\rho_0}\frac{\partial\rho_b}{\partial r}u_r - \frac{g}{\rho_0}\frac{\partial\rho_b}{\partial z}u_z + N^2 u_z + \kappa\nabla^2\rho\Big] r^2 \tau$$
$$+ \Big[\frac{1}{r}\frac{\partial r u_r}{\partial r} + \frac{1}{r}\mathrm{i}m u_\theta + \frac{\partial u_z}{\partial z}\Big] r^2 \mathtt{q} = 0 \tag{2.25}$$

The Laplace operators are second order derivatives and can be reduced by integration by parts using Green's identity:

$$\int_S \nabla^2 u \mathtt{v} = -\int_S \nabla u \nabla \mathtt{v} + \int_{\partial S} \nabla u \mathtt{v} \mathbf{n}, \tag{2.26}$$

where $\mathbf{n}$ is the outward unit surface normal to ∂S. The pressure gradient can also be reduced as

$$\int_S r^2 \nabla p \mathtt{v} = -\int_S p \nabla(r^2 \mathtt{v}) + \int_{\partial S} p r^2 \mathtt{v}, \tag{2.27}$$

When $\mathtt{v} = 0$ on ∂S, (2.25) becomes

$$\int_S -\mathrm{i}\omega r^2 (u_z \mathtt{v_z} + u_r \mathtt{v_r} + u_\theta \mathtt{v}_\theta + \rho\tau) =$$
$$\int_S \Bigg[(r^2 f u_\theta - r V_\theta(\mathrm{i}m u_r - 2u_\theta))\mathtt{v_r} - \left(r^2\left(u_r\frac{\partial V_\theta}{\partial r} + u_z\frac{\partial V_\theta}{\partial z} + f u_r\right) + rV_\theta(\mathrm{i}m u_\theta + u_r)\right)\mathtt{v}_\theta$$
$$-(r^2\rho + r(V_\theta \mathrm{i}m u_z))\mathtt{v_z} - \left(r^2\left(u_r\frac{\partial\rho_b}{\partial r} + u_z\frac{\partial\rho_b}{\partial z} - N^2 u_z\right) + rV_\theta \mathrm{i}m\rho\right)\tau$$
$$-\nu\Bigg(r^2\frac{\partial u_r}{\partial z}\frac{\partial \mathtt{v_r}}{\partial z} + r^2\frac{\partial u_r}{\partial r}\frac{\partial \mathtt{v_r}}{\partial r} + r\frac{\partial u_r}{\partial r}\mathtt{v_r} + (m^2+1)u_r\mathtt{v_r} + 2\mathrm{i}m u_\theta \mathtt{v_r}$$
$$+ r^2\frac{\partial u_\theta}{\partial z}\frac{\partial \mathtt{v}_\theta}{\partial z} + r^2\frac{\partial u_\theta}{\partial r}\frac{\partial \mathtt{v}_\theta}{\partial r} + r\frac{\partial u_\theta}{\partial r}\mathtt{v}_\theta + (m^2+1)u_\theta\mathtt{v}_\theta - 2\mathrm{i}m u_r \mathtt{v}_\theta$$
$$+ r^2\frac{\partial u_z}{\partial z}\frac{\partial \mathtt{v_z}}{\partial z} + r^2\frac{\partial u_z}{\partial r}\frac{\partial \mathtt{v_z}}{\partial r} + r\frac{\partial u_z}{\partial r}\mathtt{v_z} + m^2 u_z \mathtt{v_z}$$
$$+ \frac{1}{Sc}\left(r^2\frac{\partial\rho}{\partial z}\frac{\partial\tau}{\partial z} + r^2\frac{\partial\rho}{\partial r}\frac{\partial\tau}{\partial r} + r\frac{\partial\rho}{\partial r}\tau + m^2\rho\tau\right)\Bigg)$$
$$+ pr\left(r\frac{\partial \mathtt{v_z}}{\partial z} + r\frac{\partial \mathtt{v_r}}{\partial r} + 2\mathtt{v_r} - \mathrm{i}m\mathtt{v}_\theta\right) - \mathtt{q}r\left(r\frac{\partial u_z}{\partial z} + r\frac{\partial u_r}{\partial r} + u_r + \mathrm{i}m u_\theta\right)\Bigg]. \tag{2.28}$$

FreeFEM++ write these equations in the matrix form

$$-\mathrm{i}\omega \mathbf{B}\boldsymbol{v} = \mathbf{L}\boldsymbol{v}, \tag{2.29}$$

where $\boldsymbol{v} = [u_r, u_\theta, u_z, \rho, p]$. The matrices are sparse and the typical size of the matrices $\mathbf{B}$ and $\mathbf{L}$ is about $10^6 \times 10^6$. Dirichlet boundary conditions are applied at $r = R_{\max}$ and $z = \pm Z_{\max}$ so that all perturbations vanish. The boundary conditions at $r = 0$ differs depending on the

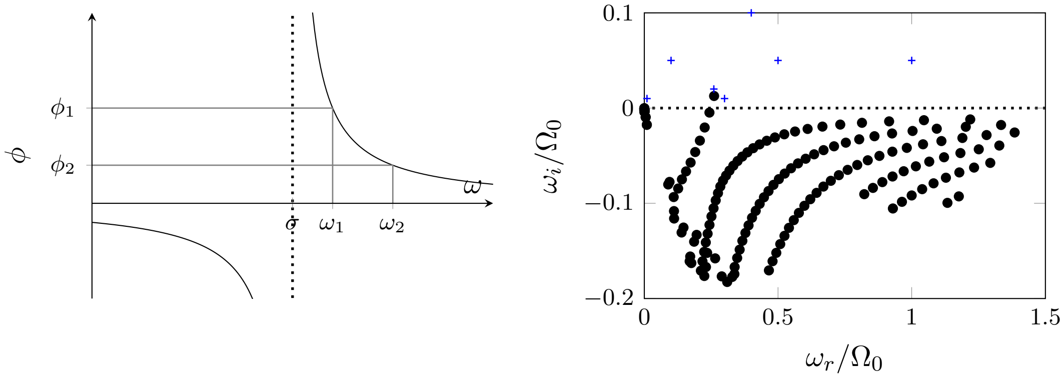

Figure 2.5: (a) The shift-and-invert spectral transformation. Image is reproduced from Roman *et al.* (2015). (b)An example of spectrum: frequency ω_r and growth rate ω_i normalized to the maximum angular velocity of base vortex Ω_0. One unstable mode ($\omega_i > 0$) is found:+ shift-values; • eigenvalues.

azimuthal wavenumber m (Ash & Khorrami, 1995; Batchelor & Gill, 1962),

$$\begin{aligned} m = 0: &\qquad u_r = u_\theta = 0, \\ m = 1: &\qquad u_z = p = \rho = 0, \\ m \geq 2: &\qquad u_r = u_\theta = u_z = p = \rho = 0. \end{aligned}$$

The dirichlet boundary conditions can be implemented in two ways in FreeFEM++. First, the boundary condition is incorporated with penalty method by distributing large values (10^{30}) at the boundaries (Hecht, 2012). In the code, boundaries are imposed directly to the matrices by a command `on`, for example for $m = 0$:

$$\texttt{on}(4, u_r = u_\theta = 0) + \texttt{on}(1, 2, 3, u_r = u_\theta = u_z = p = \rho = 0), \tag{2.30}$$

where the numbers are boundary labels. The bottom ($z = -Z_{\max}$) is labelled 1 and the numbers increases in the anti-clockwise direction. The boundary conditions are applied directly to $\mathbf{L}$ and $\mathbf{B}$. The second method is simply replacing the corresponding elements to zero (Garnaud, 2012; Zienkiewicz & Taylor, 2000). This means the substitution of

$$\boldsymbol{v}_{bc} = [u_r, u_\theta, u_z, p, \rho]^{\mathrm{T}}_{bc} = 0, \tag{2.31}$$

in (2.29). This is equivalent to reduce the number of equations and thus to reduce the total number of unknown components (Zienkiewicz & Taylor, 2000). In FreeFEM++, boundary matrix is saved in a separate file as BC. Then, the boundary condition is applied after loaded in python as $\mathbf{L}_{new} = \mathsf{BC}^{\mathsf{T}}\mathbf{L}\mathsf{BC}$ and $\mathbf{B}_{new} = \mathsf{BC}^{\mathsf{T}}\mathbf{B}\mathsf{BC}$. Since some components are deleted, the node informations are re-designated. The advantage of this way of implementation is that the boundary conditions for different azimuthal wavenumbers can be easily applied without generating new meshes. If no boundary condition is specified, Neumann boundary conditions are applied by

$$\left.\frac{\partial u}{\partial n}\right|_{bc} = 0. \tag{2.32}$$

Once discretized using FreeFEM++, $\mathbf{L}$ and $\mathbf{B}$ (and BC) are loaded in python. Python calls the external packages to compute the eigenvalue problem throughout slepc4py and petsc4py. The eigenvalue problem is solved by an iterative Krylov-Schur method using the libraries

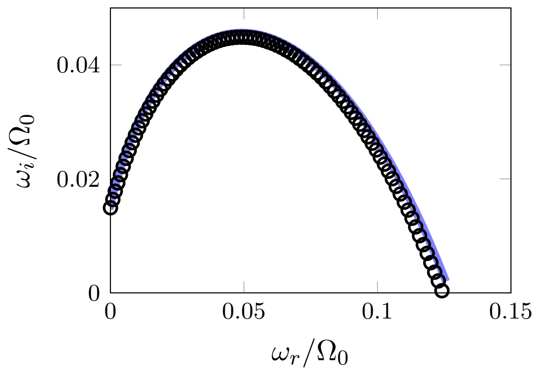

Figure 2.6: Growth rate ω_i/Ω_0 and frequency ω_r/Ω_0 spectrum for columnar (—) and pancake (○) vortices for $m = 1, F_h = 0.05$, $Ro = 0.1$ and $Re = 1000$.

SLEPc and PETSc and shift-and-invert spectral transformation is used: for a given shift value σ, the eigenvalues ω which is near σ are found (Hernandez *et al.*, 2005; Garnaud, 2012; Garnaud *et al.*, 2013; Balay *et al.*, 2014; Roman *et al.*, 2015):

$$(\mathbf{L} + i\omega\mathbf{B})^{-1}\boldsymbol{v} = \phi\boldsymbol{v}, \tag{2.33}$$

where $\phi = 1/(\omega - \sigma)$. Hence, ϕ is very large when ω is near the shift value σ. Once the wanted eigenvalues ϕ have been found, they are transformed back to eigenvalues of the original problem $\omega = \sigma + 1/\phi$ (see for example 2.5a for real eigenvalues). The eigenvectors $\boldsymbol{v}$ remain unchanged (Roman *et al.*, 2015). The number of eigenvalues computed for each shift value is between 20 to 50 in this thesis. We used generally tens of shift values to capture all the unstable modes. Spurious modes are eliminated by excluding non-repeated values (varying by more than 10^{-6}) among several shift values. Figure 2.5b shows a spectrum example. The shift-values are also shown as cross symbols. They are set only in the positive ω_i and ω_r domain. There exist only one unstable mode. The library SLEPc and PETSc enable MPI parallel computation by distributing CSR matrices to processors (Hernandez *et al.*, 2005; Garnaud, 2012; Garnaud *et al.*, 2013; Balay *et al.*, 2014; Roman *et al.*, 2015). The input and output data is saved as HDF5 file.

2.3.2 Validations

Two methods have been used to validate the code. One is to compare the 1D results for a columnar vortex and the other is to compare to previous results on pancake vortices.

Comparison to columnar vortex Figure 2.6 shows the spectrum for a columnar vortex for $m = 1, F_h = 0.05$, $Ro = 0.1$ and $Re = 1000$. Continuous line is for 1D code for Chebyshev pseudo-spectral collocation method as described in §2.2. The discrete symbols are with the present code with FreeFEM++ and SLEPc for the columnar profile (2.18). The vertical limits for FreeFEM++ have been set to large value $Z_{\max} = 120R$ and $R_{\max} = 5R$. The growth rates and the frequencies agree well.

Comparison to 3D pseudo-spectral method We have also validated the code against the results of Negretti & Billant (2013). They have investigated the stability of a vortex with

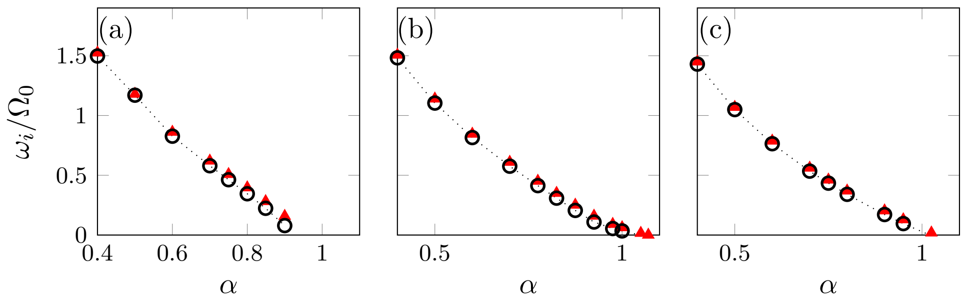

Figure 2.7: Growth rates obtained by Negretti & Billant (2013) using (▲) and with the present code (··○··) as a function of aspect ratio α for azimuthal wavenumber (a) $m = 0$, (b) $m = 1$ and (c) $m = 2$ for $F_h = 1, Ro = \infty$ and $Re = 500$.

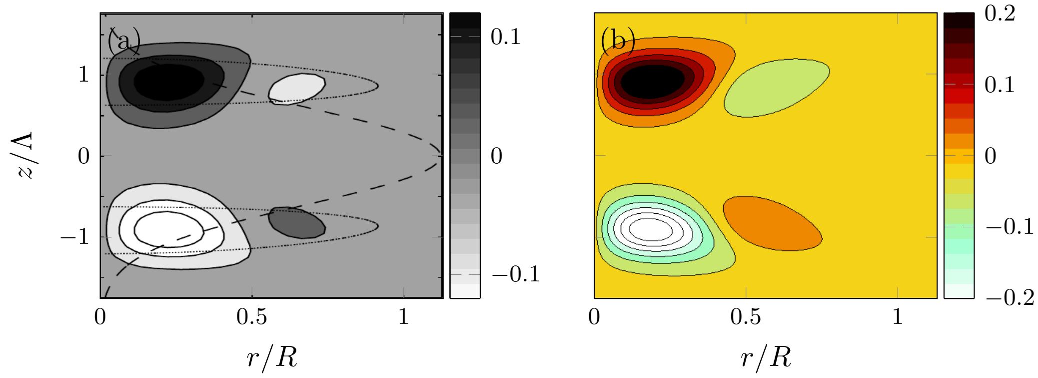

Figure 2.8: Vertical velocity perturbations $\mathrm{Re}(u_z)$ (a) obtained by Negretti & Billant (2013) and (b) with the present code for $\alpha = 0.85, m = 1, F_h = 1, Ro = \infty$ and $Re = 500$.

the angular velocity profile:

$$\Omega = \Omega_0 \frac{1 - \mathrm{e}^{-r^2/R^2}}{r^2} \mathrm{e}^{-z^2/\Lambda^2}. \tag{2.34}$$

They have computed the most unstable mode by integrating (2.12)–(2.16) over a long time by means of a pseudo-spectral code. The dominant mode for each azimuthal wavenumber is obtained by a model decomposition. Figure 2.7 show a comparison the growth rate obtained by the two methods as a function of the aspect ratio α for different azimuthal wavenumbers $m = 0, 1$ and 2. All the results agree well. Figure 2.8 shows the real part of the vertical velocity perturbation $\mathrm{Re}(u_z)$. The mode shapes are also in good agreement. The present method is faster and allows to obtain not only the dominant mode, but also the weaker unstable modes.

We also have compared the results to those of Nguyen *et al.* (2012). They used the quasi-geostrophic equation and solved the eigenvalue problem by a QZ method. Figure 2.9 shows a comparison of the modes for $m = 2$ and $Bu = (N\alpha/f)^2 = 0.3$. The modes agrees well. However, the growth rates are different: Nguyen *et al.* (2012) found that the growth rate is $\omega_i = 0.012\Omega_0$ (taking into account their normalization) in the inviscid case while we found $\omega_i = 0.006\Omega_0$ for $Re = 10000$. These differences might come from the resolution and viscous effects.

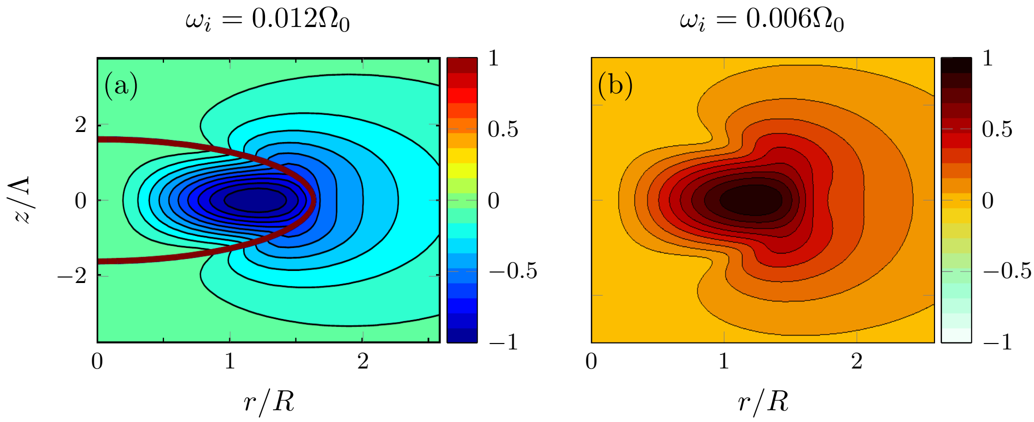

Figure 2.9: Streamfunction perturbations Re(ψ) (a) obtained by Nguyen *et al.* (2012) (figure 5a in Nguyen *et al.* (2012)) for $Bu = 0.3$ and (b) the present code for $Bu = 0.3$ ($\alpha = 0.5, m = 2, F_h = 0.15, Ro = -0.33$) and $Re = 10000$.

2

2.3.3 Parameter dependency

The convergence of the growth rate depends on the size of the meshes as well as the domain size. Here, we show the effect of these parameters. The main difficulties with the code come from choosing right meshing parameters. For the sake of saving computing times, we want to have a minimum number of meshes by choosing appropriate minimum and maximum sizes of meshes and a minimum domain size but the eigenvectors should be well resolved. The only way to achieve this is trials and errors. Here, some examples are shown. In addition, since the code is parallelized, the effect of the number of processors on the computing time is also discussed.

Effect of the size of meshes Figure 2.10 shows the effect of the mesh sizes on the maximum growth rates for $\alpha = 0.5, m = 2, F_h = 0.5, Ro = \infty$ and $Re = 10000$. Since the mesh is adapted to the base flow, the mesh size is not uniform throughout the domain. The effects of the maximum and minimum sizes are investigated separately. First, figure 2.10a shows the growth rate as a function of minimum mesh size for two different ranges of maximum sizes: $S_{\max} = 0.15R - 0.2R$ and $S_{\max} = 0.05R - 0.08R$. When $S_{\max}$ is in the range of $0.15R - 0.2R$, the growth rate varies with $S_{\min}$ and becomes constant when $S_{\min} < 0.005R$. However, when $S_{\max}$ is small ($S_{\max} = 0.05R - 0.08R$), the growth rate converges quickly and $S_{\min}$ has little effect on the growth rate. Figure 2.10b shows the effect of maximum size on the growth rates for two different ranges $S_{\min} = 0.017R - 0.022R$ and $S_{\min} = 0.003R - 0.006R$. In both cases, the growth rates become constant when $S_{\max} < 0.2R$. Hence, the maximum size should be small enough. The size of meshes are kept in the ranges $S_{\min} = 0.005R - 0.01R$ and $S_{\max} < 0.15R$. These values result in a number of triangles about $1 \cdot 10^5 - 2 \cdot 10^5$.

Effect of the domain size Depending on the control parameters, there exists different modes. The domain size also has different effects on the spectrum of each type of modes. Hence, the domain size is varied accordingly. In this section, we show some extreme examples for which the domain size affects greatly the spectrum. Figure 2.11 shows different examples of the effect of $R_{\max}$ and $Z_{\max}$ on the spectrum for $m = 2$, $\alpha = 0.5$, $F_h = 0.33$, $Ro = 0.4$ and $Re = 10000$. The growth rate varies little with $R_{\max}$. However, when the vertical limits are too small, the growth rate decreases significantly. Nevertheless, it saturates quickly when

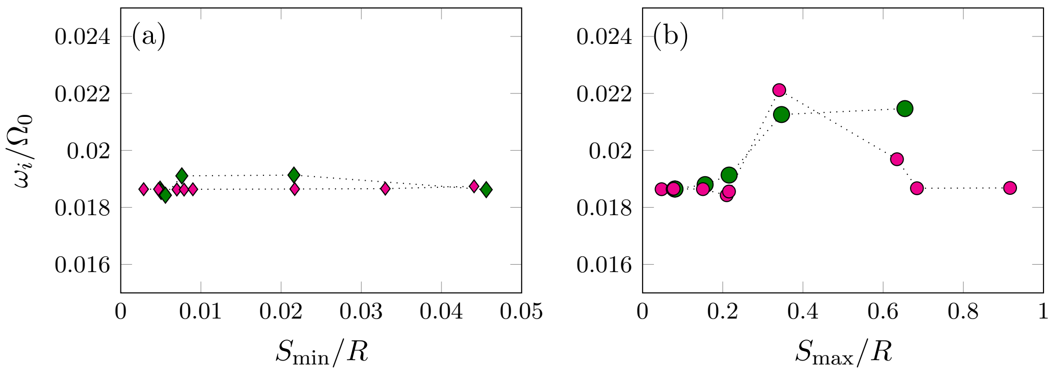

Figure 2.10: Growth rate ω_i/Ω_0 as a function of (a) minimum size of meshes S_{min} for different maximum size S_{max} of the meshes: $S_{\text{max}} = 0.15R - 0.2R$ and $S_{\text{max}} = 0.05R-0.08R$, and (b)the maximum size of S_{max} for different S_{min}: $S_{\text{min}} = 0.017R - 0.022R$ and $S_{\text{min}} = 0.003R - 0.006R$ for $\alpha = 0.5, m = 2, F_h = 0.5, Ro = \infty$ and $Re = 10000$.

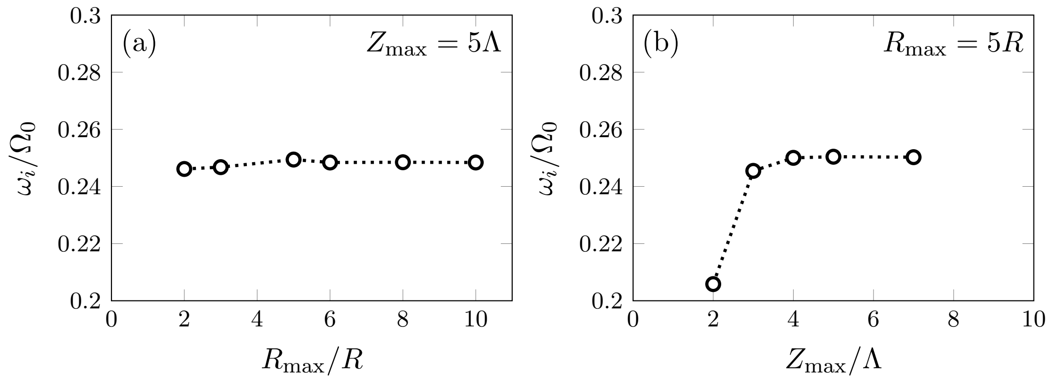

Figure 2.11: Growth rate ω_i/Ω_0 of shear modes as a function of (a) maximum radius R_{max} for $Z_{\text{max}} = 5\Lambda$ and (b) maximum height Z_{max} for $R_{\text{max}} = 5R$ for $m = 2$, $\alpha = 0.5$, $F_h = 0.33$, $Ro = 0.4$ and $Re = 10000$.

$Z_{\text{max}} > 3\Lambda$. The radial velocity perturbations are shown in figure 2.12 for two different heights.

Now, figure 2.13a shows the effect of maximum radial size on the growth rates for $Z_{\text{max}} = 5\Lambda$, $m = 2$, $\alpha = 0.5$, $F_h = 0.15$, $Ro = -8.3$ and $Re = 10000$. The growth rate is large when R_{max} is small and stabilizes only when $R_{\text{max}} > 15R$. This is due to a slow decay of the mode with r. It bounds at the boundary when R_{max} is not large enough as seen in figure 2.14. However, as long as R_{max} is kept large, the vertical boundary limits have almost no effect on the growth rate (see figure 2.14c). Hence, to resolve this kind of mode, a large R_{max} is used. In fact only this particular set of parameters has required such large R_{max}. For similar eigenvectors but for different Ro and F_h ($Ro = \infty$ and $F_h = O(1)$), the maximum radius $R_{\text{max}} = 8R$ is sufficient to have a good convergence.

As shown from the two different examples, the required size of the domain differs depending on the control parameters. Generally, the domain size is chosen as $R_{\text{max}} = 8R - 20R$ and $Z_{\text{max}} = 5\Lambda - 7\Lambda$.

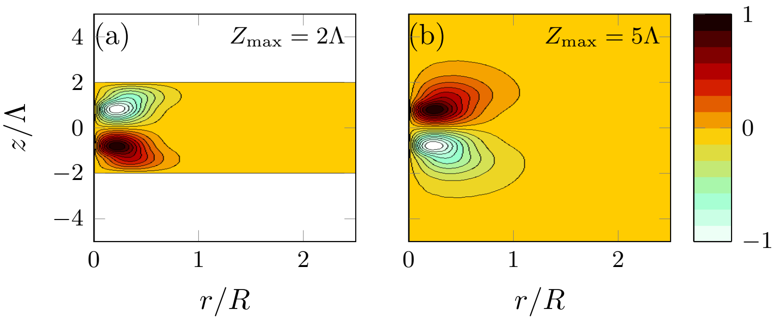

Figure 2.12: Radial velocity perturbations $\mathrm{Re}(u_r)$ for different maximum height $Z_{\max}$: (a) $Z_{\max} = 2\Lambda$ and (b) $Z_{\max} = 5\Lambda$ for $R_{\max} = 5R, \alpha = 0.5, m = 2, F_h = 0.3, Ro = 0.4$ and $Re = 10000$.

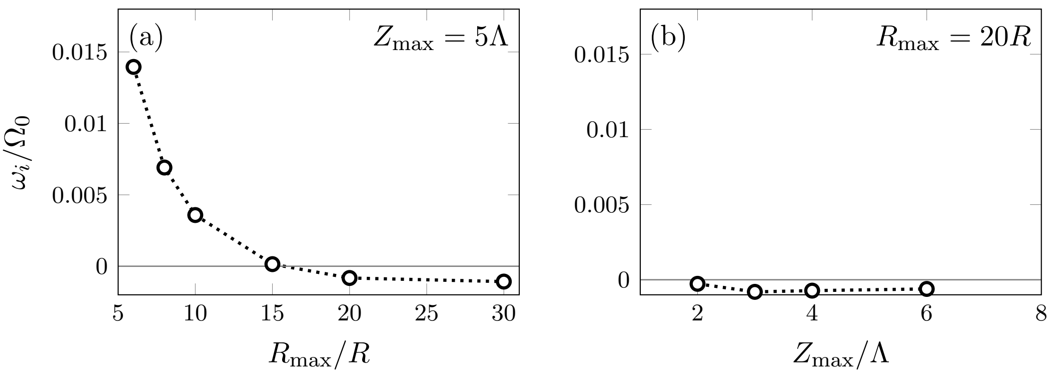

Figure 2.13: Growth rate ω_i/Ω_0 of shear modes as a function of (a) maximum radius $R_{\max}$ for $Z_{\max} = 5\Lambda$ and (b) maximum height $Z_{\max}$ for $R_{\max} = 20R$ for $m = 2$, $\alpha = 0.5$, $F_h = 0.15$, $Ro = -8.3$ and $Re = 10000$.

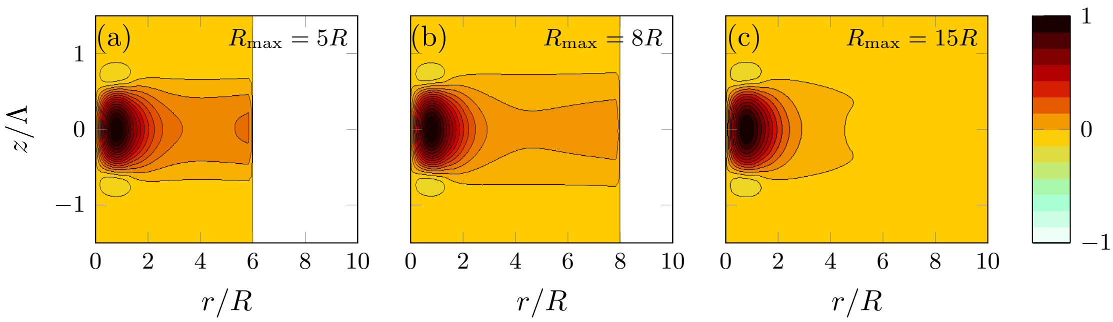

Figure 2.14: Radial velocity perturbations $\mathrm{Re}(u_r)$ for different maximum radius $R_{\max}$: (a) $R_{\max} = 6R$, (b) $R_{\max} = 8R$ and (c) $R_{\max} = 15R$ for $Z_{\max} = 5\Lambda, \alpha = 0.5, m = 2, F_h = 0.15, Ro = -8.3$ and $Re = 10000$.

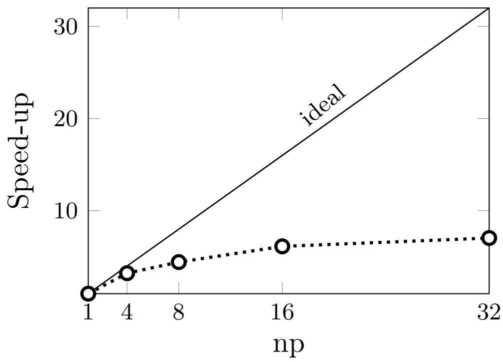

Figure 2.15: The speed-up ($= t_{\mathrm{np}=1}/t$) as a function of numbers of processor (np) for evaluating one shiftvalue.

Effect of number of cpu The code is parallelized with MPI. The time gain as a function of the number of processors (np) has been studied (figure 2.15). The time is normalized to the time when it is sequential (np= 1). The tested computer is named aplusbegalix. Aplusbegalix has 40 cores of Intel(R) Xeon(R) CPU E7-L8867 @ 2.13GHz and 128GB of shared memory. The speed-up saturates when np> 6. The computing time varies depending on the matrix size. The typical time for matrices of size $10^6 \times 10^6$ for one shiftvalue is about 20min with 4 processors.

3

Stability of a columnar vortex in stratified-rotating fluids

In stably stratified and rotating fluids, an axisymmetric columnar vortex can be unstable to a special instability with an azimuthal wavenumber $m = 1$ which bends and slices the vortex into pancake vortices (Gent & McWilliams, 1986). This bending instability, called the "Gent-McWilliams instability" herein, is distinct from the shear, centrifugal or radiative instabilities. The goals of the chapter are to better understand the origin and properties of this instability and to explain why it operates only in stratified rotating fluids. Both numerical and asymptotic stability analyses of several velocity profiles have been performed for wide ranges of Froude number $F_h = \Omega_0/N$ and Rossby number $Ro = 2\Omega_0/f$, where Ω_0 is the angular velocity on the vortex axis, N the Brunt–Väisälä frequency and f the Coriolis parameter. Numerical analyses restricted to the centrifugally stable range show that the maximum growth rate of the Gent-McWilliams instability increases with Ro and is independent of F_h for $F_h \leq 1$. In contrast, when $F_h > 1$, the maximum growth rate decreases dramatically with F_h. Long axial wavelength asymptotic analyses for isolated vortices prove that the Gent-McWilliams instability is due to the destabilization of the long-wavelength bending mode by a critical layer at the radius r_c where the angular velocity Ω is equal to the frequency ω: $\Omega(r_c) = \omega$. A necessary and sufficient instability condition valid for long wavelengths, finite Rossby number and $F_h \leq 1$ is that the derivative of the vertical vorticity of the basic vortex is positive at r_c: $\zeta'(r_c) > 0$. Such a critical layer r_c exists for finite Rossby and Froude numbers because the real part of the frequency of the long-wavelength bending mode is positive instead of being negative as in a homogeneous non-rotating fluid ($Ro = F_h = \infty$). When $F_h > 1$, the instability condition $\zeta'(r_c) > 0$ is necessary but not sufficient because the destabilizing effect of the critical layer r_c is strongly reduced by a second stabilizing critical layer r_{c2} existing at the radius where the angular velocity is equal to the Brunt–Väisälä frequency. For non-isolated vortices, numerical results show that only finite axial wavenumbers are unstable to the Gent-McWilliams instability.

Contents

On the mechanism of the Gent-McWilliams instability of a columnar vortex in stratified rotating fluids

Eunok Yim and Paul Billant

LadHyX, CNRS, École Polytechnique, F-91128 Palaiseau Cedex, France

(Published in *J. Fluid Mech.* (2015), **780**, 5-44)

3.1 Introduction

Vortices can be subjected to many instabilities in stably stratified and rotating fluids because of their own structure or because of interactions with other vortices. If we exclude the latter possibility by restricting the problem to the idealized configuration of a single vertical columnar axisymmetric vortex, there are still several instability mechanisms that can disrupt a vortex. The shear and centrifugal instabilities are not specific to a stratified rotating fluid and have been well-known since Rayleigh (1880, 1917). The former is a two-dimensional instability that can destabilize non-axisymmetric perturbations with azimuthal wavenumbers $m \geq 2$ if the vertical vorticity derivative $\zeta'(r)$ vanishes for some radius r (Rayleigh, 1880; Howard & Gupta, 1962; Carton & McWilliams, 1989; Carnevale & Kloosterziel, 1994). This necessary condition is equivalent to the inflection point condition for parallel shear flows. The centrifugal instability is intrinsically three-dimensional and most unstable for short axial wavelength and axisymmetric perturbations $m = 0$ in inviscid fluids. The classical Rayleigh criterion (Rayleigh, 1917) for the centrifugal instability can be extended to stratified rotating inviscid fluid (Kloosterziel & van Heijst, 1991; Billant & Gallaire, 2005) by replacing the circulation by the absolute circulation, i.e. a necessary and sufficient instability condition is that the square of the absolute circulation decreases for increasing radius, regardless of the stratification. Even if the axisymmetric mode is dominant in an inviscid fluid, it should be noted that non-axisymmetric modes can be the most unstable in viscous fluids owing to the combined effects of stratification and viscosity (Billant *et al.*, 2004) or confinement in shallow layers (Lahaye & Zeitlin, 2015) which damp short axial wavelengths.

Recently, a different type of instability has been shown to occur specifically in vortices in a stratified rotating fluid: the radiative instability Smyth & McWilliams (1998); Schecter & Montgomery (2004); Billant & Le Dizès (2009); Le Dizès & Billant (2009); Riedinger *et al.* (2010, 2011); Park & Billant (2012, 2013)). This instability is due to a coupling between the waves sustained by the vortex and inertial-gravity waves in the surrounding fluid. The mechanism of the instability can be interpreted as a wave over-reflection at the critical radius where the azimuthal phase velocity matches the angular velocity of the base flow, a radius which exists only for non-axisymmetric waves. The radiative instability is most unstable when the fluid is strongly stratified and non-rotating. As the background rotation increases, its growth rate decreases and vanishes in the quasi-geostrophic limit (strongly stratified and rapidly rotating fluid). This regime pertains to large scale atmospheric and oceanic vortices (See Schecter & Montgomery (2006) for a summary of the typical characteristics of various geophysical vortices).

A fourth type of instability has been evidenced by Gent & McWilliams (1986) on vortices with zero-circulation in quasi-geostrophic fluids. In contrast to the shear or centrifugal instabilities, it is most unstable for a finite axial wavenumber and occurs only for the azimuthal wavenumber $m = 1$. This instability bends and fragments the vortex into lenticular vortices (Gent & McWilliams, 1986; Hua, 1998; Smyth & McWilliams, 1998). Gent & McWilliams

(1986) called this three-dimensional instability "internal instability" as opposed to the "external instability", i.e. the two-dimensional shear instability. Here, we shall call the internal instability the "Gent-McWilliams instability" in order to distinguish it from the other types of three-dimensional instability. The Gent-McWilliams (GMW) instability is the most dangerous instability in quasi-geostrophic fluids for sufficiently steep vortex profiles such as for example the Carton & McWilliams (1989) vortex (Gaussian angular velocity profile). Even if the instability is three-dimensional, Gent & McWilliams (1986) have also shown that the necessary conditions for the shear instability (Rayleigh and Fjortoft's criteria) also apply to the GMW instability in a quasi-geostrophic fluid.

Flierl (1988) has shown that the GMW instability also occurs on vortices with a piecewise profile with two levels of non-zero uniform vorticity in quasi-geostrophic fluids. A necessary condition for instability is that $(\zeta_i - \zeta_o)\zeta_o < 0$, where ζ_i and ζ_o are the inner and outer vorticities. This is equivalent to the condition that the vorticity gradient changes sign between the two vorticity jumps. When the vortices are isolated (i.e. zero circulation), the GMW instability is of a long-wavelength nature, i.e. its growth rate is positive as soon as the axial wavenumber is non-zero. In contrast, only finite axial wavenumbers (i.e. wavenumbers above a non-zero wavenumber cutoff) are unstable when the circulation is non-zero. Flierl (1988) has also provided a simple explanation of the instability mechanism. Two different processes are involved: self-induced motion when the vortex is slightly bent along the vertical, and two-dimensional advection by the vorticity anomalies generated when the two vorticity contours are shifted relative to each other. This mechanism is illustrated in figure 3.1 and explained in details in the caption.

3

Smyth & McWilliams (1998) have studied the stability of the Carton & McWilliams vortex beyond the quasi-geostrophic regime. Most interestingly, they have shown that the GMW instability exists only in presence of both stratification and rotation. However, this observation remains unexplained. The Rayleigh and Fjortoft's stability criteria (Gent & McWilliams, 1986) indeed apply only to quasi-geostrophic fluids.

Hence, the main questions that we would like to address in this paper are: why does the GMW instability occur only in stratified rotating fluids? And is it possible to derive an instability condition valid for arbitrary rotation and stratification? These questions are intimately linked to the preliminary question: what is the general mechanism of the GMW instability? Even if a mechanism has been highlighted by Flierl (1988) for piecewise vorticity profiles in quasi-geostrophic fluids, it is not straightforward to extend it to arbitrary rotation and stratification and/or to continuous vorticity profiles.

Interestingly, Reasor & Montgomery (2001) and Reasor *et al.* (2004) have shown that certain vortices in quasi-geostrophic fluids tend to align when they are tilted, i.e. a behaviour opposite to the GMW instability. This alignment process has been attributed to a critical layer damping of the bending mode when $\zeta'(r_c) < 0$, where r_c is the critical radius where the phase velocity of the wave ω/m is equal to the angular velocity of the vortex $\Omega(r_c)$ (Briggs *et al.*, 1970; Schecter *et al.*, 2002; Schecter & Montgomery, 2003). In viscous fluids, this damping comes from viscous effects that smooth the singularity while in inviscid fluids, it can be understood from the conservation of angular momentum (Schecter *et al.*, 2000) or wave pseudo-momentum (Schecter *et al.*, 2002).

Even if they focus on the alignment process and vortex profiles for which $\zeta'(r_c) < 0$, Schecter *et al.* (2002) and Schecter & Montgomery (2003) have also predicted theoretically for profiles with a weak outer vorticity gradient that the critical layer should destabilize the bending mode when $\zeta'(r_c) > 0$ in strongly stratified and rotating fluids. Such critical layer instabilities were first reported in the case of the two-dimensional stability of vortices (Briggs *et al.*,

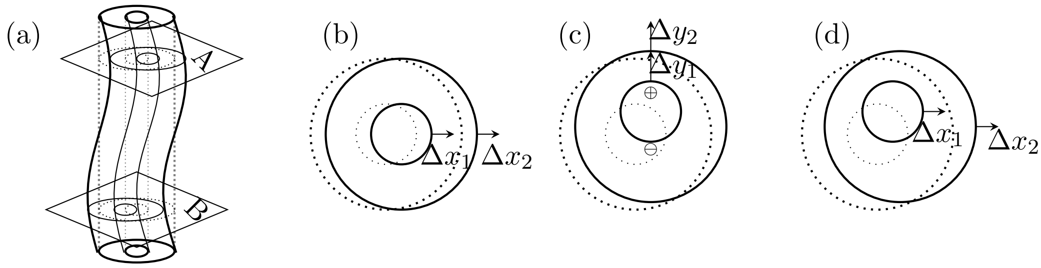

Figure 3.1: Mechanism of the GMW instability as explained by Flierl (1988) for piecewise vortex profiles in a quasi-geostrophic fluid. As sketched in (a), we consider a columnar vortex with two levels of constant vorticity which is perturbed by a long-wavelength bending perturbation. The solid and dotted lines show the perturbed and unperturbed vorticity contours, respectively. The vorticity is assumed positive in the core region and negative in the surrounding annulus. The vorticity contours in the horizontal cross-section A are represented in (b). The initial displacements of the inner and outer contours are chosen to be in the positive x direction and equal ($\Delta x_1 = \Delta x_2 > 0$). Because of the self-induction, the bent vortex will then rotate in the positive sense about its unperturbed position. As indicated in (c), this leads to displacements in the positive y direction ($\Delta y_1 > 0, \Delta y_2 > 0$) in the cross-section A. However, the two contours are not displaced by the same amount: the inner contour turns out to be more displaced than the outer one ($\Delta y_1 > \Delta y_2 > 0$). In turn, since the vorticity is not of the same sign in the inner and outer regions, this differential displacement creates positive (⊕) and negative (⊖) vorticity anomalies. As sketched in (d), this dipole of vorticity anomalies tends to further translate the vortex in the positive x direction, i.e. in the same direction as the initial displacement. The same reasoning can be applied to the motions in the cross-section B. There is therefore a positive feedback which will make the initial bending perturbation grow.

1970; Le Dizès, 2000; Schecter *et al.*, 2000) or parallel shear flows in shallow water (Balmforth, 1999; Riedinger & Gilbert, 2014). Schecter *et al.* (2002) and Schecter & Montgomery (2003) did not make a connection with the GMW instability but subsequently Reasor *et al.* (2004), while further studying vortex alignment, have also made a linear numerical simulation for a different vortex profile which leads to an exponential growth of the vortex tilt. Interestingly, Reasor *et al.* (2004) pointed out that the critical radius is located in the region of positive vorticity gradient and they speculated on the possible link between the instability observed by Gent & McWilliams (1986) on isolated vortices and a destabilization of the bending mode by a critical layer when $\zeta'(r_c) > 0$ predicted by Schecter *et al.* (2002) and Schecter & Montgomery (2003) for profiles with a weak outer vorticity gradient. Here, we shall prove this conjecture by means of long-wavelength stability analyses of the bending mode of columnar vortices in stratified rotating fluids.

Such a long-wavelength approach differs from the analyses of Schecter *et al.* (2002) and Schecter & Montgomery (2003) where a formal expression for the growth rate was derived under the assumption of a weak vorticity gradient at the critical radius and under quasi-geostrophic or asymmetric balance approximations. These derivations are based on the conservation of angular momentum or wave pseudo-momentum and are equivalent to the perturbative approach of Briggs *et al.* (1970). The resulting formula shows that the growth rate is of the same sign as the vorticity gradient at the critical radius if the vorticity gradient is negative throughout the vortex core. However, this formula is implicit since it requires prior knowledge of the eigenfunction and frequency of the mode in the vortex core. These can be computed analytically only for the Rankine vortex. Furthermore, this formula cannot predict formally the sign of the growth rate for the Carton & McWilliams vortex since the vorticity gradient changes sign in the vortex core. It may be further noted that small vorticity gradients are encountered for large radii for many vortex profiles, meaning that the assumption of a weak vorticity gradient at the critical radius implies that the critical radius should be large. This situation occurs for small frequencies, i.e. long-wavelength in the case of the bending mode. Here, we shall use the long-wavelength assumption from the outset and this will enable us to derive explicit analytical formula for the growth rate of the bending mode for several vortex profiles, including the Carton & McWilliams vortex for any finite Froude and Rossby numbers, i.e. beyond the quasi-geostrophic or asymmetric balance regimes.

These asymptotic analyses will also allow us to understand why the bending mode can be unstable only in stratified rotating fluid. The explanation can be anticipated from what is known on the behaviours of the bending mode for a vortex with a non-zero circulation. For such profiles, long-wavelength asymptotic analyses have shown that the bending mode is neutral with a negative frequency in homogeneous non-rotating fluids (Widnall *et al.*, 1971; Saffman, 1992) whereas it is neutral with a positive frequency in stratified rotating fluids when the Froude number is lower than unity: $F_h = \Omega_0/N < 1$ (Billant, 2010), where Ω_0 is the angular velocity on the vortex axis and N the Brunt–Väisälä frequency. In the latter case, a critical radius r_c where $\omega = \Omega(r_c)$ thus exists, in contrast to homogeneous non-rotating fluids. For a vortex with non-zero circulation, such a critical radius has no effect in the long-wavelength limit in stratified rotating fluids because the derivative of the vorticity gradient $\zeta'(r_c)$ is negligible. In this paper, we will show that the critical radius r_c destabilizes the long-wavelength bending mode when $\zeta'(r_c)$ is not negligible and positive. Of course, the prerequisite will be that there exists a critical radius r_c, i.e. the real part of the frequency of the long-wavelength bending mode has to be positive.

Before carrying out these asymptotic analyses, we will conduct a numerical stability analysis of the $m = 1$ azimuthal wavenumber for the Carton & McWilliams vortex. This analysis

3

will allow us to extend the previous results of Gent & McWilliams (1986) and Smyth & McWilliams (1998) on the GMW instability by showing the separate effects of the Rossby and Froude numbers. In particular, we will show that the growth rate of the GMW instability decreases as soon as the Froude number is larger than unity whatever the Rossby number. These numerical results will also serve as a basis to check the asymptotic results. At the end of the paper, the stability of other profiles that are not unstable in the long-wavelength limit will be also studied numerically.

The paper is organized as follows: the general stability problem is described in §3.2. In §3.3, the stability of the $m = 1$ azimuthal wavenumber is computed numerically for the Carton & McWilliams vortex in stratified rotating fluids. In section 3.4, a long-wavelength asymptotic stability analysis is first carried out for the Carton & McWilliams vortex. It is shown that the frequency and growth rate of the bending mode are always positive for long-wavelength in stratified rotating fluids while the bending mode is neutral with a negative frequency in homogeneous non-rotating fluids. To investigate the role of the sign of $\zeta'(r_c)$, we next consider an angular velocity profile with the non-dimensional form $\Omega \simeq a_n/r^{2n}$ for large radius r, where a_n and n are positive constants. It will be proved that the critical radius r_c can destabilize or stabilize the long-wavelength bending mode when $n > 1$ and $n < 1$, respectively. In section 3.5, the latter instability condition in the long-wavelength limit is generalized to $\zeta'(r_c) > 0$ for arbitrary angular velocity profiles with a weak vorticity gradient ζ'. Using the numerical results of section 3.3 for the Carton & McWilliams vortex, we further show that this instability condition turns out to be valid not only for small vertical wavenumber but also for any vertical wavenumber. In section 3.6, the stability of the $m = 1$ azimuthal mode is computed numerically for a family of profiles possessing regions where $\zeta' > 0$ together with a non-zero circulation. In this case, we shall see that the GMW instability occurs only for finite axial wavenumbers.

3

3.2 Problem formulation

We consider an axisymmetric vortex with velocity $\mathbf{u}(\hat{r}, \theta, \hat{z}) = [0, \hat{U}_\theta(\hat{r}), 0]$ in cylindrical coordinates $(\hat{r}, \theta, \hat{z})$ where $\hat{z}$ is the vertical coordinate. The fluid is assumed incompressible, stably stratified with constant Brunt–Väisälä frequency N and rotating about the vertical axis at a rate $f/2$ where f is the Coriolis parameter. In the following, we non-dimensionalise length by the radius of the vortex R and time by $1/\Omega_0$, where Ω_0 is the angular velocity on the axis. Quantities without a hat will denote non-dimensional variables.

The vortex is assumed to be perturbed by infinitesimal perturbations (denoted with a tilde) of velocity $[\tilde{u}_r, \tilde{u}_\theta, \tilde{u}_z]$, pressure $\tilde{p}$, and density $\tilde{\rho}$. Since the basic flow is axisymmetric and uniform along the vertical, they are written as normal modes,

$$[\tilde{u}_r, \tilde{u}_\theta, \tilde{u}_z, \tilde{p}, \tilde{\rho}] = [u_r(r), u_\theta(r), u_z(r), p(r), \rho(r)]e^{i(kz+m\theta-\omega t)} + c.c., \quad (3.1)$$

where k is axial wavenumber, m the azimuthal wavenumber and ω the frequency. We consider that k and m are positive since negative wavenumbers can be retrieved by the symmetry: $\omega(-k, m) = -\omega^*(-k, -m) = \omega(k, m)$. Under the Boussinesq approximation and in the inviscid limit, the linearized governing equations can be reduced to a single equation for $\varphi = ru_r$

$$\frac{\mathrm{d}^2\varphi}{\mathrm{d}r^2} - \left[\frac{1}{r} + \frac{Q'}{Q}\right]\frac{\mathrm{d}\varphi}{\mathrm{d}r} - \left[\frac{m^2}{r^2} + k^2F_h^2\frac{\phi - s^2}{1 - s^2F_h^2} + \frac{m}{rs}\left(\zeta' - \left(\frac{2}{Ro} + \zeta\right)\left(\frac{2}{r} + \frac{Q'}{Q}\right)\right)\right]\varphi = 0, \quad (3.2)$$

where $Q = m^2/r^2 - k^2F_h^2 s^2/(1 - s^2F_h^2)$, $s = m\Omega - \omega$ is the Doppler shifted frequency, $\phi = (2\Omega + 2/Ro)(\zeta + 2/Ro)$ is the Rayleigh discriminant, $\zeta = (1/r)\partial(rU_\theta)/\partial r$ is the vertical vorticity and $\Omega = U_\theta/r$ is the non-dimensional angular velocity of the basic vortex. The Froude number F_h and Rossby number Ro

$$F_h = \frac{\Omega_0}{N}, \qquad Ro = \frac{2\Omega_0}{f}, \tag{3.3}$$

measure the effect of the stratification and rotation, respectively. The boundary conditions impose that the perturbation is non-singular at $r = 0$ and decays or corresponds to a wave propagating outward for $r \to \infty$. This implies that $\varphi \sim r^m$ as $r \to 0$ for $m \geq 1$. To impose the outer boundary condition, we use the two following asymptotic solutions of (3.2) for $r \gg 1$

$$\varphi = \mathrm{K}_m(\beta k r) + \frac{\omega Ro}{m(2+\omega Ro)}\beta k r \mathrm{K}_{m-1}(\beta k r), \tag{3.4}$$

$$\varphi = \mathrm{H}_m^{(n)}(|\beta| k r) - \frac{\omega Ro}{m(2+\omega Ro)}|\beta| k r \mathrm{H}_{m-1}^{(n)}(|\beta| k r), \tag{3.5}$$

with $\beta^2 = (4/Ro^2 - \omega^2)/(1/F_h^2 - \omega^2)$, where K_m is the modified Bessel function of order m of the second kind and $\mathrm{H}_m^{(n)}$ is the Hankel function of order m of kind n. The solution (3.4) ensures that the perturbation decays as $r \to \infty$ except when $\omega_i = \mathrm{Im}(\omega) = 0$ and $\beta^2 < 0$. In the latter case, we use the solution (3.5) which describes an outward propagating wave if the kind is set to $n = 1$ when $\omega_r(Ro^2/4 - F_h^2) > 0$ and $n = 2$ when $\omega_r(Ro^2/4 - F_h^2) < 0$, where $\omega_r = \mathrm{Re}(\omega)$. When $\omega_i > 0$, the asymptotic solution (3.4) corresponds also to the solution which propagates outwards.

3

Equation (3.2) has been generally solved by a shooting method. The numerical integration is started from a small radius r_1 and a large radius r_2 toward a radius r_f using the asymptotic solutions of (3.2) and an initial guess for ω. This leads to two couples of values at r_f : $[\varphi_1(r_f), \varphi_1'(r_f)]$ and $[\varphi_2(r_f), \varphi_2'(r_f)]$. The value of ω for which the Wronskian $\varphi_2(r_f)\varphi_1'(r_f) - \varphi_1(r_f)\varphi_2'(r_f)$ vanishes is then searched for by an iterative scheme. The path of integration is deformed in the complex plane in order to avoid the singular radius r_c where $s = m\Omega(r_c) - \omega = 0$ or $s = \pm 1/F_h$. Since the vortex profiles that will be studied have $\Omega'(r_c) < 0$, the path is deformed in the upper complex plane in order that the inviscid solution be the proper limit of the viscous solution (Lin, 1955; Le Dizès, 2004).

The stability problem in the presence of viscous and diffusive effects has also been solved by a Chebyshev pseudo-spectral collocation method (Antkowiak & Brancher, 2004). This code has allowed us to check the results of the shooting code and to compute the structure of the eigenmodes when critical layers are present since they are smoothed by viscosity and diffusion. The Reynolds number is defined as $Re = \Omega_0 R^2/\nu$ and the Schmidt number as $Sc = \nu/D$, where ν is the kinematic viscosity and D the molecular diffusivity of the stratifying agent.

3.3 Numerical results for the Carton & McWilliams vortex

We first study numerically the stability of the azimuthal wavenumber $m = 1$ for the Carton & McWilliams (1989) vortex whose non-dimensional angular velocity is

$$\Omega = e^{-r^2}. \tag{3.6}$$

The stability of this profile has already been analysed by Gent & McWilliams (1986) in the quasi-geostrophic regime and by Smyth & McWilliams (1998) for finite Ro and F_h but only for some particular ratios: $F_h/Ro = \infty, 0.5, 0.005$ and 0. Here, we shall investigate separately the effects of F_h and Ro.

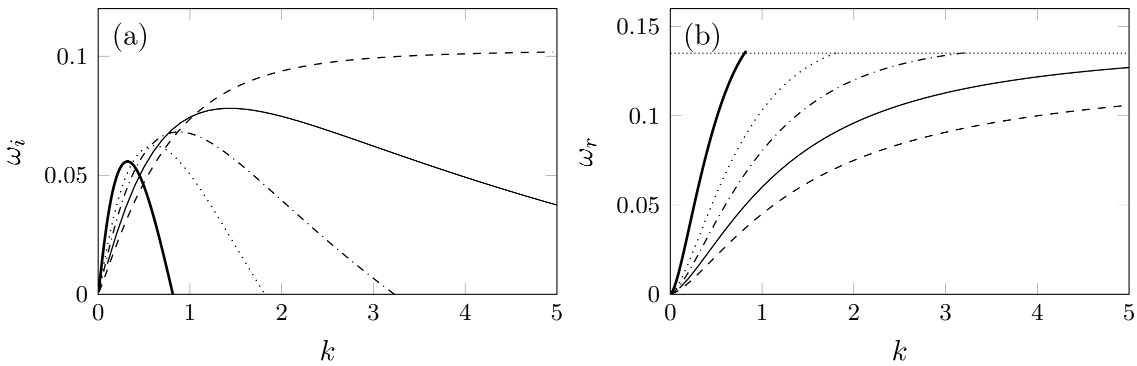

Figure 3.2: (a) Growth rate (ω_i) and (b) frequency (ω_r) as function of the vertical wavenumber k for the profile (3.6) for $m = 1$ and $F_h = 1$ for different Rossby numbers: $Ro = 1$ ——; $Ro = 2$ ⋯⋯; $Ro = 3$ -·-·-; $Ro = 5$ ——; $Ro = 10$ - - -. The horizontal dotted line in (b) shows the cutoff frequency $\omega_r = 0.135$.

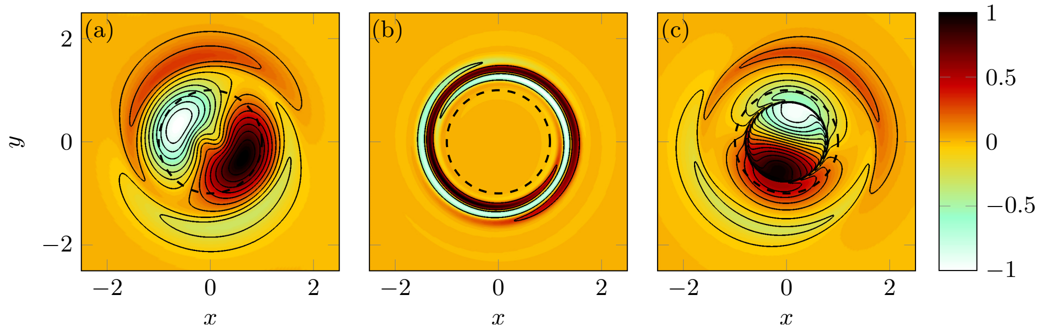

Figure 3.3: Vertical vorticity of the most unstable eigenmode for the profile (3.6) for $m = 1$ and (a) $F_h = 1, Ro = 1, k = 0.35$, (b) $F_h = 1, Ro = 10, k = 100$ and (c) $F_h = 2, Ro = 1, k = 0.1$. The dashed line represents the radius $r = 1$ where the sign of the basic vorticity changes. Note that these eigenmodes have been computed for a large but finite Reynolds number $Re = 10^6$ with $Sc = 1$ in order to resolve the critical layer in (c).

Figure 3.2 shows the growth rate and frequency of the azimuthal wavenumber $m = 1$ for a fixed Froude number $F_h = 1$ and several positive Rossby numbers from $Ro = 1$ to $Ro = 10$. The growth rate curves for $Ro \leq 5$ exhibit a bell shape as reported by Gent & McWilliams (1986) and Smyth & McWilliams (1998). When Ro increases from $Ro = 1$ to $Ro = 5$, the most amplified wavenumber increases and the maximum growth rate slightly increases. The unstable wavenumber band also widens when Ro increases but, remarkably, it corresponds to a fixed frequency range: $0 \leq \omega_r \leq 0.135$ (figure 3.2b). Note that the critical value 0.135 is very close to exp(-2). The reason for this will be seen in §3.5.

The vertical vorticity of the most unstable perturbation for $Ro = 1$ is shown in figure 3.3a. It exhibits an inner dipolar structure surrounded by outer spiraling perturbations. The inner and outer perturbations have a phase shift and are localized in the regions where the basic vorticity ζ is negative and positive, respectively. Thus, the perturbations will tend to translate the positive and negative vorticity regions of the basic vortex in different directions. This is a key feature of the mechanism of the GMW instability as discussed by Flierl (1988) and illustrated in figure 3.1.

For higher Ro, as exemplified in figure 3.2 by $Ro = 10$, the growth rate is no longer maximum for a finite axial wavenumber k but increases monotonically with k (figure 3.2a). The vertical vorticity of the eigenmode for large k is then strongly localized at a particular radius (figure 3.3b). As shown by Smyth & McWilliams (1998), this corresponds to the centrifugal instability which is most unstable for $k \to \infty$. Indeed, the minimum of the Rayleigh discriminant $\phi = (2\Omega + 2/Ro)(\zeta + 2/Ro)$ is negative when $Ro > \exp(2) = 7.39$.

For negative Rossby number, the centrifugal instability is also present when $Ro < -1$ since $\min(\phi)$ is negative. This can be seen in figure 3.4 where the growth rate and frequency are displayed for several negative Rossby numbers at $F_h = 1$. The growth rate increases monotonically with k for large k when $Ro < -1$, whereas for $Ro \geq -1$, the growth rate is maximum for a finite wavenumber k. Interestingly, there are two distinct and independent branches for $Ro = -3$ and $Ro = -5$ (figure 3.4): the GMW instability branch at low k and the centrifugal instability branch at large k. As seen in figure 3.4b, the frequencies of these two branches differ significantly. In contrast, for $Ro = -10$ and $Ro = -15$, the two branches are merged into a single continuous one with similar frequencies. Remarkably, the maximum frequency of the GMW instability branch is still $\omega_r = 0.135$ independently of Ro for $Ro \geq -5$ (figure 3.4b).

The effect of the Froude number for a fixed Rossby number $Ro = 1$ is now displayed in figure 3.5. The maximum growth rate is almost independent of the Froude number when $F_h \leq 1$ (figure 3.5a). The unstable frequency range also remains the same $0 \leq \omega_r \leq 0.135$ even if the upper vertical wavenumber cutoff varies (figure 3.5b). However, when F_h is increased above unity, the maximum growth rate decreases abruptly and the unstable frequency range shrinks. As illustrated in figure 3.3c, the vertical vorticity of the most unstable perturbation for $F_h = 2$ still exhibits a dipolar structure as for $F_h \leq 1$, but there is an additional circular region of rapid variation at a particular radius. This corresponds to a singularity of (3.2) which occurs at the radius where $s(r_{c2}) = 1/F_h$, i.e. $r_{c2} = 0.8$ for $F_h = 2$. Since such a critical layer singularity is regularized in the presence of viscous and diffusive effects, the eigenmode in figure 3.3c has been computed from the linearized Navier-Stokes equations by a Chebyshev pseudo-spectral method for $Re = 10^6$ and $Sc = \nu/D = 1$. In the next section, we will show that the growth rate is strongly reduced when $F_h > 1$ because of the damping due to this critical layer.

The separate effects of the Rossby number for $F_h = 1$ and the Froude number for $Ro = 1$ on the maximum growth rate are summarized in figure 3.6. In figure 3.6a, we see that the maximum growth rate continues to decrease when the Froude number is large but it

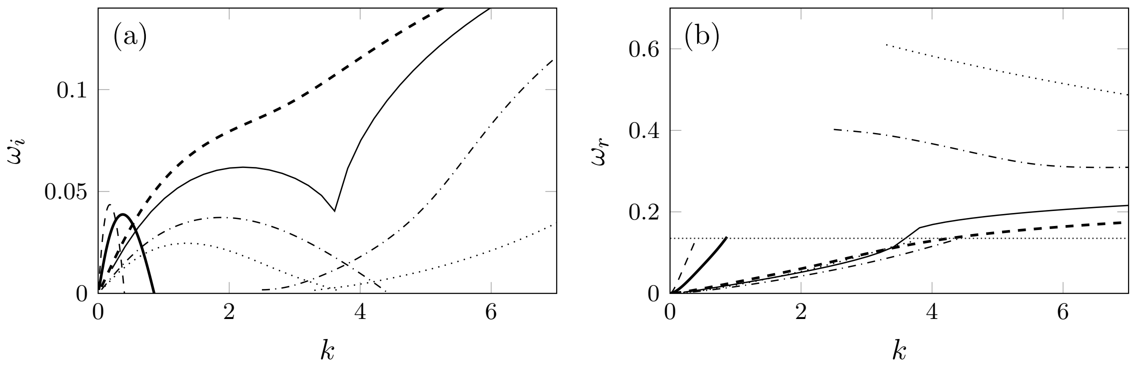

Figure 3.4: (a) Growth rate (ω_i) and (b) frequency (ω_r) as function of the vertical wavenumber for the profile (3.6) for $m = 1$ and $F_h = 1$ for different Rossby numbers: $Ro = -0.5$ - - -; $Ro = -1$ ——; $Ro = -3$ ······; $Ro = -5$ -·-·-; $Ro = -10$ ——; $Ro = -15$ - - -. The horizontal dotted line in (b) shows the cutoff frequency $\omega_r = 0.135$.

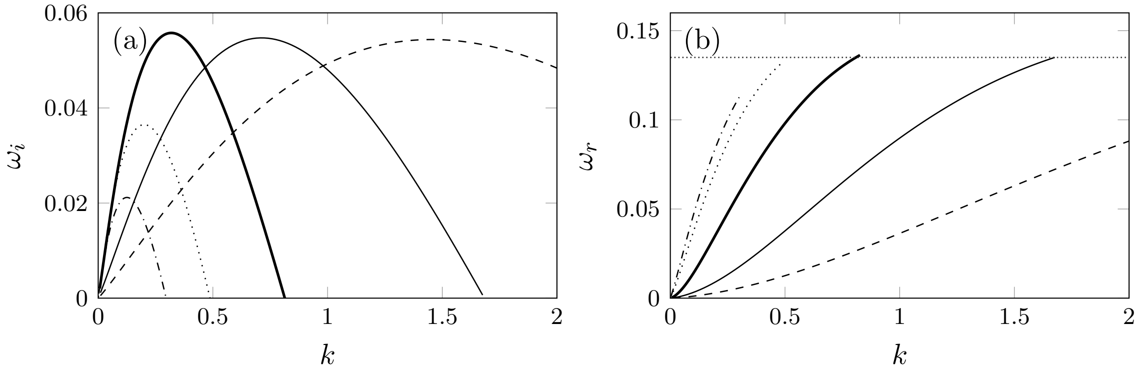

Figure 3.5: (a) Growth rate (ω_i) and (b) frequency (ω_r) as function of the vertical wavenumber k for the profile (3.6) for $m = 1$ and $Ro = 1$ for different Froude numbers: $F_h = 0.25$ - - -; $F_h = 0.5$ ——; $F_h = 1$ ——; $F_h = 1.5$ ······; $F_h = 2$ -·-·-. The horizontal dotted line in (b) shows the cutoff frequency $\omega_r = 0.135$.

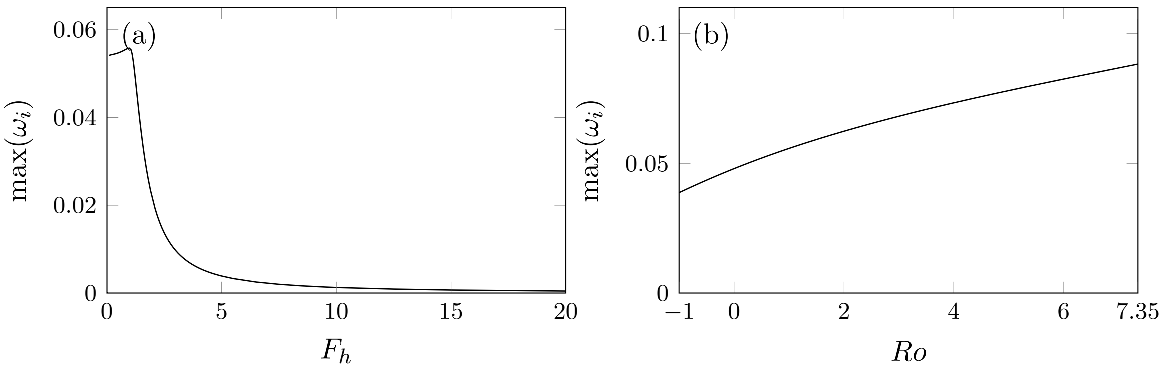

Figure 3.6: Maximum growth rate for the profile (3.6) for $m = 1$ as a function of (a) F_h for $Ro = 1$, and (b) Ro for $F_h = 1$.

remains positive even for the largest Froude number investigated: $F_h = 20$. The maximum growth rate increases monotonically with Ro (figure 3.6b): it is approximately doubled from $Ro = -1$ to $Ro = 7.39$. Only the Rossby number range: $-1 < Ro < 7.39$ is shown in figure 3.6b since outside this range, the vortex is centrifugally unstable. The centrifugal instability is then dominant over the GMW instability (figures 3.2a, 3.4a) except close to the thresholds $Ro = -1$ and $Ro = 7.39$.

Finally, the combined effects of Ro and F_h on the maximum growth rate and the most amplified wavenumber k of the GMW instability are depicted in figure 3.7. The effect of the Froude number is the same independently of Ro: the maximum growth rate is independent of F_h for $F_h \leq 1$ and decreases abruptly with F_h when $F_h > 1$. The monotonic increase of $\max(\omega_i)$ with Ro is also observed whatever F_h. The most amplified wavenumber has been scaled by $F_h/|Ro|$ in figure 3.7b. With this scaling, we see that it varies little and is around $kF_h/|Ro| \approx 0.25 \sim 0.45$ regardless of F_h and Ro.

3.4 Long-wavelength asymptotic analyses

As seen in §3.3, the GMW instability for the Carton & McWilliams profile (3.6) starts at $k = 0$, i.e. it is of a long-wavelength nature. For $k = 0$, an exact solution of (3.2) for $m = 1$ which derives from the translational invariance is $\varphi = r(\Omega - \omega)$ (Michalke & Timme, 1967). Using this solution at leading order, the frequency and eigensolution of the azimuthal wavenumber $m = 1$ can be computed for small wavenumber k by means of an asymptotic expansion. A similar asymptotic analysis has been performed in stratified rotating fluids for vortices with non-zero circulation (Billant, 2010). Using the present non-dimensionalisation and definition of F_h and Ro (see section 3.2), the frequency has been found to be

$$\omega = 2a\left(\frac{k\beta_0}{2}\right)^2\left[-\ln\left(\frac{k|\beta_0|}{2}\right) + \frac{\delta(F_h, Ro)}{a^2} - \gamma_e\right], \tag{3.7}$$

up to order k^2, where $a = \hat{\Gamma}/(2\pi R^2\Omega_0)$ with $\hat{\Gamma}$ the dimensional circulation, $\beta_0 = 2F_h/Ro$ and $\gamma_e = 0.5772$ is the Euler constant. The constant δ is given by

$$\delta(F_h, Ro) = \frac{\mathscr{A}(F_h)Ro^2}{4} + \mathscr{B}(F_h)Ro + \mathscr{D}(F_h), \tag{3.8}$$

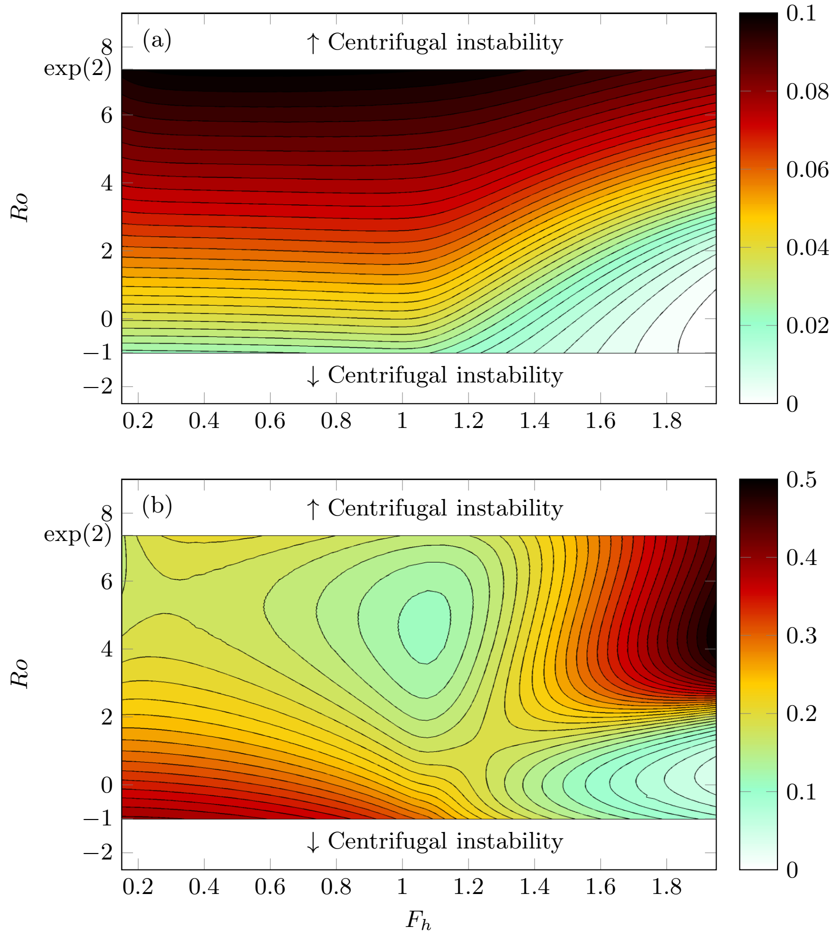

Figure 3.7: (a) Maximum growth rate and (b) scaled most amplified axial wavenumber $kF_h/|Ro|$ as a function of F_h and Ro for the profile (3.6) for $m = 1$. The contour interval is 0.002 in (a) and 0.007 in (b).

with

$$\mathscr{A}(F_h) = \int_0^\infty \frac{\xi^3\Omega^4}{1-F_h^2\Omega^2}\mathrm{d}\xi, \tag{3.9}$$

$$\mathscr{B}(F_h) = \int_0^\infty \frac{\xi^3\Omega^3}{1-F_h^2\Omega^2}\mathrm{d}\xi, \tag{3.10}$$

$$\mathscr{D}(F_h) = \lim_{\eta_0\to\infty}\int_0^{\eta_0} \frac{\xi^3\Omega^2}{1-F_h^2\Omega^2}\mathrm{d}\xi - F_3(\eta_0), \tag{3.11}$$

where

$$F_3(\eta_0) = \int^{\eta_0} \frac{\xi^3\tilde{\Omega}^2}{1-F_h^2\tilde{\Omega}^2}\mathrm{d}\xi, \tag{3.12}$$

where $\tilde{\Omega}$ denotes the asymptotic form of Ω for large radius. For vortices with non-zero circulation, we have $\tilde{\Omega} = a/r^2$, giving $F_3(\eta_0) \simeq a^2 \ln \eta_0$ for $\eta_0 \gg \sqrt{F_h}$. The factor a appears in (3.7) because time is non-dimensionalised by $1/\Omega_0$ instead of $2\pi R^2/\hat{\Gamma}$ in Billant (2010).

The frequency (3.7) is purely real when $F_h \leq 1$ whatever Ro. When $F_h > 1$, the integrands in (3.9-3.11) are singular at the radius where $\Omega(r_{c2}) = 1/F_h$. This singularity is regularized in the presence of viscous and diffusive effects and can be taken into account in the inviscid limit by bypassing the critical radius in the upper complex plane. The constant δ is then complex with a negative imaginary part implying that the mode $m = 1$ is damped. Therefore, the long-wavelength bending mode is at best neutral but never unstable when the circulation is non-zero. However, the formula (3.7) breaks down when $a = 0$, i.e. when the angular velocity does not behave as $\Omega \simeq a/r^2$ for $r \gg 1$. For this reason, specific asymptotic analyses have been carried out for the Carton & McWilliams profile (3.6) and for a profile of the form $\Omega = a_n/r^{2n}$ for $r \gg 1$, where a_n are n constants but n is different from unity. For both profiles, two regions need to be considered in order to solve (3.2) asymptotically: an inner region where $r \ll 1/k$ and an outer region such that $r \gg 1$. However, the analysis for each profile is different and so they are presented separately.

3.4.1 Carton & McWilliams vortex

A specificity of the profile (3.6) concerns the location of the critical radius r_c where $\Omega(r_c) = \omega$. When $\omega \ll 1$ and $\Omega \simeq a/r^2$, the critical radius is located at $r_c \simeq \sqrt{a/\omega}$. Hence, since (3.7) shows that $\omega = O(k^2)$, we have $r_c \sim O(1/k)$ meaning that r_c is located in the outer region. In contrast, the critical radius for the profile (3.6) is located at $r_c = \sqrt{-\ln\omega}$. If we anticipate that $\omega \simeq O(k)$ for the long-wavelength bending mode of the profile (3.6), we can deduce that the critical radius is located in the inner region: $r_c = O(\sqrt{-\ln k})$.

This asymptotic problem is solved in detail in appendix 3.A and only briefly summarized here. The inner and outer solutions are expanded in the form

$$\varphi = \varphi_0 + F_h^2 k^2 \varphi_2 + \cdots, \tag{3.13}$$

with $\varphi_0 = r(\Omega - \omega)$ in the inner region. Even if ω will eventually be small, it is simpler to consider it arbitrary to solve the inner problem. This is the reason why ω appears in the leading order inner solution φ_0. The expansion (3.13) is written in power of kF_h for convenience since k always appears multiplied by F_h in (3.2). The second order inner solution φ_2 and the outer solution are computed in appendices 3.A.1 and 3.A.2. The behaviour of the inner solution for small ω and for $r \gg 1$ is then determined in appendix 3.A.3. The matching between the inner and outer solutions for $1 \ll r \ll 1/k$ and $\omega \ll 1$ is performed in appendix 3.A.4. This leads to the dispersion relation:

$$\omega^2 = \frac{\delta k^2 \beta_0^2}{2}\left[-\frac{1}{r_c^2} + \frac{1}{r_c^4}(1+\mathrm{i}\pi\gamma) + \frac{1}{r_c^6}\left(\frac{2\pi^2}{3} - 2\mathrm{i}\pi\gamma\right) - \frac{2\pi^2}{r_c^8} + O\left(\frac{1}{r_c^{10}}, k^2\beta_0^2 \ln(k\beta_0)\right)\right], \tag{3.14}$$

where δ is the constant defined in (3.8) and $\gamma = \mathrm{sgn}(\omega_i)$. The terms inside the square brackets in (3.14) correspond to an expansion in inverse power of $r_c^2 = -\ln\omega$. Several orders have been computed since the series converges slowly for $\omega \ll 1$ because of the logarithm. The complex terms $\mathrm{i}\pi\gamma/r_c^4$ and $-2\mathrm{i}\pi\gamma/r_c^6$ come from the presence of the critical radius r_c.

The dispersion relation (3.14) is implicit since the critical radius depends on ω. To determine whether or not there exist any solutions, it is first convenient to consider only the first two leading orders in $1/r_c^2$:

$$\omega^2 = \frac{\delta k^2 \beta_0^2}{2}\left[-\frac{1}{r_c^2} + \frac{1}{r_c^4}(1+\mathrm{i}\pi\gamma)\right]. \tag{3.15}$$

By writing $\omega = \rho e^{\mathrm{i}\theta}$ and $\delta = \mu e^{\mathrm{i}\alpha}$, the real and imaginary parts of (3.15) read

$$\rho^2 \cos(2\theta - \alpha) = \frac{\mu k^2 \beta_0^2}{2}(-\varepsilon_\rho + \varepsilon_\rho^2), \tag{3.16}$$

$$\rho^2 \sin(2\theta - \alpha) = \frac{\mu k^2 \beta_0^2}{2}\varepsilon_\rho^2(\pi\gamma - \theta), \tag{3.17}$$

where $\varepsilon_\rho = -1/\ln\rho \ll 1$. Combining (3.16) and (3.17) gives

$$\tan(2\theta - \alpha) = -\varepsilon_\rho(\pi\gamma - \theta) + O(\varepsilon_\rho^2). \tag{3.18}$$

This relation is satisfied if

$$\theta = \frac{\alpha}{2} + \frac{q\pi}{2} - \frac{\varepsilon_\rho}{4}(2\pi\gamma - \alpha - q\pi) + O(\varepsilon_\rho^2), \tag{3.19}$$

where q is an integer. Inserting (3.19) into (3.16) then gives an implicit relation for $\rho = |\omega|$

$$\rho^2(-1)^q = \frac{\mu k^2 \beta_0^2}{2}(-\varepsilon_\rho + \varepsilon_\rho^2 + O(\varepsilon_\rho^3)), \tag{3.20}$$

which can be satisfied at leading order only if q is odd. Hence, the implicit dispersion relation (3.15) can be solved explicitly at leading orders by first choosing a small value for ρ. Then, the corresponding value of θ and k can be obtained directly from (3.19) and (3.20), respectively.

In order to exhibit the behaviour of the solutions, we first focus on the simplest case $F_h \leq 1$ for which there is no critical layer r_{c2} where $\Omega(r_{c2}) = 1/F_h$ so that δ is purely real and positive, i.e. $\alpha = 0$. Then, (3.19) yields two solutions: $\theta = \pi/2 - \varepsilon_\rho\pi/4$ for $q = 1$ and $\theta = -\pi/2 + \varepsilon_\rho\pi/4$ for $q = -1$. Other values of q are not relevant since $-\pi \leq \theta \leq \pi$. The dispersion relation (3.15) has therefore two solutions which are complex conjugates of each other, one unstable and the other stable, which can be written in the form:

$$\omega = \rho e^{\mathrm{i}\theta} = \rho\left[\frac{\varepsilon_\rho}{4}\pi + \mathrm{i}\right], \tag{3.21}$$

$$\omega = \rho\left[\frac{\varepsilon_\rho}{4}\pi - \mathrm{i}\right]. \tag{3.22}$$

where ρ (and $\varepsilon_\rho = -1/\ln\rho$) is related to k through (3.20). The frequency ω_r is positive and

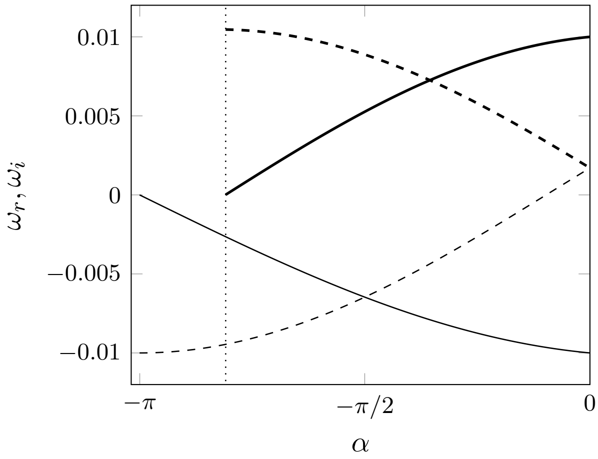

Figure 3.8: Frequency ω_r (dashed lines) and growth rate ω_i (solid lines) predicted by (3.23) (thick lines) and (3.24) (thin lines) as a function of $\alpha = \arg(\delta)$ for a given value of $\rho = 0.01$. The dotted line shows the critical value for which the solution (3.23) disappears.

$O(\varepsilon_\rho)$ smaller than the growth rate.

We now consider the case $F_h > 1$ for which δ is complex with a negative imaginary part, i.e. $-\pi < \alpha \leq 0$ because of the critical layer r_{c2} where $\Omega(r_{c2}) = 1/F_h$. In this case, the two solutions (3.21) and (3.22) become at leading order:

$$\omega = \rho\left[-\sin\frac{\alpha}{2} + \frac{\varepsilon_\rho}{4}(\pi-\alpha)\cos\frac{\alpha}{2} + \mathrm{i}\left(\cos\frac{\alpha}{2} + \frac{\varepsilon_\rho}{4}(\pi-\alpha)\sin\frac{\alpha}{2}\right)\right], \tag{3.23}$$

$$\omega = \rho\left[\sin\frac{\alpha}{2} + \frac{\varepsilon_\rho}{4}(\pi+\alpha)\cos\frac{\alpha}{2} - \mathrm{i}\left(\cos\frac{\alpha}{2} + \frac{\varepsilon_\rho}{4}(\pi+\alpha)\sin\frac{\alpha}{2}\right)\right], \tag{3.24}$$

where ρ can be still determined as a function of k by means of (3.20). The two solutions are no longer complex conjugates of each other. If we consider a fixed value of ρ, the relation (3.23), which is illustrated in figure 3.8, shows that the growth rate of the unstable solution decreases when α decreases from zero meaning that the instability is damped by the critical layer at r_{c2}. From (3.19), we can deduce that the growth rate goes to zero (i.e. $\theta = 0$) when $\alpha \simeq -\pi + \pi\varepsilon_\rho$ (dotted line in figure 3.8). When α decreases further below this critical value, (3.19) no longer has a solution for $q = 1$, i.e. the solution (3.23) does not exist anymore because the integration path has been assumed to be on the real axis. However, the solution (3.23) could be continued by deforming the integration path in the upper complex plane above the critical radius r_c. The mode (3.23) would be then non-regular and damped since the critical radius would be located between the integration path and the real axis. In contrast, the stable solution (3.24) (thin lines in figure 3.8) exists in the whole range $-\pi < \alpha < 0$. The damping rate of this mode is reduced when α decreases and vanishes for $\alpha = -\pi$. Its frequency becomes negative as soon as $\alpha < -\varepsilon_\rho\pi/2$.

Figure 3.9 shows α as a function of F_h and Ro. We see that α decreases and tends to $\alpha = -\pi$ for large Froude number for any Rossby number. This decay occurs slower when Ro is negative and moderate, i.e. $-5 \leq Ro \leq 0$. Hence, for a given value of $\varepsilon_\rho = -1/\ln|\omega|$, the growth rate of the unstable mode (3.23) should vanish for large Froude number when $\alpha \simeq -\pi + \pi\varepsilon_\rho$. This critical Froude number increases and tends to infinity since $\alpha \to -\pi$ as $|\omega|$ decreases to zero. In other words, the instability should be totally suppressed only as the Froude number tends to infinity.

However, it should be noted that the dispersion relation (3.14) (and (3.15)) is no longer

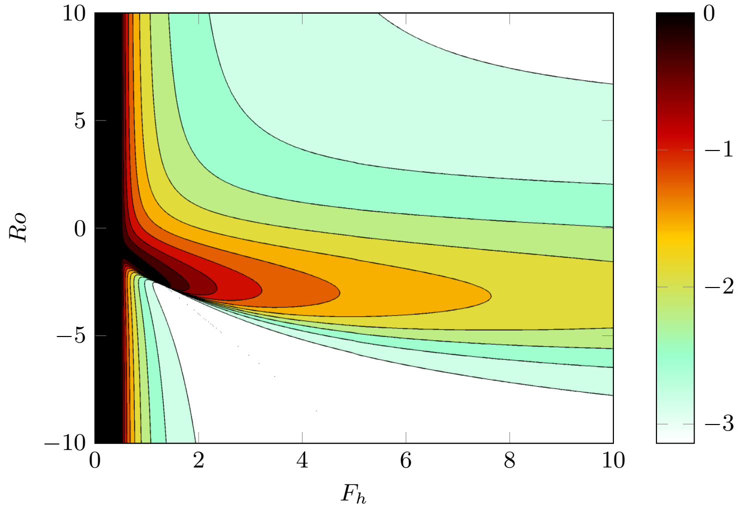

Figure 3.9: Contours of $\alpha = \arg(\delta)$ as a function of F_h and Ro for the profile (3.6). The contour interval is 0.3.

3

valid when $F_h = \infty$ when Ro is finite. The behaviour of the inner solution for large radius is indeed different in this case so that the matching performed to derive (3.14) breaks down. Nevertheless, it remains valid when $Ro = \infty$ i.e. for a stratified non-rotating fluid and this is considered in appendix 3.B. The evolution of the two solutions of (3.14) is studied as a function of F_h. In particular, it is shown that in the limit $F_h = \infty$, there remains only one solution with a negative and purely real frequency ω as predicted by (3.23) and (3.24).

We now compare the prediction of the full long-wavelength dispersion relation (3.14) for the unstable mode to the numerical results. Figure 3.10a shows the asymptotic and numerical growth rates and frequencies for small Froude and Rossby numbers ($F_h = 0.1, Ro = 0.1$) approaching the quasi-geostrophic limit. We see that they agree but only in a limited range of small wavenumbers: $kF_h/Ro \lesssim 0.05$. This relatively rapid divergence is due to the fact that the asymptotic dispersion relation (3.14) has been partly obtained as an expansion in power of the parameter $1/r_c^2 = -1/\ln\omega$. Because of the logarithm, this parameter can actually be not very small even if ω is small so that the convergence of the asymptotics is slow. Other comparisons for finite Froude and Rossby numbers are displayed in figure 3.10b, c, d. The slopes of the frequency and growth rate at $k = 0$ predicted by the asymptotics agree with the numerical results for all the values of F_h and Ro investigated. As predicted by (3.23), the growth rate remains positive for sufficiently small k even for the largest Froude number investigated $F_h = 5$ (figure 3.10b). We can see that the slope of the growth rate is smaller than the one of the frequency in figure 3.10b,d in contrast to figure 3.10a,c. As shown by (3.23) and figure 3.8,this occurs for $\alpha \lesssim -\pi/2$, i.e. when F_h is sufficiently larger than unity.

In summary, we have found that the azimuthal wavenumber $m = 1$ for the Carton & McWilliams vortex (3.6) is always unstable in the long-wavelength limit for finite Ro when $F_h \leq 1$. Thus, even if the GMW instability is dominant only in the centrifugally stable range $-1 < Ro < 7.39$, it exists for long-wavelengths outside this range of Rossby numbers. When F_h is increased above unity, the GMW instability continues to exist in the long-wavelength limit but is strongly damped by the critical layer where $\Omega(r_{c2}) = 1/F_h$. In the limit $Ro = F_h = \infty$, the long-wavelength bending mode is neutral with a negative frequency.

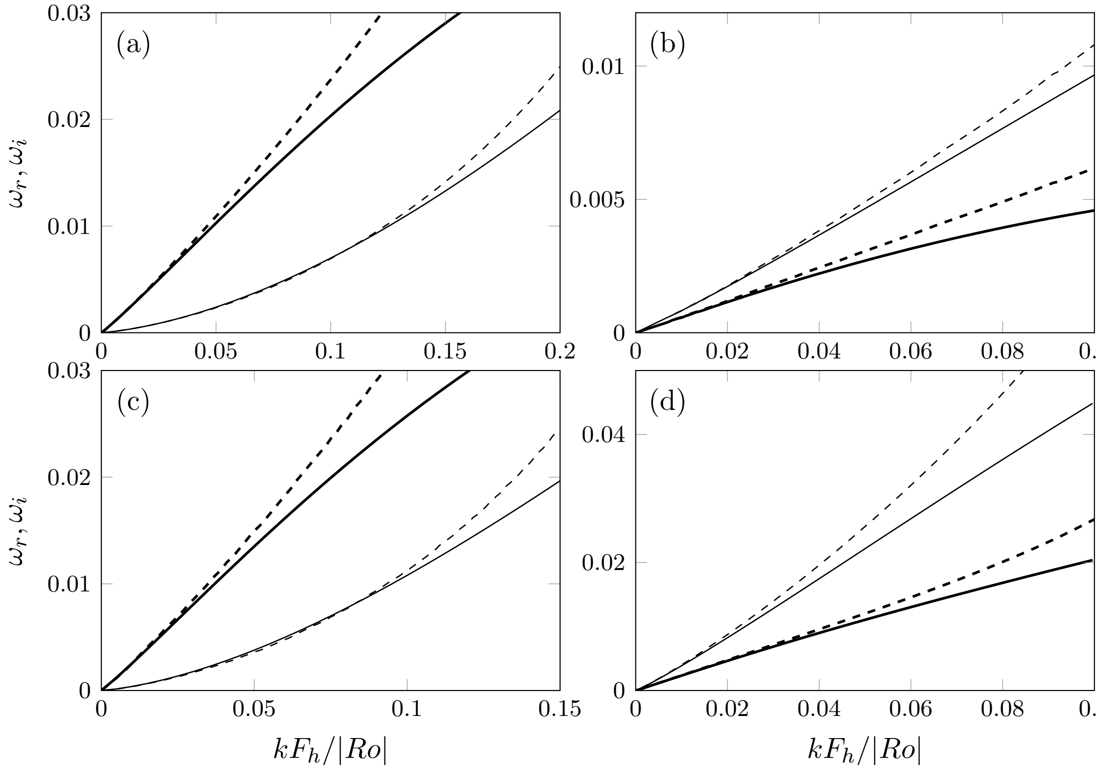

Figure 3.10: Comparison (thick lines: ω_i; thin lines: ω_r) between numerical results (solid lines) and asymptotic results (dashed lines) for the profile (3.6) for $m = 1$ for several combinations of F_h and Ro: (a) $Ro = 0.1, F_h = 0.1$; (b) $Ro = -1, F_h = 5$; (c) $Ro = 0.2, F_h = 1$; (d) $Ro = 5, F_h = 2$.

3.4.2 Vortices with algebraic decay of the angular velocity

We now investigate an angular velocity profile which behaves like $\Omega \simeq a_n/r^{2n}$ for large radii, where a_n and n are constants. This is the case of the profile

$$\Omega = 1/(1+r^2)^n, \tag{3.25}$$

considered by Gent & McWilliams (1986). The interest in this class of profiles lies in the fact that the vertical vorticity derivative $\zeta' \simeq 4a_n n(n-1)/r^{2n+1}$ for large radius can be positive or negative depending on whether $n > 1$ or $n < 1$, respectively. This will allow us to highlight the role of the sign of ζ' at the critical radius r_c. However, this asymptotic analysis can be carried out analytically only when $n = 1 + \varepsilon$ with $|\varepsilon| \ll 1$, i.e. when $\zeta'(r_c)$ is small. As discussed earlier, Briggs *et al.* (1970), Schecter *et al.* (2002) and Schecter & Montgomery (2003) also used this assumption to derive their expressions for the growth/decay rate due to the critical layer. In contrast to section 3.4.1, the critical radius r_c is located in the outer region for small wavenumber since $r_c \simeq (a_n/\omega)^{1/2n} \simeq O(1/k^{1/n})$, where it has been anticipated that $\omega \simeq O(k^2)$ at leading order. This asymptotic analysis is carried out in detail in appendix 3.C. It gives the frequency up to orders k^2 and ε in the form:

$$\omega = \omega^{(0)} + \varepsilon\omega^{(1)} + O(\varepsilon^2), \tag{3.26}$$

where

$$\omega^{(0)} = 2a_n \left(\frac{k\beta_0}{2}\right)^2 \left(-\ln\left(\frac{k|\beta_0|}{2}\right) + \frac{\delta}{a_n^2} - \gamma_e\right), \tag{3.27}$$

$$\omega^{(1)} = 2a_n \left(\frac{k\beta_0}{2}\right)^2 \left[1 - E - \gamma_e - \frac{\delta}{a_n^2} + \ln 2 + \ln(k|\beta_0|)\left(1 - 2\gamma_e - \frac{2\delta}{a_n^2} + 2\ln 2\right)\right], \tag{3.28}$$

and E is a constant defined by

$$E = \lim_{\eta_0 \to 0} \int_{\infty}^{\frac{\eta_0}{k}} \frac{4\mathrm{K}_1^2(\beta_0 k r)}{r(1-\omega^{(0)} r^2/a_n)} \mathrm{d}r + \frac{2}{\beta_0^2 \eta_0^2} - 2\ln(\eta_0\beta_0)\left[-1 + 2\gamma_e + \frac{2\omega^{(0)}}{k^2\beta_0^2 a_n} + \ln\left(\frac{\eta_0\beta_0}{4}\right)\right]. \tag{3.29}$$

The leading term $\omega^{(0)}$ in (3.26) corresponds to (3.7). When ε is non-zero and $F_h \leq 1$, all the terms in (3.26) are real except the constant E. As seen in (3.29), this constant can indeed be complex since the integrand is singular at the critical radius where $\Omega(r_c) - \omega^{(0)} \equiv a_n/r_c^2 - \omega^{(0)} = 0$. Assuming that the integration path in (3.29) is deformed in the upper complex plane since $\Omega'(r_c) < 0$, the imaginary part of E is then

$$E_i = \mathrm{imag}(E) = \pi a_{-1}, \tag{3.30}$$

with a_{-1} the residue at r_c,

$$a_{-1} = -2\mathrm{K}_1^2(k\beta_0 r_c). \tag{3.31}$$

Hence, we see that E_i is negative, implying that the growth rate $\omega_i = -\varepsilon a_n k^2 \beta_0^2 E_i/2$ is positive or negative when $\varepsilon > 0$ or $\varepsilon < 0$, respectively. Note that there also exists a decaying mode when $\varepsilon > 0$ which is the complex conjugate of the unstable mode. It can be obtained by integration in the lower complex plane. This stable mode is regular since the integration path can be deformed continuously from the real axis without encountering the critical radius r_c, unlike the stable mode when $\varepsilon < 0$.

When $F_h > 1$, the additional critical radius $\Omega(r_{c2}) = 1/F_h$ is present as for the Carton & McWilliams vortex (§3.4.1). Its effect appears again in (3.26) through δ_i the imaginary part of the constant δ. The destabilizing effect of the critical radius $\Omega(r_c) = \omega^{(0)}$ when $\varepsilon > 0$ is then in competition with the stabilizing effect due to r_{c2}. Assuming that δ_i is small, the growth rate is then at leading order

$$\omega_i = \frac{a_n k^2 \beta_0^2}{2} \left(\frac{\delta_i}{a_n^2} - \varepsilon E_i \right). \tag{3.32}$$

Therefore, there will be an instability in the long-wavelength limit only when

$$\frac{\delta_i}{a_n^2} - \varepsilon \pi a_{-1} > 0. \tag{3.33}$$

From (3.9-3.11), we can obtain

$$\delta_i = \frac{\pi r_{c2}^3}{2\Omega'(r_{c2})} \left[\frac{Ro}{2F_h} + 1 \right]^2 \frac{1}{F_h^3}. \tag{3.34}$$

This shows that δ_i depends only on (F_h, Ro) for a given velocity profile. In contrast, the residue a_{-1} depends also on kr_c and therefore varies with $(\omega^{(0)}, k)$. Thus, the condition (3.33) depends on the four parameters $(F_h, Ro, \omega^{(0)}, k)$. However, if we consider a very small wavenumber k, we have from (3.27): $\omega^{(0)} \simeq -a_n \beta_0^2 k^2 \ln(\beta_0 k/2)/2$ at leading order for finite Rossby and Froude numbers. This implies that $k\beta_0 r_c = k\beta_0 a_n/\sqrt{\omega^{(0)}} \simeq [-\ln(\beta_0 k/2)/2]^{-1/2}$ showing that $k\beta_0 r_c$ tends to zero as k tends to zero. Hence, we can estimate the residue as

$$a_{-1} = -2\mathrm{K}_1^2(k\beta_0 r_c) \simeq \ln\left(\frac{\beta_0 k}{2}\right). \tag{3.35}$$

This shows that $|a_{-1}|$ tends to infinity when k vanishes. In contrast, (3.34) is independent of the wavenumber. Therefore, if $\varepsilon > 0$, we can deduce that for any finite Rossby and Froude numbers, the condition (3.33) will be satisfied for sufficiently small wavenumber. In other words, there should always exist an instability in the long-wavelength limit for finite Froude and Rossby numbers as for the Carton & McWilliams vortex (§3.4.1). However, when either $Ro = \infty$ or $F_h = \infty$, the previous condition does not apply and it would be necessary to carry out specific analyses for these limits. In the particular limit $Ro = F_h = \infty$, it is known that the long-wavelength bending mode when $n = 1$ is neutral with a negative frequency (Widnall *et al.*, 1971; Saffman, 1992) as for the Carton & McWilliams vortex (appendix 3.B). Hence, no critical radius exists.

Figure 3.11 shows some comparisons between the predictions of (3.26) and numerical results for the angular velocity profile (3.25) for $n = 0.9$ (a,c) and $n = 1.1(b, d)$ for two Froude numbers $F_h = 0.5$ (a,b) and $F_h = 1.3$ (c,d) for a fixed Rossby number $Ro = 1$. In each case, a good agreement is found for small wavenumber. When $F_h = 0.5$, there is an instability in the long-wavelength limit when $n = 1.1$ (figure 3.11b) while the case $n = 0.9$ (figure 3.11a) is stable since ε is positive and negative, respectively. When $F_h = 1.3$, the value $n = 0.9$ (figure 3.11c) is still stable. The value $n = 1.1$ for $F_h = 1.3$ (figure 3.11d) seems also stable but if we examine on the small wavenumber region more closely, we see that the growth rate is actually positive, as predicted by (3.33). The maximum growth rate is however very small. When F_h is increased further, the maximum growth rate continues to decrease but, strictly speaking, it should remain positive for sufficiently small k when F_h is finite.

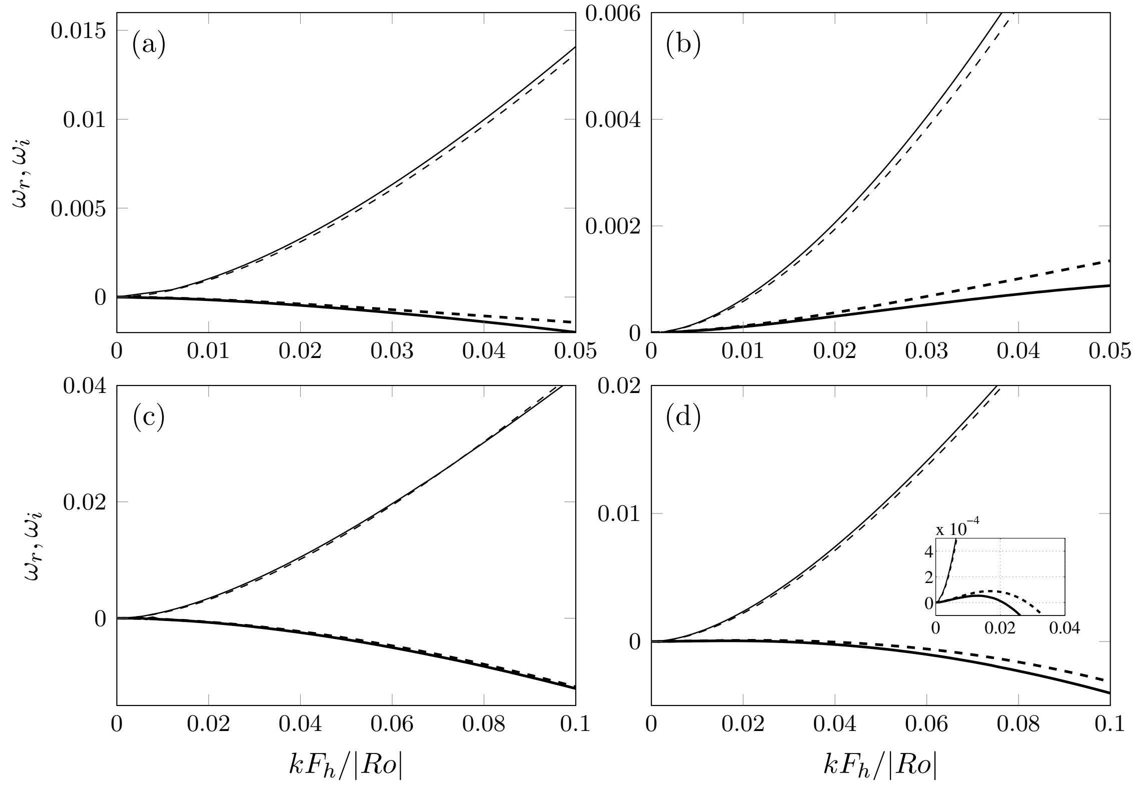

Figure 3.11: Frequency ω_r (thin lines) and growth rate ω_i (thick lines) for $m = 1$ for the profile (3.25), for $n = 0.9$ (a,c) and $n = 1.1$ (b,d) for $F_h = 0.5$ (a,b) and $F_h = 1.3$ (c,d) for $Ro = 1$. The solid and dashed lines show the numerical and asymptotic results, respectively. The insert in (d) displays a close-up view for small $kF_h/|Ro|$.

3.5 General instability condition

The long-wavelength asymptotic analysis performed in section 3.4.2 can be generalized to angular velocity profiles differing from the form $\Omega = a_n/r^{2(1+\varepsilon)}$ for large radius but still with a weak gradient of vorticity ζ' for large radius, i.e. $\Omega = a_n/r^2 + \varepsilon\Omega_1(r)$ so that $\zeta = O(\varepsilon)$. As shown in the appendix 3.C.6, the growth rate ω_i is then at leading order

$$\omega_i = \frac{a_n k^2 \beta_0^2}{2}\left[\frac{\delta_i}{a_n^2} - \frac{\pi\zeta'(r_c)\mathrm{K}_1^2(k\beta_0 r_c)}{\Omega'(r_c)}\right]. \tag{3.36}$$

Since $\delta_i \leq 0$, a general necessary condition for instability of the bending mode in the long-wavelength limit is that there exists a critical radius r_c where $\Omega(r_c) = \omega$ with $\zeta'(r_c) > 0$ since $\Omega'(r_c) \simeq -2a_n/r_c^3 < 0$. This instability condition is sufficient when $F_h \leq 1$ since $\delta_i = 0$. When $F_h > 1$, it can be also sufficient if $|\delta_i|/a_n^2$ is smaller than the destabilizing term (last term of (3.36)) as for the profiles considered in section 3.4.2. However, this depends on each particular vortex profile and therefore the instability condition will not always be sufficient for $F_h > 1$.

When $F_h < 1$, i.e. $\delta_i = 0$, the expression (3.36) closely resembles to the growth rate formula derived for weak vorticity gradient at the critical radius by Schecter *et al.* (2002) under the quasi-geostrophic approximation and Schecter & Montgomery (2003) under the asymmetric and hydrostatic balance approximations. However, the formulas of Schecter *et al.* (2002) and Schecter & Montgomery (2003) are implicit since they require prior numerical computation of the eigenfunction and frequency for zero outer vorticity gradient. These formula can become explicit only for the Rankine vortex profile with skirt (weak outer vorticity field) for which an analytic solution can be found. In this case, these formula in the limit $k \ll 1$ become identical to (3.36). In contrast, (3.36) is always explicit for any vortex profiles with small vorticity gradient at large radius. The critical radius is indeed given by $r_c = \sqrt{a_n/\omega^{(0)}}$ where the frequency at leading order $\omega^{(0)}$ is given explicitly by (3.27). The formula (3.36) is restricted to small wavenumbers k, however, the formula of Schecter *et al.* (2002) and Schecter & Montgomery (2003) are also implicitly restricted to small wavenumbers since the assumption of weak vorticity gradient at the critical radius applies when the critical radius is large, i.e. when the frequency and wavenumber are small for the bending mode. In addition, we emphasize that (3.36) is valid for any finite Froude and Rossby numbers and, therefore, is not restricted to the regime of validity of the asymmetric and hydrostatic balance approximations in contrast to the formula of Schecter & Montgomery (2003).

It is also worth noting that the instability condition $\zeta'(r_c) > 0$ is equivalent to the Rayleigh and Fjortoft necessary criteria for instability in the case of a quasi-geostrophic fluid and a vortex with a monotonically decreasing angular velocity (Gent & McWilliams, 1986). Indeed, the Rayleigh criterion requires that there exists an inflection point r_I where $\zeta'(r_I) = 0$ while the Fjortoft criterion demands that $\zeta' > 0$ for $r > r_I$ and $\zeta' < 0$ for $r < r_I$ when $\Omega'(r) < 0$ for all r. Montgomery & Shapiro (1995) have extended these criteria to flows under the asymmetric and hydrostatic balance approximations. In contrast,the present asymptotic analysis and resulting instability condition are valid for any finite Froude and Rossby numbers. However, their validity are restricted to small k and small vorticity gradient $\zeta'(r_c)$, in contrast to the Rayleigh and Fjortoft criteria.

In practice, we can show from the numerical results obtained for the profile (3.6)(section 3.3) that $\zeta'(r_c) > 0$ is a necessary condition for instability of the bending mode for any vertical wavenumber and magnitude of $\zeta'(r_c)$ for finite Froude and Rossby numbers. Figure 3.12a shows again the frequency and growth rate for $Ro = F_h = 1$ for the profile (3.6) (i.e. corresponding to the bold line in figure 3.2). The derivative of the vorticity at the

3

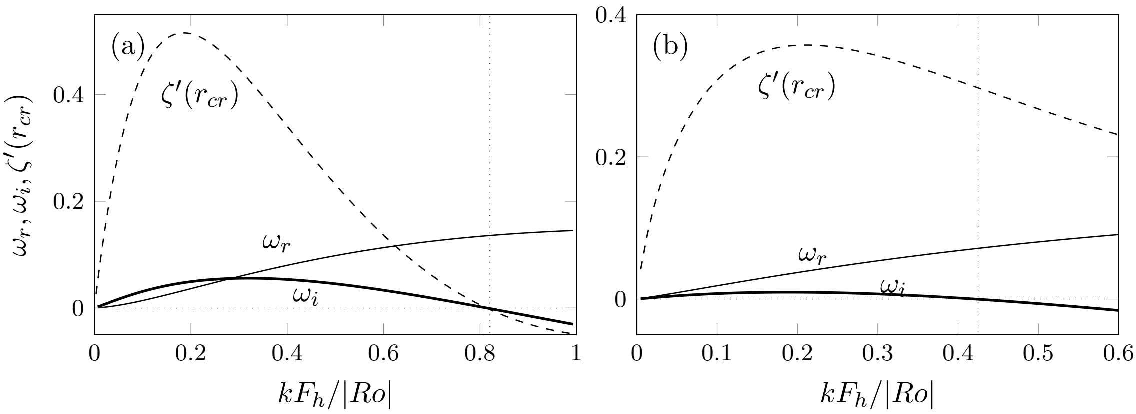

Figure 3.12: Growth rate (——: ω_i) and frequency, (——: ω_r) for the profile (3.6) for $m = 1$ as a function of $kF_h/|Ro|$ for (a) $Ro = F_h = 1$ and (b) $Ro = 1, F_h = 3$. The associated vorticity gradient $\zeta'(r_c)$ (- - -) at the location of the critical radius on the real axis r_c.

3

critical radius $\zeta'(r_{cr})$ is also plotted. Note that only the real part of r_c is considered since the imaginary part of r_c is small because ω_i is small. As seen in figure 3.12a, the growth rate ω_i and $\zeta'(r_{cr})$ are positive in the same range of vertical wavenumbers. Hence, the cutoff wavenumber $k_c F_h/|Ro| \simeq 0.8$ corresponds to the limit where $\zeta'(r_c) = 0$, i.e. when the critical radius r_c becomes equal to the inflection point $r_I = \sqrt{2}$. The maximum value of the frequency corresponds therefore to $\omega_r = \Omega(r_I) = 0.135$, as observed in section 3.3. Figure 3.13a, which shows the growth rate as a function of $\omega_r/\Omega(r_I)$, confirms that the GMW instability occurs if and only if $0 \leq \omega_r/\Omega(r_I) \leq 1$ for $F_h = 1$ for the different Rossby numbers investigated: $-0.5 \leq Ro \leq 5$ for which only the GMW instability exists.

Figure 3.12b shows the growth rate and frequency for a Froude number larger than unity: $F_h = 3$. In this case, the unstable wavenumber band corresponds only to a portion of the range where $\zeta'(r_{cr}) > 0$. This means that the instability condition $\zeta'(r_c) > 0$ is necessary but not sufficient. As shown in figure 3.13b, the range of rescaled frequency $\omega_r/\Omega(r_I)$ for which the growth rate is positive is $0 \leq \omega_r/\Omega(r_I) \leq 1$ only when $F_h \leq 1$. When $F_h > 1$, the upper frequency cutoff is lower than $\Omega(r_I)$ because of the presence of the other critical radius $\Omega(r_{c2}) = 1/F_h$ which is always stabilizing. This frequency cutoff decreases when F_h increases but the asymptotic dispersion relation (3.14) has shown that the instability is never suppressed for sufficiently small frequency ω for finite F_h and Ro for the profile (3.6).

3.6 Non-isolated vortices

In the previous sections, we have considered vortex profiles that have been shown to be unstable to the GMW instability only when their circulation is zero, i.e. when they are isolated. However, this is not generic and it is possible to have profiles with a non-zero circulation satisfying the GMW instability condition, i.e. a positive vorticity gradient for some radius. The purpose of this section is to investigate numerically the stability of the $m = 1$ azimuthal wavenumber for these vortices. To this end, we consider a family of vortices with a non-dimensional angular velocity combining a Lamb-Oseen and a Carton-McWilliams profiles:

$$\Omega(r) = a\frac{1 - e^{-r^2}}{r^2} + (1 - a)e^{-r^2}, \tag{3.37}$$

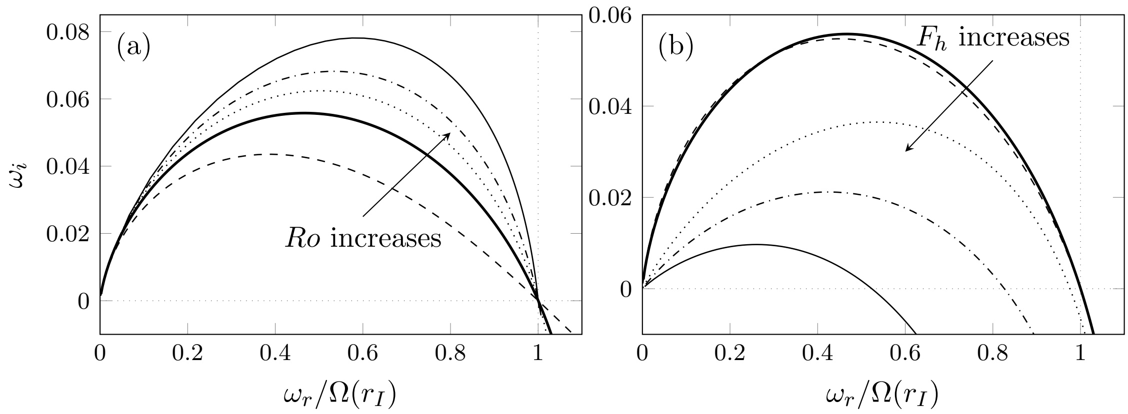

Figure 3.13: Growth rate as a function of the rescaled frequency $\omega_r/\Omega(r_I)$ for $m = 1$ for the profile (3.6) for (a) $F_h = 1$ and Ro varying: $Ro = -0.5$ - - -; $Ro = 1$ ——; $Ro = 2$ ⋯⋯; $Ro = 3$ -·-·-; $Ro = 5$ —— and (b) $Ro = 1$ and F_h varying: $F_h = 0.5$ - - -; $F_h = 1$ ——; $F_h = 1.5$ ⋯⋯; $F_h = 2$ -·-·-; $F_h = 3$ ——.

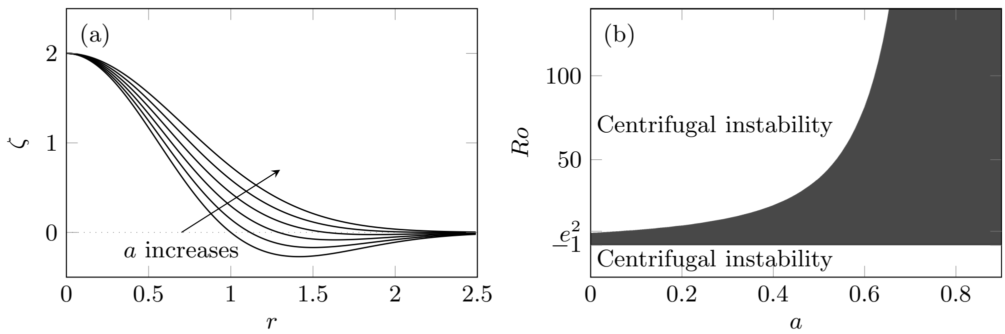

Figure 3.14: (a) Vorticity profiles corresponding to (3.37) for different values of the parameter $a = 0 : 0.2 : 1$. (b) Critical Rossby numbers for the centrifugal instability as a function of a.

where a is proportional to the non-dimensional circulation $\Gamma = 2\pi a$. When $a = 1$, the vortex is a pure Lamb-Oseen vortex while $a = 0$ corresponds to a pure Carton-McWilliams vortex. The angular velocity on the vortex axis is independent of a owing to the non-dimensionalisation. The corresponding vorticity ζ is plotted in figure 3.14a for different values of a in the range $0 \leq a \leq 1$. As a increases, the negative minimum of vorticity is reduced and disappears for $a = 1$. Accordingly, the domain of existence of the centrifugal instability (i.e. $\phi = (2\Omega + 2/Ro)(\zeta + 2/Ro) < 0$) varies with a: the upper critical Rossby number increases from $Ro_c = \exp(2)$ for $a = 0$ to $Ro_c = \infty$ for $a = 1$ (figure 3.14b). In contrast, the lower critical Rossby number remains $Ro_c = -1$ regardless of a. As in section 3.3, we shall study the GMW instability only for the Rossby numbers that are centrifugally stable.

3.6.1 Effects of the circulation parameter a and Froude number F_h

Figure 3.15 shows the growth rate and frequency of the azimuthal wavenumber $m = 1$ for $F_h = 1, Ro = 1$ for various values of the circulation parameter a. The most striking feature is that the instability no longer starts at $k = 0$ when a is non-zero. The maximum growth rate and the upper wavelength cutoff also decreases when a increases.

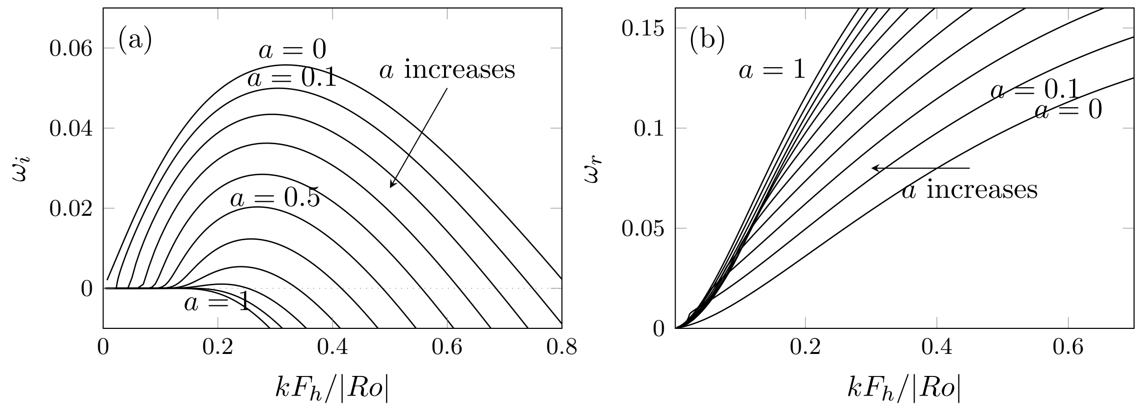

Figure 3.15: (a) Growth rate and (b) frequency as a function of $kF_h/|Ro|$ for the profile (3.37) for $m = 1$ for $F_h = 1$ and $Ro = 1$ for increasing value of a by step of 0.1.

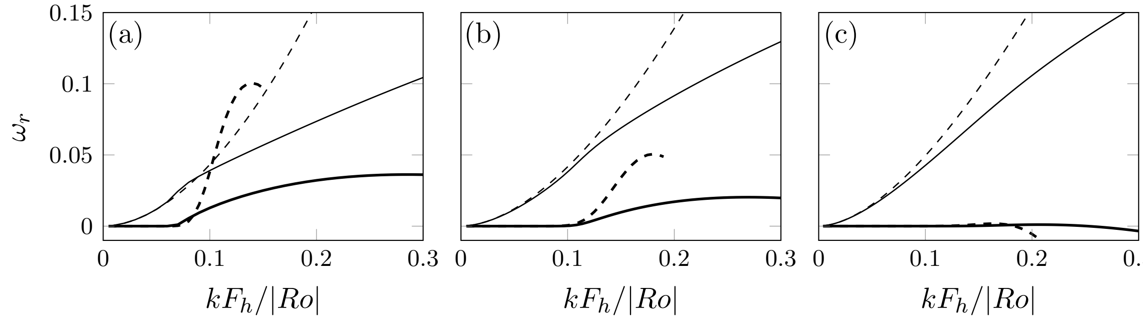

Figure 3.16: Comparison (thin lines: ω_r; thick lines: ω_i) between the numerical results (solid lines) and the asymptotic frequency (3.7) (thin dashed lines) and growth rate (3.36) (thick dashed lines) for the profile (3.37) for $m = 1$ for different values of a for $Ro = F_h = 1$: (a) $a = 0.3$; (b) $a = 0.5$; (c) $a = 0.8$.

The stabilization of small wavenumber k comes from the fact that the angular velocity now behaves like $\Omega \simeq a/r^2$ for large r. Indeed, the critical radius r_c for a given small value of ω is much larger, $r_c = \sqrt{a/\omega}$, than for $a = 0$ for which $r_c = \sqrt{-\ln\omega}$. This implies that the vorticity gradient at r_c is $O(e^{-a/\omega}\omega^{-3/2})$, i.e. exponentially small instead of being $O(\omega(\ln\omega)^{3/2})$ for $a = 0$. Since the growth rate for small wavenumber k is directly proportional to $\zeta'(r_c)$ (see (3.36)), it remains exponentially small. The frequency and growth rate are compared to the asymptotic frequency (3.7) and growth rate (3.36) in figure 3.16 for various values of a. The asymptotic frequency (3.7) and the exact frequency agree for small k and then differ as soon as the growth rate ω_i begins to rise. Remarkably, the asymptotic growth rate (3.36) also predicts well the lower wavenumber cutoff k_c at which the exact growth rate rises. However, it then quickly diverges. As seen in figure 3.16 and 3.15a, the lower wavenumber cutoff k_c increases monotonically with a. This behaviour can be understood from the fact that the growth rate becomes non-negligible when $\zeta'(r_c)$ is no longer exponentially small, i.e. approximately when $r_c \simeq 3$ whatever the value of a. Thus, the corresponding frequency $\omega_c \simeq a/r_c^2$ increases linearly with a. Since the formula (3.7) turns out to vary weakly when a varies (see figure 3.16), the corresponding wavenumber k_c, i.e. $\omega(k_c) = a/r_c^2$, increases with a.

Figure 3.17a further shows the growth rate as a function of the rescaled frequency $\omega_r/\Omega(r_I)$, where r_I is the inflection point ($\zeta'(r_I) = 0$) determined for each value of a. This figure

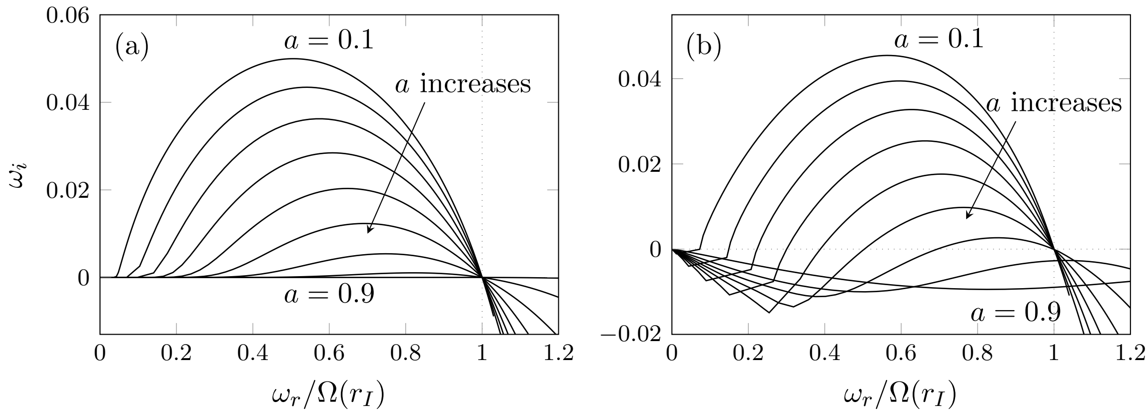

Figure 3.17: The growth rate ω_i as a function of the rescaled frequency $\omega_r/\Omega(r_I)$ for the profile (3.37) for $m = 1$ and for $Ro = 1$ for increasing values of a by step of 0.1, (a) $F_h = 1$ and (b) $F_h = 1.2$.

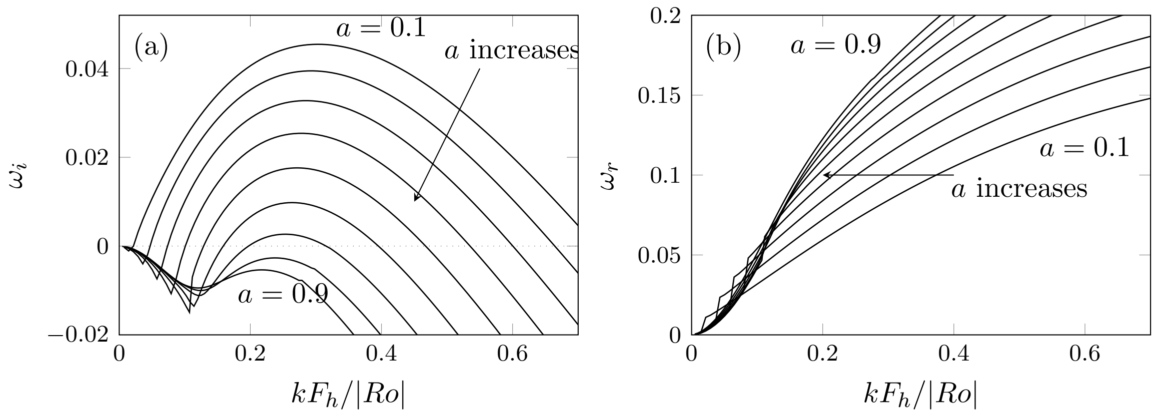

Figure 3.18: (a) Growth rate and (b) frequency as a function of $kF_h/|Ro|$ for the profile (3.37) for $m = 1$ for $F_h = 1.2$ and $Ro = 1$ for increasing values of a by step of 0.1.

demonstrates that the growth rate vanishes when $\omega_r = \Omega(r_I)$ regardless of a. Therefore, the instability occurs only when $\zeta'(r_c) > 0$ as already observed for $a = 0$ in section 3.5. The growth rate is however negligible for small rescaled frequency $\omega_r/\Omega(r_I)$ because $\zeta'(r_c)$ is then exponentially small as explained previously.

Figure 3.18 shows now the growth rate and frequency for a Froude number above unity: $F_h = 1.2$, still for $Ro = 1$. The trends when a increases are the same as for $F_h = 1$ (figure 3.15). The new feature is that the growth rate is negative for small k and then suddenly increases as for $F_h = 1$ but the maximum growth rate becomes positive only for $a \lesssim 0.7$. Figure 3.17b shows that the upper wavenumber cutoffs for $a \lesssim 0.7$ correspond to the same value of the rescaled frequency $\omega_r/\Omega(r_I)$. This critical value is very close to the threshold $\omega_r/\Omega(r_I) = 1$ in contrast to figure 3.13b where the critical rescaled frequencies $\omega_r/\Omega(r_I)$ were clearly smaller than unity for $a = 0$. This difference comes from the fact that the Froude number was larger in figure 3.13b, $F_h \geq 1.5$, than in figure 3.17b. Another difference is that the growth rate is negative for small wavenumber (i.e. small $\omega_r/\Omega(r_I)$) in figure 3.17b while for the Carton & McWilliams profile in figure 3.13b, the growth rate remains positive for small k even when $F_h > 1$. This stabilization increases with a but also with the

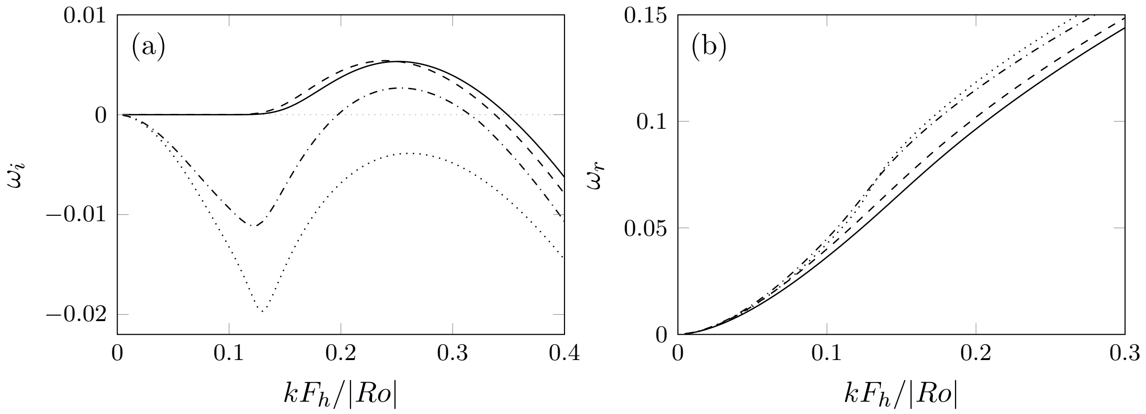

Figure 3.19: (a) Growth rate and (b) frequency as a function of $kF_h/|Ro|$ for the profile (3.37) for $m = 1$ for $a = 0.7, Ro = 1$ and varying F_h: $F_h = 0.8$ ——; $F_h = 1$ - - -; $F_h = 1.2$ -·-·-; $F_h = 1.3$ ·······.

Froude number. For example, figure 3.19 displays the growth rate and frequency for a fixed value of the circulation parameter ($a = 0.7$), but different Froude numbers. The maximum growth rate decreases when F_h is above unity and becomes negative for $F_h = 1.3$. Thus, the instability is completely suppressed when the Froude number F_h is above a critical value that depends on the circulation parameter a.

3

3.6.2 Effect of the Rossby number

The effect of the Rossby number for a fixed F_h is shown in figure 3.20. The Rossby number is varied between 0.8 and 50, i.e. within the centrifugally stable range for $a = 0.7$ ($-1 < Ro < 254$, see figure 3.14b). The maximum growth rate increases with Ro like for the Carton & McWilliams vortex (figure 3.2a).

Figure 3.21a shows the growth rate as a function of $\omega_r/\Omega(r_I)$. All the curves for $Ro \leq 10$ go to zero very close to the critical value $\omega_r/\Omega(r_I) = 1$ as previously observed. However, the growth rate for $Ro = 20$ and $Ro = 50$ remain clearly positive beyond this cutoff. Two examples of eigenmodes for $Ro = 5$ and $Ro = 50$ are depicted in figure 3.21b. The eigenmode for $Ro = 50$ exhibits oscillations outside the vortex core in contrast to the one for $Ro = 5$. Indeed, when the Rossby number is large, the eigensolution for large radius can be wavelike (see (3.5)) since the parameter $\beta^2 = (4/Ro^2 - \omega^2)/(1/Fh^2 - \omega^2)$ is negative when $|\omega_r| > 2/Ro$ (assuming $\omega_i = 0$ and $F_h < |Ro|/2$). Such outward radiation of inertia gravity waves lead to the radiative instability as shown by Smyth & McWilliams (1998), Schecter & Montgomery (2004), Billant & Le Dizès (2009), Le Dizès & Billant (2009), Riedinger *et al.* (2010), Riedinger *et al.* (2011), Park & Billant (2012) and Park & Billant (2013).

Since the maximum frequency of the GMW instability is $\max(\omega_r) = \Omega(r_I) = 0.163$ for $a = 0.7$ independently of the Rossby and Froude numbers, the critical Rossby number at which the eigenmodes become radiative for some wavenumbers can be estimated at $Ro_c = 2/\max(\omega_r) \simeq 12$. Above this Rossby number, the radiation of inertia gravity waves provides a second source of instability in addition to the critical layer at r_c. This explains why the mode $m = 1$ remains unstable beyond the cutoff frequency $\omega_r = \Omega(r_I)$ for $Ro = 20$ and $Ro = 50$ in figure 3.21a.

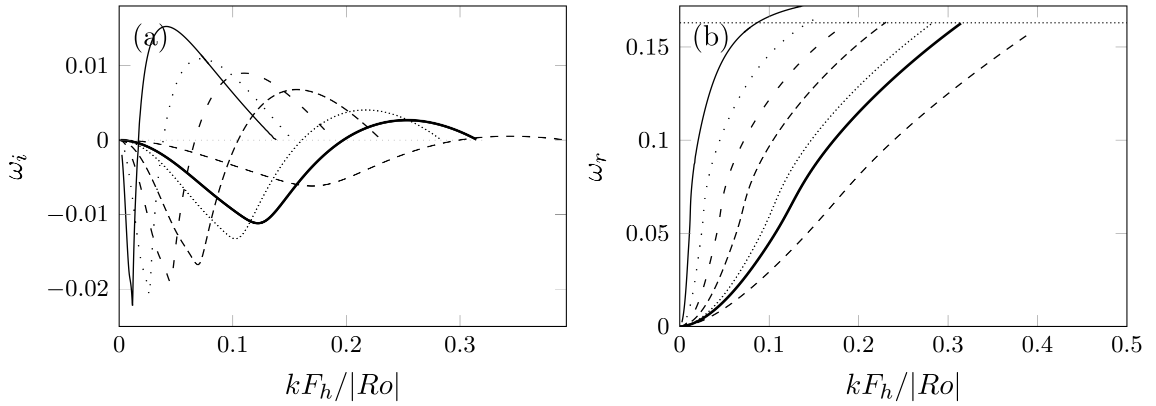

Figure 3.20: Growth rate and frequency as a function of $kF_h/|Ro|$ for the profile (3.37) for $m = 1$, $a = 0.7, F_h = 1.2$ and varying Ro: $Ro = 50$ ——; $Ro = 20$ · · · ·; $Ro = 10$ - - ; $Ro = 5$ ----; $Ro = 2$ ·········; $Ro = 1$ ——; and $Ro = -0.5$ - - - (a) growth rate, (b) frequency. The horizontal dotted line in (b) shows the cutoff frequency $\omega_r = 0.163$.

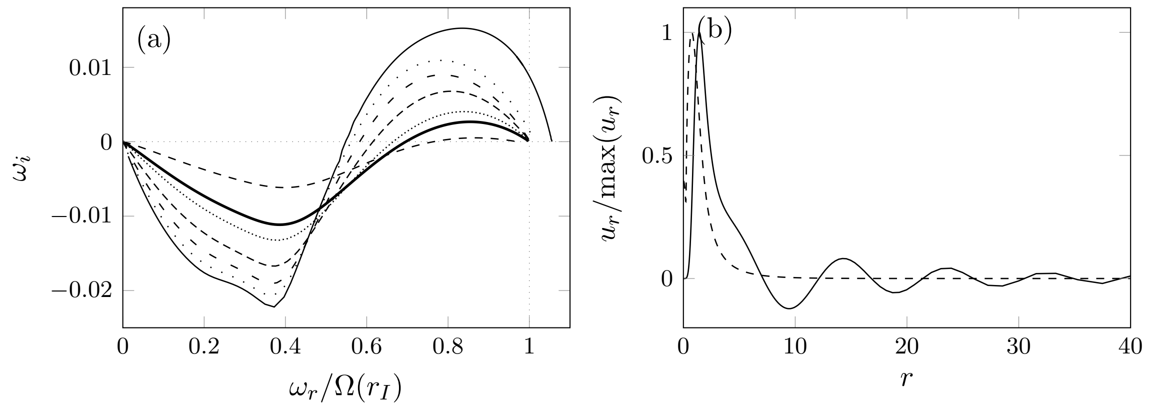

Figure 3.21: (a) Growth rate as a function of the rescaled frequency $\omega_r/\Omega(r_I)$ for the profile (3.37) for $m = 1$, $a = 0.7$, $F_h = 1.2$ and for different values of Ro : $Ro = 50$ ——; $Ro = 20$ · · · ·; $Ro = 10$ - - ; $Ro = 5$ ----; $Ro = 2$ ·········; $Ro = 1$ ——; and $Ro = -0.5$ - - -. (b) Radial velocity of the eigenmode for $F_h = 1.2, a = 0.7$ for ($Ro = 50$, $kF_h/|Ro| = 0.086$: ——) and ($Ro = 5$, $kF_h/|Ro| = 0.15$:- - -).

3.7 Conclusions

In this paper, we have investigated the stability of the azimuthal wavenumber $m = 1$ of an axisymmetric columnar vortex in a stratified and rotating fluid. As shown by Gent & McWilliams (1986) and Smyth & McWilliams (1998), this azimuthal wavenumber can be unstable to an instability which bends the vortex and leads to the formation of lenticular vortices when the fluid is both stratified and rotating. This three-dimensional instability, called the "Gent-McWilliams (GMW) instability" herein, can occur in the centrifugally stable regime and in the quasi-geostrophic limit. These properties make this instability clearly different from all other known instabilities of columnar axisymmetric vortices: shear instability, centrifugal instability and radiative instability. We have carried out both numerical and asymptotical stability analyses of several vortex profiles to better understand the origin of this instability, to explain why it occurs only in stratified rotating fluids and to derive an instability condition valid outside the quasi-geostrophic regime.

We have first recovered and extended the numerical results of Gent & McWilliams (1986) and Smyth & McWilliams (1998) for the stability of the azimuthal wavenumber $m = 1$ for the Carton & McWilliams vortex. In the centrifugally stable regime $-1 \leq Ro \leq 7.39$, we have shown that the maximum growth rate of the GMW instability increases with Ro and is independent of F_h for $F_h \leq 1$. In contrast, when $F_h > 1$, the maximum growth rate abruptly decreases with F_h and the eigenmode exhibits a critical layer singularity at the radius where $\Omega(r_{c2}) - \omega = 1/F_h$. Thereby, the maximum growth rate becomes very small for large Froude number.

These numerical results for the Carton & McWilliams vortex have been completed by an asymptotic analysis of the long-wavelength bending mode. Such mode is a generic mode which derives from the translational invariances in the two-dimensional limit. Hence, its frequency ω vanishes for $k = 0$ and can be computed by an asymptotic expansion for small wavenumber k. We have found that there exist two long-wavelength bending modes with complex conjugate frequency ω. The real part of the frequency ω_r and growth rate ω_i of the unstable mode are always positive for finite Rossby and Froude numbers for sufficiently small wavenumbers and are in good agreement with those of the GMW instability computed numerically. This shows that the GMW instability exists for long-wavelengths not only in the centrifugally stable regime: $-1 \leq Ro \leq 7.39$, but also outside of this regime. As the Froude number is increased above unity, the GMW instability continues to exist but the slope of the growth rate with k rapidly decreases and becomes negligible because of the damping by the critical layer r_{c2} where $\Omega(r_{c2}) = 1/F_h$. The asymptotic results have also allowed us to study the transition from a stratified to an homogeneous fluid in the case of a non-rotating fluid ($Ro = \infty$). We have found that the range of wavenumbers of the unstable long-wavelength bending mode shrinks to zero as the Froude number becomes infinite because of the damping by the critical layer r_{c2}. In contrast, the stable long-wavelength bending mode continues to exist as F_h increases. It becomes neutral with a negative frequency as $F_h \to \infty$ as for the vortices with a non-zero circulation (Widnall *et al.*, 1971).

This asymptotic analysis for the Carton & McWilliams vortex shows that the GMW instability is intimately linked to the existence of a critical radius r_c where $\Omega(r_c) = \omega$ as conjectured by Reasor *et al.* (2004). In order to prove the role played by the sign of the vorticity gradient $\zeta'(r_c)$ at the critical radius r_c, a second long-wavelength asymptotic analysis has been carried out for vortices exhibiting an algebraic decay of the angular velocity $\Omega \sim a_n/r^{2n}$ for large radius, with n close to unity. The sign of ζ' is positive if $n > 1$ and conversely is negative if $n < 1$. In the particular case of $n = 1$, corresponding to a vortex with a constant circulation, the long-wavelength bending mode for finite Rossby and Froude numbers is known to have a positive frequency ω_r with zero growth rate if $F_h \leq 1$ and a negative growth rate if $F_h > 1$ because of the critical layer r_{c2} where $\Omega(r_{c2}) = 1/F_h$ (Billant, 2010). Here, we have shown that the critical layer r_c where $\Omega(r_c) = \omega$ has a positive or negative contribution to the growth rate if $n > 1$ or $n < 1$, respectively. For finite Rossby and Froude numbers, this positive contribution overcomes the negative contribution of the critical layer r_{c2} for sufficiently small wavenumber. Thereby, the bending mode is always unstable for sufficiently long wavelength if $n > 1$.

For general vorticity profiles, the latter instability condition becomes $\zeta'(r_c) > 0$ in agreement with the condition derived by Schecter *et al.* (2002) and Schecter & Montgomery (2003) under the quasi-geostrophic and asymmetric balance approximations, respectively. This condition is also equivalent to the Rayleigh inflection point and Fjortoft necessary criteria derived by Gent & McWilliams (1986) in quasi-geostrophic fluids and by Montgomery & Shapiro (1995) under the asymmetric balance approximation. However, the necessary instability condition derived herein is not restricted to the quasi-geostrophic or asymmetric balance regimes but is valid for any finite Froude and Rossby numbers. Furthermore, it is necessary and sufficient if $F_h \leq 1$. Nevertheless, we stress that it is restricted to small vorticity gradients ζ' and has been derived in the long-wavelength limit. The numerical results for the Carton & McWilliams (1989) vortex show that this necessary instability condition is in practice valid for any axial wavenumber k and magnitude of ζ' for finite Froude and Rossby numbers.

Finally, we have investigated the stability of a family of vortices combining a Lamb-Oseen and Carton & McWilliams profiles. These vortices exhibit both positive vorticity gradient $\zeta'(r) > 0$ for some radii and a non-zero circulation in contrast to the two profiles previously studied. We have shown that these non-isolated vortices are also unstable to the GMW instability in stratified rotating fluids, but only for finite axial wavenumbers as previously observed by Flierl (1988) for piecewise vorticity profiles in quasi-geostrophic fluids. The long-wavelength limit $k \ll 1$ is stable (or marginally unstable) because the vorticity gradient at the critical radius $\zeta'(r_c)$ is exponentially small. This result comes from the fact that the critical radius r_c is very large when the circulation ($\Gamma = 2\pi a$) is non-zero and the frequency is small: $r_c \simeq (a/\omega)^{1/2}$. Another particularity of the GMW instability for these non-isolated vortices is that the damping effect of the critical radius r_{c2} where $\Omega(r_{c2}) = 1/F_h$ can completely overcome the destabilizing effect of the critical radius r_c when the Froude number is sufficiently large.

In summary, the origin of the GMW instability can be traced to a destabilization of the long-wavelength bending mode of a columnar vortex by a critical layer r_c where $\Omega(r_c) = \omega/m$ when $\zeta'(r_c) > 0$. This mode is specific to the azimuthal wavenumber $m = 1$ since it derives from the translational invariances. However, more generally, three-dimensional modes for other azimuthal wavenumbers $m \geq 2$ could be also destabilized by a critical layer if their frequency range lies in the range $0 < \omega/m < \Omega_0$. Some vortex waves for these azimuthal wavenumbers may indeed have a frequency in this range, both in homogeneous fluids (Kelvin, 1880; Fabre *et al.*, 2006) and stratified rotating fluid (Schecter *et al.*, 2002; Park & Billant, 2013). It would be interesting to investigate their stability for vortex profiles satisfying the condition $\zeta'(r_c) > 0$.

Acknowledgments

We thank M.T. Montgomery and W.D. Smyth for their comments to improve this manuscript. This work was supported by the National Research Agency (ANR 2011 Blanc SIMI 5-6 012-02).

3

3.A Long-wavelength analysis for the Carton & McWilliams vortex in stratified rotating fluids

In this appendix, the equation (3.2) is solved asymptotically for small kF_h and $m = 1$ for the Carton & McWilliams vortex (3.6) using the expansion (3.13). The frequency ω is first considered arbitrary for simplicity. Two regions are considered: an inner region where $r \ll 1/k$ and an outer region where $r \gg 1$. The matching of the solutions in these two regions will lead to the dispersion relation.

3.A.1 Inner region

At leading order in kF_h, (3.2) reduces to

$$\frac{\mathrm{d}^2\varphi_0}{\mathrm{d}r^2} + \frac{1}{r}\frac{\mathrm{d}\varphi_0}{\mathrm{d}r} - \left[\frac{1}{r^2} + \frac{\zeta'}{rs}\right]\varphi_0 = 0. \tag{3.38}$$

The solution which is non-singular at $r = 0$, is

$$\varphi_0 = Crs. \tag{3.39}$$

where C is a constant and we recall that $s = \Omega - \omega$. At second order, we have

$$\frac{\mathrm{d}^2\varphi_2}{\mathrm{d}r^2} + \frac{1}{r}\frac{\mathrm{d}\varphi_2}{\mathrm{d}r} - \left[\frac{1}{r^2} + \frac{\zeta'}{rs}\right]\varphi_2 = H\frac{\mathrm{d}\varphi_0}{\mathrm{d}r} + \left[\frac{\phi - s^2}{1 - s^2F_h^2} - \frac{1}{rs}\left(\frac{2}{Ro} + \zeta\right)H\right]\varphi_0, \tag{3.40}$$

where

$$H = -2rs\frac{r\Omega' + s(1 - s^2F_h^2)}{(1 - s^2F_h^2)^2}. \tag{3.41}$$

The solution can be found by reduction of order in the form

$$\varphi_2 = \varphi_0 J, \tag{3.42}$$

where

$$J = \int_0^r \eta\frac{s(2\Omega - s + 2/Ro)}{1 - F_h^2s^2}\mathrm{d}\eta + \int_0^r \frac{1}{\eta^3s^2}\left[I_1(\eta) + \frac{4I_2(\eta)}{Ro} + \frac{4I_3(\eta)}{Ro^2}\right]\mathrm{d}\eta, \tag{3.43}$$

and

$$I_p(\eta) = \int_0^\eta \frac{\xi^3s^{5-p}}{1 - F_h^2s^2}\mathrm{d}\xi, \tag{3.44}$$

with $p = 1, 2,$ or 3. The inner solution is therefore

$$\varphi_{in} = \varphi_0[1 + k^2F_h^2J] + \cdots. \tag{3.45}$$

3.A.2 Outer region

In the outer region, we define a rescaled radius such that $U = kr$ with $U = O(1)$. Since Ω and ζ are exponentially small for $r = O(1/k) \gg 1$, (3.2) becomes at leading order

$$\frac{\mathrm{d}^2\varphi}{\mathrm{d}U^2} - \frac{1}{U}\left[1 + G\right]\frac{\mathrm{d}\varphi}{\mathrm{d}U} - \left[\frac{1}{U^2} + \beta^2 + \frac{4 + 2G}{\omega U^2 Ro}\right]\varphi = 0, \tag{3.46}$$

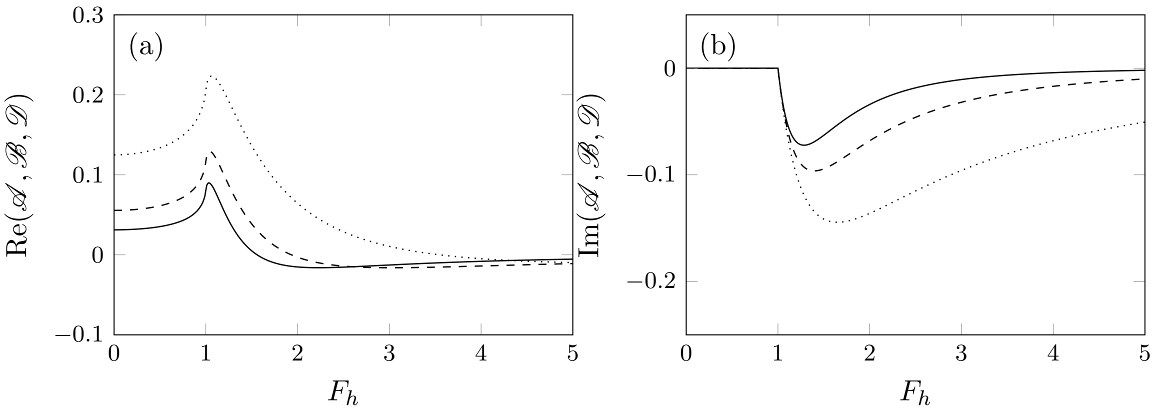

Figure 3.22: Parameters $\mathscr{A}$(——), $\mathscr{B}$(- - -) and $\mathscr{D}$(······) as a function of F_h for the Carton & McWilliams vortex (3.6): (a) real part and (b) imaginary part.

where

$$G = \frac{-2(1-\omega^2 F_h^2)}{1-\omega^2 F_h^2 - \omega^2 U^2}, \tag{3.47}$$

and $\beta^2 = (4/Ro^2 - \omega^2)/(1/F_h^2 - \omega^2)$. Assuming that $\beta^2 > 0$ and $\omega_i = 0$ or $\omega_i \neq 0$, the solution which satisfies the boundary condition at infinity is

$$\varphi_{out} = E\Big[\mathrm{K}_1(\beta U) + \frac{\omega Ro}{2+\omega Ro}\beta U \mathrm{K}_0(\beta U)\Big] + O(k^2 F_h^2), \tag{3.48}$$

where E is a constant.

3.A.3 Behaviour of J for large r

Before matching the inner and outer solutions, we need to determine the behaviour of the function J defined in (3.43) for $r \gg 1$. To this end, we assume now that ω is small. We first determine the behaviour of the integrals $I_p(\eta)$ defined in (3.44) for $\eta \gg 1$. We have

$$I_1(\eta) = \mathscr{A}(F_h) + O(\omega, \omega^4\eta^4), \tag{3.49}$$
$$I_2(\eta) = \mathscr{B}(F_h) + O(\omega, \omega^3\eta^4), \tag{3.50}$$
$$I_3(\eta) = \mathscr{D}(F_h) + F_3(\eta) + O(\omega, \omega^2\eta^4), \tag{3.51}$$

provided that $1 \ll \eta \ll 1/\sqrt{\omega}$ and $\omega F_h \ll 1$. The constants $(\mathscr{A}, \mathscr{B}, \mathscr{D})$ are defined in (3.9), (3.10) and (3.11) and the function F_3 in (3.12). For the Carton & McWilliams profile (3.6), the angular velocity decays exponentially with r so that the asymptotic form of Ω for large r can be taken as $\tilde{\Omega} = 0$, leading to $F_3(\eta_0) = F_3(\eta) = 0$. Accordingly, we have $I_3(\eta) = \mathscr{D}(F_h)$ for $\eta \gg 1$. The constants $(\mathscr{A}, \mathscr{B}, \mathscr{D})$ are plotted as a function of the Froude number in figure 3.22. We see that they are real and positive for $F_h < 1$ and complex with a negative imaginary part when $F_h > 1$. As mentioned in section 3.4.1, this is because the integrands are singular at the critical radius r_{c2} where $\Omega(r_{c2}) = 1/F_h$ and the integration path is deformed in the upper complex plane. From (3.49 − 3.51), we deduce that the behaviour of J for large r is at leading order

$$J_{r\gg 1} = \frac{4}{Ro^2}\delta(F_h, Ro)\int^r \frac{1}{\eta^3 s^2}\mathrm{d}\eta, \tag{3.52}$$

where δ is defined in (3.8). In order to further integrate (3.52), it is first convenient to write $\omega = \rho e^{i\theta}$ and to use a change of variable $x = e^{-\eta^2}/\rho$. This yields

$$J_{r\gg 1} = -\frac{2\delta\varepsilon_\rho^2}{\omega^2 Ro^2}\int^{e^{-r^2}/\rho}\frac{1}{x(1-bx)^2(1-\varepsilon_\rho\ln x)^2}\mathrm{d}x, \tag{3.53}$$

where $b = e^{-i\theta}$ and $\varepsilon_\rho = -1/\ln\rho$.

Since ω is assumed to be small, the integral (3.53) can be computed asymptotically in power of the small parameter ε_ρ when $\varepsilon_\rho|\ln x| \ll 1$, i.e. when

$$\rho \ll x \ll \frac{1}{\rho}. \tag{3.54}$$

The integration range in (3.53) is therefore split into three intervals:

$$\int^{e^{-r^2}/\rho} = \int^{x_1} + \int_{x_1}^{x_2} + \int_{x_2}^{e^{-r^2}/\rho}, \tag{3.55}$$

where the bounds (x_1, x_2) are chosen such that $\rho \ll x_2 \ll 1$ and $1 \ll x_1 \ll 1/\rho$. The three corresponding integrals are denoted J_1, J_2 and J_3.

In the first interval, we have $x \gg 1$ so that we can write

$$J_1 = -\frac{2\delta\varepsilon_\rho^2}{\omega^2 Ro^2}\int^{x_1}\frac{1}{x(1-bx)^2(1-\varepsilon_\rho\ln x)^2}\mathrm{d}x = -\frac{2\delta\varepsilon_\rho^2}{\omega^2 Ro^2}\int^{x_1}\frac{1+O(1/x)}{b^2x^3(1-\varepsilon_\rho\ln x)^2}\mathrm{d}x, \tag{3.56}$$

This yields

$$J_1 = \frac{2\delta}{\omega^2 b^2 Ro^2}\left(2e^{-2/\varepsilon_\rho}\mathrm{Ei}(2(\varepsilon_\rho^{-1}-\ln x_1)) - \frac{\varepsilon_\rho}{x_1^2(1-\varepsilon_\rho\ln x_1)} + O\left(\frac{1}{x_1^3}\right)\right), \tag{3.57}$$

where Ei is the exponential integral (Abramowitz & Stegun, 1972). Similarly, we have $x \ll 1$ throughout the third interval so that

$$J_3 = -\frac{2\delta\varepsilon_\rho^2}{\omega^2 Ro^2}\int_{x_2}^{e^{-r^2}/\rho}\frac{1}{x(1-bx)^2(1-\varepsilon_\rho\ln x)^2}\mathrm{d}x = -\frac{2\delta\varepsilon_\rho^2}{\omega^2 Ro^2}\int_{x_2}^{e^{-r^2}/\rho}\frac{1+O(x)}{x(1-\varepsilon_\rho\ln x)^2}\mathrm{d}x, \tag{3.58}$$

giving

$$J_3 = -\frac{2\delta\varepsilon_\rho^2}{\omega^2 Ro^2}\left[\frac{1}{\varepsilon_\rho^2 r^2} - \frac{1+O(x_2)}{\varepsilon_\rho(1-\varepsilon_\rho\ln x_2)}\right]. \tag{3.59}$$

Finally, in the intermediate interval, we have $\varepsilon_\rho|\ln x| \ll 1$ leading to

$$\begin{aligned} J_2 &= -\frac{2\delta\varepsilon_\rho^2}{\omega^2 Ro^2}\int_{x_1}^{x_2}\frac{1}{x(1-bx)^2(1-\varepsilon_\rho\ln x)^2}\mathrm{d}x \\ &= -\frac{2\delta\varepsilon_\rho^2}{\omega^2 Ro^2}\int_{x_1}^{x_2}\frac{1+2\varepsilon_\rho\ln x+3\varepsilon_\rho^2(\ln x)^2+O(\varepsilon_\rho^3)}{x(1-bx)^2}\mathrm{d}x. \end{aligned} \tag{3.60}$$

This gives

$$\begin{aligned}
J_2 &= -\frac{2\delta\varepsilon_\rho^2}{\omega^2 Ro^2}\left[\frac{1}{1-bx} - \ln\left(\frac{1-bx}{x}\right)\right.\\
&+ \varepsilon_\rho\left(\ln x\left(\ln x - 2 + \frac{2}{1-bx} - 2\ln(1-bx)\right) + 2\ln(1-bx) - 2\mathrm{Li}_2(bx)\right)\\
&+ \varepsilon_\rho^2 \ln x\left(\frac{3bx\ln x}{1-bx} + (\ln x)^2 + 6\ln(1-bx) - 3\ln x\ln(1-bx)\right)\\
&- \left. 6\varepsilon_\rho^2\left((-1+\ln x)\mathrm{Li}_2(bx) - \mathrm{Li}_3(bx)\right) + O(\varepsilon_\rho^3)\right]_{x_1}^{x_2}, \qquad (3.61)
\end{aligned}$$

where Li_n is the polylogarithm function of order n (Abramowitz & Stegun, 1972). We can also expand J_1 and J_3 with ε_ρ since $\varepsilon_\rho \ln x_1 \ll 1$ and $\varepsilon_\rho \ln x_2 \ll 1$. This gives

$$J_1 = \frac{\delta\varepsilon_\rho^2}{\omega^2 b^2 x_1^2 Ro^2}\left(1 + \varepsilon_\rho(1 + 2\ln x_1) + \frac{3}{2}\varepsilon_\rho^2\left(2\ln x_1 + 2(\ln x_1)^2\right) + O(\varepsilon_\rho^3)\right), \qquad (3.62)$$

$$J_3 = -\frac{2\delta\varepsilon_\rho^2}{\omega^2 Ro^2}\left(\frac{1}{\varepsilon_\rho^2 r^2} - \frac{1}{\varepsilon_\rho} - \ln x_2 - \varepsilon_\rho(\ln x_2)^2 - \varepsilon_\rho^2(\ln x_2)^3 + O(\varepsilon_\rho^3)\right). \qquad (3.63)$$

The integral J_2 can be also simplified using the fact that $x_2 \ll 1$ and $x_1 \gg 1$:

$$\begin{aligned}
J_2 &= -\frac{2\delta\varepsilon_\rho^2}{\omega^2 Ro^2}\left[1 + \ln(-b) + \ln x_2 + \frac{1}{2b^2x_1^2}\right.\\
&- \varepsilon_\rho\left(\frac{\pi^2}{3} + 2\ln(-b) + (\ln(-b))^2 - (\ln x_2)^2 - \frac{1+2\ln x_1}{2b^2x_1^2}\right)\\
&+ \varepsilon_\rho^2\Bigg((\ln x_2)^3 + \pi^2 + \pi^2\ln(-b) + 3\ln(-b)^2 + \ln(-b)^3\\
&+ \left.\frac{3(1+2\ln x_1 + 2(\ln x_1)^2)}{4b^2x_1^2}\Bigg)\right] \qquad (3.64)
\end{aligned}$$

Collecting the three integrals, we obtain

$$\begin{aligned}
&J_{r\gg1} = J_1 + J_2 + J_3 =\\
&\quad -\frac{2\delta}{\omega^2 Ro^2}\left[\frac{1}{r^2} - \varepsilon_\rho + \varepsilon_\rho^2(1+\ln(-b)) - \varepsilon_\rho^3\left(\frac{\pi^2}{3} + 2\ln(-b) + (\ln(-b))^2\right)\right.\\
&\quad \left.+ \varepsilon_\rho^4\left(\pi^2 + \pi^2\ln(-b) + 3\ln(-b)^2 + \ln(-b)^3\right) + O(\varepsilon_\rho^5)\right]. \qquad (3.65)
\end{aligned}$$

Since the small parameter depends on the logarithm of $|\omega|$: $\varepsilon_\rho = -1/\ln|\omega|$, the convergence of (3.65) is quite slow for small ω. This is the reason why we have computed $J_{r\gg1}$ up to order ε_ρ^4. It should be noted that (3.65) can be simplified by using as small parameter $\tilde{\varepsilon}_\rho = -1/\ln\omega$, i.e. equivalently $\tilde{\varepsilon_\rho} = 1/r_c^2$. It yields

$$J_{r\gg1} = -\frac{2\delta}{\omega^2 Ro^2}\left[\frac{1}{r^2} - \tilde{\varepsilon}_\rho + \tilde{\varepsilon}_\rho^2(1 + \mathrm{i}\pi\gamma) - \tilde{\varepsilon}_\rho^3\left(-2\frac{\pi^2}{3} + 2\mathrm{i}\pi\gamma\right) - \tilde{\varepsilon}_\rho^4 2\pi^2 + O(\tilde{\varepsilon}_\rho^5)\right]. \qquad (3.66)$$

where $\gamma = 1$ when $0 < \theta < \pi$ and $\gamma = -1$ when $-\pi < \theta < 0$, if the integration is performed on the real axis. All the complex terms in (3.66) are included in the parameter $\tilde{\varepsilon}_\rho$ except two. These two terms correspond to the residue at the singular radius $r_c = \sqrt{-\ln\omega}$.

3.A.4 Matching

The inner and outer solutions should match in the overlap region $1 \ll r \ll 1/k$ where they are both valid. To this end, we consider the behaviours of the inner solution (3.45) for $r \gg 1$ and the outer solution (3.48) for $U = kr \ll 1$. Using the behaviour of the function J determined in the previous section for $r \gg 1$ and $\omega \ll 1$, the inner solution for $r \gg 1$ is

$$\varphi_{in} = -C\omega r + C\frac{2F_h^2k^2}{Ro^2}\frac{\delta}{\omega}\left[\frac{1}{r} - \frac{r}{r_c^2} + \frac{r}{r_c^4}(1+\mathrm{i}\pi\gamma) - \frac{r}{r_c^6}\left(-\frac{2\pi^2}{3} + 2\mathrm{i}\pi\gamma\right)\right. \\ \left. -\frac{2\pi^2 r}{r_c^8} + \left(\frac{1}{r_c^{10}}\right)\right] + O(F_h^4k^4). \tag{3.67}$$

In turn, the outer solution (3.48) becomes at leading order for $kr \ll 1$ and $\omega \ll 1$

$$\varphi_{out} = \frac{E}{\beta_0 kr} + \frac{E\beta_0 kr}{2}\left[\ln\left(\frac{\beta kr}{2}\right) + \gamma_e - \frac{1}{2}\right], \tag{3.68}$$

where $\beta_0 = 2F_h/Ro$. The expressions (3.67) and (3.68) match at leading order if

$$E = \frac{k^3\beta_0^3 C\delta}{2\omega}, \tag{3.69}$$

$$-\omega + \frac{\delta k^2\beta_0^2}{2\omega}\left[-\frac{1}{r_c^2} + \frac{1}{r_c^4}(1+\mathrm{i}\pi\gamma) + \frac{1}{r_c^6}\left(\frac{2\pi^2}{3} - 2\mathrm{i}\pi\gamma\right) - \frac{2\pi^2}{r_c^8}\right] = O\left(\frac{\beta_0^4k^4}{\omega}\ln(\beta_0 k)\right). \tag{3.70}$$

The latter relation yields a dispersion relation valid for small k:

$$\omega^2 = \frac{k^2\beta_0^2\delta}{2}\left[-\frac{1}{r_c^2} + \frac{1}{r_c^4}(1+\mathrm{i}\pi\gamma) + \frac{1}{r_c^6}\left(\frac{2\pi^2}{3} - 2\mathrm{i}\pi\gamma\right) - \frac{2\pi^2}{r_c^8}\right]. \tag{3.71}$$

We can check a posteriori that it is legitimate to neglect the right-hand side of (3.70). In fact, (3.71) simply imposes the condition that the inner solution (3.67) decays with r and this condition could have been obtained from (3.67) without solving the outer problem. An alternative way of writing (3.71) is

$$\omega^2 = \frac{k^2\beta_0^2\delta}{2}\left[-\varepsilon_\rho + \varepsilon_\rho^2(1+\mathrm{i}\Theta) - \varepsilon_\rho^3\left(\frac{\pi^2}{3} + 2\mathrm{i}\Theta - \Theta^2\right) + \varepsilon_\rho^4(\pi^2 + \mathrm{i}\pi^2\Theta - 3\Theta^2 - \mathrm{i}\Theta^3)\right], \tag{3.72}$$

where $\Theta = \pi\ \mathrm{sgn}(\theta) - \theta$, $\varepsilon_\rho = -1/\ln|\omega|$ and $\theta = \arg(\omega)$.

3.B Effect of the Froude number on the long-wavelength bending mode of the Carton & McWilliams vortex in non-rotating fluids

When $Ro = \infty$, the matched asymptotic analysis conducted in appendix 3.A and section 3.4.1 for the Carton & McWilliams vortex (3.6) remains valid whatever the Froude number F_h. In this case, we have therefore the opportunity to study the transition from a stratified fluid to an homogeneous fluid $F_h = \infty$.

In the limit $Ro = \infty$, the dispersion relation (3.14) can be rewritten in the convenient form

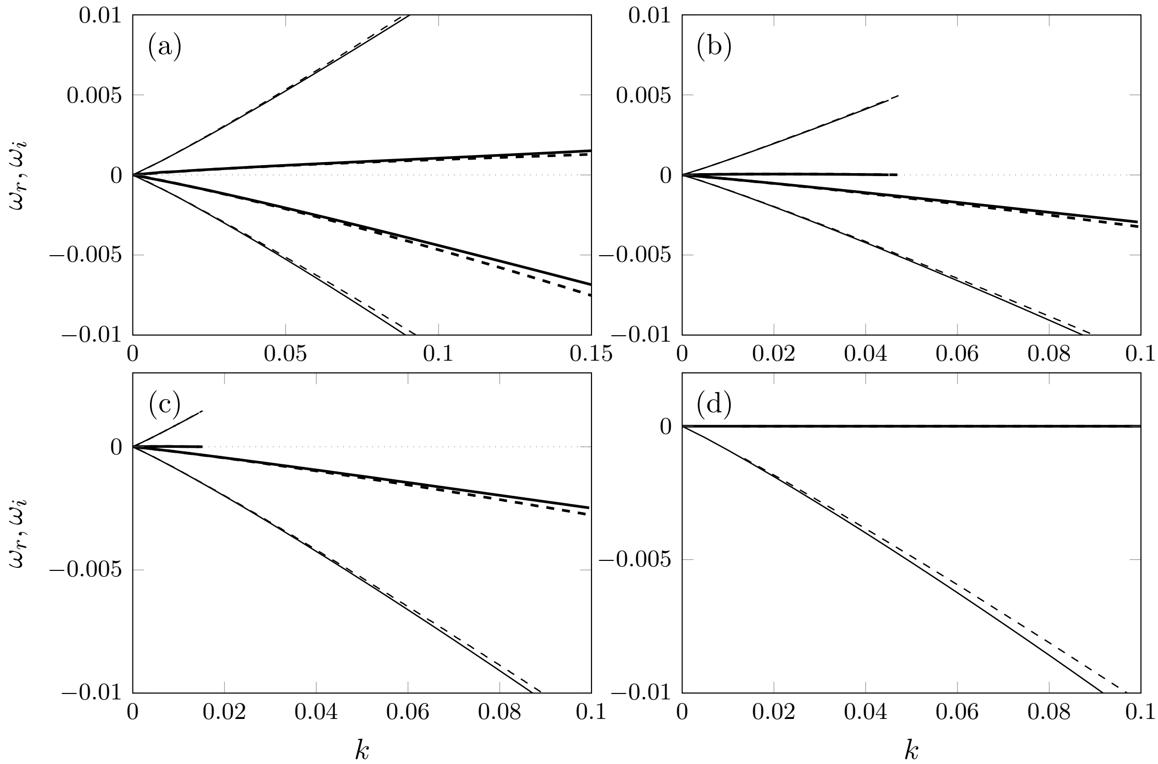

Figure 3.23: Frequency ω_r (thin lines) and growth rate ω_i (thick lines) as a function of k for the azimuthal wavenumber $m = 1$ for the Carton & McWilliams vortex (3.6) for (a) $F_h = 3$, (b) $F_h = 4$, (c) $F_h = 4.5$ and (d) $F_h = \infty$ for $Ro = \infty$. The solid lines show the numerical results while the dashed line represents the asymptotic frequency (3.73).

(see (3.72))

$$\omega^2 = \frac{k^2\Lambda}{2}\left[-\varepsilon_\rho + \varepsilon_\rho^2(1+\mathrm{i}\Theta) - \varepsilon_\rho^3\left(\frac{\pi^2}{3} + 2\mathrm{i}\Theta - \Theta^2\right) + \varepsilon_\rho^4\left(\pi^2 + \mathrm{i}\pi^2\Theta - 3\Theta^2 - \mathrm{i}\Theta^3\right)\right], \tag{3.73}$$

where

$$\Lambda = F_h^2\mathscr{A} = F_h^2\int_0^\infty \frac{\xi^3\Omega^4}{1 - F_h^2\Omega^2}\mathrm{d}\xi, \tag{3.74}$$

where $\mathscr{A}$ is defined in (3.9).

In the limit $F_h \to \infty$, Λ tends to a finite value which is real and negative: $\Lambda = -\int_0^\infty \xi^3\Omega^2\mathrm{d}\xi$. Hence, it is straightforward to see that (3.73) has a solution where ω is purely real and negative (i.e. $\Theta = 0$)

$$\omega^2 = -\frac{k^2\Lambda}{2}\left[\varepsilon_\rho - \varepsilon_\rho^2 + \varepsilon_\rho^3\frac{\pi^2}{3} - \varepsilon_\rho^4\pi^2\right]. \tag{3.75}$$

In fact, this is the only solution of (3.73). As for vortices with a non-zero circulation (Widnall *et al.*, 1971), the long-wavelength bending mode of the Carton & McWilliams vortex in homogeneous non-rotating fluid is therefore neutral with a negative frequency. This implies that there is no critical radius $\Omega(r_c) = \omega$.

Figure 3.23 shows the two solutions of (3.73) for several Froude numbers from $F_h = 3$ to

$F_h = \infty$ and compares them to numerical results. We see that the branch with positive growth rate predicted by (3.73) exists only for small wavenumbers when $F_h = 4$ (figure 3.23b). It disappears when the growth rate vanishes because the integration path is on the real axis. For $F_h = 4.5$, this branch shrinks further, and when $F_h = \infty$ it has completely disappeared. In contrast, the other branch continues to exist as F_h increases. Its frequency remains negative but its damping rate diminishes as F_h increases. It becomes neutral in the limit $F_h = \infty$. For all the Froude numbers investigated, (3.73) is in good agreement with the numerical results for small wavenumber.

3.C Long-wavelength analysis for vortices with angular velocity decaying algebraically in stratified rotating fluid

In this appendix, a long-wavelength asymptotic analysis similar to the asymptotic analysis of appendix 3.A is carried out for vortices with an angular velocity behaving like $\Omega \simeq a_n/r^{2n}$ for large radius. In contrast to appendix 3.A, it is more convenient to assume that ω is small from the outset and expanded with $k^2F_h^2$

$$\omega = 0 + F_h^2 k^2 \omega_2 + \cdots . \tag{3.76}$$

As before, the inner and outer solutions are expanded in the form

$$\varphi = \varphi_0 + F_h^2 k^2 \varphi_2 + \cdots . \tag{3.77}$$

The inner solution will be determined for arbitrary n while the outer solution can be computed analytically only for $n = 1 + \varepsilon$ with $|\varepsilon| \ll 1$.

3.C.1 Inner region

In the inner region, the solutions φ_0 and φ_2 have the same form as in (3.39) and (3.42) except that, since $\omega = \omega_2 k^2 F_h^2 + \cdots$, s can be approximated by Ω and the term $-r\omega C$ in the leading order solution (3.39) appears in the second order solution φ_2:

$$\varphi_0 = Cr\Omega, \tag{3.78}$$

$$\varphi_2 = \varphi_0 \left[\int_0^r \eta \frac{\Omega(\Omega + 2/Ro)}{1 - F_h^2\Omega^2} \mathrm{d}\eta + \int_0^r \frac{1}{\eta^3\Omega^2} \left(\tilde{I}_1(\eta) + \frac{4\tilde{I}_2(\eta)}{Ro} + \frac{4\tilde{I}_3(\eta)}{Ro^2} \right) \mathrm{d}\eta \right] - C\omega_2 r, \tag{3.79}$$

where

$$\tilde{I}_p(\eta) = \int_0^\eta \frac{\xi^3\Omega^{5-p}}{1 - F_h^2\Omega^2} \mathrm{d}\xi, \tag{3.80}$$

with $p = 1, 2$ or 3.

3.C.2 Outer region

As in appendix 3.A.2, the outer solution can be determined by defining a rescaled radius $U = kr$ with $U = O(1)$. However, the angular velocity Ω and vorticity ζ are now not negligible since $\Omega \sim a_n/r^{2n}$ for $r \gg 1$. Indeed, the rescaling of (3.2) gives for such a profile:

$$\frac{\mathrm{d}^2\varphi}{\mathrm{d}U^2} + \frac{1}{U}\left[1+M\right]\frac{\mathrm{d}\varphi}{\mathrm{d}U} - \varphi\left[\frac{1}{U^2} + {\beta_0}^2 + O(F_h^2\omega^2, F_h^2k^{4n}, F_h^2k^{2n}\omega) \right.$$
$$\left. -\frac{4n(1-n)}{U^2(1-\frac{\omega U^{2n}}{a_n k^{2n}})} + \frac{MU^{2n-1}}{(k^{2n}-\omega U^{2n}/a_n)}\left[\frac{2}{Ro} + \frac{2(1-n)k^{2n}}{U^{2n}}\right]\right] = 0, \tag{3.81}$$

where $M = O(F_h^2\omega^2, F_h^2k^{4n}, F_h^2k^{2n}\omega)$ and $\beta_0 = 2F_h/Ro$.

Hence, since $\omega = \omega_2 k^2 F_h^2$, (3.81) reduces at leading order to:

$$\frac{\mathrm{d}^2\varphi}{\mathrm{d}U^2} + \frac{1}{U}\frac{\mathrm{d}\varphi}{\mathrm{d}U} - \varphi\left[\frac{1}{U^2} + \beta_0^2 - \frac{4n(1-n)}{U^2[1-k^{2(1-n)}F_h^2\omega_2 U^{2n}/a_n]}\right] = 0. \tag{3.82}$$

This equation can be solved asymptotically when $n = 1+\varepsilon$ with $|\varepsilon| \ll 1$. To do so, we expand the outer solution and ω_2 with ε

$$\varphi_{out} = \varphi_0^{(0)} + \varepsilon\varphi_0^{(1)} + \cdots, \tag{3.83}$$
$$\omega_2 = \omega_2^{(0)} + \varepsilon\omega_2^{(1)} + \cdots. \tag{3.84}$$

The solution at leading order is

$$\varphi_0^{(0)} = \mathrm{K}_1\left(\beta_0 U\right). \tag{3.85}$$

At the next order, we have

$$\frac{\mathrm{d}^2\varphi_0^{(1)}}{\mathrm{d}U^2} + \frac{1}{U}\frac{\mathrm{d}\varphi_0^{(1)}}{\mathrm{d}U} - \varphi_0^{(1)}\left[\frac{1}{U^2} + \beta_0^2\right] = \frac{4\varphi_0^{(0)}}{U^2(1-F_h^2\omega_2^{(0)}U^2/a_n)}. \tag{3.86}$$

The solution is found by reduction of order

$$\varphi_0^{(1)} = \mathrm{K}_1(\beta_0 U)\int_\infty^U \frac{1}{\eta \mathrm{K}_1^2(\beta_0\eta)}\int_\infty^\eta \frac{4\mathrm{K}_1^2(\beta_0\xi)}{\xi(1-F_h^2\omega_2^{(0)}\xi^2/a_n)}\mathrm{d}\xi\mathrm{d}\eta, \tag{3.87}$$

where the integration constants have been chosen such that $\varphi_0^{(1)}$ tends to zero for $U \to \infty$.

3.C.3 Behaviour of the inner solution for large r

In preparation for the matching, we determine the behaviour of the inner solution for $r \gg 1$. We start by determining the behaviours of the integrals $\tilde{I}_p(\eta)$ defined in (3.80). Because $\Omega \sim a_n/r^{2n}$ as $r \to \infty$, we have for $\eta \gg (a_n F_h)^{1/2n}$

$$\tilde{I}_1(\eta) \sim \mathscr{A}(F_h) + O(1/\eta^{8n-4}), \tag{3.88}$$
$$\tilde{I}_2(\eta) \sim \mathscr{B}(F_h) + O(1/\eta^{6n-4}), \tag{3.89}$$
$$\tilde{I}_3(\eta) \sim \mathscr{D}(F_h) + F_3(\eta), \tag{3.90}$$

where $\mathscr{A}, \mathscr{B}, \mathscr{D}$ are defined in (3.9), (3.10), (3.11) and F_3 in (3.12). Using the asymptotic form of Ω for large radius $\tilde{\Omega} = a_n/r^{2n}$ gives the function:

$$F_3(\eta) = \int^\eta \frac{\tilde{\Omega}^2\xi^3}{1-F_h^2\tilde{\Omega}^2}\mathrm{d}\xi = a_n^2\left[\frac{\eta^{4-4n}-1}{4-4n}\right]. \tag{3.91}$$

The behaviour of the second order inner solution (3.79) for $r \gg \max(F_h^{1/2n}, 1)$ is therefore

$$\varphi_2 \sim C\left[\frac{4}{a_n Ro^2}\frac{\delta r^{2n-1}}{4n-2} + \frac{a_n}{2Ro^2(1-n)}\left(r^{3-2n} - \frac{r^{2n-1}}{2n-1}\right) - \omega_2 r\right], \tag{3.92}$$

where δ is defined in (3.8). The behaviour of the inner solution for large r is then

$$\begin{aligned}\varphi_{in} \sim & C\left[\frac{a_n}{r^{2n-1}} + F_h^2 k^2\left[\frac{4}{a_n Ro^2}\frac{\delta r^{2n-1}}{4n-2} + \frac{1}{2Ro^2(1-n)}\left(r^{3-2n} - \frac{r^{2n-1}}{2n-1}\right) - \omega_2 r\right]\right] \\ & + O(F_h^4 k^4).\end{aligned} \tag{3.93}$$

If we now further assume that $n = 1 + \varepsilon$ with $|\varepsilon| \ll 1$, we obtain

$$\begin{aligned}\varphi_{in} = C a_n & \left[\frac{1}{r} - 2\varepsilon\frac{\ln r}{r} + k^2 F_h^2 r\left[\frac{2\delta}{a_n^2 Ro^2} + \frac{2\ln r - 1}{Ro^2} - \frac{\omega_2^{(0)}}{a_n}\right.\right. \\ & \left.\left. + \varepsilon\left(-\frac{\omega_2^{(1)}}{a_n}\frac{4\delta}{a_n^2 Ro^2}(\ln r - 1) + \frac{1}{Ro^2}(2 - 2\ln r)\right)\right]\right] + O(\varepsilon^2, k^4 F_h^4).\end{aligned} \tag{3.94}$$

3.C.4 Behaviour of the outer solution for small U

3

In order to match the inner and outer solutions, we need also to determine the behaviour of (3.87) for $U \ll 1$, i.e. for $r \ll 1/k$. To do so, we first rewrite (3.87) in the form $\varphi_0^{(1)} = M(U)\mathrm{K}_1(\beta_0 U)$ where

$$M(U) = \int_\infty^U \frac{\chi(\eta)}{\eta \mathrm{K}_1^2(\beta_0\eta)}\mathrm{d}\eta, \tag{3.95}$$

and

$$\chi(\eta) = \int_\infty^\eta \frac{4\mathrm{K}_1^2(\beta_0 U)}{U(1 - F_h^2\omega_2^{(0)}U^2 a_n^{-1})}\mathrm{d}U. \tag{3.96}$$

When η is small, we have

$$\chi(\eta) = E - \frac{2}{\beta_0^2\eta^2} + 2\ln(\eta\beta_0)\left(-1 + 2\gamma_e + \frac{2\omega_2^{(0)}F_h^2}{\beta_0^2 a_n} + \ln\frac{\eta\beta_0}{4}\right) + O(\eta^2), \tag{3.97}$$

where E is a constant defined as

$$\begin{aligned}E = & \int_\infty^{\eta_0} \frac{4\mathrm{K}_1^2(\beta_0 U)}{U(1 - F_h^2\omega_2^{(0)}U^2 a_n^{-1})}\mathrm{d}U + \frac{2}{\beta_0^2\eta_0^2} \\ & - 2\ln(\eta_0\beta_0)\left(-1 + 2\gamma_e + \frac{2\omega_2^{(0)}F_h^2}{\beta_0^2 a_n} + \ln\left(\frac{\eta_0\beta_0}{4}\right)\right),\end{aligned} \tag{3.98}$$

with $0 < \eta_0 \ll 1$. Using (3.97), we can now determine the behaviour of M for small U. We obtain

$$\begin{aligned}M = & G - 2\ln(U\beta_0) + \beta_0^2 U^2\left[\frac{E}{2} - \frac{F_h^2\omega_2^{(0)}}{\beta_0^2 a_n} + \ln(U\beta_0)\left(-1 + 2\gamma_e + \frac{2F_h^2\omega_2^{(0)}}{\beta_0^2 a_n} - 2\ln 2\right)\right] \\ & + \beta_0^2 U^2(\ln U\beta_0)^2 + O(U^4),\end{aligned} \tag{3.99}$$

where G is a constant. This constant can be set to zero without loss of generality by a simple rescaling of the leading order solution. This implies that $\varphi_0^{(1)}$ for small U is of the form:

$$\varphi_0^{(1)} = M\mathrm{K}_1(\beta_0 U) = -\frac{2\ln(U\beta_0)}{\beta_0 U} + \frac{\beta_0 U}{2}\left[E - \frac{2F_h^2\omega_2^{(0)}}{\beta_0^2 a_n}\right. \\ \left. + \ln(U\beta_0)\left(-1 + 2\gamma_e + \frac{4F_h^2\omega_2^{(0)}}{\beta_0^2 a_n} - 2\ln 2\right)\right] + O(U^3). \qquad (3.100)$$

We can then deduce that the outer solution (3.84) becomes for small $U = kr$

$$\varphi_{out} = \frac{1}{\beta_0 kr} + \frac{\beta_0 kr}{2}\left[\frac{\ln(\beta_0 kr)}{2} + \gamma_e - \frac{1}{2}\right] + \varepsilon\left[-\frac{2\ln(\beta_0 kr)}{\beta_0 kr}\right. \\ \left. + \frac{\beta_0 kr}{2}\left(E - \frac{2F_h^2\omega_2^{(0)}}{\beta_0^2 a_n} + \ln(\beta_0 kr)\left(-1 + 2\gamma_e + \frac{4F_h^2\omega_2^{(0)}}{\beta_0^2 a_n} - 2\ln 2\right)\right)\right] + \cdots. \qquad (3.101)$$

3.C.5 Matching

The expressions of the inner and outer solutions (3.94) and (3.101) match if

$$Ca_n = \frac{1}{\beta_0 k}(1 - 2\varepsilon\ln(k\beta_0)), \qquad (3.102)$$

$$2Ca_n k^2 \frac{F_h^2}{Ro^2}\left(1 + \varepsilon\left(\frac{2\delta}{a_n^2} - 1\right)\right) = \frac{\beta_0 k}{2} + \frac{\varepsilon\beta_0 k}{2}\left(-1 + 2\gamma_e - 2\ln 2 + \frac{4F_h^2\omega_2^{(0)}}{\beta_0^2 a_n}\right), \qquad (3.103)$$

$$Cak^2F_h^2\left[\frac{2\delta}{a_n^2 Ro^2} - \frac{1}{Ro^2} - \frac{\omega_2^{(0)}}{a_n} + \varepsilon\left(-\frac{4\delta}{a_n^2 Ro^2} + \frac{2}{Ro^2} - \frac{\omega_2^{(1)}}{a_n}\right)\right] = \frac{\beta_0 k}{2}\left(\ln\frac{\beta_0 k}{2}\right. \\ \left. + \gamma_e - \frac{1}{2}\right) + \frac{\varepsilon\beta_0 k}{2}\left[E - \frac{2F_h^2\omega_2^{(0)}}{\beta_0^2 a_n} + \ln(k\beta_0)\left(-1 + 2\gamma_e + \frac{4F_h^2\omega_2^{(0)}}{\beta_0^2 a_n} - 2\ln 2\right)\right]. \qquad (3.104)$$

The first relation gives the constant C while the two others give the dispersion relation

$$\omega = F_h^2 k^2(\omega_2^{(0)} + \varepsilon\omega_2^{(1)}) = \frac{a_n\beta_0^2 k^2}{2}\left(-\ln\frac{\beta_0 k}{2} - \gamma_e + \frac{\delta}{a_n^2}\right) + \varepsilon a_n \frac{\beta_0^2 k^2}{2}\left[1 - E - \gamma_e - \frac{\delta}{a_n^2}\right. \\ \left. + \ln 2 + \ln(\beta_0 k)\left(1 - 2\gamma_e - \frac{2\delta}{a_n^2} + 2\ln 2\right)\right] + O(\varepsilon^2, k^4\ln(k)). \qquad (3.105)$$

3.C.6 Generalization to arbitrary profiles with a weak gradient of vorticity for large radius

In this section, we consider an angular velocity profile different from the form $\Omega \simeq a_n/r^{2(1+\varepsilon)}$ but still with a weak gradient of vorticity for large radii. In other words, its angular and vorticity profiles for large radii can be written in the general form

$$\Omega = \Omega_0(r) + \varepsilon\Omega_1(r), \qquad \zeta = \varepsilon\zeta_1(r), \qquad (3.106)$$

where $\Omega_0(r) = a_n/r^2$, $\varepsilon \ll 1$ and (Ω_1, ζ_1) are of order unity. In this case, the outer solution has the same form as found in §3.C.2 except that (3.87) is replaced by

$$\varphi_0^{(1)} = \mathrm{K}_1(\beta_0 U) \int_\infty^U \frac{1}{\eta \mathrm{K}_1^2(\beta_0 \eta)} \int_\infty^\eta \frac{\zeta_1'(\xi/k)\mathrm{K}_1^2(\beta_0 \xi)}{k(\Omega_0(\xi/k) - \omega^{(0)})} \mathrm{d}\xi \mathrm{d}\eta, \tag{3.107}$$

This implies that the frequency will be of the same form as in (3.26) with $\omega^{(0)}$ given by (3.27) and $\omega^{(1)}$ by

$$\omega^{(1)} = 2a_n \left(\frac{k\beta_0}{2}\right)^2 \left(-E + g_1(k, \omega^{(0)}, F_h, Ro)\right), \tag{3.108}$$

where

$$E = \lim_{\eta_0 \to 0} \int_\infty^{\frac{\eta_0}{k}} \frac{\zeta_1'(r)\mathrm{K}_1^2(\beta_0 kr)}{(\Omega_0(r) - \omega^{(0)})} \mathrm{d}r + g_2(k, \eta_0, \omega^{(0)}, F_h, Ro), \tag{3.109}$$

where the functions g_1 and g_2 will be different for each particular profile considered and would have to be determined by matching the inner and outer solutions. However, without determining the explicit expression of these functions, it is easy to see that they should be real if $\omega^{(0)}$ is real. Hence, if δ_i is small, we can deduce that the growth rate will be at leading order

$$\omega_i = 2a_n \left(\frac{k\beta_0}{2}\right)^2 \left[\frac{\delta_i}{a_n^2} - \varepsilon\pi \frac{\zeta_1'(r_c)\mathrm{K}_1^2(k\beta_0 r_c)}{\Omega_0'(r_c)}\right] + O(\varepsilon\delta_i), \tag{3.110}$$

since the residue of the integral in (3.109) at r_c is $a_{-1} = \zeta_1'(r_c)\mathrm{K}_1^2(k\beta_0 r_c)/\Omega_0'(r_c)$. Equation (3.110) can be also rewritten in terms of the full profiles (3.106)

$$\omega_i = 2a_n \left(\frac{k\beta_0}{2}\right)^2 \left[\frac{\delta_i}{a_n^2} - \pi \frac{\zeta'(r_c)\mathrm{K}_1^2(k\beta_0 r_c)}{\Omega'(r_c)}\right] + O(\varepsilon\delta_i). \tag{3.111}$$

4

Stability of a pancake vortex in stratified fluids

In order to understand the dynamics of pancake-like shape vortices in stably stratified fluids, we perform a linear stability analysis of an axisymmetric vortex with Gaussian angular velocity in both radial and axial directions with an aspect ratio α. The results are compared to those for a columnar vortex ($\alpha = \infty$) in order to identify the instabilities. The centrifugal instability occurs when $\mathcal{R} > c(m)$ where $\mathcal{R} = ReF_h^2$ is the buoyancy Reynolds number, F_h the Froude number, Re the Reynolds number and $c(m)$ a constant which differs for the three unstable azimuthal wavenumbers $m = 0, 1, 2$. The maximum growth rate depends mostly on $\mathcal{R}$ and is almost independent of the aspect ratio α. For sufficiently large buoyancy Reynolds number, the axisymmetric mode is the most unstable centrifugal mode whereas for moderate $\mathcal{R}$, the mode $m = 1$ is the most unstable. The shear instability for $m = 2$ develops only when $F_h \leq 0.5\alpha$. By considering the characteristics of the shear instability for a columnar vortex for the same parameters, this condition is shown to be such that the vortex thickness is larger than the minimum wavelength of the shear instability in the columnar case. For larger Froude number $F_h \geq 1.5\alpha$, the isopycnals overturn and the gravitational instability can operate. Just below this threshold, the azimuthal wavenumbers $m = 1, 2, 3$ are unstable to the baroclinic instability. A simple model shows that the baroclinic instability develops only above a critical vertical Froude number F_h/α because of confinement effects.

Contents

Analogies and differences between the stability of an isolated pancake vortex and a columnar vortex in stratified fluid

Eunok Yim and Paul Billant

LadHyX, CNRS, École Polytechnique, F-91128 Palaiseau Cedex, France

(Submitted to *J. Fluid Mech.*)

4.1 Introduction

Several studies have been devoted to the stability of a columnar vertical vortex in stably stratified fluids. Axisymmetric columnar vortices can be unstable to the centrifugal instability when the Rayleigh discriminant is negative (Smyth & McWilliams, 1998; Billant & Gallaire, 2005). Shear instability may also occur when the vorticity gradient vanishes at some radius (Rayleigh, 1880) since it is a two-dimensional instability. In addition, the vortex can spontaneously radiate internal waves owing to an over-reflection mechanism (Smyth & McWilliams, 1998; Le Dizès & Billant, 2009; Billant & Le Dizès, 2009; Riedinger *et al.*, 2010). However, many studies have shown that vortices have a pancake or lenticular shape in stratified fluids rather than being columnar. For example, interacting columnar vortices are unstable to the zigzag instability (Billant & Chomaz, 2000; Otheguy *et al.*, 2006; Billant, 2010; Billant *et al.*, 2010; Deloncle *et al.*, 2011) and evolve into pancake vortices with a small aspect ratio. Coherent vortices generated from wakes or turbulence in stratified fluids have also a pancake shape (Lin *et al.*, 1992; Chomaz *et al.*, 1993; Spedding *et al.*, 1996; Fincham *et al.*, 1996; Bonnier *et al.*, 2000). In laboratory experiments, pancake vortices can be directly generated by different devices imposing a rotation to a layer of fluid (Flór & van Heijst, 1996; Beckers *et al.*, 2001). Many pancake vortices are also observed in oceans. Famous examples are the Mediterranean eddies (Meddies) which are formed by salty water flowing from Mediterranean sea in mid-Atlantic ocean (Armi *et al.*, 1989; Hobbs, 2007). Meddies have typically an horizontal extension of $O(100)$km and vertical thickness of $O(1)$km (Richardson *et al.*, 2000). For these vortices, planetary rotation has an important effect in addition to the stable stratification but this effect will not be considered in the present paper.

Despite the ubiquity of pancake vortices in stratified fluids, only few studies on their structure and stability exist. The internal structure of a pancake vortex in stably stratified fluids has been investigated by Flór & van Heijst (1996), Bonnier *et al.* (2000) and Beckers *et al.* (2001). Flór & van Heijst (1996) conducted an experimental study on monopolar pancake vortices using three different generation methods (rotating sphere, rotating rod and injection of fluids). They found that disturbances with azimuthal wavenumber $m = 2$ or $m = 3$ are unstable when the Froude number $F = V_{\max}/NR_{\mathrm{vmax}}$ is larger than $F > 0.1$, where $V_{\max}$ is the maximum azimuthal velocity, N the Brunt–Väisälä frequency, and R_{vmax} the radius of maximum azimuthal velocity. They also showed that the nonlinear evolution of the instabilities (formations of tripole ($m = 2$) and dipole splitting), is similar to those for two-dimensional vortices. Some differences come from the faster decay rate of the satellites compared to the core for pancake vortices. Bonnier *et al.* (2000) investigated experimentally the dynamics of vortices in the far-wake of a towed sphere. The density field inside the vortices shows a pinching of the isopycnals in order to satisfy the hydrostatic and cyclostrophic balances. Beckers *et al.* (2001) found similar isopycnal deformations experimentally and numerically. They have shown that, when the vortex is not initially in cyclostrophic or hydrostatic balances, adjustment processes occur and lead to the generation of internal gravity waves. A Kirchhoff elliptic pancake vortex in cyclostrophic balance also emits gravity wave (Plougonven & Zeitlin, 2002). Balanced vortices exhibit particular momentum and density diffusions. Beckers *et al.* (2001) and Godoy-Diana & Chomaz (2003) have studied the effect of the Schmidt number $Sc = \nu/\kappa$ which is the ratio of the diffusion rates of momentum ν and density κ. When $Sc \gg 1$, secondary circulations slow down the decay of the vortex. In contrast, when $Sc < 1$, these secondary circulations accelerate the decay of the vortex.

The stability of a pancake vortex as a function of Reynolds number and Froude number is discussed in Beckers *et al.* (2003) experimentally and numerically for a vortex profile with angular velocity $\Omega = \Omega_0 \exp(-(r/R)^q - (z/\Lambda)^2)$, where Ω_0 is the maximum angular velocity, q is the steepness parameter and α the aspect ratio fixed to $\alpha = \Lambda/R = 0.4$ with R is the radius and Λ the thickness. Beckers *et al.* (2003) have determined only the most unstable modes by performing nonlinear numerical simulations of azimuthally perturbed vortices using the Navier-Stokes equations under the Boussinesq approximation. They focused on perturbations with azimuthal wavenumbers $m \geq 2$ with a Reynolds number up to $\tilde{Re} = 10000$ where $\tilde{Re} = 2\sqrt{\pi}\Lambda R\Omega_0/\nu$. They have shown that pancake vortices with $q > 2$ are generally unstable to barotropic (i.e. shear) instability in the range of $500 \leq \tilde{Re} \leq 10000$ and $0.1 \leq \tilde{F} \leq 0.8$ where $\tilde{F} = 2\sqrt{\pi}\Lambda\Omega_0/(RN)$. The instability is similar to the shear instability of two dimensional vortices with the most unstable azimuthal wavenumber increasing with the steepness parameter q (Carton & Legras, 1994). When $q = 2$, they found that the vortex is stable.

Recently, Negretti & Billant (2013) have conducted a linear stability analysis of a pancake vortex with a Gaussian vertical vorticity profile in radial and vertical directions. They found that the vortex is unstable to gravitational instability when the vortex aspect ratio α is small such that $\alpha/F_h < 1.1$, where $F_h = \Omega_0/N$. When this condition is satisfied, the isopycnals are indeed so deformed by the pancake shape that they overturn. The barotropic shear instability does not exist because the vorticity gradient does not vanish for a Gaussian vertical vorticity profile. The vertical shear is also never sufficient to trigger an instability when $\alpha/F_h > 1.1$.

In this paper, we investigate the stability of an axisymmetric pancake vortex with the same angular velocity profile as in Beckers *et al.* (2003) in a stably stratified fluid. The steepness parameter will be set to $q = 2$ throughout the paper. In contrast to Beckers *et al.* (2003), all the unstable modes will be determined by solving the eigenvalue problem by means of an iterative method. The Reynolds number will be increased up to $Re \equiv \Omega_0 R^2/\nu = 100000$ and various aspect ratios and Froude numbers will be studied. We have found that the vortex can be also unstable under some condition to the $m = 2$ shear instability when $q = 2$. In addition, we will show that other types of instability exist: the counterpart of the centrifugal instability of columnar vortices and two instabilities specific to pancake vortices: the gravitational instability already extensively studied by Negretti & Billant (2013) but also the baroclinic instability that has not been observed before in purely stratified fluids.

The paper is organized as follows: we first define the linear stability problem in §5.2. In §4.3, typical spectra and eigenmodes for the azimuthal wavenumbers $m = 0, 1$, and 2 will be presented. The origin of the different modes will be identified thanks to stability criteria and by comparison to the instabilities of columnar vortices. In §4.4, a parametric study of the most unstable modes for each m will be then conducted as a function of the aspect ratio, Froude and Reynolds numbers. From the fact that the centrifugal and shear instabilities in pancake and columnar vortices have many resemblances, we further show in §4.5 and §4.6, that their occurrence in pancake vortices can be understood from their growth rate dependence with the vertical wavenumber in columnar vortices. The instabilities specific to pancake vortices will be discussed in §4.7. At last, all the different instabilities for each azimuthal wavenumber m are summarized in §5.8 in the parameter space: Froude number, Reynolds number for $Re \leq 10000$. In §4.9, comparisons to previous experimental and numerical studies are presented.

4.2 Problem formulation

4.2.1 The base state

We consider as base flow an axisymmetric pancake vortex with only azimuthal velocity $\boldsymbol{u_b}(r,\theta,z) = [u_r, u_\theta, u_z] = [0, r\Omega(r,z), 0]$ in cylindrical coordinates (r,θ,z). The angular velocity is chosen Gaussian in both radial and vertical directions

$$\Omega(r,z) = \Omega_0 \mathrm{e}^{-\left(\frac{r^2}{R^2}+\frac{z^2}{\Lambda^2}\right)}, \tag{4.1}$$

where R is the radius, Λ is the half thickness and Ω_0 is the maximum angular velocity. The total pressure and density are decomposed as follows:

$$p_t = p_0 + \bar{p}(z) + p_b(r,z), \tag{4.2}$$
$$\rho_t = \rho_0 + \bar{\rho}(z) + \rho_b(r,z), \tag{4.3}$$

where the values with the subscript 0 are reference values, those with a bar indicate the background vertical profiles and those with a subscript b correspond to the perturbations due to the base vortex. The Euler equations under the Boussinesq approximation are in the radial and vertical directions

$$-r\Omega^2 = -\frac{1}{\rho_0}\frac{\partial p_t}{\partial r}, \tag{4.4}$$
$$\frac{g}{\rho_0}\rho_t = -\frac{1}{\rho_0}\frac{\partial p_t}{\partial z}, \tag{4.5}$$

corresponding to cyclostrophic and hydrostatic balances, where g is the gravity. Combining (4.4) and (4.5) gives the thermal-wind relation:

$$\frac{\partial r\Omega^2}{\partial z} = -\frac{g}{\rho_0}\frac{\partial \rho_b}{\partial r}. \tag{4.6}$$

Hence, ρ_b is given by

$$\rho_b(r,z) = -z\frac{\rho_0}{\mathrm{g}}\left(\frac{R}{\Lambda}\right)^2 \Omega_0^2 \mathrm{e}^{-2\left(\frac{r^2}{R^2}+\frac{z^2}{\Lambda^2}\right)}. \tag{4.7}$$

4.2.2 Linearized equations

The vortex is perturbed by infinitesimal perturbations (denoted with prime) of velocity $\boldsymbol{u}' = [u_r', u_\theta', u_z']$, pressure p', and density ρ' as

$$\boldsymbol{u}(r,\theta,z) = \boldsymbol{u_b} + \boldsymbol{u}' = (0, r\Omega(r,z), 0) + (u_r', u_\theta', u_z'), \tag{4.8}$$
$$p = p_t + p', \tag{4.9}$$
$$\rho = \rho_t + \rho'. \tag{4.10}$$

Since the vortex is axisymmetric, the perturbations are written as normal modes in the azimuthal direction

$$[u'_r, u'_\theta, u'_z, p', \rho'] = [u_r(r,z), u_\theta(r,z), u_z(r,z), \rho_0 p(r,z), \frac{\rho_0}{g}\rho(r,z)]\mathrm{e}^{-\mathrm{i}\omega t + \mathrm{i}m\theta} + \mathrm{c.c.}, \tag{4.11}$$

where ω is the frequency and m the azimuthal wavenumber. We consider that m is positive since negative wavenumbers can be recovered by the symmetry: $\omega(m) = \omega^*(-m)$. Under the Boussinesq approximations, the linearized Navier-Stokes equations are

$$-\mathrm{i}(\omega - m\Omega)u_r - 2\Omega u_\theta = -\frac{\partial p}{\partial r} + \nu\left(\nabla^2 u_r - \frac{1}{r^2}u_r - \frac{2}{r^2}\mathrm{i}mu_\theta\right) \tag{4.12}$$

$$-\mathrm{i}(\omega - m\Omega)u_\theta + \zeta u_r + \frac{\partial r\Omega}{\partial z}u_z = -\frac{\mathrm{i}m}{r}p + \nu\left(\nabla^2 u_\theta - \frac{1}{r^2}u_\theta + \frac{2}{r^2}\mathrm{i}mu_r\right) \tag{4.13}$$

$$-\mathrm{i}(\omega - m\Omega)u_z = -\frac{\partial p}{\partial z} - \rho + \nu\nabla^2 u_z \tag{4.14}$$

$$-\mathrm{i}(\omega - m\Omega)\rho + \frac{g}{\rho_0}\frac{\partial \rho_b}{\partial r}u_r + \frac{g}{\rho_0}\frac{\partial \rho_b}{\partial z}u_z = N^2 u_z + \kappa\nabla^2\rho \tag{4.15}$$

$$\frac{1}{r}\frac{\partial r u_r}{\partial r} + \frac{1}{r}\mathrm{i}mu_\theta + \frac{\partial u_z}{\partial z} = 0 \tag{4.16}$$

where $\zeta = 1/r\partial(r^2\Omega)/\partial r$ is the vertical vorticity, $N = \sqrt{-\mathrm{g}/\rho_0 \mathrm{d}\bar{\rho}/\mathrm{d}z}$ the Brunt–Väisälä frequency which is assumed constant, ν the viscosity and κ the diffusivity of the stratifying agent. The problem is governed by four non-dimensional numbers: aspect ratio (α), Froude number (F_h), Reynolds number (Re) and Schmidt number (Sc), defined as follows:

$$\alpha = \frac{\Lambda}{R}, \qquad F_h = \frac{\Omega_0}{N}, \qquad Re = \frac{\Omega_0 R^2}{\nu}, \qquad Sc = \frac{\nu}{\kappa}. \tag{4.17}$$

In this paper, we keep $Sc = 1$ for simplicity and in order to avoid the double-diffusion phenomenon between momentum and mass diffusion (McIntyre, 1970).

4

4.2.3 Numerical method

Equations (4.12) – (4.16) are discretized with finite element method using FreeFem++ (Hecht, 2012; Garnaud, 2012; Garnaud *et al.*, 2013). Velocity, density and pressure $(\boldsymbol{u}, \rho, p)$ are approximated with (P2, P1, P1) elements, respectively. The mesh is adapted to the base state and refined around the vortex core. The domain is restricted to positive radius $r = [0, R_{\max}]$ and is set to $z = [-Z_{\max}, Z_{\max}]$ along the vertical. The boundary conditions at $r = 0$ differ depending on the azimuthal wavenumber m (Batchelor & Gill, 1962; Ash & Khorrami, 1995),

$$\begin{aligned} m = 0: &\qquad u_r = u_\theta = 0, \\ m = 1: &\qquad u_z = p = \rho = 0, \\ m \geq 2: &\qquad u_r = u_\theta = u_z = p = \rho = 0. \end{aligned}$$

At the other boundaries $r = R_{\max}$ and $z = \pm Z_{\max}$, all perturbations are enforced to vanish. The sizes of the domain are chosen large $Z_{\max} = 6\Lambda$ and $R_{\max} = 8R$ compared to the vortex core sizes. The resulting discretized equations (4.12) – (4.16) are written in the form

$$-\mathrm{i}\omega\mathbf{B}\boldsymbol{v} = \mathbf{L}\boldsymbol{v}, \tag{4.18}$$

Run	S_{min}	S_{max}	No. of triangles	Growth rate (ω_i)
1		$0.7R$	40144	$0.022116\Omega_0$
2	$0.004R$	$0.15R$	74807	$0.018641\Omega_0$
3		$0.075R$	189396	$0.018639\Omega_0$
4		$0.04R$	306144	$0.018638\Omega_0$
5	$0.040R$		88128	$0.018740\Omega_0$
6	$0.010R$	$0.075R$	171596	$0.018635\Omega_0$
7	$0.004R$		189396	$0.018639\Omega_0$

Table 4.1: Growth rate for different minimum and maximum mesh sizes S_{min} and S_{max} for $m = 2$, $\alpha = 0.5$, $F_h = 0.5$ and $Re = 10000$. The number of triangles is also indicated.

where $\boldsymbol{v} = [u_r, u_\theta, u_z, p, \rho]$. The typical size of the matrices $\mathbf{B}$ and $\mathbf{L}$ is about $10^6 \times 10^6$. The generalized eigenvalue problem (4.18) is solved with an iterative Krylov-Schur method using the libraries SLEPc and PETSc (Hernandez *et al.*, 2005; Garnaud, 2012; Garnaud *et al.*, 2013; Balay *et al.*, 2014). The shift-invert spectral transformation is used to find the most unstable eigenvalues/vectors around shift values. Spurious modes are eliminated by excluding eigenvalues varying by more than 10^{-6} between two successive shift values.

Table 4.1 shows examples of the convergence of the growth rate as a function of the mesh size. The growth rate varies significantly when the maximum mesh size is varied from $0.7R$ to $0.15R$ (see runs 1 and 2) but becomes almost constant when S_{max} is smaller than $0.15R$ (see runs 2 to 4). In turn, when the maximum mesh size is fixed to $S_{\text{max}} = 0.075R$, the growth rate varies very little when the minimum mesh size S_{min} is lower than $0.01R$ (see runs 6 to 7). The mesh adaptation to the base vortex allows to use sufficiently fine meshes in the vortex core while keeping a reasonable total number of triangles. In the following, the numerical results are mostly computed for the mesh with the maximum size $0.075R$ and minimum size $0.004R$ (run 3 or 7).

For comparison purposes we have also conducted some stability analyses of a columnar vortex with base angular velocity $\Omega = \exp(-r^2)$. The vertical dependence of the perturbations can then be expressed in terms of normal modes with a vertical wavenumber k. The equations (4.12) – (4.16) have been solved by means of Chebyshev pseudo-spectral collocation method (Antkowiak & Brancher, 2004). The numerical code based on FreeFem++ and SLEPc for $\alpha \to \infty$ has been also successfully checked against the Chebyshev code.

4.3 Some typical examples of spectrum

In this section, we show typical examples of spectrum and eigenmodes for the different azimuthal wavenumbers $m = 0, 1$, and 2. The Reynolds number will be fixed to $Re = 10000$ but the Froude number and aspect ratio will vary from one azimuthal wavenumber to the other in order to show the most general spectrum for each m. To identify the instability, the spectra are compared to the corresponding spectra of a columnar vortex for the same control parameters (F_h, Re). Detailed comparisons between the eigenmodes of columnar and pancake vortices are also carried out.

4.3.1 $m = 0$

Figure 4.1 shows an example of spectrum for the parameters $m = 0$, $\alpha = 1$, $F_h = 0.5$, and $Re = 10000$. The frequency (ω_r) and growth rate (ω_i) are non-dimensionalized by

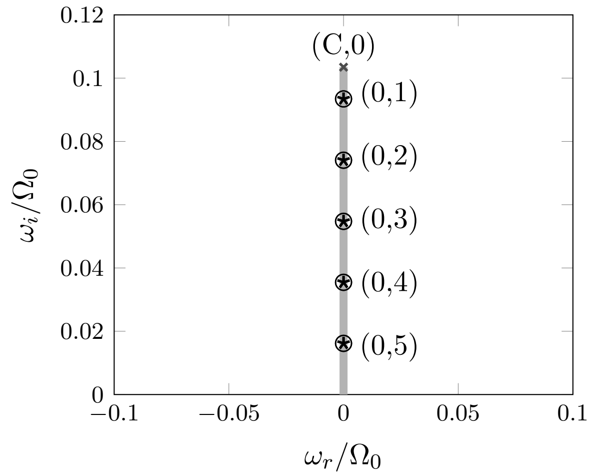

Figure 4.1: Growth rate (ω_i/Ω_0) and frequency (ω_r/Ω_0) spectra for a pancake vortex ($\alpha = 1$) (○: for symmetric and ⋆ for anti-symmetric modes) and for a columnar vortex ($\alpha = \infty$) (▬) for $m = 0$, $F_h = 0.5$, and $Re = 10000$. The mode (C,0) corresponds to the most unstable mode of the columnar vortex.

the maximum angular velocity Ω_0. The unstable mode are displayed by symbols and are labelled (m, i) where i denotes the ith mode. For each point, there are actually two modes with a different symmetry with respect to $z = 0$: symmetric (○) and anti-symmetric (⋆). All the modes have zero frequency. The real part of the radial velocity perturbation Re(u_r) of the most unstable anti-symmetric mode (marked (0,1) in figure 4.1) is depicted in figure 4.2a. The perturbation lies at the periphery of the vortex core $r/R \geq 1$ and in the central region $-0.5 \leq z/\Lambda \leq 0.5$ along the vertical. A well-defined axial wavelength about $\lambda \simeq 0.2\Lambda$ can be seen. The symmetric mode marked as (0,3) (figure 4.2b) is similar to the mode (0,1) but with a larger extent in the vertical direction $-0.7 \leq z/\Lambda \leq 0.7$ with a slightly smaller wavelength $\lambda \simeq 0.17\Lambda$. The other modes (0,2), (0,4) and (0,5) have similar characteristics as these two modes: they only differ by the number of nodes along the vertical.

4

To determine the origin of this instability, we consider the Rayleigh criterion for the centrifugal instability extended to baroclinic vortices (Solberg, 1936; Eliassen & Kleinschmidt, 1957). Centrifugal instability is expected when the circulation decreases with the radius along isopycnal surfaces

$$\Phi = \frac{1}{r^3}\frac{\partial(r^2\Omega)^2}{\partial r}\bigg|_{\rho_t} < 0, \tag{4.19}$$

for some radius. The region where Φ is negative for $\alpha = 1, F_h = 0.5$ is shaded in figure 4.3. It extends from $r = 1$ to infinity with a minimum of Φ reached near $r = 1.2R$ and $z = 0$. As shown by the dashed lines in figure 4.2, the modes are localized in this region. This shows that these modes are due to the centrifugal instability. In order to further understand their properties, the spectrum of a columnar vortex ($\alpha = \infty$) has been computed for the same parameters ($m = 0, F_h = 0.5$, $Re = 10000$). It is plotted in figure 4.1 as a grey continuous line. Although the spectrum is discretized for $\alpha = 1$ and continuous for $\alpha = \infty$ since the vertical wavenumber varies continuously, the maximum growth rate in both cases are very close. Note that there exists a single unstable mode for each wavenumber in the columnar case. The secondary centrifugal modes with more radial oscillations become unstable only for larger Froude or Reynolds numbers. Furthermore, their growth rates are much smaller than the primary modes both for columnar and pancake vortices.

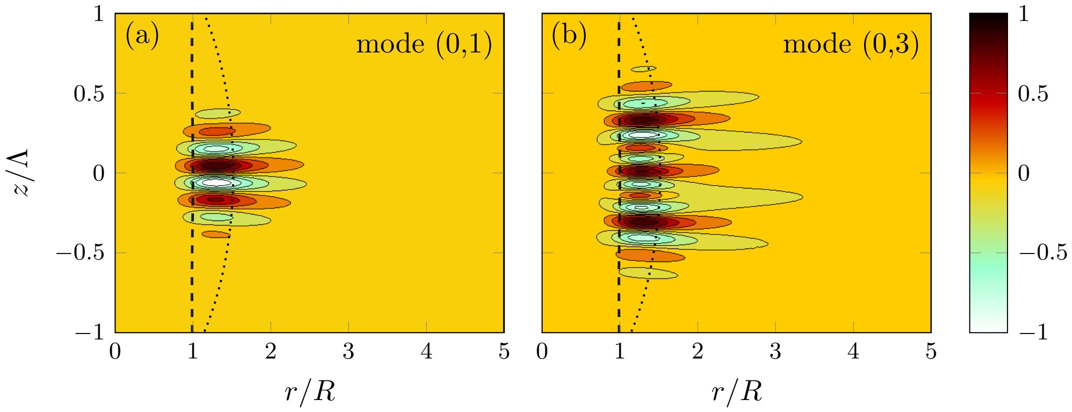

Figure 4.2: (color online) Real part of the radial velocity perturbation $\mathrm{Re}(u_r)$ of (a) anti-symmetric mode (0,1) and (b) symmetric mode (0,3) of figure 4.1. The radius r and height z are rescaled with the radius R and half height Λ of the base vortex, respectively. The dashed line represents the contour where the Rayleigh discriminant Φ vanishes. The dotted line indicates the contour where the angular velocity Ω of the base vortex is $0.1\Omega_0$.

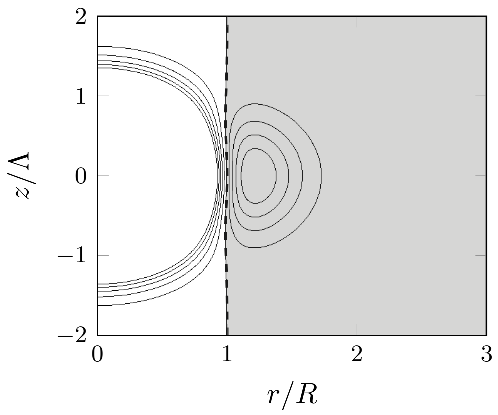

Figure 4.3: Contours of $\Phi/|\Phi_{min}|$ for $\alpha = 1, F_h = 0.5$. The regions where Φ is negative are shaded. The contour interval is 0.2.

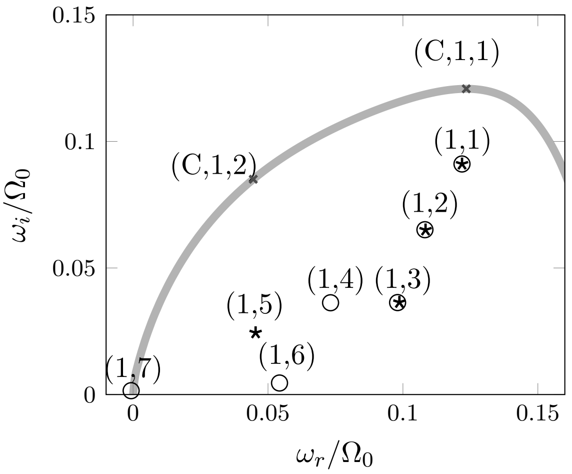

Figure 4.4: Growth rate (ω_i/Ω_0) and frequency (ω_r/Ω_0) spectra for a pancake vortex for $\alpha = 0.5$ (○: for symmetric and $\star$ for anti-symmetric modes) and for a columnar vortex (▬) for $m = 1$, $F_h = 1/3$, and $Re = 10000$. The modes (C,1,1) and (C,1,2) correspond to modes of the columnar vortex whose frequencies are the same as the modes (1,1) and (1,5), respectively.

4.3.2 $m = 1$

The symbols in figure 4.4 show a typical example of spectrum for $m = 1, \alpha = 0.5$, $F_h = 1/3$, and $Re = 10000$. Several unstable modes exist (labelled (1,1)–(1,7) using the same notation as for $m = 0$). This time, all modes have non-zero frequency. Figure 4.5a shows the real part of the radial velocity of the most unstable mode (1,1). The mode is maximum near $r/R = 1$ and localized within $-1 < z/\Lambda < 1$ with a typical wavelength $\lambda \simeq 0.57\Lambda$. It resembles to the $m = 0$ centrifugal modes (figure 4.2) except that the perturbations overshoot in the region of positive generalized Rayleigh discriminant. The modes (1,2) and (1,3) are similar to the mode (1,1) excepted that they exhibit more oscillations along the vertical. In contrast, the mode (1,5) is different (figure 4.5b): the perturbation is localized within the vortex core $r/R < 1$ and maximum near $z = \pm\Lambda$. The perturbation is mainly located in a region where Φ is positive and is therefore probably not a centrifugal mode. To identify this instability, it is useful to compare the spectrum to the one of a columnar vortex for the same parameters (shown by a thick line in figure 4.4).

The maximum growth rate for a columnar vortex first increases with frequency and then decreases owing to viscous stabilization since the corresponding vertical wavenumber is large. Figure 4.6a,b compare the radial profiles of the horizontal velocity (u_r, u_θ) of the most unstable modes of the pancake and columnar vortices (labelled (1,1) and (C,1,1) in figure 4.4, respectively). The profiles for the pancake vortex are taken at the level z_m where u_r is maximum. The velocities are normalized to the maximum radial velocity in each case. We can see that the profiles are very close confirming that the mode (1,1) originates from the centrifugal instability. A similar comparison is made in figure 4.7 between the mode (1,5) and the mode (C,1,2) of the columnar vortex (figure 4.4). The latter mode has been chosen for the comparison since it has the same frequency as the mode (1,5). The radial velocity profiles of these modes for the pancake and columnar vortices are very similar. For the columnar vortex, the mode (C,1,2) corresponds to a mixed mode between the centrifugal instability and the Gent-McWilliams instability. The latter instability comes from a destabilization of the long-wavelength bending more by the critical layer where $\Omega(r_c) = \omega_r$ when the vorticity

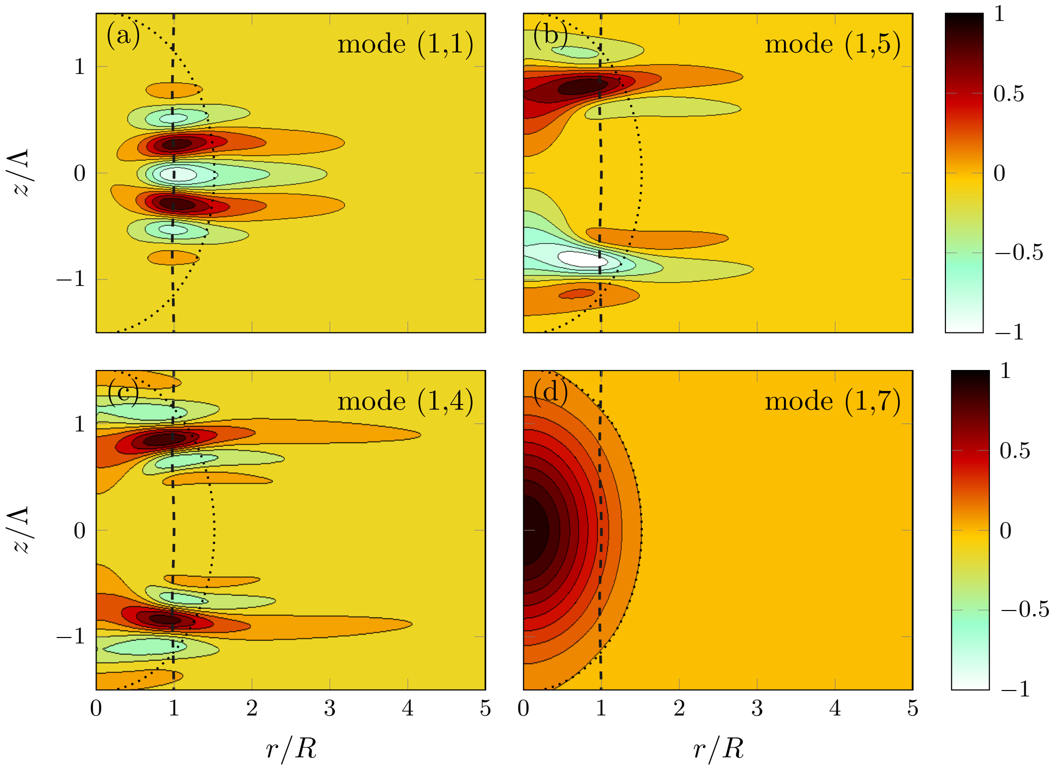

Figure 4.5: (color online) Real part of the radial velocity perturbation $\mathrm{Re}(u_r)$ of modes (a) (1,1), (b) (1.5), (c) (1,4) and (d) (1,7) of figure 4.4. The dotted line indicates the contour where the angular velocity of the base vortex is $\Omega = 0.1\Omega_0$. The dashed line represents the contour where the Rayleigh discriminant Φ vanishes.

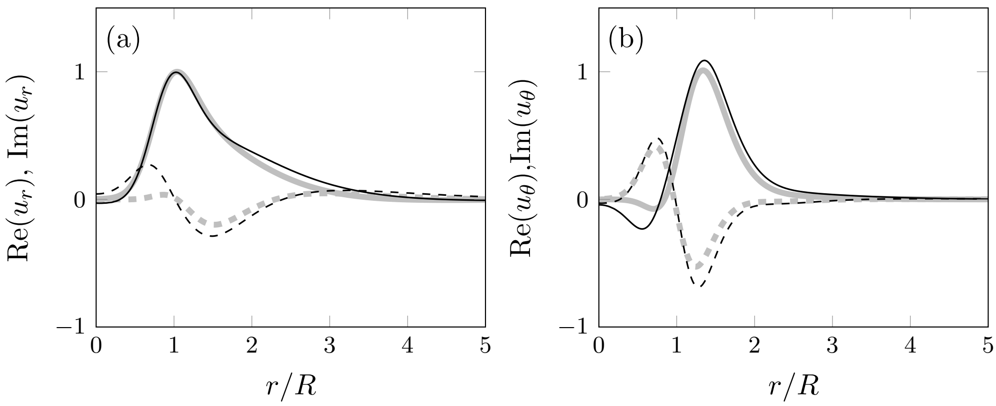

Figure 4.6: Comparison between the (a) radial u_r and (b) azimuthal u_θ velocities of the eigenmodes (C,1,1) of columnar (thick grey lines) and (1,1) of pancake vortices (light black lines) in figure 4.4. ——; Real and ——; Imaginary parts.

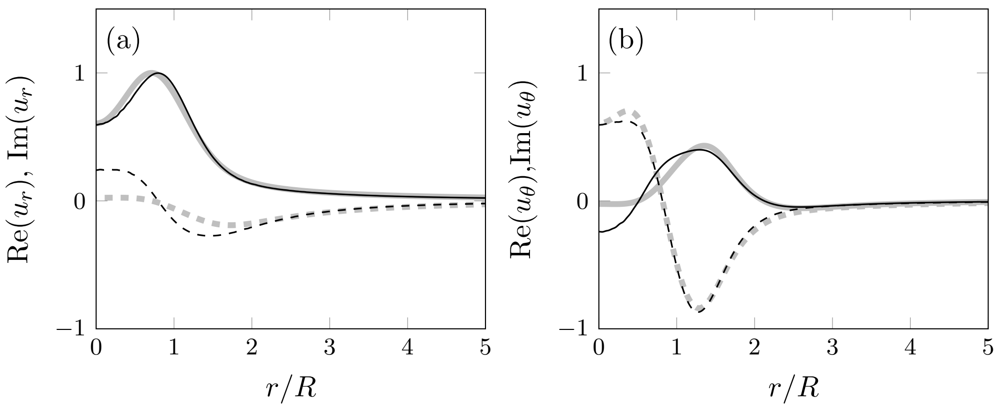

Figure 4.7: Same as in figure 4.6 but for the modes (C,1,2) and (1,5).

gradient is positive $\zeta'(r_c) > 0$ (Yim & Billant, 2015). We can notice that the radial and azimuthal velocity components of the perturbation are non-zero on the axis in contrast to the centrifugal mode (1,1) (figure 4.5a). Thus, the perturbation will partially bend the vortex. For a strongly stratified non-rotating columnar vortex, such bending mode transforms continuously into a centrifugal mode explaining why there is a single continuous branch in figure 4.4. However, in presence of strong rotation, the centrifugal instability disappears and only the Gent-McWilliams instability (also called internal instability) remains (Gent & McWilliams, 1986; Smyth & McWilliams, 1998; Yim & Billant, 2015). For the stratified pancake vortex, a continuous transition is also observed: the modes (1,4) and (1,6) exhibit also the characteristics of the centrifugal mode and but with a non-zero velocity on the axis like the mode (1,5) as seen in figure 4.5c. Interestingly, these modes seem to concentrate in the regions where the vertical shear $|\partial V_\theta/\partial z|$ is maximum $|z| = r \simeq 0.71$. The mode (1,7) in figure 4.4 has a very small growth rate and its frequency is slightly negative. As shown in Appendix 4.C, the radial velocity of this mode (figure 4.5d) is almost identical to the base angular velocity. It corresponds to the displacement mode which derives from translational invariance and translates the base flow horizontally (see Appendix 4.C).

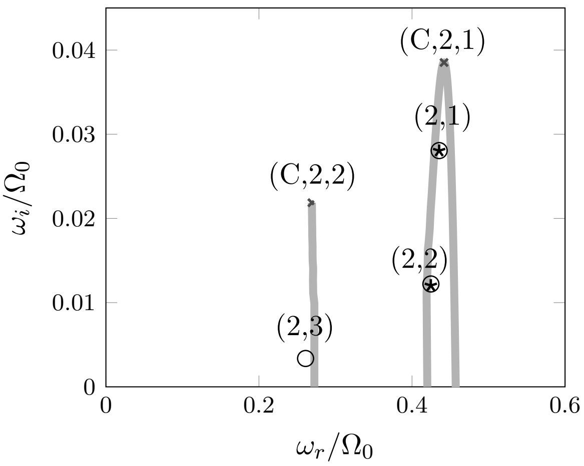

Figure 4.8: Growth rate (ω_i/Ω_0) and frequency (ω_r/Ω_0) spectra for a pancake vortex ($\alpha = 1.2$) (○: for symmetric and ⋆ for anti-symmetric modes) and for a columnar vortex ($\alpha = \infty$) (▬) for $m = 2$, $F_h = 0.5$, and $Re = 10000$. The modes (C,2,1) and (C,2,1) correspond to modes of the columnar vortex whose frequencies are the same as the modes (2,1) and (2,3), respectively.

4.3.3 $m = 2$

Figure 4.8 shows an example of spectrum for $m = 2$, $F_h = 0.5$, and $Re = 10000$. For a pancake vortex with aspect ratio $\alpha = 1.2$, there are three unstable modes (labelled (2,1)–(2,3)). The radial velocity perturbation of the most unstable mode (2,1) is shown in 4.9a. The perturbation is maximum near $r/R = 1$ and localized within $-0.5 < z/\Lambda < 0.5$ with a typical wavelength $\lambda \simeq 0.26\Lambda$. In the vortex core, it resembles closely the most unstable centrifugal modes for $m = 0$ (figure 4.2a) and $m = 1$ (figure 4.5a). However, inclined rays can also be seen outside the vortex core. We shall see in §4.4.2 that these perturbations outside the vortex core correspond to internal gravity waves radiated by the centrifugal mode. For $m = 1$, such radiation of internal waves also exists but their amplitude is too weak to be visible in figure 4.5a. The mode (2,2) in figure 4.8 is a centrifugal mode similar to the mode (2,1) but the mode (2,3) is different. As seen in figure 4.9b, its radial velocity is localized in the core and does not exhibit many oscillations along the vertical. For a columnar vortex, the spectra possess two separate branches (thick grey lines in figure 4.8). The branch near $\omega_r \simeq 0.45\Omega_0$ corresponds to the centrifugal instability while the one near $\omega_r = 0.27\Omega_0$ corresponds to the shear instability.

We see that there is a good correspondence with the spectrum of the pancake vortex. This confirms that the modes (2,1) and (2,2) are centrifugal modes and shows that the mode (2,3) is due to the shear instability. In addition, the radial velocity profiles of the eigenmodes of columnar and pancake vortices are very close both for the centrifugal (figure 4.10) and shear (figure 4.11) instabilities. Oscillations for large radius corresponding to radiations of gravity waves are also observed for the centrifugal mode of the columnar vortex (figure 4.10a).

4.4 Parametric study on the most unstable mode

In this section, we investigate the effects of the three main control parameters (α, F_h, Re) on the most unstable mode of each instability type for $m = 0, 1, 2$. The control parameters are varied only in the range $F_h/\alpha \leq \exp(3/4)/\sqrt{2} \simeq 1.5$, ensuring that the total density gradient

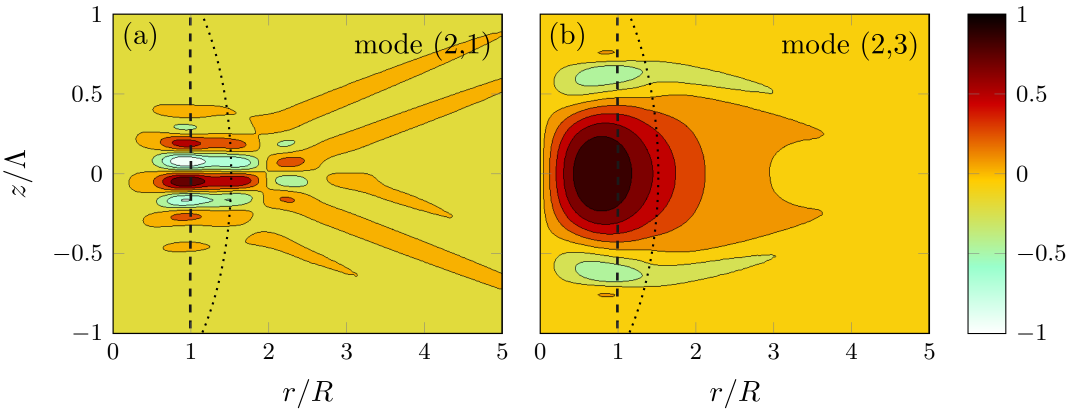

Figure 4.9: (color online) Real part of the radial velocity perturbation $\mathrm{Re}(u_r)$ of (a) mode (2,1) and (b) mode (2.3) of figure 4.8. The dotted line indicates the contour where the angular velocity of the base vortex is $\Omega = 0.1\Omega_0$. The dashed line represents the contour where the Rayleigh discriminant Φ vanishes.

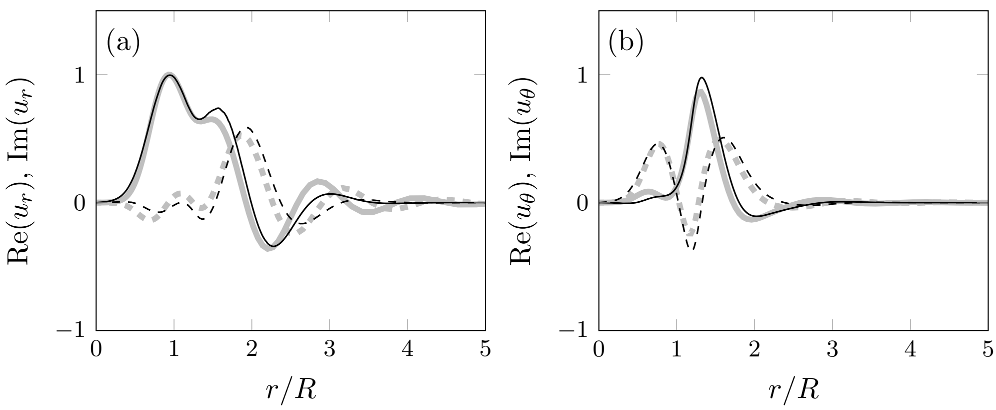

Figure 4.10: Comparison between the (a) radial u_r and (b) azimuthal u_θ velocities of the eigenmodes (C,2,1) of columnar (thick grey lines) and (2,1) of pancake vortices (light black lines) in figure 4.8. ——; Real and ——; Imaginary parts.

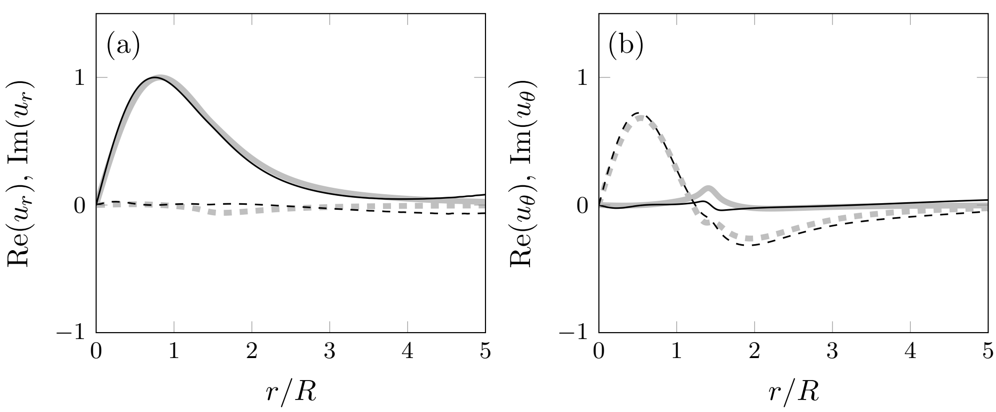

Figure 4.11: Same as in figure 4.10 but for the modes (C,2,2) and (2,3).

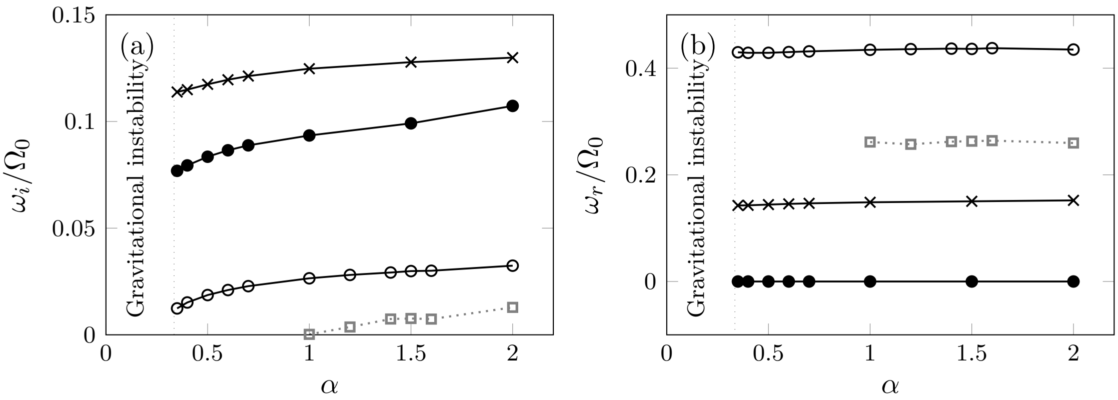

Figure 4.12: (a) Growth rate and (b) frequency of the most unstable modes of each instability type as a function of α, for $F_h = 0.5$ and $Re = 10000$. Centrifugal modes: —●—; $m = 0$, —×—; $m = 1$,—○—; $m = 2$; Shear mode: ··□··, $m = 2$.

$\partial\rho_t/\partial z = -\rho_0 N^2/g + \partial\rho_b/\partial z$ is everywhere negative. When $F_h/\alpha \geq 1.5$, the maximum density gradient which is located at $r = 0$, $z = \pm\sqrt{3}/2$, is positive so that the gravitational instability can occur.

4.4.1 Effect of the aspect ratio

When the aspect ratio is increased from $\alpha = 0.35$ to $\alpha = 2$ for $F_h = 0.5, Re = 10000$, the growth rate of the most unstable centrifugal modes for $m = 0, 1$ and 2 increase slightly while the corresponding frequencies are almost constant (figure 4.12). The lower limit $\alpha = 0.35$ corresponds to the appearance of the gravitational instability. It is interesting to notice that the overall most unstable centrifugal mode for these parameters is not the axisymmetric mode but the azimuthal wavenumber $m = 1$. The growth rate of the most unstable shear mode ($m = 2$) is positive only for $\alpha \geq 1$ and increases with α. The most unstable centrifugal eigenmode and shear eigenmode for $m = 2$ are displayed in figure 4.13 for different values of the aspect ratio. The vertical scale is non-dimensionalised by R instead of Λ in order to have the same reference vertical scale for the three plots. Hence, we can see that the wavelength of the centrifugal instability (figure 4.13a-c) is approximately the same whatever α but the number of oscillations along the vertical increases as the vortex becomes taller. Correspondingly, the number of distinct centrifugal modes increases with α since the vertical confinement decreases: for example for $m = 2$, for $\alpha = 0.5$ there is one unstable mode; for $\alpha = 1$, two modes and for $\alpha = 2$, five modes (not shown). In contrast, the height of the shear mode (figure 4.13d-e) is proportional to the aspect ratio.

4.4.2 Effect of the Froude number

Figure 4.14 shows that the growth rate of the most unstable centrifugal modes for $m = 0, 1, 2$ increase with the Froude number for $\alpha = 1, Re = 10000$. The growth rates seem to asymptote to constant values as the Froude number increases but the pancake vortex becomes gravitationally unstable beyond $F_h = 1.5$ for $\alpha = 1$. The centrifugal modes for $m = 0$ and $m = 2$ are stabilized when the Froude number goes below $F_h = 0.3 - 0.35$. In contrast, the centrifugal mode $m = 1$ continues to be unstable for smaller Froude number. Hence, the mode $m = 1$ is the most unstable mode when $F_h \leq 0.8$ while the axisymmetric mode is most unstable only above this threshold. The shear mode for $m = 2$ exists when $F_h \leq 0.5$ and its growth rate increases as the Froude number decreases. As seen in figure

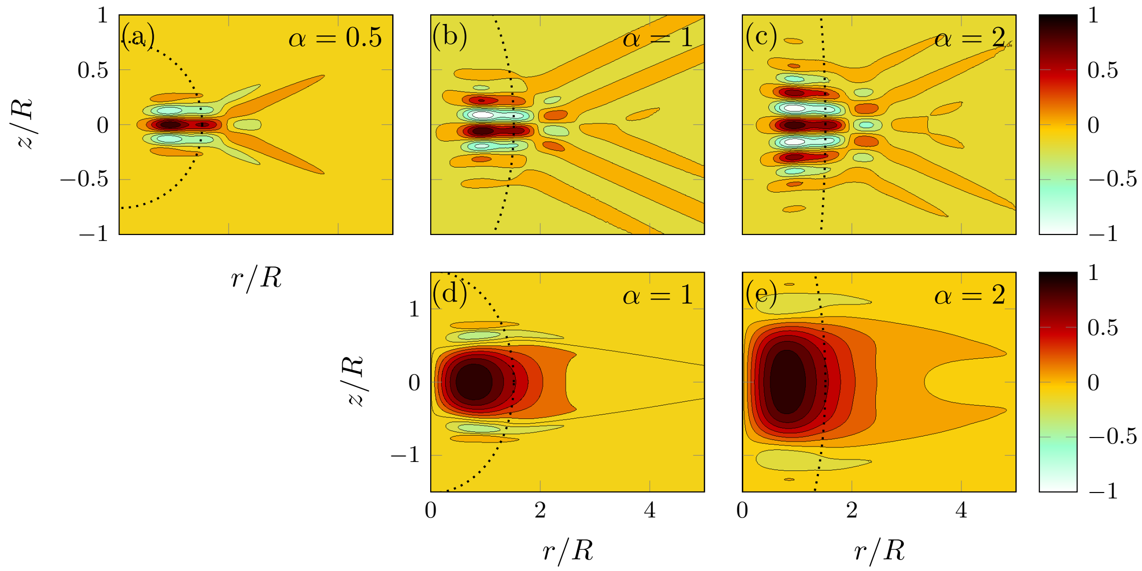

Figure 4.13: (color online) Real part of the radial velocity perturbation $\mathrm{Re}(u_r)$ of the most unstable mode for different aspect ratios: the centrifugal instability for $m = 2$ for (a) $\alpha = 0.5$, (b) $\alpha = 1$, (c) $\alpha = 2$ and the shear instability for $m = 2$ for (d) $\alpha = 1$, (e) $\alpha = 2$ for $F_h = 0.5$ and $Re = 10000$. The dotted line indicates the contour where the angular velocity of the base vortex is $\Omega = 0.1\Omega_0$. Note that the vertical scale is not scaled by Λ as before but by R.

4.14b, the frequencies of the modes are almost independent of the Froude number except for $m = 1$ for low Froude number $F_h \leq 0.5$. The most unstable eigenmodes for $m = 1$ and $m = 2$ and are shown in figure 4.15 for different Froude numbers. When F_h decreases, the location of the maximum of the eigenmode for $m = 1$ (figure 4.15a,b,c) moves from $r/R = 1$ to the axis $r = 0$. Thus, the centrifugal mode transforms continuously into a bending mode (Gent & McWilliams instability) as F_h decreases. In contrast, the centrifugal instability for $m = 2$ (figure 4.15d-f) remains at the same radial location but the angle θ of the rays with respect to the vertical decreases when the Froude number increases. This angle is in good agreement with the dispersion relation of internal waves $\cos\theta = \omega_r/N$ where $\omega_r \simeq 0.45$ is the frequency of the centrifugal mode. Therefore, the perturbations outside the vortex core correspond to internal waves forced by the centrifugal instability. We can also notice in figure 4.15d-f that the typical wavelength of the centrifugal mode for $m = 2$ increases slightly with the Froude number: $\lambda \simeq 0.28\Lambda(F_h = 0.4); \lambda \simeq 0.34\Lambda(F_h = 1)$ and $\lambda \simeq 0.36\Lambda(F_h = 1.5)$. The height of the shear mode (figure 4.15g-i) also increases weakly with the Froude number.

4.4.3 Effect of Reynolds number

Finally, figure 4.16 shows the dependence of the growth rate and frequency of the most unstable modes on the Reynolds number for a fixed aspect ratio and Froude number: $\alpha = 0.5, F_h = 0.5$. The general tendency with Re is similar to the one with the Froude number: the growth rate of the centrifugal modes increases with Re for all azimuthal wavenumber m and asymptotes to a constant. For $Re \leq 30000$, the centrifugal mode $m = 1$ is the most unstable mode while it is the axisymmetric mode above. The centrifugal modes for $m = 0$ and 2 are both stabilized when $Re \leq 5000$ whereas $m = 1$ remains unstable even for small Re. The eigenmode for $m = 1$ then changes gradually to the bending mode. The shear mode

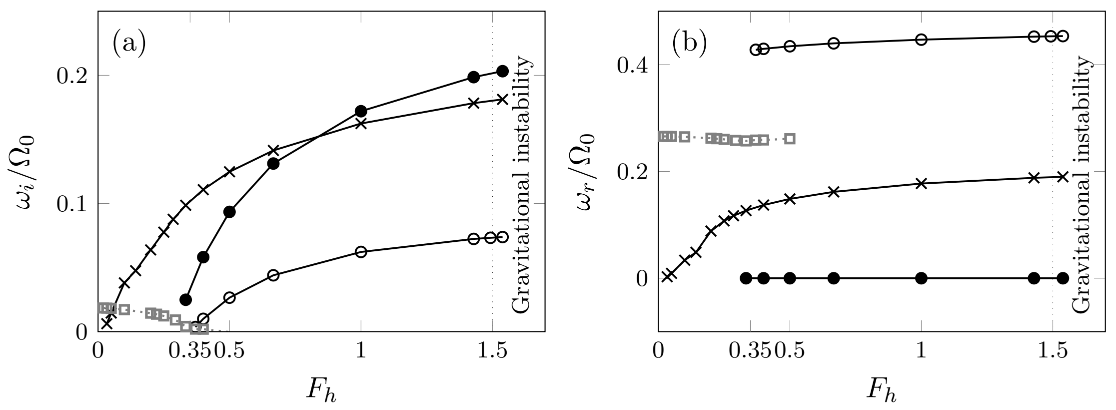

Figure 4.14: (a) Growth rate and (b) frequency as a function of F_h, for $\alpha = 1$ and $Re = 10000$. Centrifugal modes: —●—; $m = 0$, —×—; $m = 1$,—○—; $m = 2$; Shear mode: ··□··, $m = 2$.

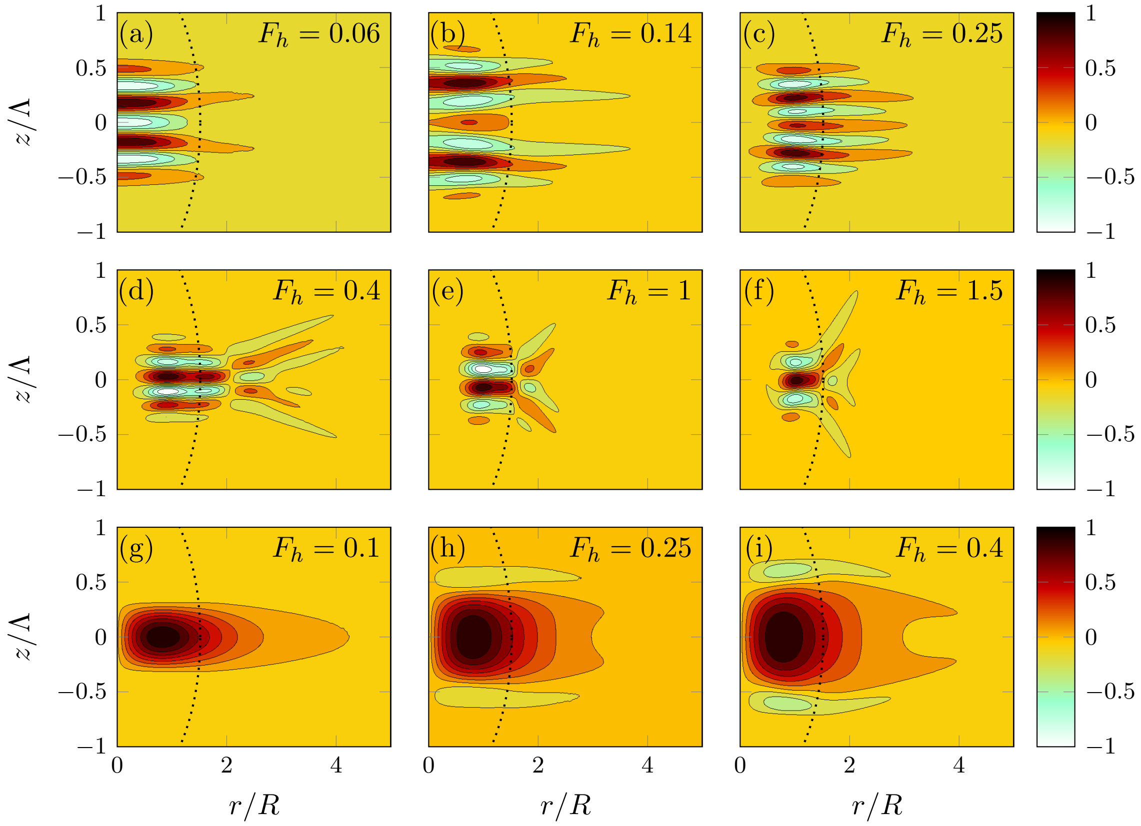

Figure 4.15: (color online) Real part of the radial velocity perturbation $\mathrm{Re}(u_r)$ of the most unstable modes for different Froude numbers: the centrifugal instability for $m = 1$ for (a) $F_h = 0.06$, (b) $F_h = 0.14$ and (c) $F_h = 0.25$, for the centrifugal instability $m = 2$ for (d) $F_h = 0.4$, (e) $F_h = 1$, (f) $F_h = 1.5$, and the shear instability for $m = 2$ for (g) $F_h = 0.1$, (h) $F_h = 0.25$ and (i)$F_h = 0.4$ for $\alpha = 1$ and $Re = 10000$. The dotted lines indicate the contour where the angular velocity of the base vortex is $\Omega = 0.1\Omega_0$.

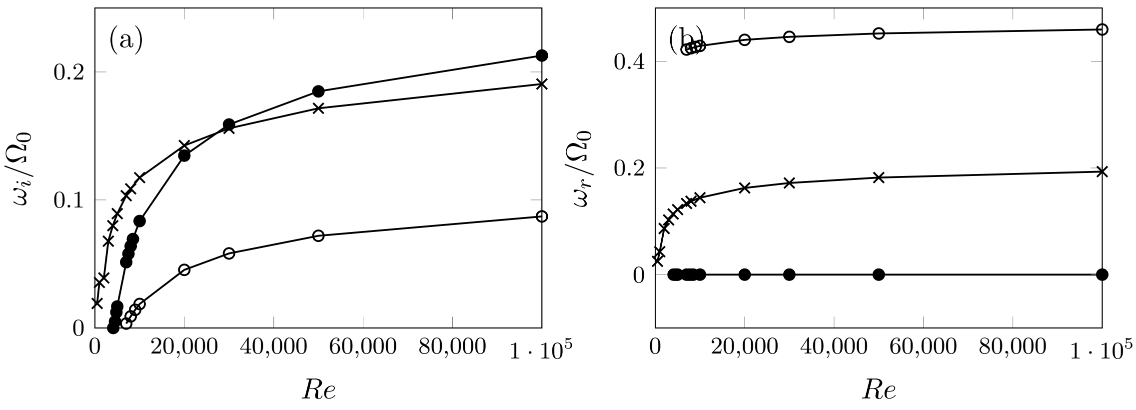

Figure 4.16: (a) Growth rate and (b) frequency as a function of Re, for $\alpha = 0.5$ and $F_h = 0.5$. Centrifugal modes: —●—; $m = 0$, —×—; $m = 1$,—○—; $m = 2$.

for $m = 2$ is not present for any Reynolds number for the parameters $\alpha = 0.5, F_h = 0.5$. The reasons why will be explained in section 4.6. Figure 4.17 shows the radial velocity of the dominant eigenmode for $m = 1$ and $m = 2$ for different Re. As observed when F_h decreases (§4.4.2), the centrifugal mode for $m = 1$ (figure 4.17a,b,c) changes continuously into a bending mode when Re decreases. The typical wavelength increases significantly as re increases. Regarding the centrifugal mode for $m = 2$ (figure 4.17d,e,f), the typical vertical wavelength clearly decreases with Re: $\lambda = 0.3\Lambda, 0.2\Lambda$ and 0.13Λ, for $Re = 8000, 30000$ and 100000, respectively. However, the number of oscillations along the vertical remains approximately the same leading to a concentration of the mode toward the mid-plane $z = 0$.

4.5 Scaling laws for the growth rate of the centrifugal instability

Billant & Gallaire (2005) have derived an asymptotic formula for the growth rate of the centrifugal instability for columnar vortices for large vertical wavenumber ($k \gg 1$) in the inviscid limit:

$$\omega = \omega^{(0)} - \frac{\omega^{(1)} N}{k} + O\left(\frac{1}{k^2}\right), \tag{4.20}$$

where

$$\omega^{(0)} = m\Omega(r_0) + \mathrm{i}\sqrt{-\phi(r_0)}, \tag{4.21}$$

$$\omega^{(1)} = \frac{(2n+1)\mathrm{i}}{2\sqrt{2}} \sqrt{\frac{\phi''(r_0) - 2m^2\Omega'(r_0)^2 + 2\mathrm{i}m\sqrt{-\phi(r_0)}\Omega''(r_0)}{-\phi(r_0)}} \sqrt{1 - \frac{\phi(r_0)}{N^2}}, \tag{4.22}$$

with n a non-negative integer, $\phi = 2\Omega\zeta$ and r_0 is given by

$$\phi'(r_0) = -2\mathrm{i}m\Omega'(r_0)\sqrt{-\phi(r_0)}. \tag{4.23}$$

Here, we show that the formula (4.20) can be used to predict the growth rate of the centrifugal instability in pancake vortices. First, since the centrifugal instability is most unstable in the limit $k \to \infty$ in inviscid fluids, viscous effects can be easily taken into account at leading order in k by adding a damping term of the form νk^2 (Lazar *et al.*, 2013*b*). Thus, (4.20) becomes at leading order:

$$\omega = \omega^{(0)} - \frac{\omega^{(1)} N}{k} - \mathrm{i}\nu k^2. \tag{4.24}$$

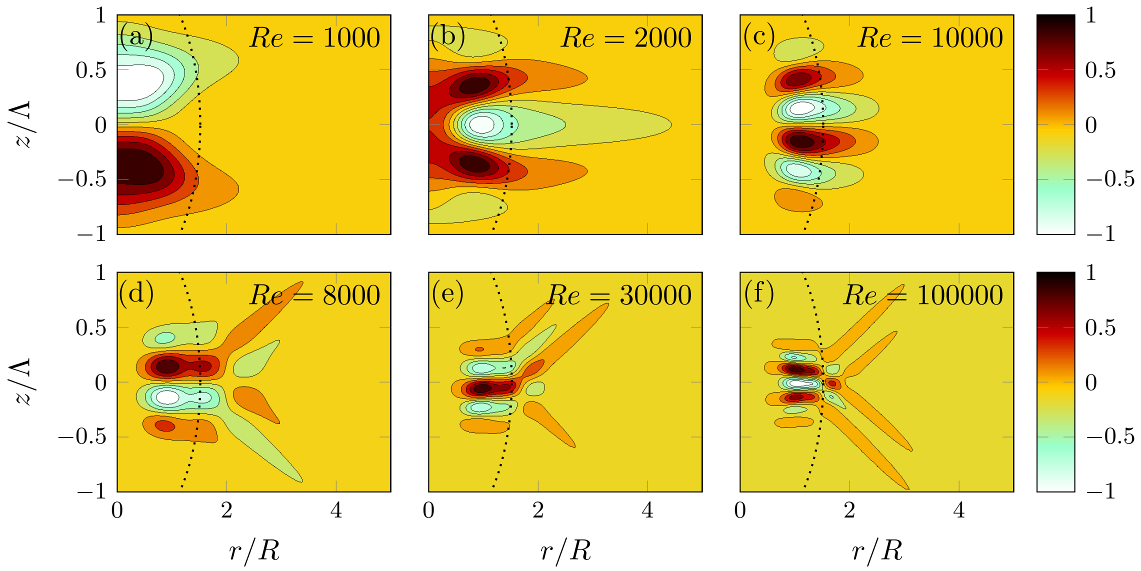

Figure 4.17: (color online) Real part of the radial velocity perturbation $\mathrm{Re}(u_r)$ of the most unstable mode for different Reynolds numbers: for $m = 1$ for (a) $Re = 1000$, (b) $Re = 2000$ and (c) $Re = 30000$ and for $m = 2$ for (d) $Re = 8000$, (e) $Re = 30000$, (f) $Re = 100000$ for $\alpha = 0.5$ and $F_h = 0.5$. The dotted lines indicate the contour where the angular velocity of the base vortex is $\Omega = 0.1\Omega_0$.

Using (4.24) and imposing

$$\frac{\partial \omega_i}{\partial k} = 0, \tag{4.25}$$

we can deduce that the most amplified wavenumber is given by

$$k_{\max} R = \left(\frac{\omega_i^{(1)} Re R}{2F_h} \right)^{1/3}, \tag{4.26}$$

where n should be set to zero in (4.22) to have the most unstable mode. Substituting k_{max} into (4.24) gives the maximum growth rate,

$$(\omega_i)_{\max} = \omega_i^{(0)} - \frac{3\Omega_0}{F_h^{2/3} Re^{1/3}} \left(\omega_i^{(1)} \frac{R}{2} \right)^{2/3}. \tag{4.27}$$

For small Froude number F_h (i.e. large N), $\omega^{(1)}$ becomes independent of F_h. Hence, (4.27) shows that the maximum growth rate of the centrifugal instability is a linear function of $(F_h^2 Re)^{-1/3}$. In other words, the maximum growth rate is only a function of the buoyancy Reynolds number $\mathcal{R} = ReF_h^2$ and independent of the aspect ratio. The same result applies to the corresponding frequency:

$$\omega_r = \omega_r^{(0)} - (2R^2)^{1/3} \Omega_0 \omega_r^{(1)} / (\omega_i^{(1)} \mathcal{R})^{1/3}. \tag{4.28}$$

Figure 4.18 shows the growth rate and frequency of pancake vortices (symbols) as a function of $(F_h^2 Re)^{-1/3}$ for different Reynolds number, Froude numbers and aspect ratios. They all gather on a single curve for each azimuthal wavenumber $m = 0, 1, 2$. The theoretical prediction (4.27) is also plotted with thin grey lines. It agrees quite well with the numerical results for pancake vortices for $m = 0$ and $m = 2$. However, the growth rate for $m = 1$

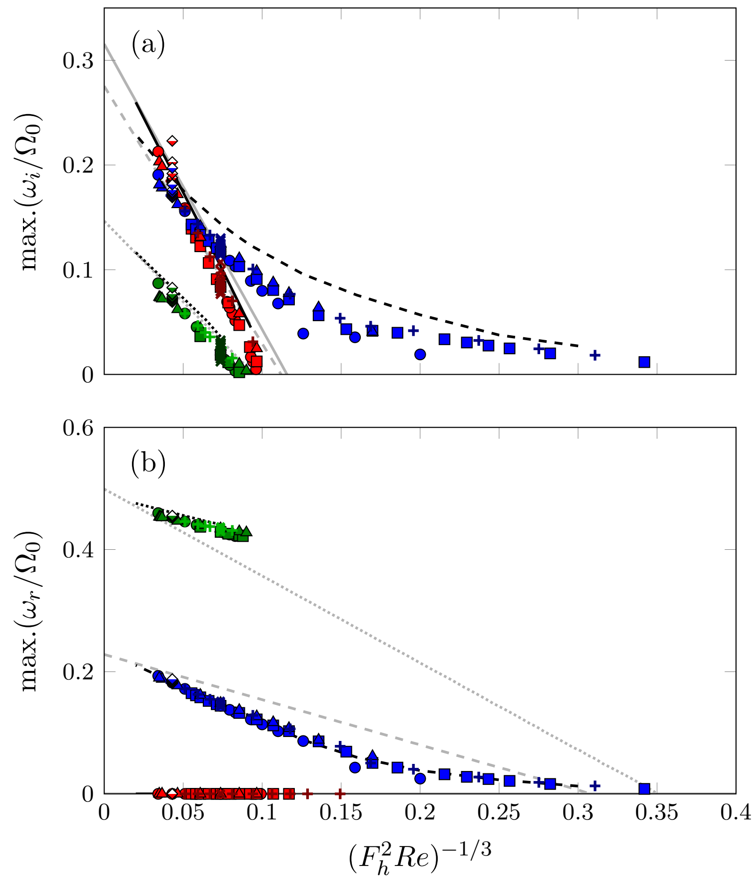

Figure 4.18: (color online) Maximum growth rate (a) and corresponding frequency (b) of the centrifugal instability as a function of $(F_h^2 Re)^{-1/3}$ for pancake vortices for $m = 0$ (red symbols), $m = 1$ (blue symbols) and $m = 2$ (green symbols) for different control parameters. The grey thin lines show the theoretical prediction (4.27) and the light black lines correspond to numerical results for a columnar vortex for $F_h = 0.5$ and various Re. The different symbols correspond to: ● various Re for $\alpha = 0.5, F_h = 0.5$; ■ various F_h for $\alpha = 0.5, Re = 10000$; ▲ various F_h for $\alpha = 1, Re = 10000$; + various F_h for $\alpha = 0.5, Re = 30000$; × various α for $F_h = 0.5, Re = 10000$; ◇ various α for $F_h = 0.5, Re = 50000$.

decreases with $(F_h^2 Re)^{-1/3}$ slower than predicted. The growth rate and frequency computed for a columnar vortex for $F_h = 0.5$ and various Re are also shown in figure 4.18 by thick black lines. They also agree with the predictions of (4.27) except for $m = 1$ for which the decrease of the growth rate with $(F_h^2 Re)^{-1/3}$ is also slower than predicted. This slow decrease for large $(F_h^2 Re)^{-1/3}$ is due to the transition between the centrifugal and bending modes for long-wavelength. The formula (4.24) no longer applies in this limit. From figure 4.18, we can deduce that the centrifugal instability for $m = 0$ and $m = 2$ is stabilized when $\mathcal{R} = ReF_h^2 \lesssim 1000$ while the mode $m = 1$ becomes stable only when $\mathcal{R} \lesssim 16$. The mode $m = 1$ is more unstable than $m = 0$ when $\mathcal{R} \lesssim 4600$.

4.6 Condition of existence of the shear instability

In section 4.4, we have observed that the shear instability for $m = 2$ does not always exist depending on the aspect ratio and Froude number. The purpose of this section is to derive a condition for its existence. To this end, we first consider the stability of a

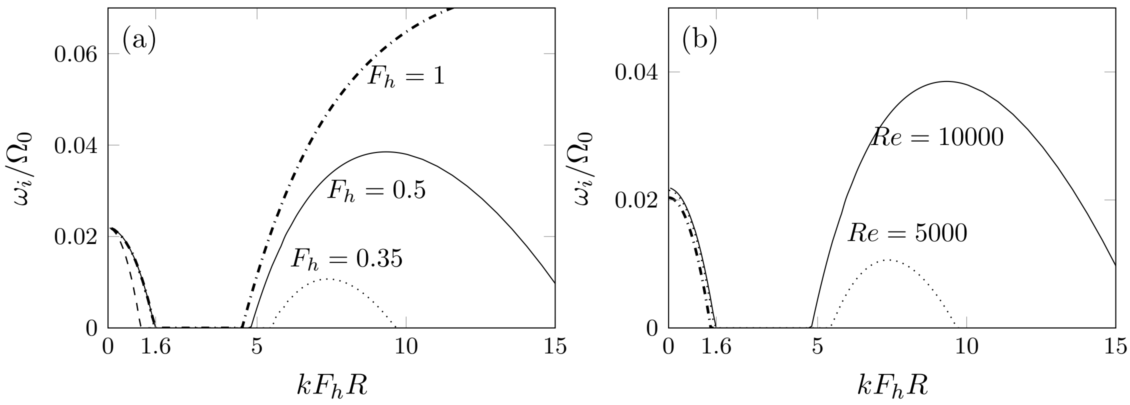

Figure 4.19: Growth rate for $m = 2$ for a columnar vortex as a function of the rescaled axial wavenumber kRF_h (a) for different Froude numbers F_h at fixed $Re = 10000$: - - -, $F_h = 0.1$; ⋯⋯, $F_h = 0.35$; ——, $F_h = 0.5$; -·-·-, $F_h = 1$. (b) For different Reynolds numbers Re at fixed $F_h = 0.5$: -·-·-, $Re = 2000$; ⋯⋯, $Re = 5000$; ——, $Re = 10000$.

columnar vortex for different F_h and Re. Figure 4.19a shows the growth rate for $m = 2$ as a function of the rescaled axial wavenumber kRF_h for different Froude numbers for $Re = 10000$. There exist two distinct branches: the shear instability for $kRF_h < 1.6$ and the centrifugal instability for $kRF_h \geq 5$. The shear instability is most unstable in the 2D limit ($k = 0$) while the centrifugal instability is intrinsically 3D. Even if the Froude number is varied, the growth rate curves for the shear instability remain almost identical when represented as a function of kRF_h as reported by Deloncle *et al.* (2007) for parallel horizontally sheared flows. In contrast, the centrifugal instability branch varies greatly with F_h and becomes more unstable as F_h increases because its maximum growth rate is a function of $F_h^2 Re$ for small F_h as shown by (4.27). The scaling of the shear branch is consistent with the self-similarity of strongly stratified flows (Billant & Chomaz, 2001). Such scaling applies as long as the Froude number is small and viscous effects, as measured by the buoyancy Reynolds number ReF_h^2, are negligible. This is the case of all the parameters investigated in figure 4.19 except $F_h = 0.1$. The growth rate of the shear instability for this Froude number departs slightly from the others because of viscous effects. Similarly, figure 4.19b shows the growth rate for $m = 2$ for different Reynolds numbers for a fixed Froude number $F_h = 0.5$. Similar behaviours are observed, the shear instability branch is almost independent of the Reynolds number provided that the buoyancy Reynolds number is not too small. In contrast, the centrifugal instability branch is strongly dependent of Re. Because of these different behaviours, the shear instability becomes most unstable for small Froude numbers (see the curve for $F_h = 0.35$ and $Re = 10000$ in figure 4.19a) and small Reynolds numbers (see the curve for $Re = 5000$ and $F_h = 0.5$ in figure 4.19b).

Nevertheless, the shear instability is always present in columnar vortices for the range of parameters investigated. In order to explain why it is absent for some parameters for pancake vortices, confinement effects have to be considered. Figure 4.19 shows that the upper wavenumber cutoff of the shear instability is $k_M R = 1.6/F_h$. In other words, the minimum wavelength is $\lambda_m \simeq 4F_hR$. Since the typical thickness of the pancake vortex is $L_v \simeq 2\Lambda$, a condition for the existence of the shear instability is that at least one wavelength fits along the vertical $\lambda_m \leq L_v$, i.e.

$$\frac{F_h}{\alpha} \leq 0.5. \tag{4.29}$$

4

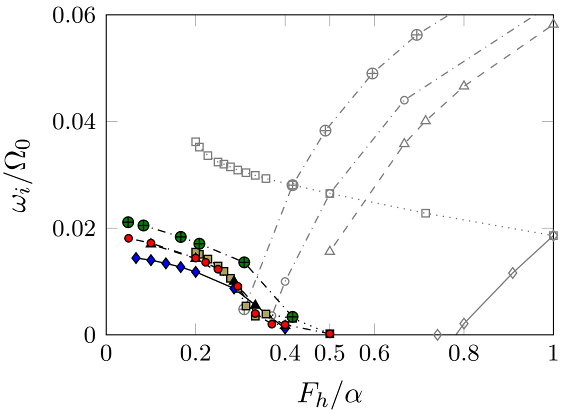

Figure 4.20: Growth rate of the most unstable shear (colored filled symbols) and centrifugal (grey open symbols) modes as a function of F_h/α for different F_h for fixed α and Re: $\alpha = 0.5$, $Re = 10000$, $\alpha = 0.5$, $Re = 30000$; $\alpha = 1$, $Re = 10000$; $\alpha = 1.2$, $Re = 10000$ and for different α for $F_h = 0.5$ and $Re = 10000$.

Figure 4.20 summarizes the growth rate of the most unstable shear and centrifugal modes for $m = 2$ as a function of F_h/α for various combinations of F_h, Re and α. The growth rates of the shear instability collapse approximately into a single curve. This curve has the same shape as the growth rate curve of the shear instability as a function of kRF_h for a columnar vortex (figure 4.19). Furthermore, the growth rate goes to zero for $F_h/\alpha = 0.5$ in agreement with (4.29). Hence, the shear instability is not present in figure 4.16 because the Froude number $F_h = 0.5$ and aspect ratio $\alpha = 0.5$ do not meet the criterion (4.29). In contrast, the growth rate of the most unstable centrifugal mode for $m = 2$ varies in a disorganized way when represented as a function of F_h/α (grey symbols in figure 4.20). This should be contrasted to figure 4.18 where a very good collapse for the centrifugal mode was observed when plotted as a function of $(F_h^2 Re)^{-1/3}$.

Finally, figure 4.21 shows the growth rate for $m = 2$ as a function of Re for $F_h/\alpha = 0.41$, i.e. when (4.29) is satisfied. Both centrifugal (dashed line) and shear (solid line) instabilities exist. The growth rate of the centrifugal instability strongly depends on Re and vanishes when $Re \leq 5500$ while the growth rate of the shear instability is independent of Re for $Re \geq 7000$ but eventually goes to zero around $Re = 3000$.

4.7 Instabilities specific to pancake vortices

In the previous sections, we identified and characterized the centrifugal and shear instabilities in pancake vortices by comparison to their counterparts in columnar vortices. We restricted the parameter range to $F_h/\alpha < 1.5$ in order to avoid the occurrence of the gravitational instability. In this section, we now focus on the range of parameters close to $F_h/\alpha = 1.5$. We shall see that another type of instability can occur in addition to the gravitational instability.

Figure 4.22 shows two examples of spectra for two different Froude numbers such that: $F_h/\alpha = 1.49$ and $F_h/\alpha = 1.67$ for otherwise the same parameters: $\alpha = 0.5$, $m = 2$ and $Re = 10000$. In figure 4.22a, there exist two distinct groups of modes which have different frequencies: the first group (labelled CI) is located around $\omega_r/\Omega_0 = 0.4$ while the second group (labelled BI) is around $\omega_r/\Omega_0 = 0.8$. The maximum growth rate of these two groups

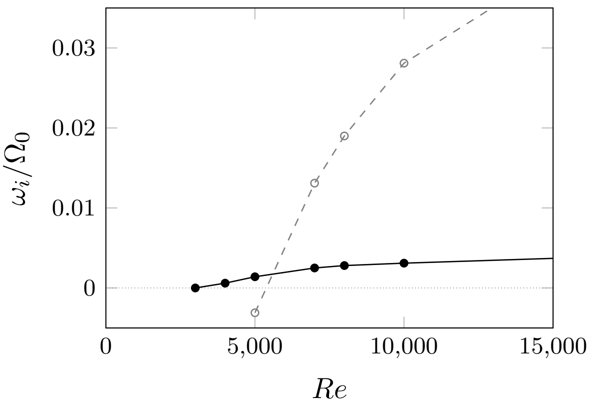

Figure 4.21: Growth rate as a function of Re for $m = 2$ for $\alpha = 1.2$, $F_h = 0.5$: most unstable centrifugal mode; most unstable shear mode.

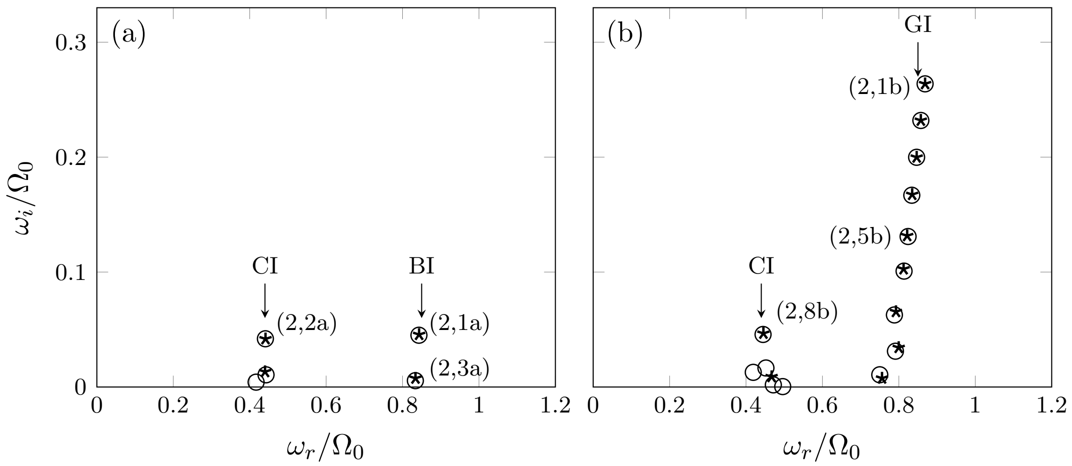

Figure 4.22: Growth rate (ω_i/Ω_0) and frequency (ω_r/Ω_0) spectra for a pancake vortex (○: for symmetric and ⋆ for anti-symmetric modes) for (a) $F_h/\alpha = 1.49$ (b) $F_h/\alpha = 1.67$ for the same parameters $m = 2, \alpha = 0.5$ and $Re = 10000$.

are comparable for these parameters. Two distinct groups are also seen for $F_h/\alpha = 1.67$ (figure 4.22b), i.e. when the parameters are above the threshold for the gravitational instability. The frequencies are approximately the same as for $F_h/\alpha = 1.49$ but the second group near $\omega_r/\Omega = 0.8$ (labelled GI) has now a much larger maximum growth rate.

Figure 4.23 shows the radial velocity perturbation of the CI and BI modes labelled (2,2a), (2,1a) and (2,3a) in figure 4.22a. The thick dashed line in figure 4.23 indicates the contour where the generalized Rayleigh discriminant changes sign. The CI mode (2,2a) is a centrifugal mode with similar characteristics as those described previously. The BI mode (2,1a), however, shows different properties. The mode is concentrated near $r/R = 0$ and $z/\Lambda = \pm 0.7$ which is near the regions of maximum total density vertical gradient. Yet, the flow is stable to gravitational instability since $F_h/\alpha = 1.49 \leq 1.5$. The second BI mode (2,3a) is located in the same regions but exhibits more radial oscillations and some internal rays.

The GI and CI modes (2,1b), (2.5b) and (2,8b) of figure 4.22b are shown in figure 4.24. The GI mode (2,1b) (figure 4.24a) is localized in the regions delimited by thick dashed lines where the vertical gradient of total density $\partial\rho_t/\partial z$ is positive. This proves that this mode

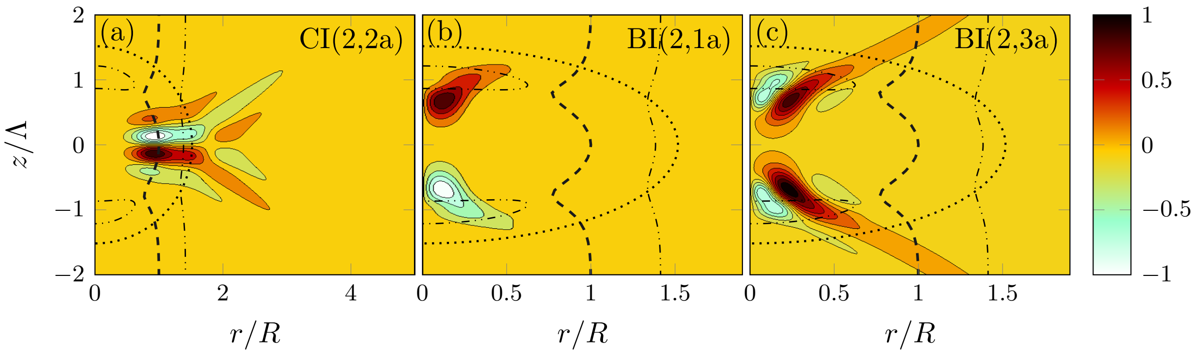

Figure 4.23: (color online) Real part of the radial velocity perturbation $\mathrm{Re}(u_r)$ for $F_h/\alpha = 1.49, m = 2, Re = 10000, \alpha = 0.5$ of the modes: (a) (2,2a) (b) (2,1a) (c) (2,3a) (see figure 4.22a). The thick dashed line represents the contour where the Rayleigh discriminant Φ vanishes. The dotted line indicates the contour where the angular velocity of the base vortex is $\Omega = 0.1\Omega_0$. The potential vorticity radial gradient along isopycnal changes sign on the double dotted dashed lines.

corresponds to the gravitational instability. The GI mode (2,5b) (figure 4.24b) shows more complicated structures but is also localized near the regions of positive vertical gradient of total density. The phase velocity of these gravitational modes $\omega_r/m \simeq 0.45\Omega_0$ is close to the angular velocity of the base flow $\Omega \simeq 0.47\Omega_0$ at the point $(r = 0, z = \sqrt{3}/2\Lambda)$ where the total density vertical gradient is maximum.

The CI mode (2,8b) is a centrifugal mode similar to mode (2,2a) shown in 4.23a. Figure 4.25a shows the growth rate of the most unstable BI modes as a function of F_h/α in the vicinity of the threshold $F_h/\alpha = 1.5$ for different m for two different fixed aspect ratios $\alpha = 0.4$ and $\alpha = 0.5$ for varying F_h, and for fixed $F_h = 0.74$ for varying α and $Re = 20000$. As can be seen, the azimuthal wavenumbers $m = 1, 2, 3$ are unstable but not $m = 0$ and $m \geq 4$. The growth rates are mostly a function of F_h/α only for all m. The curve for $m = 3$ and $\alpha = 0.4$ departs however slightly from the two other curves. BI modes only exist in a small range: $1.43 \leq F_h/\alpha \leq 1.5$, i.e. just below the threshold for the gravitational instability. This means that BI modes are unstable only when the isopycnals are strongly deformed. Figure 4.25b further shows that the growth rates of the BI modes decrease when the Reynolds number decreases for a fixed aspect ratio and Froude number $\alpha = 0.5, F_h = 0.74$. When $Re \leq 3000$, BI modes are stable.

In order to understand the origin of BI modes, figures 4.26b,c show the total base density ρ_t for the same Froude numbers $F_h/\alpha = 1.49$ and $F_h/\alpha = 1.67$ as in figure 4.22. The density ρ_t for a smaller Froude number $F_h/\alpha = 1.33$ is also displayed for comparison (figure 4.26a). When F_h/α increases, the isopycnals are more and more deformed in the vortex core due to the thermal-wind relation (4.6). This suggests that BI modes could be due to the baroclinic instability. A necessary condition for the baroclinic instability is that the potential vorticity gradient along isopycnals

$$\left.\frac{\partial \Pi}{\partial r}\right|_{\rho_t} = \frac{\partial \Pi}{\partial r}\frac{\partial \rho_t}{\partial z} - \frac{\partial \Pi}{\partial z}\frac{\partial \rho_t}{\partial r}, \tag{4.30}$$

changes sign somewhere in the flow (Hoskins *et al.*, 1985; Eliassen, 1983). The potential vorticity reads $\Pi = \boldsymbol{\omega}_b \cdot \nabla \rho_t$ where $\boldsymbol{\omega}_b$ is the base vorticity $\boldsymbol{\omega}_b = -\partial(r\Omega)/\partial z \boldsymbol{e}_r + 1/r \partial(r^2\Omega)/\partial r \boldsymbol{e}_z$. The double dotted dashed lines in figure 4.23 indicate the contours where (4.30) vanishes. The BI modes are located in the vortex core in the vicinity of the lines. This strongly suggests that BI modes are due to the baroclinic instability. However, the condition (4.30) is

4

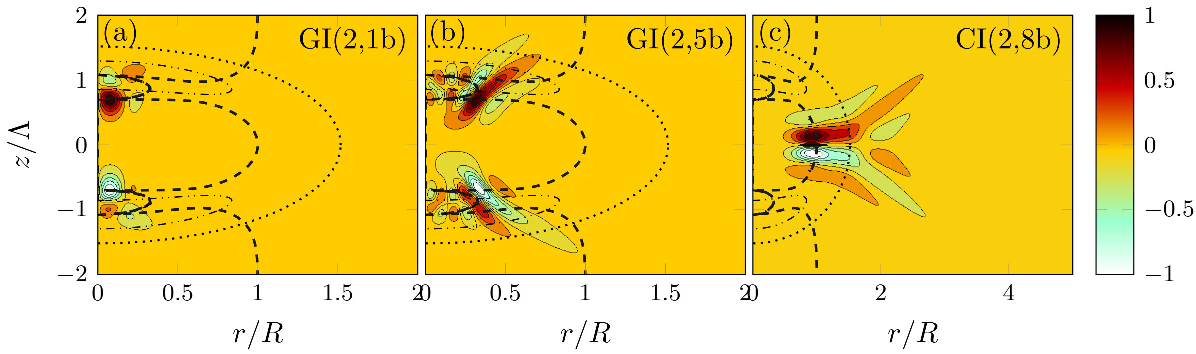

Figure 4.24: (color online) Real part of the radial velocity perturbation $\mathrm{Re}(u_r)$ for $F_h/\alpha = 1.67, m = 2, Re = 10000, \alpha = 0.5$ of the modes: (a) (2,1b), (b) (2,5b) and (c) (2,8b) (see figure 4.22b). The thick dashed line represents the contour where the Rayleigh discriminant Φ vanishes. The thick dash dotted line delimits the regions where the vertical gradient of total density $\partial\rho_t/\partial z$ is positive. The dotted line indicates the contour where the angular velocity of the base vortex is $\Omega = 0.1\Omega_0$. The potential vorticity radial gradient along isopycnal changes sign on the double dotted dashed lines.

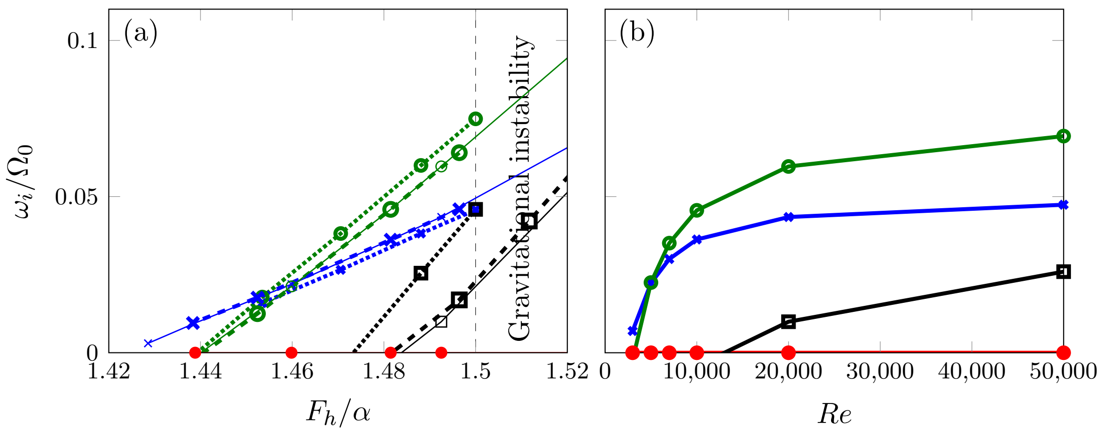

Figure 4.25: Growth rate of the most unstable BI modes as a function of (a) F_h/α: for $\alpha = 0.4$, $\alpha = 0.5$ and $F_h = 0.74$ and $Re = 20000$ and (b) as a function of Re for $\alpha = 0.5$ and $F_h = 0.74$ for different azimuthal wavenumbers: $m = 0$, $m = 1$, $m = 2$ and $m = 3$.

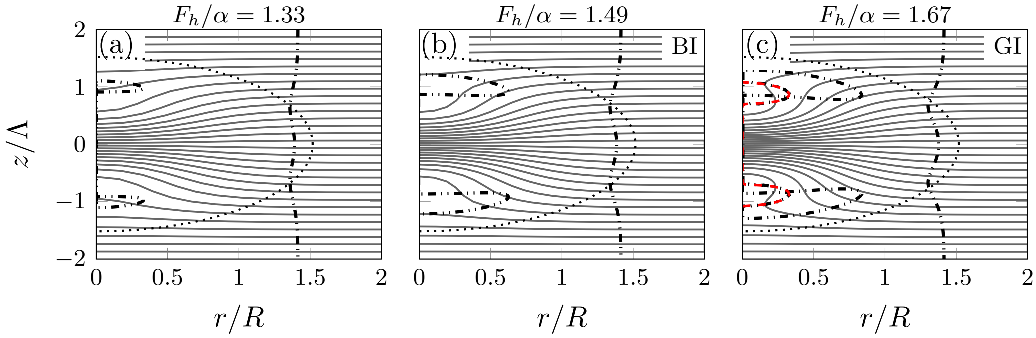

Figure 4.26: Isopycnals of the base vortex for $\alpha = 0.5$ for different Froude numbers (a) $F_h/\alpha = 1.33$, (b) $F_h/\alpha = 1.49$, (c) $F_h/\alpha = 1.67$. The vertical gradient of total density $\partial\rho_t/\partial z = 0$ vanishes on the thick dashed line - - - in (c). The dotted lines ······ indicate the contour where the angular velocity of the base vortex is $\Omega = 0.1\Omega_0$. The potential vorticity radial gradient along isopycnals changes sign on the double dotted dashed lines.

also satisfied for $F_h/\alpha = 1.33$ (figure 4.26a) and continues to be satisfied as F_h/α decreases further while BI modes disappear for $F_h/\alpha \leq 1.43$ for $\alpha = 0.5$ and $Re = 20000$ (figure 4.25a).

To understand this, it is interesting to consider a simple model consisting in a vortex with uniform angular velocity along the radial direction but varying linearly along the vertical direction:

$$\Omega = \tilde{\Omega}_0 - \tilde{\Omega}_1 z, \tag{4.31}$$

where $\tilde{\Omega}_0$ and $\tilde{\Omega}_1$ are constants. The corresponding base density is given from the thermal-wind relation (4.6) as

$$\rho_b = \frac{\rho_0}{g} r^2 \tilde{\Omega}_1(\tilde{\Omega}_0 - \tilde{\Omega}_1 z). \tag{4.32}$$

Such angular velocity and density fields are the simplest local approximation of the base flow in the regions where the BI modes develop. For simplicity, we further consider that the base flow (4.31) - (4.32) is bounded in a rigid cylinder of radius R and height H between $z = -H/2$ and $z = H/2$. We also assume that the vertical variations of the angular velocity are weak, i.e. $\tilde{\Omega}_1 H \ll \tilde{\Omega}_0$. In appendix 4.A, it is shown that the linearized equations (4.12)–(4.16) in the inviscid limit can be approximated at leading order in $\tilde{\Omega}_1$ by a single equation for the pressure

$$\frac{1}{r}\frac{\partial}{\partial r}\left(r\frac{\partial p}{\partial r}\right) + \left[-\frac{m^2}{r^2} + 4\tilde{F_h}^2\frac{\partial^2}{\partial z^2}\right] p = 0 + O(\tilde{\Omega}_1), \tag{4.33}$$

where $\tilde{F_h} = \tilde{\Omega}_0/N$. The general solution of (4.33) which is finite at $r = 0$ is

$$p = \mathrm{J}_m(2\tilde{F_h}kr)[A\cosh kz + B\sinh kz], \tag{4.34}$$

where J_m is the Bessel function of order m of the first kind and A and B are constants. By imposing that the vertical velocity vanishes at the top and bottom: $u_z(z = \pm H/2) = 0$, we obtain the dispersion relation

$$\omega = m\tilde{\Omega}_0 + \frac{m\tilde{\Omega}_1}{k}\sqrt{\left(1 - \frac{kH}{2\tanh(kH/2)}\right)\left(1 - \frac{kH\tanh(kH/2)}{2}\right)}. \tag{4.35}$$

This relation is very similar to the well-known dispersion relation for the baroclinic instability of a linear shear flow in quasi-geostrophic fluid (Eady, 1949). In order that the normal velocity vanishes at $r = R$, we have also to impose

$$2\tilde{F}_h kR = \mu_{m,n}, \tag{4.36}$$

where $\mu_{m,n}$ is the nth root of the Bessel function of the first kind of order m. As it is well-known from the Eady problem (Vallis, 2006), (4.35) requires $kH \leq 2.4$ to have an instability. Combining this condition with (4.36) gives therefore

$$\frac{\tilde{F}_h}{\tilde{\alpha}} \geq \frac{\mu_{m,n}}{4.8}, \tag{4.37}$$

where $\tilde{\alpha} = H/R$ is the aspect ratio of the base vortex. Since $\mu_{m,n} \geq \mu_{1,1} = 3.83$, (4.37) gives the condition for instability $\tilde{F}_h/\tilde{\alpha} > 0.8$. Below this threshold, the unstable modes predicted by (4.35) are too large to fit inside the cylinder containing the base flow. Although this model is very crude, it explains qualitatively why the baroclinic instability for the Gaussian vortex (4.1) develops only when the vertical Froude number F_h/α is above a critical value.

4.8 Instability map for $Re < 10000$

In this section, we build a map of the domains of existence of the different instabilities in the parameter space (Re, F_h) summarizing the results derived in the previous sections. We focus on the ranges of Reynolds numbers $Re \leq 10000$ and low Froude number $F_h \leq 0.5\alpha$ which pertains to laboratory experiments in the strongly stratified regime. The centrifugal instability has been found to occur when $\mathcal{R} = ReF_h^2 \geq 1000, 16$ and 1600 for $m = 0, 1,$ and 2, respectively. These thresholds are shown by solid lines in figure 4.27a,b,c for $m = 0, 1, 2$, respectively. A symbol is plotted in these figures for each parameter combination (Re, F_h) that has been computed numerically for the aspect ratio $\alpha = 0.5$. The different symbols indicate if an instability exists or not and its nature. As seen in figures 4.27a and 4.27c, the threshold for the centrifugal instability in terms of the buoyancy Reynolds number $\mathcal{R}$ discriminates well the centrifugally unstable and stable domains for $m = 0$ and $m = 2$. For $m = 1$, the threshold $ReF_h^2 = 16$ departs slightly from the observed limit between the stable and unstable regions for moderate Reynolds numbers. This threshold, which has been derived from results for $Re \geq 10000$ (see figure 4.18), is therefore more approximative for moderate Re. For $m = 2$, the shear instability develops when $F_h \leq 0.5\alpha$ for large Re (dashed line in figure 4.27c). For low Re, this threshold becomes dependent of the Reynolds number and the dashed line corresponds to an empirical fit to the observations. Finally, when $F_h > 1.5\alpha$ (dotted lines), the gravitational instability can develop for any azimuthal wavenumber. For Froude number just below this threshold, the baroclinic instability can also occur for $m \geq 1$ for sufficiently large Reynolds number.

All these thresholds are plotted together in a single diagram in figure 4.27d for the aspect ratio $\alpha = 0.5$. Only low Reynolds numbers are stable. The maximum Reynolds number Re_M which is stable is given by the crossing of the thresholds for the shear instability and the $m = 1$ centrifugal instability, i.e. $0.5\alpha \simeq 4/\sqrt{Re_M}$ giving $Re_M \simeq 63/\alpha^2$. Hence, the size of the stable domain depends strongly on the aspect ratio.

4.9 Comparison to previous works

It is now possible to attempt some comparisons between the present results and the laboratory experiments of Flór & van Heijst (1996) and the numerical simulations of Beckers *et al.* (2003).

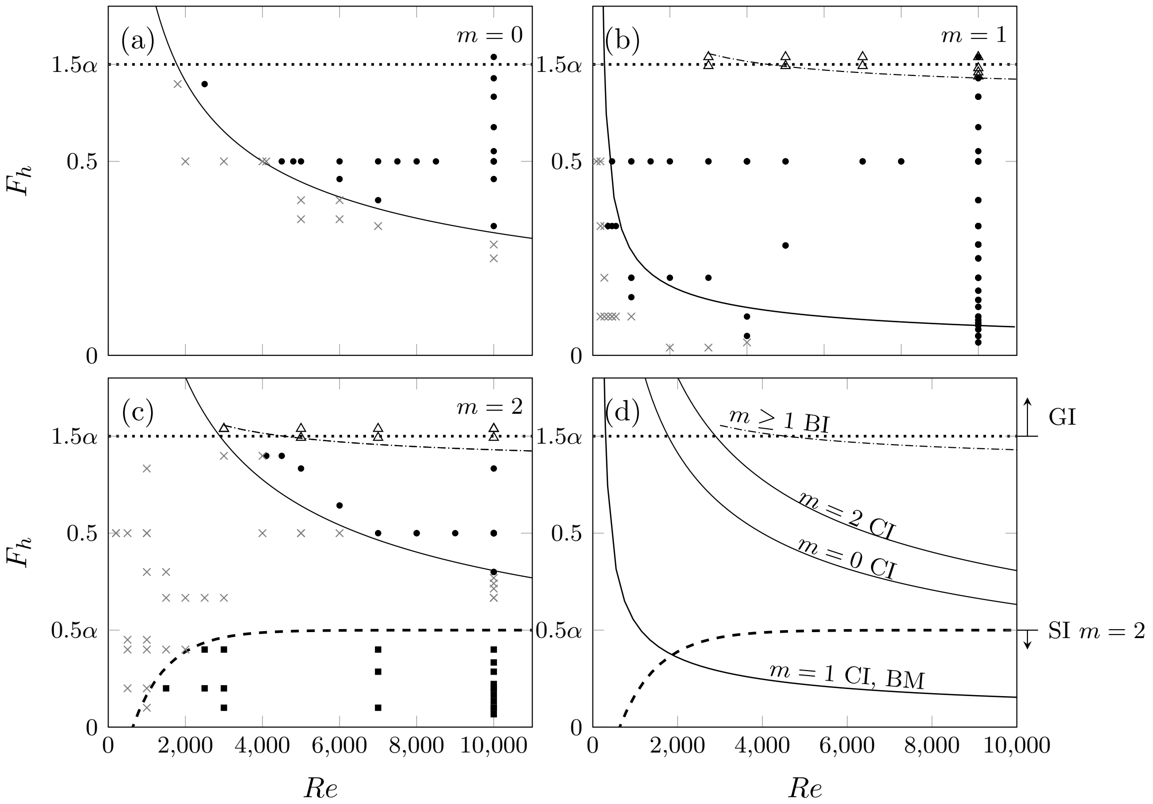

Figure 4.27: Stability diagram for $\alpha = 0.5$ as a function of Re and F_h for different azimuthal wavenumber m: (a) $m = 0$, (b) $m = 1$, (c) $m = 2$. The symbols indicate: • centrifugal instability, ▪ shear instability, ▵ baroclinic instability and × stable. The solid lines represent the thresholds for the centrifugal instability: —— $F_h^2 Re = 1000$ for $m = 0$; $F_h^2 Re = 16$ for $m = 1$; $F_h^2 Re = 1600$ for $m = 2$. The dashed line - - - in (c) is fitted curve to numerical results and shows the threshold for the shear instability. (d) Schematic diagram of stability for all azimuthal wavenumbers. —— centrifugal instability (CI) threshold for each m; - - - shear instability (SI) threshold for $m = 2$; -·-·- baroclinic instability (BI) and ······ gravitational instability (GI) threshold. Note that for $m = 1$, due to the bending mode which is unstable in the long-wavelength limit, the centrifugal instability (CI) threshold is also marked with bending mode (BM).

4

Flór & van Heijst (1996) have observed unstable monopolar vortices that evolved into multipolar vortices when $F = V_{\max}/NR_{\max} > 0.1$, where $V_{\max}$ and $R_{\max}$ are the maximum azimuthal velocity and corresponding radius. In the case of the profile (4.1), we have $F_h = 1.7F$. Since the aspect ratio of their vortices is around unity $\alpha \sim 1$, the condition $F \geq 1$ corresponds to $F_h/\alpha \geq 0.17$. At first sight, this seems incompatible with the condition derived herein for the existence of the shear instability $F_h/\alpha \leq 0.5$. However, the laboratory experiments of Flór & van Heijst (1996) are for low Reynolds numbers $O(100)$ so that the lower left part of the stability diagram for $m = 2$ (figure 4.27c) should be considered. Furthermore, the Reynolds number varies together with the Froude number since it is the maximum velocity which is varied. Hence, we travel along a straight oblique line starting from the origin in figure 4.27c. If the slope of this line is not too high, it is therefore possible to enter the unstable domain as the Froude number increases. This would mean that the stabilization observed by Flór & van Heijst (1996) for $F < 0.1$ is mostly due to viscous effects.

Beckers *et al.* (2003) have also performed experiments and numerical simulations on pancake vortices with an aspect ratio $\alpha \sim 0.4$. In their numerical simulations, they have not observed any instability for the profile (4.1) in the Reynolds number range $[500, 10000]$ and Froude number range $[0.1, 0.8]$. Their definitions of the Reynolds and Froude numbers are related to our definitions by: $\tilde{Re} = VR/\nu = 2\alpha\sqrt{\pi}Re$ and $\tilde{F} = V/RN = 2\alpha\sqrt{\pi}F_h$ since they have taken as velocity scale $V = 2\sqrt{\pi}\Lambda\Omega_0$. Hence, using our definitions of Re and F_h, these ranges correspond to $340 < Re < 6700$ and $0.2 < F_h/\alpha < 1.3$. Therefore, according to our results, they should have observed the shear instability when $F_h/\alpha < 0.5$ and Re is sufficiently large. However, Beckers *et al.* (2003) have obtained their results from perturbed non-linear simulations. Thus, the base vortex decays during the simulations and could become rapidly attenuated since viscous effects due to vertical shear scale like $1/(\alpha^2 Re)$ and can be significant for small aspect ratio even if the Reynolds numbers Re is large. In contrast, for steeper angular velocity profiles with $q \geq 3$, Beckers *et al.* (2003) observed the shear instability when the Reynolds number is sufficiently large. Furthermore, they reported that the growth rate of the shear instability decreases when the Froude number increases which is consistent with our results.

4.10 Conclusions

In this paper, we have investigated the stability of an axisymmetric pancake vortex with Gaussian angular velocity in both radial and vertical directions in a stratified fluid. The instabilities of columnar vortices such as the centrifugal and shear instabilities have been observed in spite of this pancake shape. The maximum growth rate of the centrifugal instability is almost independent of the aspect ratio α meaning that it is weakly affected by the pancake shape. The asymptotic formula for the growth rate of the centrifugal instability for short-wavelength derived by Billant & Gallaire (2005) for inviscid columnar vortices has been extended to viscous fluids and applied to pancake vortices. It shows that the maximum growth rate for each azimuthal wavenumber $m = 0, 1, 2$ depends only on the buoyancy Reynolds number $\mathcal{R} = ReF_h^2$ in good agreement with the numerical results for pancake vortices. The critical Froude number for the apparition of the centrifugal instability is therefore of the form $F_h = c/\sqrt{Re}$, where the constant c depends on m. We have also found that the azimuthal wavenumber $m = 1$ is more unstable than the axisymmetric mode for moderate buoyancy Reynolds numbers $\mathcal{R} \lesssim 4600$. In contrast, the shear instability occurring for $m = 2$, is strongly affected by the pancake shape and observed only when $F_h \leq 0.5\alpha$ for sufficiently large Reynolds number. This condition can be understood by considering again the columnar configuration: it ensures that the vortex thickness is larger than the minimum wavelength $\lambda_m \simeq 4F_hR$ of the shear instability for a columnar vortex for the same parameters. For $m = 1$, a displacement mode exists with almost zero frequency and growth rate.

Two other instabilities specific to the pancake shape have been found. They are due to the deformations of the isopycnals of the base flow. The gravitational instability can occur when the isopycnals overturn, i.e. when $F_h \geq 1.5\alpha$. For Froude numbers just below this threshold $F_h \geq 1.43\alpha$, the baroclinic instability have been also observed. In order to explain this threshold, we have considered a simple model consisting in a sheared vortex with an angular velocity uniform in the radial direction but varying linearly and weakly along the vertical. When the vortex is assumed to be bounded in a cylinder of radius R and height H, the baroclinic instability occurs only when the vertical Froude number is above a threshold. Although this model is only qualitative, it highlights the fact that the baroclinic instability can not always occur because of confinement effects even if the necessary condition of sign reversal of the potential vorticity gradient is satisfied. In the future, it would be interesting to study the non-linear dynamics of these instabilities.

4.A Stability equations for a vortex with almost uniform angular velocity

In this section, we derive the stability equation (4.33) for a base vortex with the angular velocity (4.31), i.e. uniform in the radial direction and varying linearly along the vertical. The assosiated density field is given by (4.32). In the inviscid limit, (4.12) and (4.13) yield the radial and azimuthal velocities

$$u_r = \frac{\mathrm{i}s\frac{\partial p}{\partial r} + 2\Omega \mathrm{i}m\frac{p}{r} + 2r\Omega\frac{\partial \Omega}{\partial z}u_z}{s^2 - 4\Omega^2}, \tag{4.38}$$

$$u_\theta = \frac{-2\Omega\frac{\partial p}{\partial r} - sm\frac{p}{r} + \mathrm{i}rs\frac{\partial \Omega}{\partial z}u_z}{s^2 - 4\Omega^2}, \tag{4.39}$$

where $s = m\Omega - \omega$. The vertical velocity is obtained from the vertical momentum and density equations (4.14) and (4.15)

$$u_z = \frac{\frac{g}{\rho_0}\frac{\partial \rho_b}{\partial r}u_r - \mathrm{i}s\frac{\partial p}{\partial z}}{N^2 - s^2 - \frac{g}{\rho_0}\frac{\partial \rho_b}{\partial z}}. \tag{4.40}$$

Combining (4.38) and (4.40) gives

$$u_z = \frac{\frac{g}{\rho_0}\frac{\partial \rho_b}{\partial r}\frac{\mathrm{i}s\frac{\partial p}{\partial r} + 2\Omega \mathrm{i}m\frac{p}{r}}{s^2 - 4\Omega^2} - \mathrm{i}s\frac{\partial p}{\partial r}}{N^2 - s^2 - \frac{g}{\rho_0}\frac{\partial \rho_b}{\partial z} - \frac{g}{\rho_0}\frac{\partial \rho_b}{\partial r}\frac{2r\Omega\frac{\partial \Omega}{\partial z}}{s^2 - 4\Omega^2}}. \tag{4.41}$$

We now assume that $H\tilde{\Omega}_1 \ll \tilde{\Omega}_0$ and $\omega = m\tilde{\Omega}_0 + \omega_1$ with $\omega_1 = O(\tilde{\Omega}_1 H)$. This implies

$$s = -\omega_1 - m\tilde{\Omega}_1 z = O(\tilde{\Omega}_1 H). \tag{4.42}$$

Hence, the velocity perturbations can be simplified at leading order in $\tilde{\Omega}_1$ to:

$$u_r = \frac{\mathrm{i}s\frac{\partial p}{\partial r} + 2\mathrm{i}m(\tilde{\Omega}_0 - \tilde{\Omega}_1 z)\frac{p}{r}}{-4\tilde{\Omega}_0^2 + 8\tilde{\Omega}_0\tilde{\Omega}_1 z} + O(\tilde{\Omega}_1^2), \tag{4.43}$$

$$u_\theta = \frac{-2(\tilde{\Omega}_0 - \tilde{\Omega}_1 z)\frac{\partial p}{\partial r} - \frac{sm}{r}p}{-4\tilde{\Omega}_0^2 + 8\tilde{\Omega}_0\tilde{\Omega}_1 z} + O(\tilde{\Omega}_1^2), \tag{4.44}$$

$$u_z = \frac{-\mathrm{i}\tilde{\Omega}_1 mp - \mathrm{i}s\frac{\partial p}{\partial r}}{N^2} + O(\tilde{\Omega}_1^2). \tag{4.45}$$

Substituting (4.43) – (4.45) into the continuity equation (4.16) gives

$$\mathrm{i}s\left[\frac{1}{r}\frac{\partial}{\partial r}\left(r\frac{\partial p}{\partial r}\right) - \frac{m^2}{r^2}p + \frac{4\tilde{\Omega}_0^2}{N^2}\frac{\partial^2 p}{\partial z^2}\right] = 0 + O(\tilde{\Omega}_1^2). \tag{4.46}$$

Since s is different from zero, (4.46) reduces to the equation (4.33) for the pressure. The general solution is given by (4.34). The boundary conditions at $r = R$ and $z = \pm H/2$ are assumed to be

$$u_r(r = R) = 0, \tag{4.47}$$

$$u_z(z = \pm\frac{H}{2}) = 0. \tag{4.48}$$

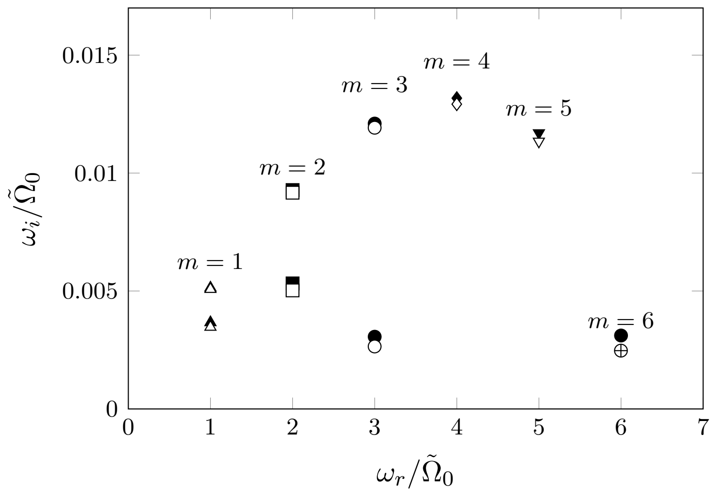

Figure 4.28: Spectrum of the model for different azimuthal wavenumbers: △ $m = 1$; □ $m = 2$; ○ $m = 3$; ◇ $m = 4$; ▽ $m = 5$; ⊕ $m = 6$. Filled symbols indicate spectrum predicted by (4.52) and blank symbols show the numerical results for $\tilde{\Omega}_0 = 1$, $\tilde{\Omega}_1 = 0.01$, $R = 5$, $H = 2$, and $N = 1.2$. For numerical computation $Re = 10000$ is used.

Using (4.43) and (4.45), these boundary conditions will be satisfied at leading order in $\tilde{\Omega}_1$ if

$$p = 0 \qquad \text{at} \qquad r = R, \tag{4.49}$$

$$s\frac{\partial p}{\partial z} + m\tilde{\Omega}_1 p = 0 \qquad \text{at} \qquad z = \pm\frac{H}{2}. \tag{4.50}$$

Equation (4.49) leads to the relation (4.36). Using (4.33), (4.50) implies

$$\begin{bmatrix} -\tilde{\Omega}_1 m \sinh\frac{kH}{2} - (\omega_1 - m\tilde{\Omega}_1\frac{H}{2})k\cosh\frac{kH}{2} & \tilde{\Omega}_1 m\cosh\frac{kH}{2} + (\omega_1 - m\tilde{\Omega}_1\frac{H}{2})k\sinh\frac{kH}{2} \\ \tilde{\Omega}_1 m \sinh\frac{kH}{2} - (\omega_1 + m\tilde{\Omega}_1\frac{H}{2})k\cosh\frac{kH}{2} & \tilde{\Omega}_1 m\cosh\frac{kH}{2} - (\omega_1 + m\tilde{\Omega}_1\frac{H}{2})k\sinh\frac{kH}{2} \end{bmatrix} \begin{bmatrix} A \\ B \end{bmatrix} = 0. \tag{4.51}$$

This leads to the dispersion relation

$$\omega_1 = \frac{m\tilde{\Omega}_1}{k}\sqrt{\left(1 - \frac{kH}{2\tanh(kH/2)}\right)\left(1 - \frac{kH\tanh(kH/2)}{2}\right)}, \tag{4.52}$$

so that $\omega = m\tilde{\Omega}_0 + \omega_1$ is given by (4.35). The stability of the base flow (4.31)–(4.32) has also been directly computed numerically for $\tilde{\Omega}_0 = 1, \tilde{\Omega}_1 = 0.01, R = 5, H = 2, N = 1.2$ for a large Reynolds number $Re = 10000$. Figure 4.28 shows that the predictions of (4.35) and the numerical results are in good agreement. For $m = 1, 2$ and 3, the secondary mode, i.e. when $2\tilde{F}_h Rk = \mu_{m,2}$, is also unstable in addition to the first mode $2\tilde{F}_h Rk = \mu_{m,1}$.

4.B Secondary modes of the centrifugal instability

In this appendix, secondary centrifugal modes for columnar and pancake vortices are presented. Figure 4.29 shows the growth rate of the centrifugal instability as a function of the scaled vertical axial wavenumber kRF_h for a columnar vortex for $F_h = 0.5$ and $F_h = 1$ for $m = 0$ and $Re = 10000$. When F_h is small as in figure 4.29a, there only exist only one mode and the stabilization at large k is due to the viscous effect. When F_h is larger (figure 4.29b), however, the growth rate of the first mode is now increased and a second mode exists with small growth rate. Hence, a second mode is observed when the first mode is sufficiently unstable, i.e. large F_h and Re. The first mode has the simplest radial velocity structure as shown in figure 4.30a while the second mode exhibits one more radial oscillation as depicted in figure 4.30b.

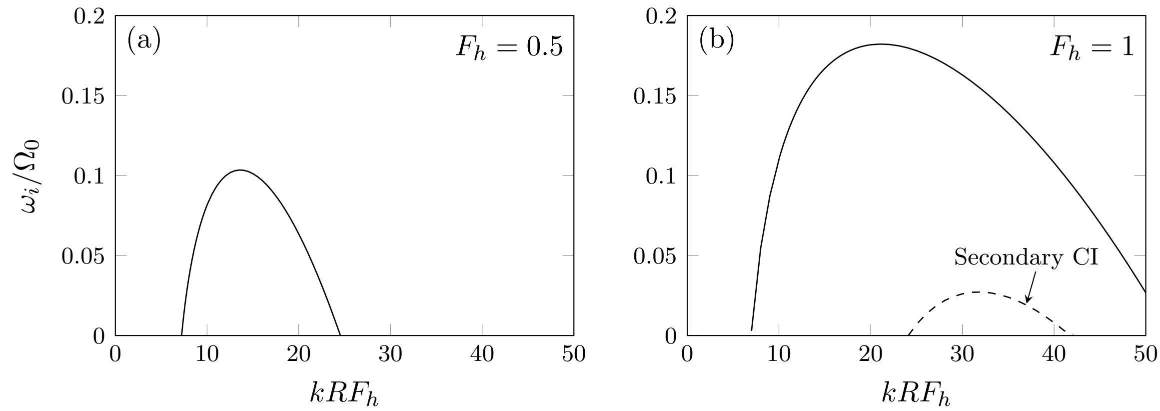

Figure 4.29: Growth rate ω_i/Ω_0 as a function of vertical wavenumber kRF_h for (a) $F_h = 0.5$ and (b) $F_h = 1$ for a columnar vortex with $m = 0, Re = 10000$.

Now figure 4.31a shows a spectrum for pancake vortices for $\alpha = 1, m = 0, F_h = 1$ and $Re = 10000$. As shown in previous sections, the frequency for $m = 0$ is zero. There exist 12 modes and selected radial velocity perturbations are shown in figure 4.31b,c,d,e. The most unstable mode has the simplest radial and vertical structures. Modes with smaller growth rate show more vertical oscillations. In addition, a secondary mode exists as for the columnar vortex. The velocity perturbation shows only few vertical oscillations like the most unstable mode but has one more radial oscillation (figure 4.31d). Nevertheless, the growth rates of the secondary centrifugal mode are much smaller than the first modes.

4.C The $m = 1$ displacement mode

For $m = 1$, there exists a displacement mode. This mode displaces the base flow horizontally. The stream function ψ of the base vortex is

$$\psi = -\frac{1}{2} r \exp\left(-\frac{r^2}{R^2} - \frac{z^2}{\Lambda^2}\right). \tag{4.53}$$

Let us consider a small horizontal displacement Δx and Δy of the base flow in Cartesian coordinate x and y. Assuming that $\Delta x = \Delta y \ll 1$,

$$\psi(x + \Delta x, y + \Delta y) \simeq \psi + \underbrace{\frac{\partial \psi}{\partial x}\Delta x + \frac{\partial \psi}{\partial y}\Delta y}_{\hat{\psi}}. \tag{4.54}$$

Using chain rule, the streamfunction $\hat{\psi}$ of the perturbation reads

$$\hat{\psi} = \frac{\partial \psi}{\partial r} \underbrace{\frac{\partial r}{\partial x}}_{\cos\theta} \Delta x + \frac{\partial \psi}{\partial r} \underbrace{\frac{\partial r}{\partial y}}_{\sin\theta} \Delta y. \tag{4.55}$$

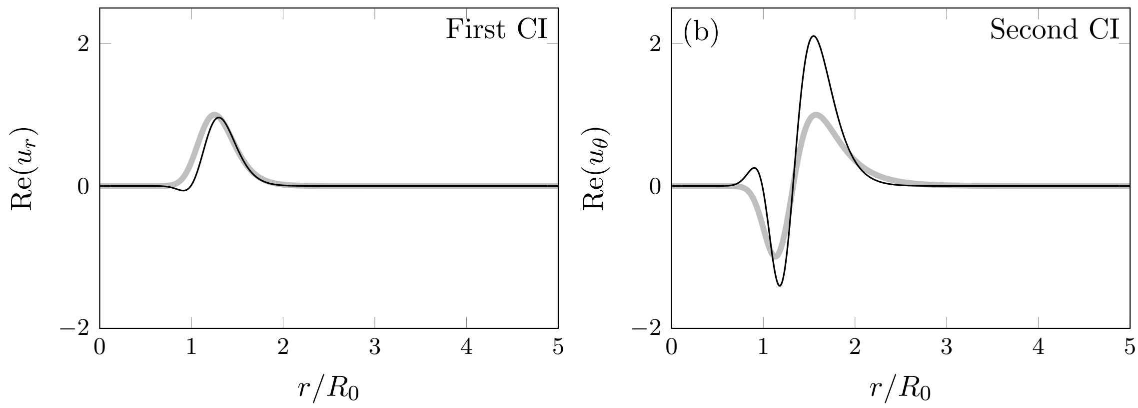

Figure 4.30: The radial u_r (▬) and azimuthal u_θ (—) velocities of the (a) first and (b) second centrifugal modes of a columnar vortex for $kRF_h = 30$, $F_h = 1$ and $Re = 10000$.

Replacing $\cos\theta = (\exp(\mathrm{i}\theta) + \exp(-\mathrm{i}\theta))/2$ and $\sin\theta = (\exp(\mathrm{i}\theta) - \exp(-\mathrm{i}\theta))/2\mathrm{i}$. The radial and azimuthal velocity perturbations are

$$\hat{u_r} = \frac{1}{r}\frac{\partial\hat{\psi}}{\partial\theta} = \frac{1}{r}\frac{\partial\psi}{\partial r}\left[\left(\frac{\Delta x}{2\mathrm{i}} - \frac{\Delta y}{2}\right)\mathrm{e}^{\mathrm{i}\theta} - \left(\frac{\Delta x}{2\mathrm{i}} + \frac{\Delta y}{2}\right)\mathrm{e}^{-\mathrm{i}\theta}\right], \tag{4.56}$$

$$\hat{u_\theta} = \frac{\partial\hat{\psi}}{\partial r} = \mathrm{i}\frac{\partial}{\partial r}\left(\frac{\partial\psi}{\partial r}\right)\left[\left(\frac{\Delta x}{2\mathrm{i}} - \frac{\Delta y}{2}\right)\mathrm{e}^{\mathrm{i}\theta} - \left(\frac{\Delta x}{2\mathrm{i}} + \frac{\Delta y}{2}\right)\mathrm{e}^{-\mathrm{i}\theta}\right], \tag{4.57}$$

Equation (4.56) and (4.57) mean that the horizontal velocity components are functions of the base stream function ψ as

$$u_r = \frac{1}{r}\frac{\partial\psi}{\partial r} = \frac{V_\theta}{r}, \tag{4.58}$$

$$u_\theta = \mathrm{i}\frac{\partial}{\partial r}\left(\frac{\partial\psi}{\partial r}\right) = \mathrm{i}\frac{\partial V_\theta}{\partial r}. \tag{4.59}$$

Figure 4.32a,b show (4.58) and (4.59), respectively and figure 4.32c,d show velocity perturbations of the displacement mode for $m = 1$: Re(u_r) and Im(u_θ) computed for $\alpha = 0.5, F_h = 0.5, Ro = \infty$ and $Re = 10000$. As can be seen, they are almost identical.

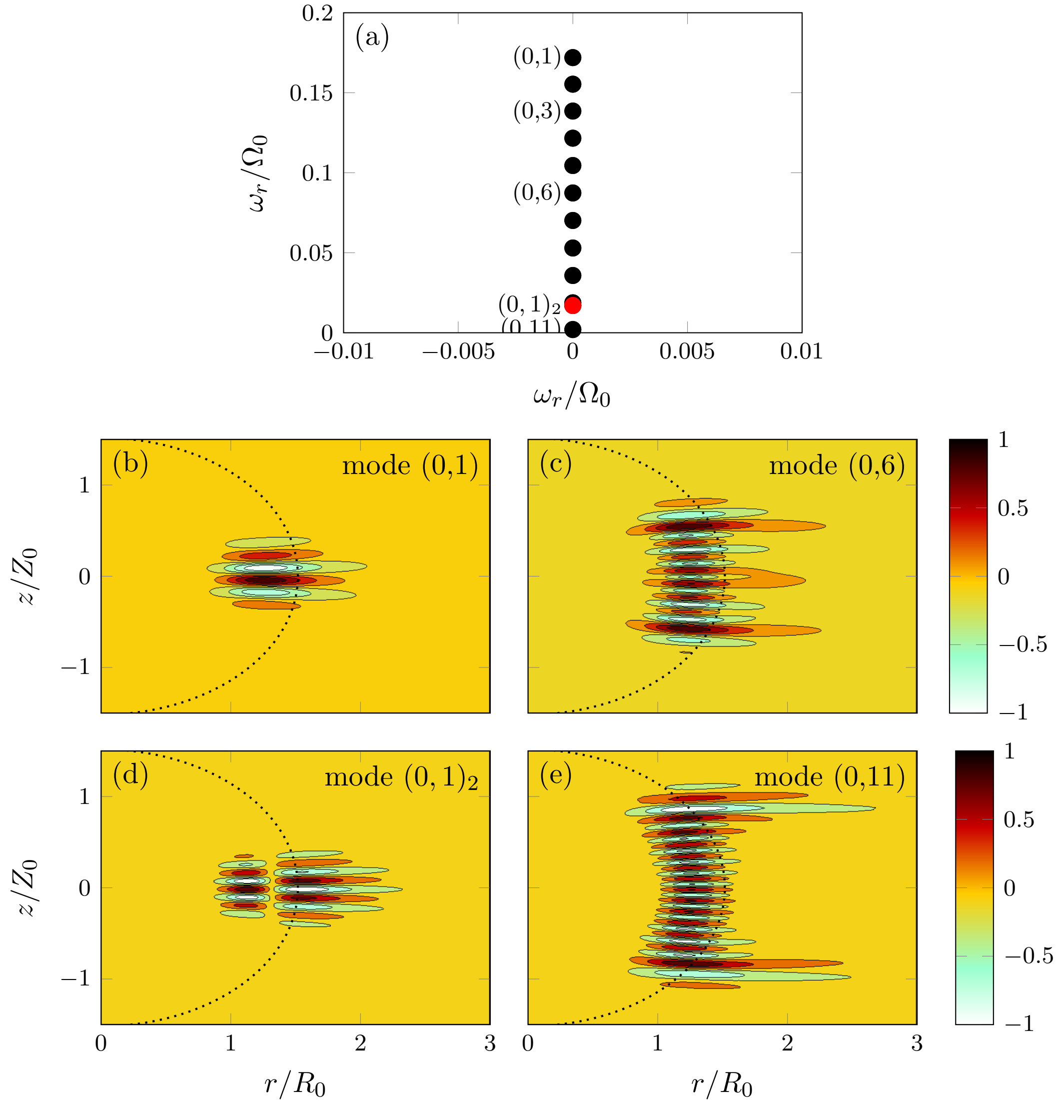

Figure 4.31: (a) Growth rate and frequency spectrum for $\alpha = 1$, $m = 0$, $F_h = 1$ and $Re = 10000$. Real part of radial velocity perturbations $\mathrm{Re}(u_r)$ for the modes (b) (0,1), (c) (0,3), (d) the second mode $(0,1)_2$ and (e) (0,11).

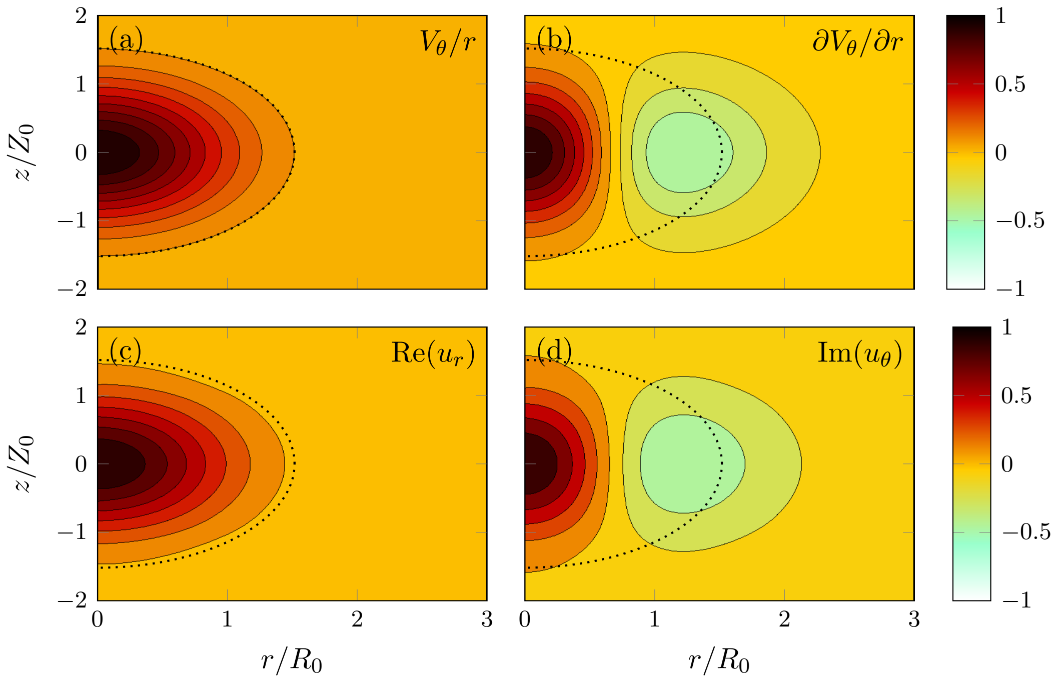

Figure 4.32: (a) The base angular velocity V_θ/r and (b) radial gradient $\partial V_\theta/\partial r$ and the velocity perturbations (c) $\mathrm{Re}(u_r)$ and (d) $\mathrm{Im}(u_\theta)$ of the displacement mode for $m = 1, \alpha = 0.5, F_h = 0.5, Ro = \infty$ and $Re = 10000$. The dotted line indicates the contour where the angular velocity of the base vortex is $\Omega = 0.1\Omega_0$.

5

Stability of a pancake vortex in stratified-rotating fluids

This chapter investigates the stability of an axisymmetric pancake vortex with Gaussian angular velocity in radial and vertical directions in stratified rotating fluids. The different instabilities are mapped in the parameter space: Rossby number Ro, Froude number F_h, Reynolds number Re and aspect ratio α. The centrifugal instability is dominant when the absolute Rossby number $|Ro|$ is large and is stabilized for small and moderate $|Ro|$ since the generalized Rayleigh discriminant is positive everywhere. The Gent-McWilliams instability is then dominant for the azimuthal wavenumber $m = 1$. It continuously changes to a mixed baroclinic-Gent-McWilliams instability for Burger number $Bu = \alpha^2 Ro^2/(4F_h^2) < 1$ when the Rossby number is not too large. The shear instability for $m = 2$ exists when F_h/α is below a threshold depending on Ro. Similarly, when $Bu < 1$ and $Ro \leq O(10)$, the shear instability transforms in the form of a mixed baroclinic-shear instability. The baroclinic instability develops when $F_h/\alpha|1 + 1/Ro| > 1.46$ in qualitative agreement with the analytical predictions for a bounded vortex with angular velocity slowly varying along the vertical.

Contents

Stability of an isolated pancake vortex in stratified-rotating fluids

Eunok Yim[1], Paul Billant[1] and Claire Ménesguen[2]

[1] LadHyX, CNRS, École Polytechnique, F-91128 Palaiseau Cedex, France
[2] LPO, IFREMER, CNRS, BP 70, 29280 Plouzané, France

(In preparation to submit to *J. Fluid Mech.*)

5.1 Introduction

Vortices in geophysical flows have received much attention especially in the oceans due to their important role in energy and scalar transports as well as mixing. Meddies (Mediterranean eddies) are one of the well-known vortices that are formed by warm salty water flowing from Mediterranean sea into Atlantic ocean and can live years traveling in the ocean (Armi *et al.*, 1989; Hobbs, 2007). The thickness of these mesoscale vortices is about 1km and their diameter about 100km (Richardson *et al.*, 2000). Similar eddies called Ulleung eddies are formed by warm northward and cold southward currents in East/Japan sea. Once formed, the eddies are trapped in Ulleung basin near Ulleng island (Chang *et al.*, 2004). These eddies are also pancake shaped with both warm and cold core, and a life time around a couple of years. The characteristics of these mesoscale eddies are important because they can greatly affect the fisheries (Kim *et al.*, 2012). In many places, there exist actually numerous observations of mesoscale eddies for example Reddies (Red ocean eddies) (Meschanov & Shapiro, 1998) and Swoddies (Slope water oceanic eddies) (Pingree & Le Cann, 1992; Carton, 2001; Carton *et al.*, 2013).

Idealized models of these vortices have been studied experimentally and numerically with a layered density stratification (Saunders, 1973; Griffiths & Linden, 1981; Hopfinger & van Heijst, 1993; Baey & Carton, 2002; Benilov, 2003; Thivolle-Cazat *et al.*, 2005; Aubert *et al.*, 2012; Lahaye & Zeitlin, 2015) as well as in continuously stratified fluids (Nguyen *et al.*, 2012; Lazar *et al.*, 2013*b*,*a*; Hua *et al.*, 2013). Saunders (1973) studied experimentally the stability of a vortex produced by releasing a cylindrical volume of fluid into a fluid with a lighter density placed on a turntable rotating at a constant speed. The spreading of the denser fluid at the bottom resulted in an anticyclonic vortex which was stable when the Burger number $Bu = (\delta\rho g/\rho)H/f^2R^2 > 1.8$, where $\delta\rho$ is the density difference between the two fluids, H the height, f the Coriolis parameter and R the radius of the inner cylinder. In contrast when $Bu < 1.8$, azimuthal disturbances grow on the vortex due to the baroclinic instability. The azimuthal wavenumber m scaled like $m \sim 1.8Bu^{-1/2}$ and the smallest wavenumber observed was a $m = 1$ wandering mode of the whole vortex. Similar observation have been later reported by Griffiths & Linden (1981) and Thivolle-Cazat *et al.* (2005) when the inner cylinder volume of fluid is less dense and has smaller depth than the surrounding fluid. However, $m = 1$ wandering mode has not been observed for these surface vortices. Numerical simulations performed by Verzicco *et al.* (1997) found good agreement with the results of Griffiths & Linden (1981). Griffiths & Linden (1981) also conducted experiments when a fluid is injected at constant flux into a rotating fluid with a different constant density or with a continuous stratification. In this case, barotropic instability first developed and then baroclinic instability as the anticyclonic vortex grew in size. In the case of the continuous stratification, they also observed layers above and below the vortex core that they attributed to the viscous-diffusive instability of McIntyre (1970). A similar instability was observed by

Hedstrom & Armi (1988) but no non-axisymmetric disturbances were observed to grow in contrast to Griffiths & Linden (1981). Hedstrom & Armi (1988) have also shown that the aspect ratio and velocity field were in good agreement with the prediction of the lens model of Gill (1981) in quasi-geostrophic fluids. Recently, Aubert *et al.* (2012) and Hassanzadeh *et al.* (2012) have proposed and validated a universal law valid in general stratified-rotating fluids which takes into account a density gradient in the vortex core.

Baey & Carton (2002) have studied the linear stability and the nonlinear evolution of elliptically perturbed circular vortices in a two-layer shallow-water model. They found that the two-layer model agrees generally with the quasi-geostrophic model except that cyclones are more unstable than anticyclones at $Bu \simeq 2$. Lazar *et al.* (2013*b*,*a*) studied experimentally and theoretically the stability of vortices in linearly stratified and rotating viscous fluids with respect to the axisymmetric centrifugal instability. Taking into account the vertical viscous effects which scale like k^2 for large vertical wavenumber k, they obtained analytic predictions for the most amplified vertical wavenumber and the marginal stability curves in terms of the Burger, Ekman and Rossby numbers. Lahaye & Zeitlin (2015) have investigated the linear stability and non-linear dynamics of anticyclones with a α-Gaussian profile in a two-layer shallow-water. They have shown that asymmetric centrifugal modes are more unstable than the axisymmetric mode for small Rossby number Ro or large Burger number Bu. For even smaller Ro or higher Bu, the barotropic shear instability is dominant. Billant *et al.* (2004) have carried out experiments on a columnar counter-rotating vertical vortex pair in stratified-rotating fluid. They have shown that the dominant centrifugal instability developing on the anticyclone is non-axisymmetric with an azimuthal wavenumber $m = 1$ for small Rossby number and small Froude number.

Nguyen *et al.* (2012) have conducted a numerical stability analysis of a pancake vortex in quasi-geostrophic fluids. In the case of a Gaussian angular velocity in both radial and vertical directions, they found that the dominant instability when the Burger number $Bu = N^2\Lambda^2/f^2R^2 < 1$ (where N is the Brunt-Väisälä frequency, Λ the half thickness of the vortex and R its radius) is generally a baroclinic instability with an azimuthal wavenumber $m = 2$. For $Bu > 1$, the dominant mode is an anti-symmetric $m = 1$ mode. For very small $Bu < 0.1$, higher azimuthal modes $m > 2$ become dominant. Hua *et al.* (2013) have performed non-linear simulations of the dynamics of a lens-shape vortex in quasi-geostrophic fluids. In addition to the development of asymmetric disturbances, they evidenced layering in the vicinity of critical levels where the azimuthal phase speed equal the angular velocity of the vortex. In chapter 4, we have analysed the stability of a Gaussian pancake vortex in stratified non-rotating fluids. Instabilities similar to those of columnar vortices have been found. The centrifugal instability occurs when the buoyancy Reynolds number ReF_h^2 is sufficiently large: $ReF_h^2 > 10^3$, where $F_h = \Omega_0/N$ is the Froude number based on the maximum angular velocity Ω_0 and $Re = \Omega_0 R^2/\nu$, where ν is the viscosity. The shear instability can develop when $F_h/\alpha < 0.5$ where α is the aspect ratio of the pancake vortex. In addition, instabilities specific to pancake vortices can exist: the baroclinic instability when $F_h/\alpha \geq 1.43$ and the gravitational instability when $F_h/\alpha \geq 1.5$.

In this paper, we will continue these stability analyses in the case of a stratified-rotating fluid in order to link the infinite Rossby number limit (chapter 4) and the small Rossby number limit (Nguyen *et al.*, 2012). We show that new types of instabilities arise as Ro is varied while some instabilities can be traced continuously from the stratified non-rotating limit to the quasi-geostrophic limit.

This paper is organized as follows: the stability problem and methods are formulated in §5.2. The effect of the Rossby number is investigated in §5.3 while the effects of the other parameters (F_h, α and Re) are studied in §5.4. Conditions of existence for the shear instability, Gent-McWilliams instability and baroclinic instability are derived in §5.5, §5.6 and §5.7, respectively. Finally §5.8 summarizes the domains of existence of each type of instability in the parameter space (F_h/α, Ro).

5.2 Problem formulation

The problem formulation is the same as in chapter 4 except that the fluid is not only stably stratified but also rotating about the vertical axis at rate $f/2$. Nevertheless, the main steps of the problem are recalled here.

5.2.1 The base state

As in Nguyen *et al.* (2012) and chapter 4, we consider an axisymmetric pancake vortex with angular velocity

$$\Omega(r,z) = \Omega_0 \mathrm{e}^{-\left(\frac{r^2}{R^2}+\frac{z^2}{\Lambda^2}\right)}, \tag{5.1}$$

where (r,θ,z) are cylindrical coordinates, R the radius, Λ the typical half thickness and Ω_0 is the maximum angular velocity. The radial and vertical inviscid momentum equations for such steady base flow are

$$-r\Omega^2 - fr\Omega = -\frac{1}{\rho_0}\frac{\partial p_t}{\partial r}, \tag{5.2}$$

$$0 = -\frac{1}{\rho_0}\frac{\partial p_t}{\partial z} - \frac{g}{\rho_0}\rho_t, \tag{5.3}$$

where p_t and ρ_t are the total pressure and density, respectively. Combining (5.2) and (5.3) gives the thermal-wind equation

$$\frac{\partial \rho_t}{\partial r} = -\frac{\rho_0}{g}\frac{\partial}{\partial z}(r\Omega^2 + fr\Omega), \tag{5.4}$$

yielding

$$\rho_t = \rho_0 + \bar{\rho}(z) + \rho_b(r,z), \tag{5.5}$$

with ρ_0 a constant, $\bar{\rho}(z) = -N^2\rho_0 z/g$ where $N = \sqrt{-g/\rho_0(\mathrm{d}\bar{\rho}/\mathrm{d}z)}$ is the Brunt-Väisälä frequency which is assumed constant and

$$\rho_b(r,z) = -z\frac{\rho_0}{\mathrm{g}}\left(\frac{R}{\Lambda}\right)^2(\Omega + f)\,\Omega. \tag{5.6}$$

5.2.2 Linearized Equations

We subject this vortex to infinitesimal perturbations of velocity $\boldsymbol{u}' = [u_r', u_\theta', u_z']$, pressure p', and density ρ' written as

$$[u_r', u_\theta', u_z', p', \rho'] = [u_r(r,z), u_\theta(r,z), u_z(r,z), \rho_0 p(r,z), \frac{\rho_0}{g}\rho(r,z)]\mathrm{e}^{-\mathrm{i}\omega t + \mathrm{i}m\theta} + \mathrm{c.c.}, \tag{5.7}$$

where $\omega = \omega_r + \mathrm{i}\omega_i$, ω_r the frequency, ω_i the growth rate and m the azimuthal wavenumber. The linearized Navier-Stokes equations under the Boussinesq approximations are

$$-\mathrm{i}(\omega - m\Omega)u_r - (2\Omega + f)u_\theta = -\frac{\partial p}{\partial r} + \nu\left(\nabla^2 u_r - \frac{1}{r^2}u_r - \frac{2}{r^2}\mathrm{i}mu_\theta\right) \tag{5.8}$$

$$-\mathrm{i}(\omega - m\Omega)u_\theta + (\zeta + f)u_r + \frac{\partial r\Omega}{\partial z}u_z = -\frac{\mathrm{i}m}{r}p + \nu\left(\nabla^2 u_\theta - \frac{1}{r^2}u_\theta + \frac{2}{r^2}\mathrm{i}mu_r\right) \tag{5.9}$$

$$-\mathrm{i}(\omega - m\Omega)u_z = -\frac{\partial p}{\partial z} - \rho + \nu\nabla^2 u_z \tag{5.10}$$

$$-\mathrm{i}(\omega - m\Omega)\rho + \frac{g}{\rho_0}\frac{\partial \rho_b}{\partial r}u_r + \frac{g}{\rho_0}\frac{\partial \rho_b}{\partial z}u_z = N^2 u_z + \kappa\nabla^2\rho \tag{5.11}$$

$$\frac{1}{r}\frac{\partial r u_r}{\partial r} + \frac{1}{r}\mathrm{i}mu_\theta + \frac{\partial u_z}{\partial z} = 0 \tag{5.12}$$

where ζ is the vertical vorticity, ν the viscosity, κ the diffusivity of the stratifying agent. The problem is governed by five non-dimensional numbers: aspect ratio (α), Froude number(F_h), Rossby number (Ro), Reynolds number(Re), Schmidt number(Sc), defined as follows:

$$\alpha = \frac{\Lambda}{R}, \qquad F_h = \frac{\Omega_0}{N}, \qquad Ro = \frac{2\Omega_0}{f}, \qquad Re = \frac{\Omega_0 R^2}{\nu}, \qquad Sc = \frac{\nu}{\kappa}. \tag{5.13}$$

The Schmidt number is set to $Sc = 1$ throughout the paper. As explained in chapter 4, equations (5.8) – (5.12) are discretized with finite element methods using FreeFEM++ (Hecht, 2012; Garnaud, 2012) in the domain $0 \le r \le R_{\max}$ and $-Z_{\max} \le z \le Z_{\max}$. The size is taken as $R_{\max} \ge 10R$ and $Z_{\max} = 5\Lambda$. They are slightly different compared to chapter 4 because some modes are more sensitive to radial confinement in the presence of background rotation. The mesh is adapted to the base flow so that the mesh is finer ($\sim 0.001R$) inside the vortex core than outside ($\sim 0.1R$). The boundary conditions at $r = 0$ are $u_r = u_\theta = 0$ for $m = 0$, $u_z = p = \rho = 0$ for $m = 1$ and $\boldsymbol{u} = p = \rho = 0$ for $m \ge 2$. At the other boundaries, $R = R_{\max}$ and $z = \pm Z_{\max}$, the perturbations are imposed to vanish: $\boldsymbol{u} = p = \rho = 0$. The matrix version of (5.8) – (5.12) built by FreeFEM++ is then solved by means of an iterative Krylov-Schur scheme and a shift-invert method using the SLEPc and PETSc libraries (Hernandez *et al.*, 2005; Garnaud, 2012; Garnaud *et al.*, 2013; Balay *et al.*, 2014; Roman *et al.*, 2015). More details can be found in chapter 4. The limit $\alpha \to \infty$ corresponding to a columnar vortex has been solved by means of a Chebyshev collocation spectral method (Antkowiak & Brancher, 2004).

5

5.3 Overview of the effect of the Rossby number

We first present an overview of the effect of the Rossby number starting from the strongly stratified non-rotating limit ($F_h < 1$ and $Ro = \infty$) previously studied in chapter 4. As the absolute Rossby number is decreased, some instabilities are stabilized or modified while new ones arise. This will enable us to connect the purely stratified limit to the quasi-geostrophic limit studied by Nguyen *et al.* (2012). Throughout the paper, the exploration of the parameter space will be restricted to the region stable to the gravitational instability, i.e. where the total density gradient

$$\frac{\partial \rho_t}{\partial z} = -\frac{\rho_0 N^2}{g} + \frac{\partial \rho_b}{\partial z}, \tag{5.14}$$

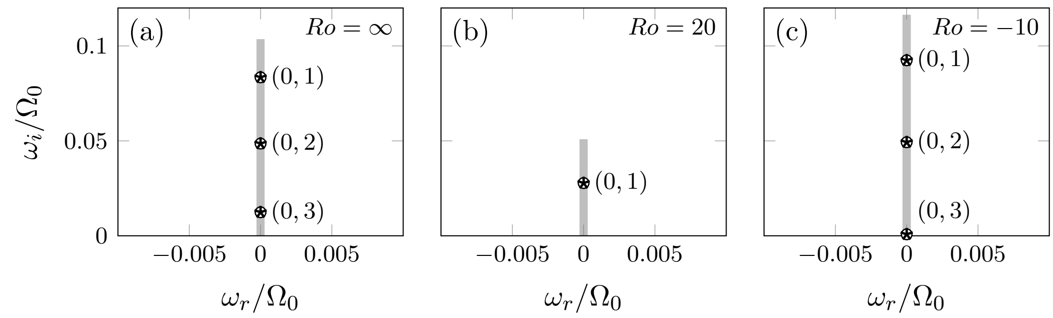

Figure 5.1: Growth rate (ω_i/Ω_0) and frequency (ω_r/Ω_0) spectra for $m = 0$ for different Rossby numbers Ro: (a) $Ro = \infty$, (b) $Ro = 20$ and (c) $Ro = -10$ $F_h = 0.5$ and $Re = 10000$. Discrete symbols (○: for symmetric and ⋆ for anti-symmetric modes) are for pancake vortices for $\alpha = 0.5$ and thick continuous lines (▬) are for columnar vortices ($\alpha = 0.5$).

is everywhere negative. This condition can be rewritten in the form

$$\frac{F_h}{\alpha} < c(Ro), \tag{5.15}$$

where c is a constant depending on the Rossby number. However, it cannot be expressed analytically in terms of Ro.

5.3.1 $m = 0$

For $m = 0$, it has been found in chapter 4 that only the centrifugal instability exists in stratified fluid when the buoyancy Reynolds number ReF_h^2 is sufficiently high. This remains true when the Rossby number is varied. Figure 5.1 shows two examples of spectra for $Ro = 20$ and $Ro = -10$ together with the one for $Ro = \infty$, all for the same set of parameters: $\alpha = 0.5, F_h = 0.5$ and $Re = 10000$. The unstable modes are shown by symbols and are labelled (m, i) where i is the mode number. The maximum growth rate and the number of modes vary with Ro but these variations are consistent with the spectra of the most unstable mode of a columnar vortex for the same control parameters (grey continuous lines). For each point, there exist actually two modes with different symmetry with respect to the mid-plane $z = 0$: anti-symmetric (⋆) and symmetric (○). Some examples of modes are shown in figure 5.2. The modes are localized inside the region delimited by red dashed lines where the Rayleigh discriminant

$$\Phi = \frac{1}{r^3}\frac{\partial}{\partial r}\left(r^2\left(\Omega + \frac{f}{2}\right)^2\right)\bigg|_{\rho t}, \tag{5.16}$$

is negative. The number of oscillations along the vertical increases with the mode number but there is always only one radial oscillation for the parameters of figure 5.1. The variation of the growth rate of the most unstable mode as a function of Ro for $\alpha = 0.5, F_h = 0.5$ and $Re = 10000$ is summarized in figure 5.3 (dashed line with symbols). The centrifugal instability is stabilized for small Rossby number in the range $-3.5 < Ro < 17$. A similar evolution of the maximum growth rate is observed for a columnar vortex (grey continuous line). As shown in chapter 4, the growth rate of the centrifugal instability can be predicted using the asymptotic formula of Billant & Gallaire (2005) for large axial wavenumber k for

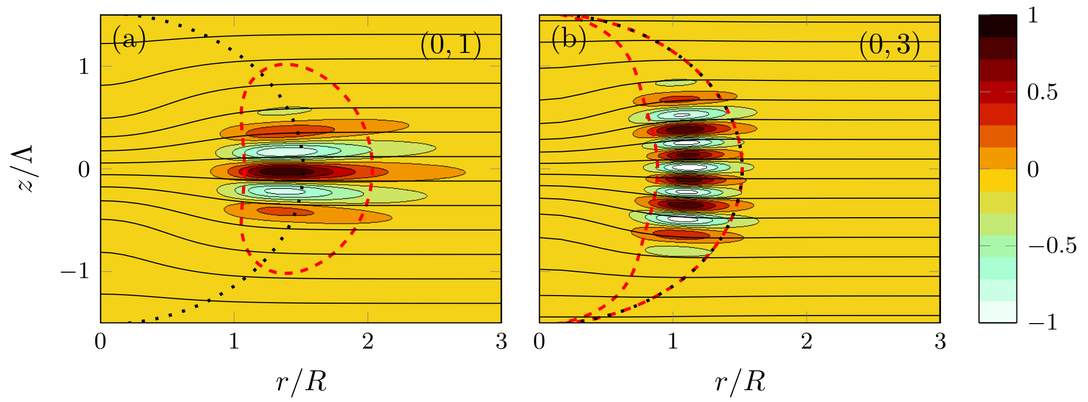

Figure 5.2: (Colour online) Real part of the radial velocity perturbation $\mathrm{Re}(u_r)$ of the centrifugal instability: (a) mode $(0,1)$ for $Ro = 20$ and (b) mode $(0,3)$ for $Ro = -10$ indicated in figure 5.1. The horizontal lines are isopycnals of the base density field. The dotted line indicates the extension of the base flow where $\Omega = 0.1\Omega_0$. The thick dashed line (- - -) indicates the contour where the Rayleigh discriminant Φ vanishes.

a columnar vortex with the addition of the leading viscous term as in Lazar *et al.* (2013*b*):

$$\omega = \omega^{(0)} - \frac{\omega^{(1)} N}{k} - \mathrm{i}\nu k^2, \tag{5.17}$$

where

$$\omega^{(0)} = m\Omega(r_0) + \mathrm{i}\sqrt{-\phi(r_0)}, \tag{5.18}$$

$$\omega^{(1)} = \frac{n\mathrm{i}}{2\sqrt{2}}\sqrt{\frac{\phi''(r_0) - 2m^2\Omega'(r_0)^2 + 2\mathrm{i}m\sqrt{-\phi(r_0)}\Omega''(r_0)}{-\phi(r_0)}}\sqrt{1 - \frac{\phi(r_0)}{N^2}}, \tag{5.19}$$

with n a non-negative integer, $\phi = (2\Omega + f)(\zeta + f)$ and r_0 is given by

$$\phi'(r_0) = -2\mathrm{i}m\Omega'(r_0)\sqrt{-\phi(r_0)}. \tag{5.20}$$

The maximum growth rate predicted by (5.17) for $F_h = 0.5$ and $Re = 10000$ is shown by the dashed grey line in figure 5.3. It is close to the maximum growth rate for both columnar and pancake vortices. It is worth to point out that the maximum growth rate for $F_h = 0.5$ and $Re = 10000$ is approximately three times smaller than the theoretical upper limit for the growth rate of the centrifugal instability which is $\sqrt{-\min(\phi)}$ for $m = 0$ (solid line in figure 5.3) and which is attained in the limit $k \to \infty$ and $\nu \to 0$. Note also that $\min(\phi)$=$\min(\Phi)$ since $\min(\Phi)$ is minimum on the symmetry plane $z = 0$.

5.3.2 $m = 1$

The centrifugal instability has been also observed for $m = 1$ in stratified non-rotating fluids (chapter 4). This corresponds to the mode (1,1)–(1,3),(1,5) and (1,8) in figure 5.4a for $\alpha = 0.5, F_h = 0.5$, $Ro = \infty$ and $Re = 10000$. In addition, there exists a mode (1,4) in figure 5.4a which exhibits both the characteristics of the centrifugal and the Gent-McWilliams instability. The latter instability bends the vortex (Gent & McWilliams, 1986; Smyth & McWilliams, 1998; Yim & Billant, 2015). Finally, the radial velocity perturbation of mode (1,9) in figure 5.4a is almost identical to the angular velocity of the base flow such that it

5

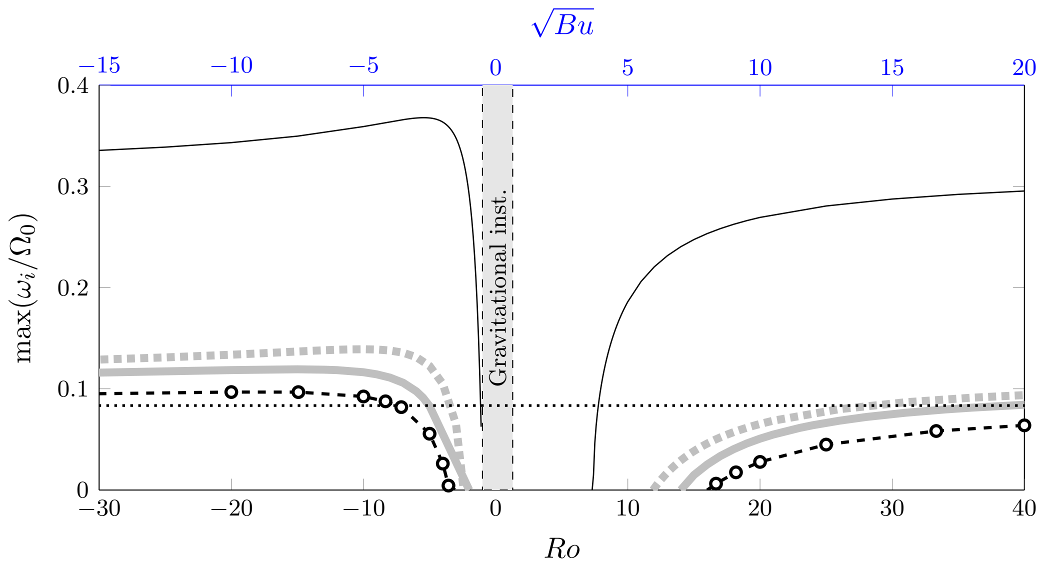

Figure 5.3: Maximum growth rate of the centrifugal instability for $m = 0$ as a function of Ro for a pancake vortex for $\alpha = 0.5$ (-o-) and a columnar vortex (▬) for $F_h = 0.5$ and $Re = 10000$. The dashed grey line (▪▪▪▪) shows the asymptotic maximum growth rate (5.17) and the solid line (——) shows the upper limit for the growth rate of the centrifugal instability for $m = 0$: $\sqrt{-\min(\Phi)}$. The horizontal dotted line (⋯⋯) indicates the maximum growth rate of the pancake vortex for $Ro = \infty$. The vertical shaded region is the region unstable to gravitational instability.

displaces the vortex. This mode, which is almost neutral with zero frequency, corresponds to the displacement mode. The modes (1,6) and (1,7) are mixed modes presenting which exhibit both characteristics of the centrifugal and bending modes. The spectrum of a columnar vortex for the same parameter is also shown in figure 5.4a by a continuous grey line for comparison.

When the Rossby number is decreased to $Ro = 20$ keeping the other parameters fixed (figure 5.4b), the spectrum remains qualitative similar to $Ro = \infty$ with the three main types of modes: centrifugal ((1,1)–(1,4), (1,6)–(1,8)), mixed bending-centrifugal (1,5) and displacement (1,9) modes. The structure of these three categories of modes is displayed in figure 5.5 for $Ro = 20$. Again the series of the centrifugal modes differ by the number of oscillations along the vertical (compare (1,1) to (1,3) in figure 5.5) but they have all a single oscillation along the radial direction. They are localized near the region where Φ is negative and they tend to be aligned along the base isopycnals. The bending and displacement modes, which are represented in figures 5.5c,d, are almost identical to those found for $Ro = \infty$ (chapter 4).

A similar spectrum is observed for $Ro = -10$ (figure 5.4c) except that there is a clear separation between the centrifugal mode and the bending mode. This is similar to the columnar vortex case (grey solid line) where the Gent-McWilliams instability and the centrifugal instability correspond to two distinct growth rate maxima for negative Rossby numbers in contrast to positive Rossby numbers (Yim & Billant, 2015). The structure of the centrifugal modes (figure 5.6a) is similar to those for $Ro = 20$ (figure 5.5a,b). The bending mode (figure 5.6b) is more localized in the vortex core and corresponds more clearly to a bending of the vortex as a whole than for $Ro = 20$ (figure 5.5c) where the mixed bending-centrifugal mode tends to concentrate at the top and bottom of the pancake vortex.

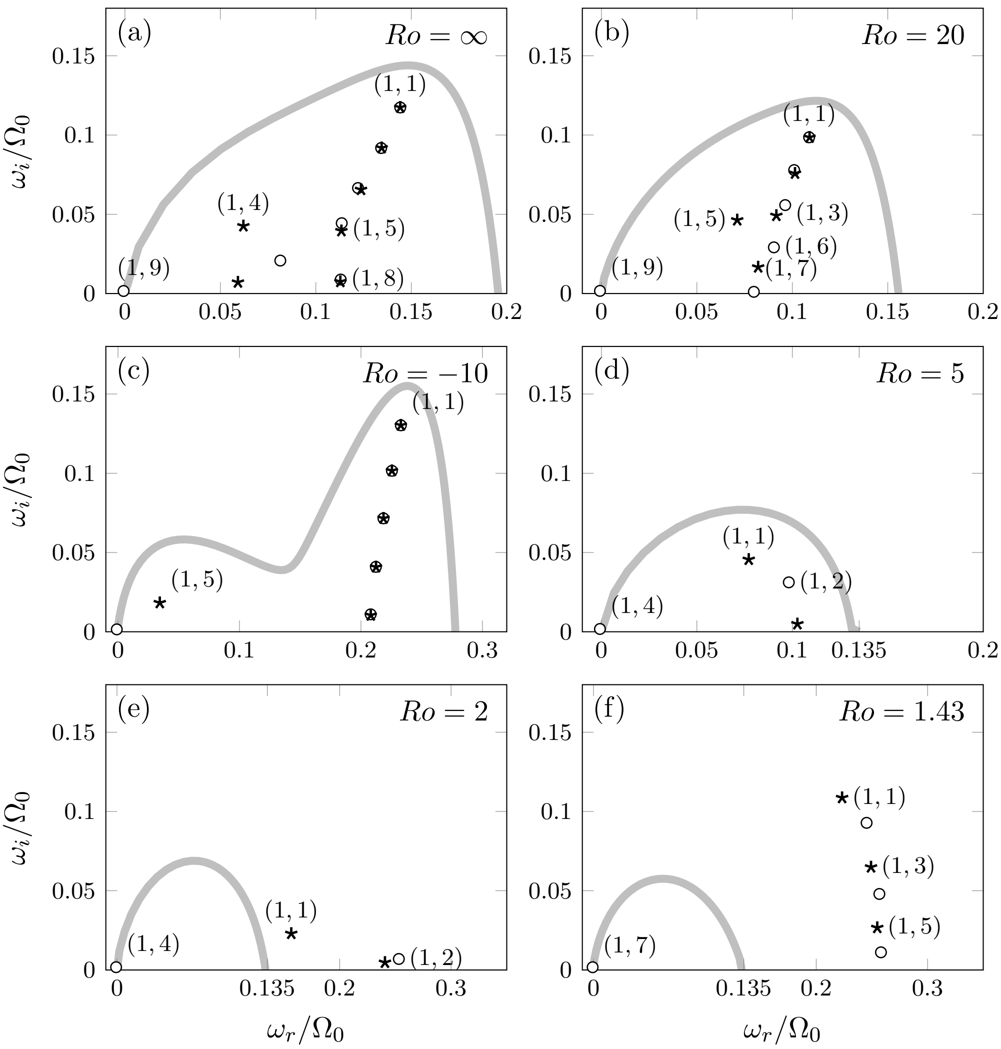

Figure 5.4: Growth rate (ω_i/Ω_0) and frequency (ω_r/Ω_0) spectra for $m = 1$ for different Rossby numbers Ro: (a) $Ro = \infty$, (b) $Ro = 20$, (c) $Ro = -10$ (d) $Ro = 5$, (e) $Ro = 2$ and (f) $Ro = 1.43$ for $F_h = 0.5$ and $Re = 10000$. Discrete symbols (○: for symmetric and ⋆ for anti-symmetric modes) correspond to pancake vortices for $\alpha = 0.5$ and thick continuous lines (▬) are for columnar vortices ($\alpha = \infty$).

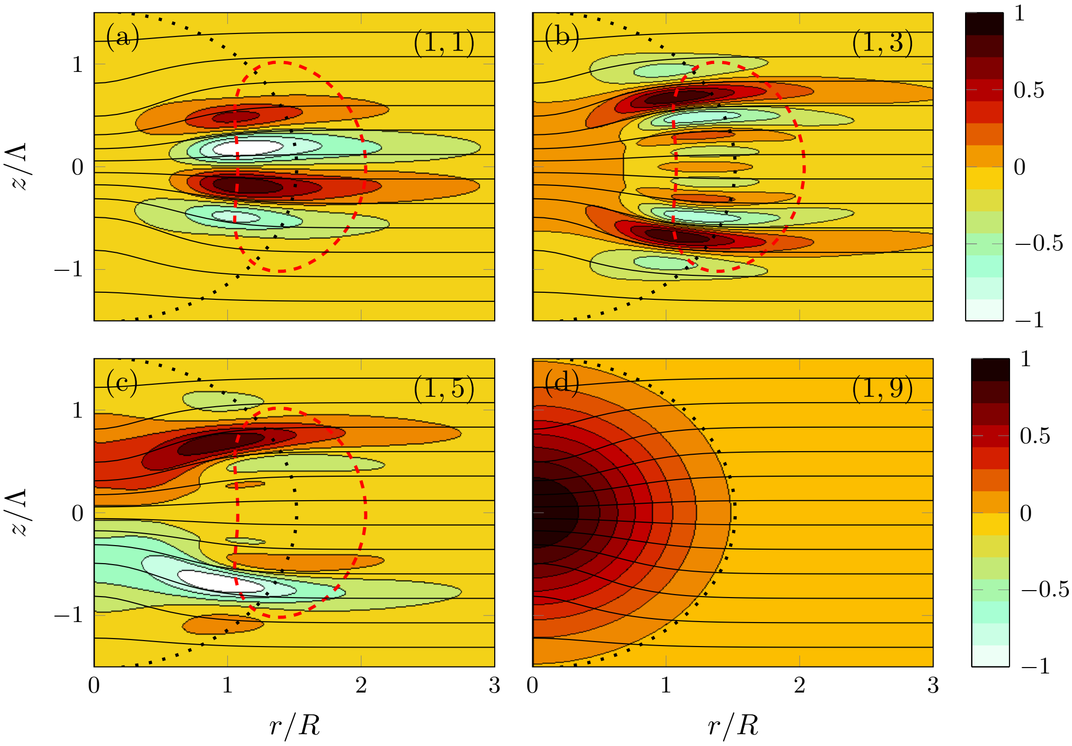

Figure 5.5: (Colour online) Real part of the radial velocity perturbation $\mathrm{Re}(u_r)$ of (a) the centrifugal mode $(1, 1)$ and (b) mode $(1, 3)$, (c) the mixed bending-centrifugal mode $(1, 5)$ and (d) the displacement mode $(1, 9)$ for $Ro = 20$ (figure 5.4b). The horizontal lines are isopycnals. The dotted line indicates the extension of the base flow where $\Omega = 0.1\Omega_0$. The thick dashed line (- - -) indicates the contour where the Rayleigh discriminant Φ vanishes.

5

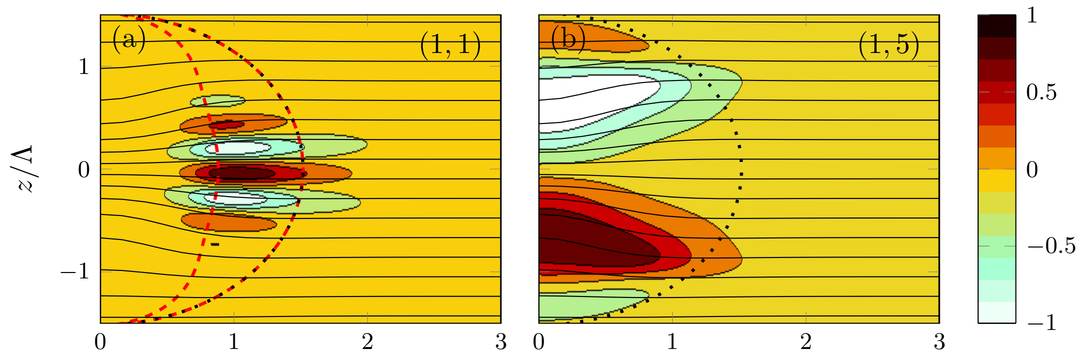

Figure 5.6: (Colour online) Real part of the radial velocity perturbation $\mathrm{Re}(u_r)$ of (a) the centrifugal mode $(1,1)$ and (b) the bending mode $(1,5)$ for $Ro = -10$ (figure 5.4c). The horizontal lines are isopycnals. The dotted line indicates the extension of the base flow where $\Omega = 0.1\Omega_0$. The thick dashed line (- - -) indicates the contour where the Rayleigh discriminant Φ vanishes.

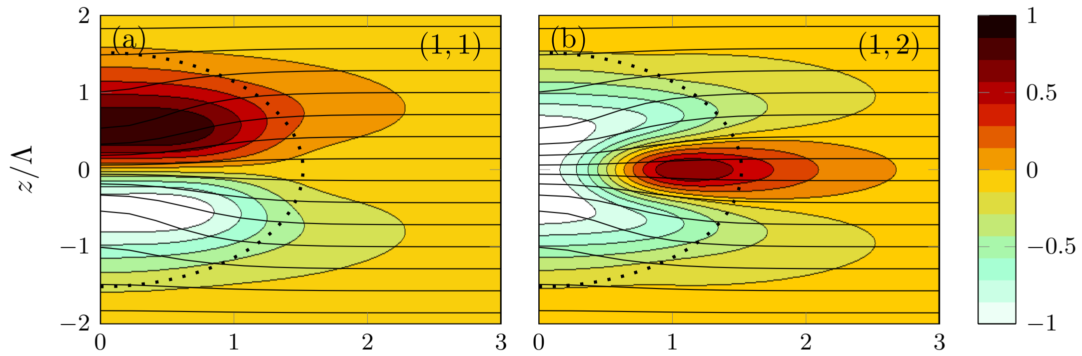

Figure 5.7: (Colour online) Real part of the radial velocity perturbation $\mathrm{Re}(u_r)$ of the Gent-McWilliams instability: (a) mode $(1,1)$ and (b) mode $(1,2)$ for $Ro = 5$ (figure 5.4d). The horizontal lines are isopycnals. The dotted line indicates the extension of the base flow where $\Omega = 0.1\Omega_0$.

When the absolute value of the Rossby number is further decreased, the centrifugal instability disappears when $\Phi > 0$ everywhere and only the Gent-McWilliams instability remains as exemplified in figure 5.4d for $Ro = 5$. In this case, there are three unstable bending modes and the first two are displayed in figure 5.7. The first one (figure 5.7a) is similar to the one previously shown in figure 5.6b for $Ro = -10$ while the second one exhibits one more oscillation along the vertical and is thus symmetric (figure 5.7b). There is still also the displacement mode ((1,4) in figure 5.4d) with a very weak frequency and growth rate since this mode derives from the translational invariance. All these modes are close to the spectrum of a columnar vortex shown by the grey solid line (figure 5.4d). The maximum frequency of the unstable branch of the columnar vortex is $\omega_r = \Omega_0 \mathrm{e}^{-2} = 0.135\Omega_0$. This corresponds to the maximum frequency for which the gradient of the vertical vorticity $\zeta'(r_c)$ is positive at the critical radius r_c where $\Omega(r_c) = \omega_r$. This is the condition of existence of the Gent-McWilliams instability for a columnar vortex (Gent & McWilliams, 1986; Yim & Billant, 2015).

So far, all the unstable modes observed for a pancake vortex derived from those for a columnar vortex. However, when the Rossby number is further decreased to $Ro = 2$ (figure 5.4e) and to $Ro = 1.43$ (figure 5.4f), all the unstable modes for pancake vortices have no

5

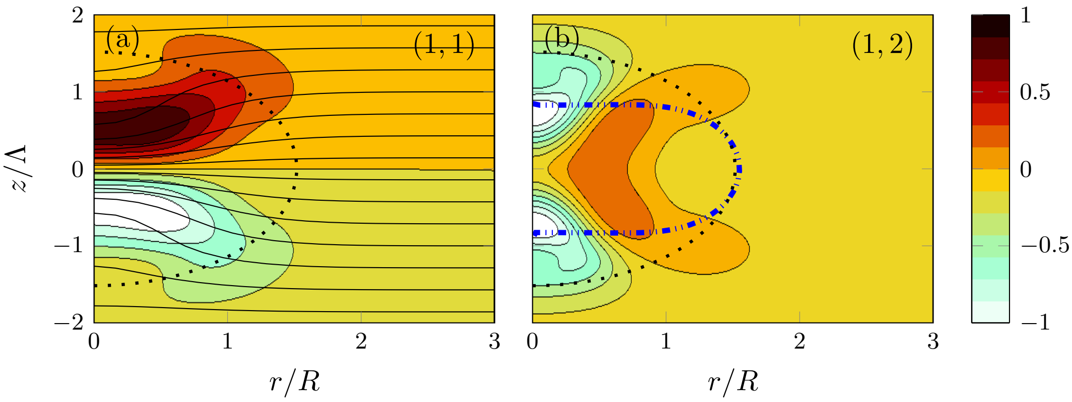

Figure 5.8: (Colour online) Real part of the radial velocity perturbation $\mathrm{Re}(u_r)$ of the mixed baroclinic-Gent-McWilliams instability:(a) mode $(1,1)$ and (b) mode $(1,2)$ for $Ro = 2$ (figure 5.4e). The horizontal lines are isopycnals. The dotted line indicates the extension of the base flow where $\Omega = 0.1\Omega_0$.

counterparts in columnar vortices except the displacement mode near the origin ((1,4) in figure 5.4e and (1,7) in figure 5.4f). For $Ro = 2$, the most unstable mode (1,1) has a frequency larger than 0.135 but is still close to the spectra of the columnar vortex. The structure of the mode (figure 5.8a) is also similar to the Gent-McWilliams mode for $Ro = 5$ (figure 5.7a) but it tends to be distorted near $r = R$. Hence, we shall call this mixed mode as baroclinic-Gent-McWilliams mode. Secondary modes also observed near the frequency $\omega_r \sim 0.25\Omega_0$ (figure 5.4e). Although different, their shape (figure 5.8b) has still a resemblance with the secondary Gent-McWilliams mode for $Ro = 5$ (figure 5.7b). For $Ro = 1.43$, there is now a series of modes aligned near the frequency $\omega_r \sim 0.25\Omega_0$ and with a much larger growth rate than for $Ro = 2$. A selection of these mode are depicted in figure 5.9. The first two modes (1,1) and (1,2) show some similarities with those for $Ro = 2$ (figure 5.8) but they are clearly more concentrated in the vortex core for $r/R_0 \leq 0.5$ and are maximum at a slightly higher vertical level $z/\Lambda = \pm 0.7$. The next modes exhibit more radial oscillations (figure 5.9c,d) but with still two vertical oscillations, i.e. one per half vertical plane. Similar modes have been observed in stratified non-rotating fluids when the isopycnal deformations are sufficiently strong and have been shown to originate from the baroclinic instability. The deformations indeed increase when the Rossby number decreases for given aspect ratio and Froude number. The isopycnals even overturn and are subjected to the gravitational instability when $Ro \leq 1.3$ for $\alpha = 0.5$ and $F_h = 0.5$. In quasi-geostrophic fluids, a necessary condition for the baroclinic instability is the sign change of the potential vorticity gradient along isopycnal (Eliassen, 1983; Hoskins *et al.*, 1985; Ménesguen *et al.*, 2012):

$$\left.\frac{\partial \Pi}{\partial r}\right|_{\rho_t} = \frac{\partial \Pi}{\partial r} - \frac{\partial \Pi}{\partial z}\frac{\frac{\partial \rho_t}{\partial r}}{\frac{\partial \rho_t}{\partial r}} = 0, \tag{5.21}$$

where $\Pi = (\zeta + f)\partial\rho_t/\partial z - r\partial\Omega/\partial z\partial\rho_t/\partial r$ is the potential vorticity and ζ is the vertical vorticity of the base flow. The double dotted dashed line in figure 5.9 shows where $\partial\Pi/\partial r|_{\rho_t} = 0$. As can be seen, the modes develop in the vicinity of this line. The baroclinic instability will be observed in more details in section 5.7.

The effect of the Rossby number on the growth rate and frequency of the most unstable modes of each instability for $m = 1$ is summarized in figure 5.10. As already seen for $m = 0$, the centrifugal instability (dashed line with circles) is stabilized for small Ro in the range

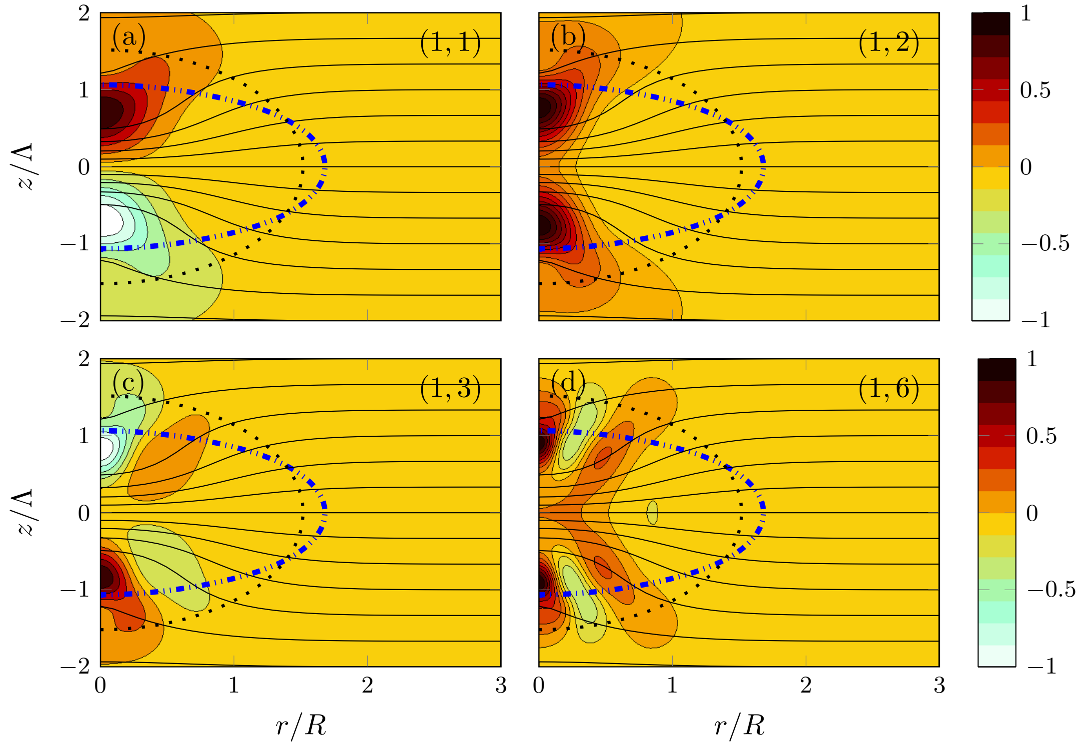

Figure 5.9: (Colour online) Real part of the radial velocity perturbation $\mathrm{Re}(u_r)$ of the baroclinic instability: (a) mode $(1, 1)$, (b) mode $(1, 2)$, (c) mode $(1, 3)$ and (d) mode $(1, 6)$ for $Ro = 1.43$ (figure 5.4f). The horizontal lines are isopycnals. The dotted line indicates the extension of the base flow where $\Omega = 0.1\Omega_0$. The double dotted dashed line (-··-) shows where the isopycnal potential vorticity gradient (5.21) changes sign.

$-2 \lesssim Ro \lesssim 8$. The threshold for positive Rossby number has not been located precisely because of the difficulty in distinguishing the centrifugal and Gent-McWilliams instabilities when their growth rates are comparable. As already mentioned, there is indeed a smooth transition between these two instabilities for positive Rossby number in columnar vortices (Yim & Billant, 2015). The growth rate of the Gent-McWilliams instability (dashed line with triangle) is almost constant for large Rossby number. For negative Rossby number, the Gent-McWilliams instability stabilizes around $Ro \sim -2$ like the centrifugal instability. For positive Rossby number, the Gent-McWilliams instability becomes dominant over the centrifugal instability when $Ro \lesssim 7$. However, its growth rate decreases as the Rossby number decreases and becomes minimum for $Ro = 2$ corresponding to a Burger number $Bu = (\alpha Ro/2F_h)^2 \equiv (N\Lambda/fR)^2$ around unity as indicated in the upper x axis. Below this Rossby number, the frequency (figure 5.10b) increases beyond the cutoff frequency $\omega_r = 0.135\Omega_0$ above which the Gent-McWilliams instability no longer exists in the case of a columnar vortex (Yim & Billant, 2015). Simultaneously, the growth rate re-increases and the instability becomes a mixed baroclinic-Gent-McWilliams instability. For smaller Rossby number, the instability becomes the pure baroclinc instability (dashed line with diamond) with a growth rate increasing dramatically as Ro decreases. However, the frequency saturates at $\omega_r \simeq 0.25\Omega_0$. The growth rate of the displacement mode (dashed line with square) remains very low for any Rossby number.

Similar results have been obtained by Nguyen *et al.* (2012) in quasi-geostrophic fluids except that the centrifugal instability is absent since $Ro \ll 1$. Thus, they have reported only two modes that they distinguish by their symmetry: a symmetric and an anti-symmetric modes. When the Burger number $Bu = \alpha^2 Ro^2/(4F_h^2)$ is larger than unity, the symmetric mode corresponds to the displacement mode herein and the anti-symmetric mode is similar to the Gent-McWilliams most unstable mode. In contrast, when $Bu < 1$, the symmetric and anti-symmetric modes correspond to the leading baroclinic modes herein. The growth rate of the anti-symmetric mode is minimum for $Bu = 1$ like in figure 5.10 when the transition between Gent-McWilliams and baroclinic instabilities occurs.

Finally, figure 5.11 compares the maximum growth rate and corresponding frequency of the centrifugal instability for pancake (dashed line with circle) and columnar (grey continuous line) vortices. As can be seen, they are close. The maximum growth rate and associated frequency predicted by (5.17) is also represented by a dashed line. It underestimates the observed growth rate of both pancake and columnar vortices, especially for positive Rossby number. This discrepancy probably comes from the smooth transition between Gent-McWilliams and centrifugal instabilities and the difficulty in distinguishing clearly these two instabilities when their growth rates are comparable.

In summary, for $m = 1$, the baroclinic instability dominates when Ro is small and the centrifugal instability takes the place when Ro is large. In between, there exists the Gent-McWilliams instability for positive Ro. For negative Ro, centrifugal instability is always dominant. Although, only one particular set of parameters ($\alpha = 0.5, F_h = 0.5$ and $Re = 10000$) has been presented, we shall see in the next section that this picture is typical of other parameter combinations in the strongly stratified regime with moderate and strong rotation.

5.3.3 $m = 2$

Finally, we present the effect of the Rossby number on the stability of the azimuthal wavenumber $m = 2$ for the set of parameters: $\alpha = 1.2, F_h = 0.5$ and $Re = 10000$. Note that the aspect ratio is also changed to show a typical example of spectrum. In the strongly strat-

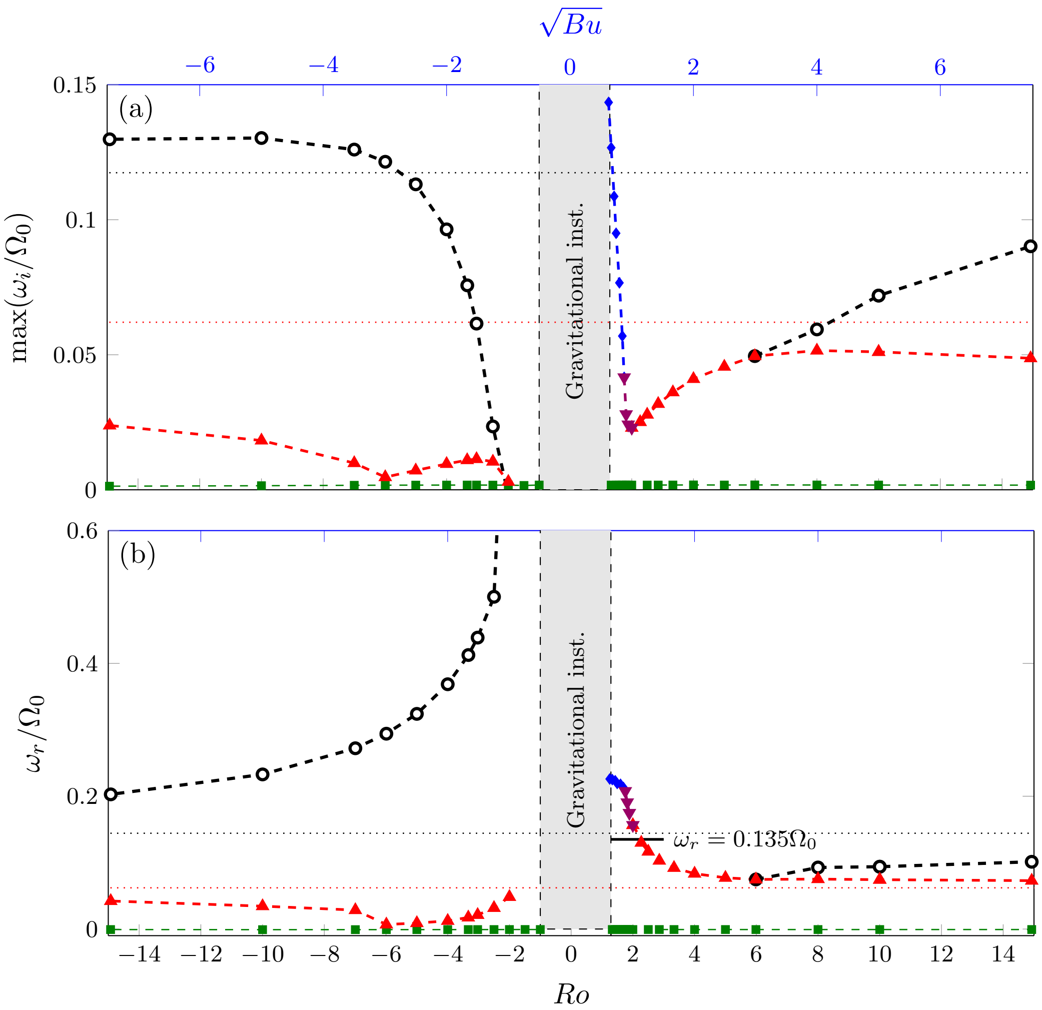

Figure 5.10: (a) Maximum growth rates and (b) corresponding frequencies of the different types of instabilities as a function of Ro for $m = 1$, $\alpha = 0.5, F_h = 0.5$ and $Re = 10000$: centrifugal instability -○-, symmetric displacement mode -■-, Gent-McWilliams instability -▲-, mixed baroclinic Gent-McWilliams instability -▼- and baroclinic instability -◆-. The upper x axis indicates the corresponding value of the square root of the Burger number $\sqrt{Bu}$. The horizontal dotted lines (⋯⋯) indicate the growth rates and frequencies for $Ro = \infty$ for the centrifugal and Gent-McWilliams instabilities. The shaded region is gravitationally unstable.

5

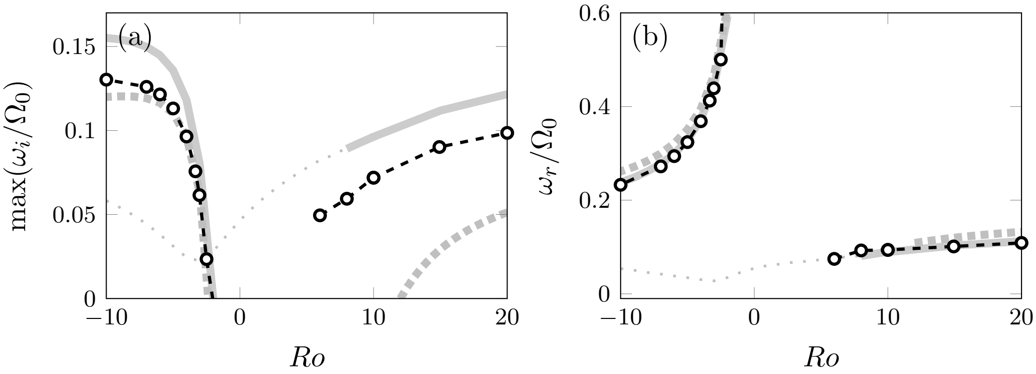

Figure 5.11: (a) Maximum growth rate and (b) corresponding frequency of the centrifugal instability ( ) for columnar (thick continuous lines) and pancake ($\alpha = 0.5$) ( ) vortices for $m = 1, F_h = 0.5$ and $Re = 10000$. The dashed grey line shows the asymptotic maximum growth rate (5.17). The dotted line indicates the Gent-McWilliams instability.

ified non-rotating case, two instabilities have been found: the centrifugal instability for sufficiently large buoyancy Reynolds number ReF_h^2 and the shear instability when $F_h/\alpha \leq 0.5$ (chapter 4). These corresponds to the modes (2,1)–(2,2) and (2,3), respectively in figure 5.12a. When the Rossby number is decreased, a scenario similar to the one described for $m = 1$ occurs. The centrifugal instability becomes less dominant for moderate Rossby number (see figure 5.12b for $Ro = 20$) and disappears for small Rossby number (see figure 5.12c for $Ro = 0.8$). An example of the structure of a centrifugal mode for $Ro = 20$ is depicted in figure 5.13b. In contrast, the baroclinic instability appears for small Rossby number (modes (2,1)–(2,4) in figure 5.12d for $Ro = 0.25$). As for $m = 1$, these baroclinic modes differ by the number of oscillations in the radial direction and by their symmetry with respect to the mid-plane $z = 0$ (figure 5.15a,b,c).

For all the Rossby numbers presented in figure 5.12, shear instability remains present around the same frequency in the vicinity of the shear instability branch of the columnar vortex (grey continuous line near $\omega_r/\Omega_0 = 0.26$). However, its growth rate for the pancake vortex varies with Ro while the maximum growth rate for the columnar vortex is independent of the Rossby number since the dominant mode is two-dimensional. Accordingly, the shape of the shear instability mode varies somewhat with the Rossby number (see figure 5.13a for $Ro = 20$, figure 5.14 for $Ro = 0.8$ and for figure 5.15d for $Ro = 0.25$). The mode for $Ro = 20$ is almost identical to the one found for $Ro = \infty$ (chapter 4). The mode for $Ro = 0.25$ (figure 5.15d) is similar but extends vertically around $r/R = r_I/R = 1.4$ where r_I is the inflection point where $\zeta'(r_I) = 0$. The same mode has been found by Nguyen *et al.* (2012) in quasi-geostrophic fluids. They argued that this mode originates from a baroclinic instability induced by the critical layer where $\omega_r = m\Omega$. As can be seen in figure 5.15d, the mode tends indeed to be distorted along the critical layer which is shown as a thin solid line. However, figure 5.12 shows that this mode derives continuously from the shear instability. For this reason, we will call here this instability: mixed baroclinic-shear instability.

Figure 5.16 outlines the effect of the Rossby number on the maximum growth rate and associated frequency of each instability. The centrifugal instability (dashed line with circle) is stabilized for $-3 \leq Ro \leq 17$ and is stronger for negative Rossby number than for positive ones as already observed for $m = 0$ and $m = 1$. Strikingly, the opposite behaviour is observed for the shear instability (dashed line with filled circle): it tends to be enhanced for moderate positive Rossby numbers and attenuated for finite negative Rossby numbers.

5

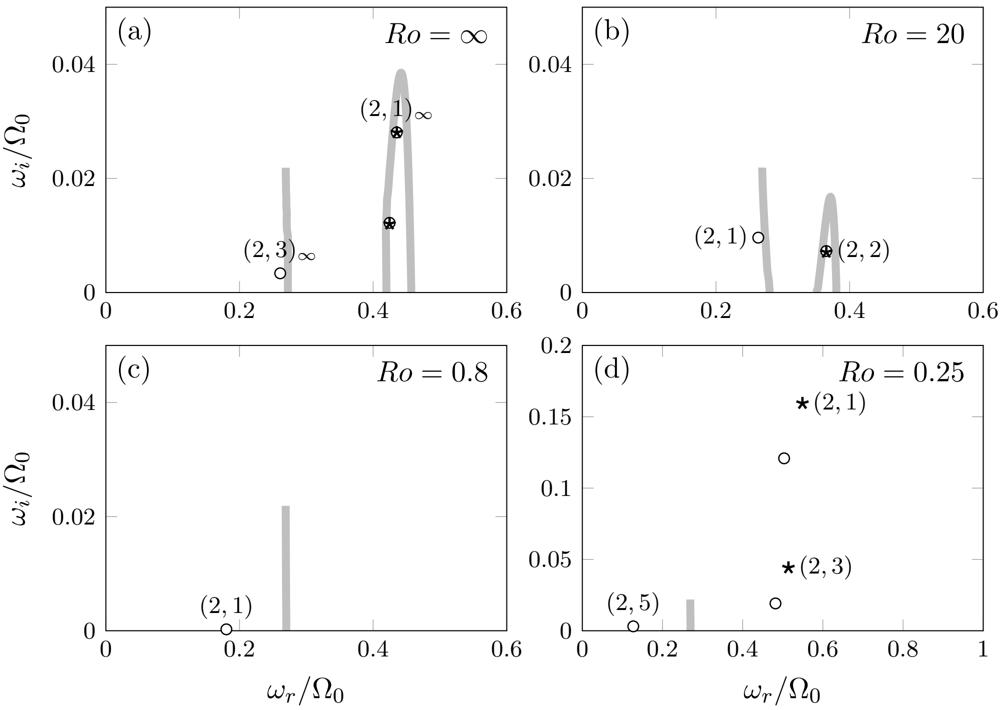

Figure 5.12: Growth rate (ω_i/Ω_0) and frequency (ω_r/Ω_0) spectra for $m = 2$ for different Rossby numbers Ro: (a) $Ro = \infty$, (b) $Ro = 20$, (c) $Ro = 0.8$ and (d) $Ro = 0.25$ for $F_h = 0.5$ and $Re = 10000$. Discrete symbols (○: for symmetric and ⋆ for anti-symmetric modes) are for pancake vortices for $\alpha = 1.2$ and thick continuous lines (▬) are for columnar vortices ($\alpha = \infty$).

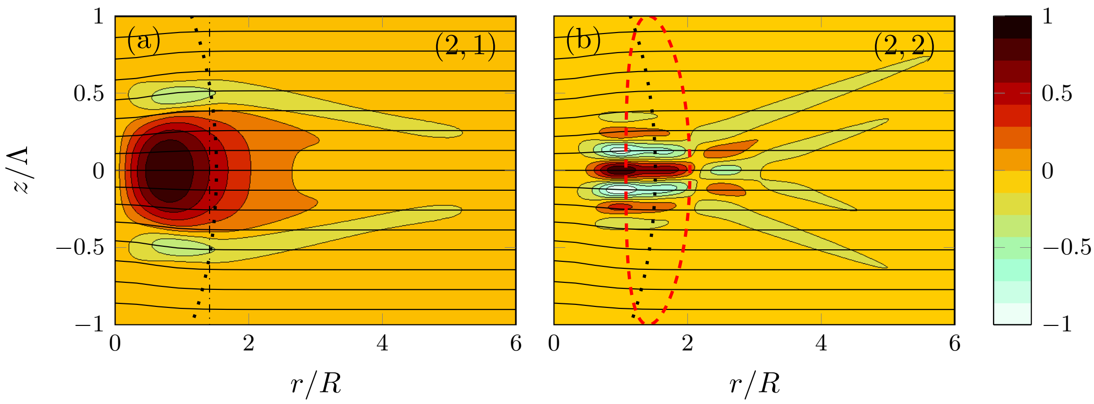

Figure 5.13: (Colour online) Real part of the radial velocity perturbation $\mathrm{Re}(u_r)$ of (a) the shear mode $(2,1)$ and (b) the centrifugal mode $(2,2)$ for $Ro = 20$ (figure 5.12b). The horizontal lines are isopycnals. The dotted line indicates the extension of the base flow where $\Omega = 0.1\Omega_0$. The thin dash dotted line in (a) shows the inflection radius r_I where $\zeta'(r_I) = 0$. The thick dashed line (- - -) in (b) indicates the contour where the Rayleigh discriminant Φ vanishes.

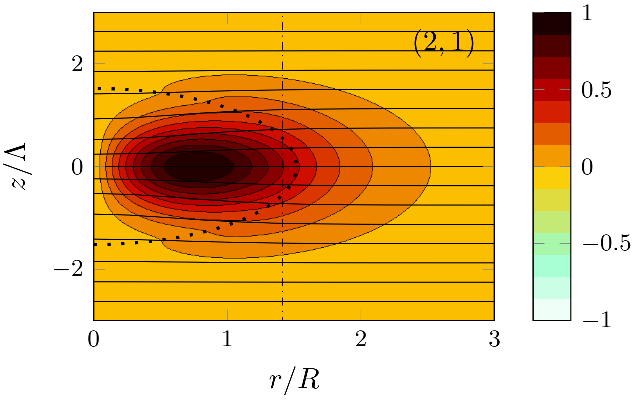

Figure 5.14: (Colour online) Real part of the radial velocity perturbation $\mathrm{Re}(u_r)$ of the mixed baroclinic-shear mode $(2, 1)$ for $Ro = 0.8$ (figure 5.12c). The horizontal lines are isopycnals. The dotted line indicates the extension of the base flow where $\Omega = 0.1\Omega_0$. The thin dash dotted line shows the inflection radius r_I where $\zeta'(r_I) = 0$.

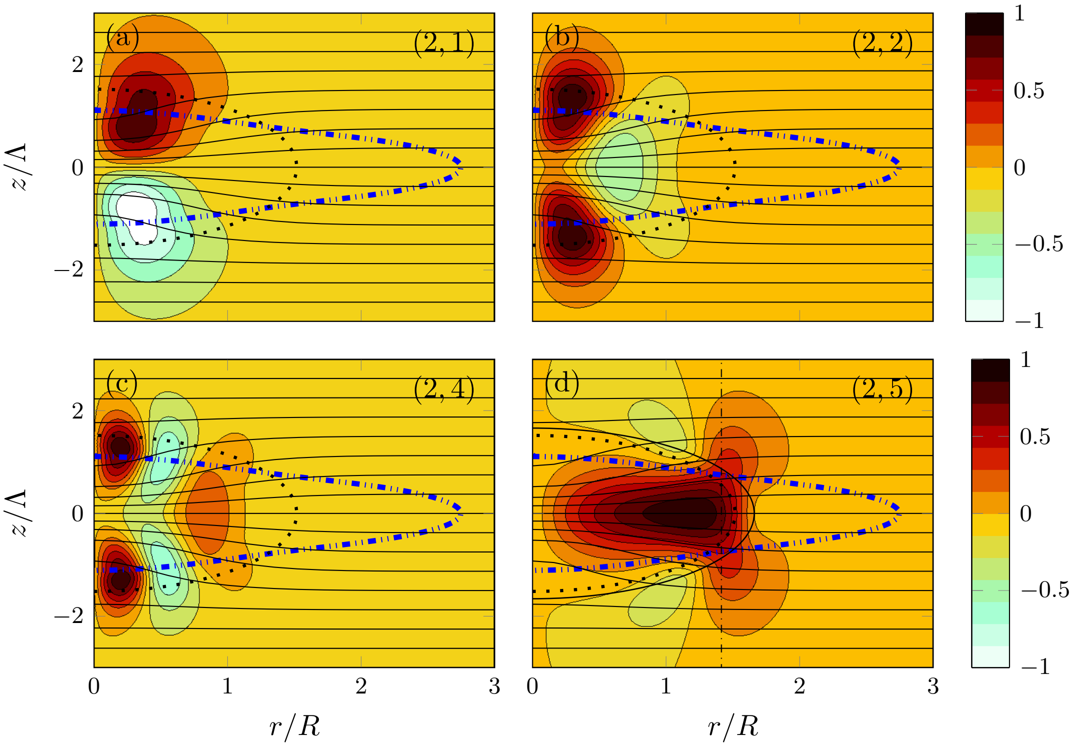

Figure 5.15: (Colour online) Real part of the radial velocity perturbation $\mathrm{Re}(u_r)$ of the baroclinic instability: (a) mode $(2, 1)$, (b) mode $(2, 2)$ and (c) mode $(2, 4)$, and (d) the mixed baroclinic-shear mode $(2, 5)$ for $Ro = 0.25$ (figure 5.12d). The horizontal lines are isopycnals. The dotted line indicates the extension of the base flow where $\Omega = 0.1\Omega_0$. The double dotted dashed line (-··-) shows where the isopycnal potential vorticity gradient (5.21) changes sign. The thin solid and dash dotted lines in (d) show the critical layer where $\omega_r = m\Omega(r, z)$ and inflection radius r_I where $\zeta'(r_I) = 0$, respectively.

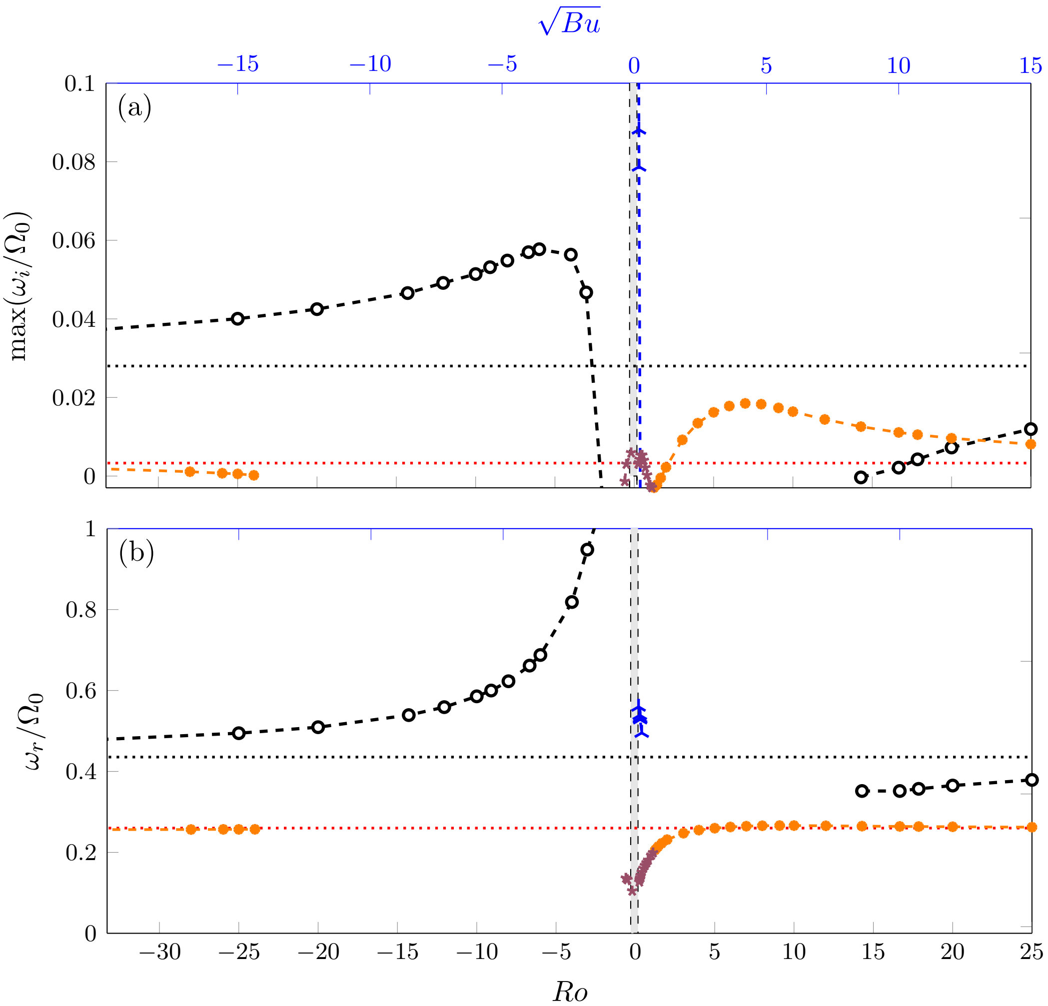

Figure 5.16: (a) Maximum growth rates and (b) corresponding frequencies of the different types of instabilities as a function of Ro for $m = 2, \alpha = 1.2, F_h = 0.5$ and $Re = 10000$: centrifugal instability -o-, shear instability -•-, baroclinic-shear instability -*- and baroclinic instability -⅄-. The upper x axis indicates the corresponding value of the square root of the Burger number $\sqrt{Bu}$. The horizontal dotted lines (······) indicate the growth rates and frequencies for $Ro = \infty$ of the centrifugal and shear instabilities. The shaded region is gravitationally unstable.

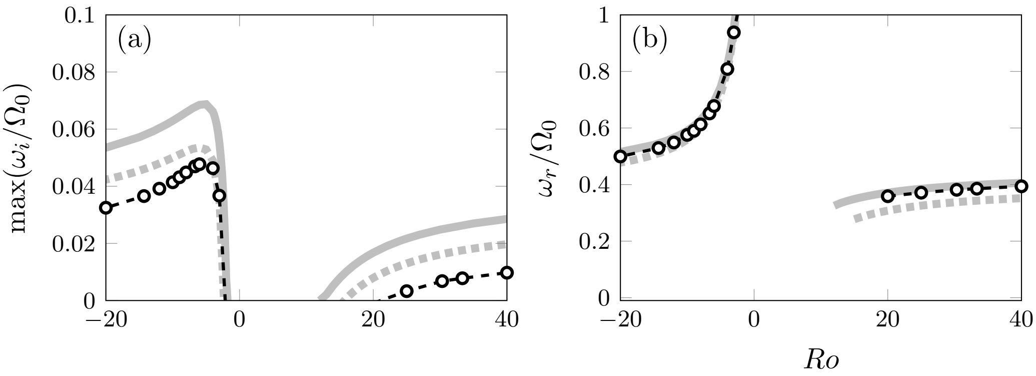

Figure 5.17: (a) Maximum growth rates and (b) corresponding frequencies of the centrifugal instability for columnar (thick continuous lines,) and pancake ($\alpha = 1.2$) (symboled lines,) vortices for $m = 2, F_h = 0.5$ and $Re = 10000$. The dashed grey line () shows the asymptotic maximum growth rate (5.17).

However, the growth rate of the shear instability decreases to zero as Ro decreases from $Ro = 7$ to $Ro = 1$. Below $Ro = 1$ (which corresponds to $Bu = 1$ as indicated in the upper x axis), it starts to re-increase but the instability is then of the mixed type: baroclinic-shear instability. Such growth rate minimum for $Bu \simeq 1$ is consistent with the results of Nguyen *et al.* (2012). This mixed instability exists down to $Ro = -0.6$ while the classical shear instability reappears for $Ro = -23$. The baroclinic instability co-exists for small Rossby numbers in the range $0 \le Ro \le 0.4$. Its growth rate becomes very high as soon as the Rossby number threshold is crossed but its frequency remains almost constant $\omega_r = 0.5\Omega_0$ figure 5.16b.

In figure 5.17, the maximum growth rate and associated frequency of the centrifugal instability for $m = 2$ for a pancake vortex is further compared to the one for a columnar vortex. As already seen for $m = 0$ and $m = 1$, they are close. The asymptotic formula (5.17) predicts quite well their characteristics.

5.4 Effect of the other parameters for a fixed Rossby number around unity

In this section, we now fix the Rossby number to $Ro = 1.25$ and vary the other control parameters: Reynolds number, Re, aspect ratio, α and Froude number, F_h. For this value of the Rossby number, the centrifugal instability is not active but all the other instabilities seen in section 5.3 may occur for some parameter combinations. Only the most unstable mode for each type of instability will be studied and the two azimuthal wavenumbers $m = 1$ and $m = 2$ will be presented together ($m = 0$ is stable for $Ro = 1.25$).

5.4.1 Effect of the Reynolds number

Figure 5.18 shows the effect of the Reynolds number on the maximum growth rate and associated frequency for $\alpha = 0.5, F_h = 0.3$ and $Ro = 1.25$. The growth rates of the Gent-McWilliams instability (dashed line with triangle) and shear instability (dashed line with filled circle) asymptote to a constant value for large Re and decreases to zero for $Re \simeq 1000$ and $Re \simeq 2000$, respectively. Surprisingly, the growth rate of the displacement mode (dashed line with square) first increases when the Reynolds number decreases. Thereby, it is most unstable for a finite Reynolds number $Re = 500$. The instability of the displacement mode

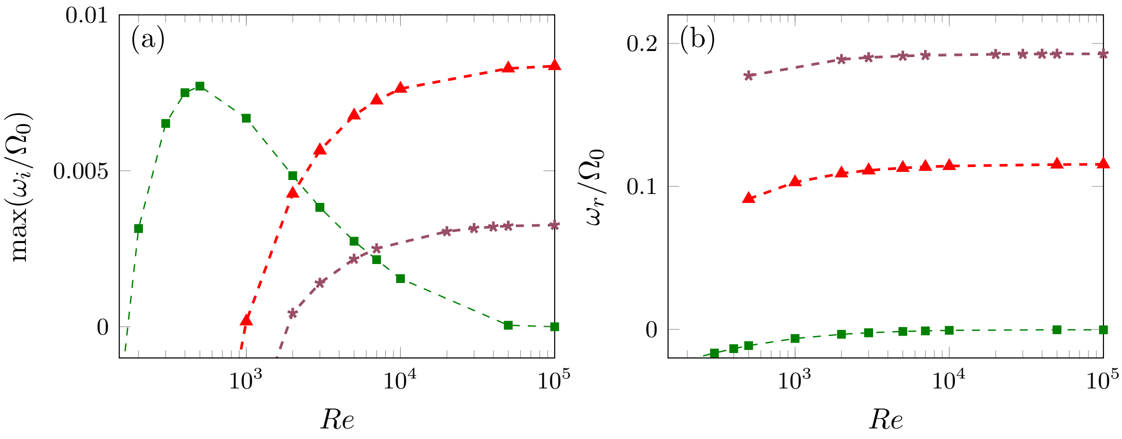

Figure 5.18: (a) Maximum growth rates and (b) corresponding frequencies of the Gent-McWilliams instability (-▲-), displacement mode (-■-) for $m = 1$ and baroclinic-shear instability (-*-) for $m = 2$ as a function of the Reynolds number *Re* for $\alpha = 0.5$, $F_h = 0.3$, and $Ro = 1.25$.

is therefore of viscous origin. A similar viscous instability of the displacement mode of a columnar vortex exists in stratified-rotating fluids (Billant, 2010). In summary, for the given parameters $\alpha = 0.5, F_h = 0.5$ and $Ro = 1.25$, the $m = 1$ displacement instability is dominant for $Re < 2000$ while the $m = 1$ Gent-McWilliams instability is dominant for higher *Re*.

5.4.2 Effect of the Froude number

The Froude number is now varied for $Re = 10000$ still for $\alpha = 0.5$ and $Ro = 1.25$ (figure 5.19). The displacement mode (dashed line with squares) keeps a very low growth rate and frequency independently of the Froude number. In contrast, the growth rate of the Gent-McWilliams instability (dashed line with triangle) fluctuates with F_h: it exhibits two successive maxima as the Froude number increases before increasing widely when it transforms into the mixed baroclinic-Gent-McWilliams instability. The structure of the mode for some selected Froude numbers is displayed in figure 5.20. For $F_h = 0.05$, the mode exhibits five oscillations along the vertical and is symmetric while for $F_h = 0.2$, it has only two oscillations occupying the whole pancake vortex and is anti-symmetric as seen before (see figure 5.7a). This change of structure explains why there is a slight frequency jump in figure 5.19b (dashed line with triangles) and two growth rate maxima (figure 5.19a). For $F_h = 0.4$ (figure 5.20c), the mode is of mixed type: baroclinic-Gent-McWilliams with a frequency above the cutoff $\omega_r = 0.135\Omega_0$ of the Gent-McWilliams instability and below the frequency $\omega_r = 0.25\Omega_0$ of the baroclinic instability (figure 5.19b).

The shear instability for $m = 2$ (dashed line with filled circles in figure 5.19) is most unstable for $F_h \simeq 0$ and stabilizes for $F_h \simeq 0.1$. However, it becomes again unstable for $F_h \geq 0.3$ but under the mixed form of the shear-baroclinic instability (dashed line with stars). When $F_h \geq 0.4$, the baroclinic instability for $m = 2$ (dashed line with crosses) becomes quickly strongly unstable as F_h increases but with a constant frequency $\omega_r \simeq 0.5\Omega_0$. Three examples of mode corresponding to these three types of instability for $m = 2$ are shown in figure 5.21. For small F_h, the shear mode (figure 5.21a) is strongly localized near $z = 0$ where the radial shear is maximum. In contrast, the shear-baroclinic mode (figure 5.21b,c) occupies the whole pancake vortex as already seen in section 5.3.3.

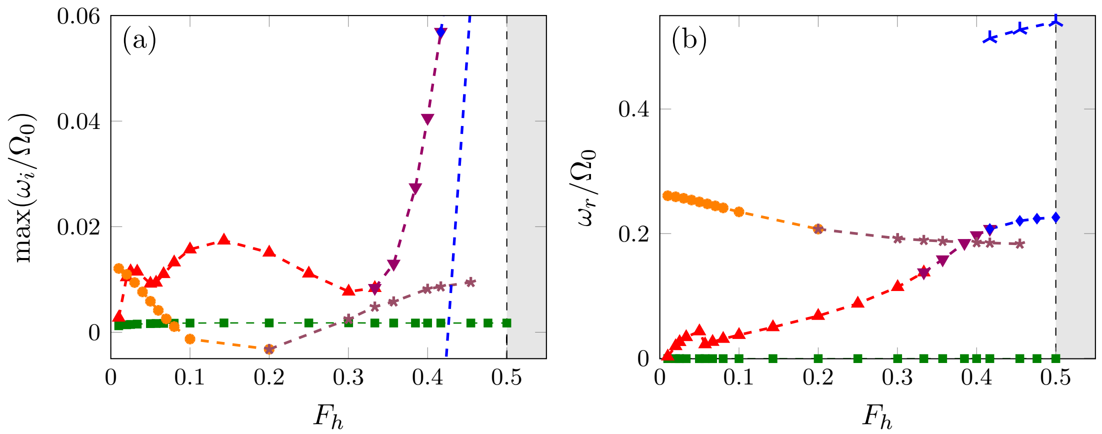

Figure 5.19: (a) Maximum growth rates and (b) corresponding frequencies as a function of the Froude number F_h for $\alpha = 0.5$, $m = 1$ and 2, $Ro = 1.25$ and $Re = 10000$ for different instabilities: displacement mode (-■-); Gent-McWilliams instability (-▲-); baroclinic-Gent-McWilliams instability (-▼-); baroclinic instability (-◆-) for $m = 1$; shear instability (-●-); baroclinic-shear instability (-★-) and baroclinic instability for $m = 2$ (-⅄-). The shaded area indicates the gravitationally unstable region.

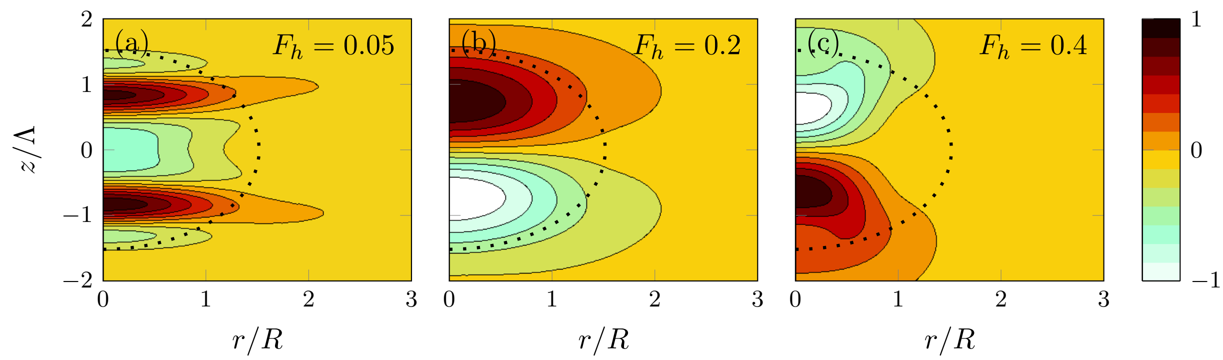

Figure 5.20: Real part of the radial velocity perturbation $\mathrm{Re}(u_r)$ of the most unstable mode for different Froude numbers: the Gent-McWilliams insatiability (a) $F_h = 0.05$ and (b) $F_h = 0.2$, and (c) the mixed baroclinic-Gent-McWilliams instability $F_h = 0.4$ for $m = 1, \alpha = 0.5, Ro = 1.25$, and $Re = 10000$. The dotted line indicates the extension of the base flow where $\Omega = 0.1\Omega_0$.

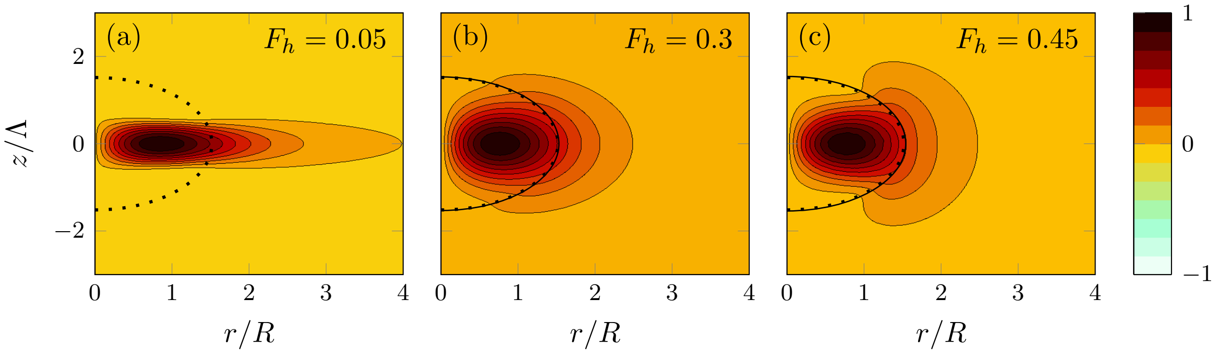

Figure 5.21: Real part of the radial velocity perturbation $\mathrm{Re}(u_r)$ of the most unstable modes for different Froude numbers: the shear instability (a) $F_h = 0.05$ and the mixed baroclinic-shear instability (b) $F_h = 0.3$ and (c) $F_h = 0.45$ for $m = 2, \alpha = 0.5, Ro = 1.25$ and $Re = 10000$. The dotted line indicates the extension of the base flow where $\Omega = 0.1\Omega_0$. The solid lines (—) are the critical layer (r_c, z_c) where $m\Omega(r_c, z_c) = \omega_r$.

5.4.3 Effect of the aspect ratio

We now vary the aspect ratio keeping the other parameters to the same values as before: $F_h = 0.3, Ro = 1.25$ and $Re = 10000$ (figure 5.22). For $m = 1$, the displacement mode (dotted line with squares) remains only marginally unstable while the growth rate of the Gent-McWilliams instability (dashed line with triangles) is large but varies non-monotonically with the aspect ratio. It exhibits two maxima, for $\alpha \simeq 1$ and for large α. For very small α, the growth rate rises again but the instability is then under the form of the mixed baroclinic-Gent-McWilliams instability. The full spectra for three aspect ratios are displayed in figure 5.23 along with the spectra for $\alpha = \infty$, i.e. for a columnar vortex (solid line). For small aspect ratio (figure 5.23a), there exist only two unstable modes: the displacement mode near the origin and the baroclinic-Gent-McWilliams instability near $\omega = 0.2\Omega_0$ whose eigenmode is shown in figure 5.24a. This markedly differs from the columnar case (solid line). In contrast, for larger aspect ratios ($\alpha = 3$, figure 5.23b), many modes appear within the frequency range of the columnar vortex. They are however less unstable than for $\alpha = 0.38$. At even larger aspect ratio $\alpha = 10$ (figure 5.23c), the spectrum becomes denser with a bell shape resembling the spectra of the columnar vortex. However, the maximum growth rate for the columnar vortex is still higher. The most unstable eigenmode for $\alpha = 10$ (figure 5.24c) presents a vertical wavelength $\lambda \simeq 5.23R$ close to the most amplified wavelength of the columnar vortex $\lambda \simeq 4.5R$. A longer typical wavelength $\lambda \simeq 6.16R$ is observed for $\alpha = 3$ (figure 5.24b).

As seen in figure 5.22a, the shear instability (dashed line with filled circles) is only unstable for large aspect ratio $\alpha \geq 2$. However, for small α, it reappears in the form of the mixed baroclinic-shear instability (dashed line with stars). The pure baroclinic instability for $m = 2$ (dashed line with cross) also arises for very small aspect ratio.

5.4.4 Scaling in terms of the vertical Froude number

The two previous sections have revealed different growth rate variations as a function of the Froude number and aspect ratio. However, figure 5.25 shows that the growth rate variations are actually almost identical when represented as a function of the vertical Froude number F_h/α. The transition from Gent-McWilliams instability to baroclinic-Gent-McWilliams

5

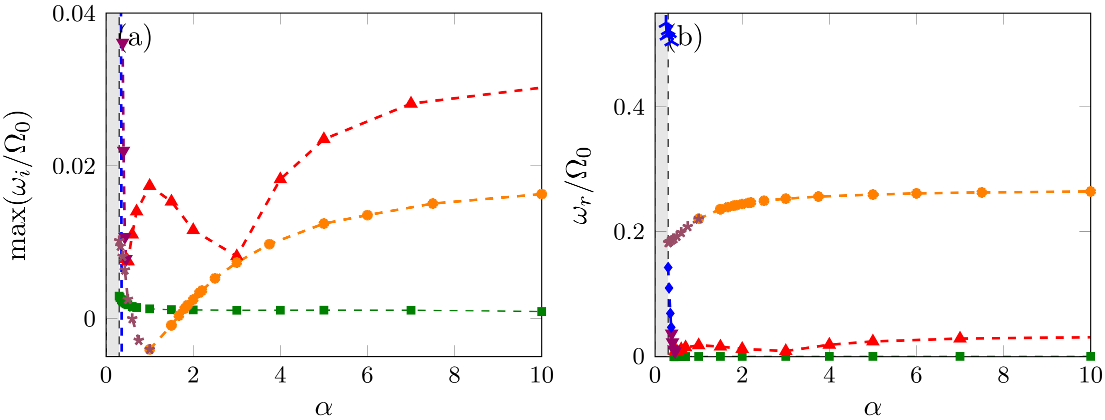

Figure 5.22: (a) Maximum growth rates and (b) corresponding frequencies as a function of aspect ratio α for $F_h = 0.3$, $m = 1$ and 2, $Ro = 1.25$ and $Re = 10000$ for different instabilities: displacement mode (- ■ -); Gent-McWilliams instability (- ▲ -); baroclinic-Gent-McWilliams instability (- ▼ -); baroclinic instability (- ♦ -) for $m = 1$; shear instability (- ● -); baroclinic-shear instability (- ★ -) and baroclinic instability for $m = 2$ (- ⅄ -). The shaded area indicates the gravitationally unstable region.

5

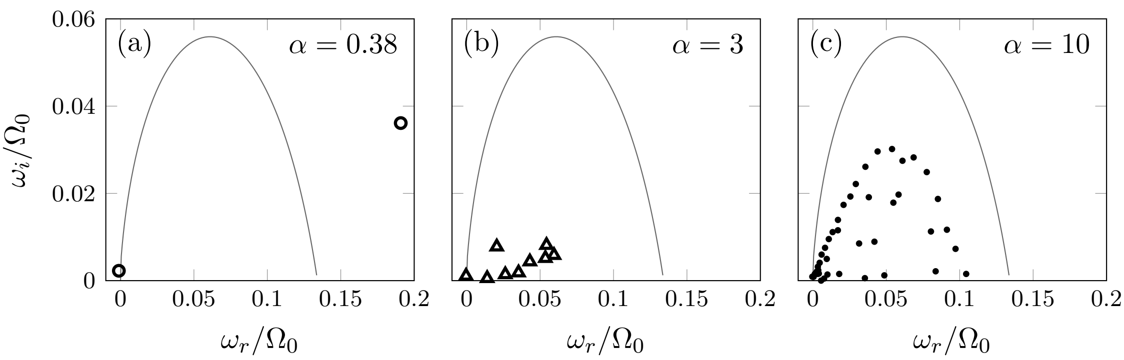

Figure 5.23: Growth rate (ω_i/Ω_0) and frequency (ω_r/Ω_0) spectra for $m = 1$ for different aspect ratios: (a) $\alpha = 0.38$, (b) $\alpha = 3$ and (c) $\alpha = 10$ for $F_h = 0.3, Ro = 1.25,$ and $Re = 10000$. The solid line (——) indicates the spectrum for the columnar vortex for the same F_h, Ro and Re.

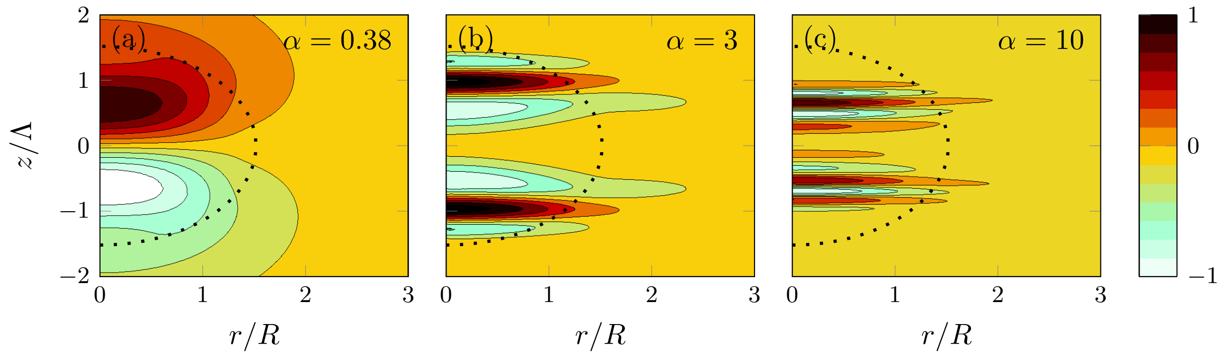

Figure 5.24: Real part of the radial velocity perturbation $\mathrm{Re}(u_r)$ of the most unstable mode for different aspect ratios: the mixed baroclinic-Gent-McWilliams instability (a) $\alpha = 0.38$ and the Gent-McWilliams instability (b) $\alpha = 3$ and (c) $\alpha = 10$ for $F_h = 0.3, Ro = 1.25$ and $Re = 10000$. The dotted line indicates the extension of the base flow where $\Omega = 0.1\Omega_0$.

instability occurs near $Bu \simeq 1$ (see the upper x axis) as found in quasi-geostrophic fluid (Nguyen *et al.*, 2012). The only deviation from this self-similarity is for small F_h/α: when $F_h/\alpha < 0.1$, the growth rate of the Gent-McWilliams instability grows with decreasing F_h/α when α is varied and F_h kept constant whereas it decreases when α is fixed and F_h is varied. This difference comes partly from viscous effects due to vertical shear since they scale like $1/ReF_h^2$ because the typical vertical scale L_v scales like $L_v \sim F_h R$. Thus, they increase when the Froude number decreases keeping the Reynolds number constant. A small discrepancy is also observed for $m = 2$ when F_h/α is small.

5.4.5 Energy budget

The previous section has evidenced a transform of both the shear and Gent-McWilliams instabilities into mixed baroclinic instabilities when the vertical Froude number is above a threshold. This transformation is apparent from the frequency and the structure of the modes. In order to confirm these transformations from the point of view of the energetics, we have computed the energy budget of the modes (Ménesguen *et al.*, 2012). To do so, the linearized equations (5.8) – (5.11) have been multiplied by the complex conjugate $(u_r^*, u_\theta^*, u_z^*, \rho^*)$, respectively and their real part have been integrated over the flow domain. This gives the energy balances:

$$\omega_i E_k - S_k = -B - D_k, \tag{5.22}$$

$$\omega_i E_p - S_p = B - D_p, \tag{5.23}$$

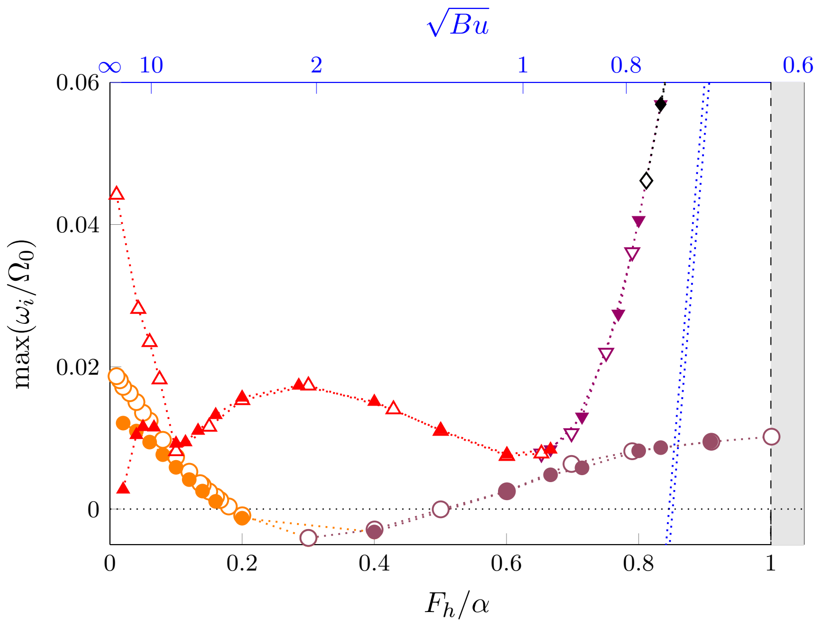

Figure 5.25: Maximum growth rates as a function of vertical Froude number F_h/α for $m = 1$ and 2, $Ro = 1.25$ and $Re = 10000$. The upper x axis indicates the corresponding value of $\sqrt{Bu}$. The filled symbols indicate when F_h is varied for $\alpha = 0.5$ and open symbols when α is varied for $F_h = 0.3$. Different symbols are used for each instability: Gent-McWilliams (··△··), baroclinic-Gent-McWilliams (··▽··), baroclinic (··◇··) instabilities for $m = 1$, and shear (··○··), baroclinic-shear (··○··) and baroclinic (··◇··) instabilities for $m = 2$.

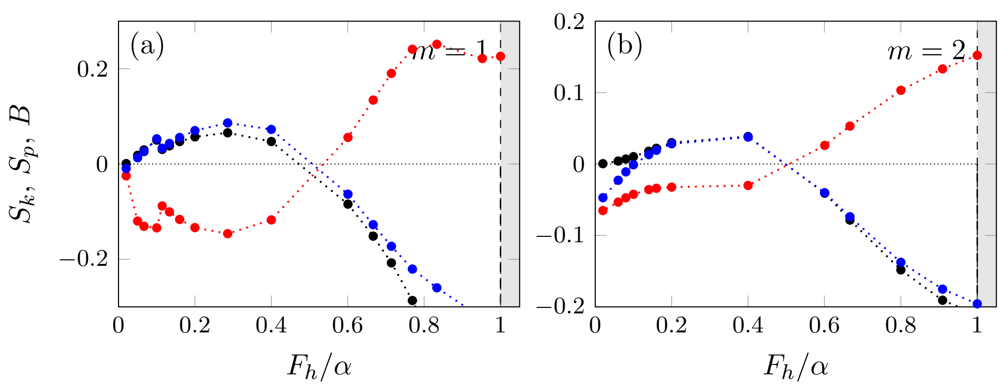

Figure 5.26: Kinetic and potential energy transfer S_k (··•··) and S_p (··•··) and energy conversion B (··•··) of the energy balances (5.22) and (5.23) (a) for $m = 1$ and (b) $m = 2$ for $\alpha = 0.5$, $Ro = 1.25$ and $Re = 10000$.

where

$$E_k = \int_{-Z_{\max}}^{Z_{\max}} \int_{0}^{R_{\max}} \frac{1}{2} \left(u_r u_r^* + u_\theta u_\theta^* + u_z u_z^* \right) r \mathrm{d}r \mathrm{d}z, \tag{5.24}$$

$$E_p = \int_{-Z_{\max}}^{Z_{\max}} \int_{0}^{R_{\max}} \frac{\rho \rho^*}{2N^2} r \mathrm{d}r \mathrm{d}z, \tag{5.25}$$

$$S_k = -\frac{1}{4} \int_{-Z_{\max}}^{Z_{\max}} \int_{0}^{R_{\max}} r \frac{\partial \Omega}{\partial r} \left(u_r^* u_\theta + u_\theta^* u_r \right) + r \frac{\partial \Omega}{\partial z} (u_z^* u_\theta + u_z u_\theta^*) \mathrm{d}r \mathrm{d}z, \tag{5.26}$$

$$S_p = -\frac{1}{4} \int_{-Z_{\max}}^{Z_{\max}} \int_{0}^{R_{\max}} \left(\frac{g}{\rho_0 N^2} \frac{\partial \rho_b}{\partial r} (u_r^* \rho + \rho^* u_r) + \frac{g}{\rho_0 N^2} \frac{\partial \rho_b}{\partial z} (u_z^* \rho + \rho^* u_z) \right) r \mathrm{d}r \mathrm{d}z, \tag{5.27}$$

$$B = \frac{1}{4} \int_{-Z_{\max}}^{Z_{\max}} \int_{0}^{R_{\max}} (\rho u_z^* + \rho^* u_z) r \mathrm{d}r \mathrm{d}z. \tag{5.28}$$

E_k and E_p are the kinetic and potential energies of the perturbation. The term S_k (S_p) represents the transfer of kinetic (potential) energy from the base flow to the perturbation. The term B is the energy conversion from the kinetic to potential energy of the perturbation. D_k and D_p are the kinetic and potential energy dissipations. They are small and will not be considered here. The transfers are plotted in figure 5.26 as a function of F_h/α for $m = 1$ and $m = 2$ for $\alpha = 0.5, Ro = 1.25$ and $Re = 10000$. These parameters correspond to the filled symbols in figure 5.25. For both $m = 1$ (figure 5.26a) and $m = 2$ (figure 5.26b), the kinetic energy transfer S_k is positive for $F_h/\alpha < 0.5$ ($Bu > 1.5$), while the potential energy transfer S_p is smaller and negative. This means that the source of the instability is the kinetic energy of the base flow. For $m = 1$, a part of the kinetic energy of the perturbation is converted to potential energy since B is positive. For $m = 2$ (figure 5.26b), the energy conversion B is negative for $F_h/\alpha < 0.1$ and then positive and of the same order as S_k. In contrast, when $F_h/\alpha > 0.5$ ($Bu < 1.5$), the potential energy transfer S_p becomes positive while S_k is negative. The energy source of the instability is therefore the potential energy of the base flow. This confirms that the baroclinicity then plays an important role and the instabilities are of mixed nature: baroclinic-Gent-McWilliams and baroclinic-shear instabilities.

5.5 Condition of existence of the shear instability

In this section, we will show that the variations of the growth rate of the shear instability for $m = 2$ as a function of Ro, F_h and α can be directly understood from the characteristics of the shear instability for a columnar vortex. As demonstrated for stratified non-rotating fluids in chapter 4, the shear instability for columnar vortices only exists for vertical wavenumbers k in the range $kRF_h < 1.6$. The minimum wavelength is therefore $\lambda_{\min} \simeq 4F_hR$. One wavelength will fit in the thickness of the pancake vortex $2\alpha R$ only if $F_h/\alpha < 0.5$. This condition turns out to explain very well the existence of the shear instability for pancake vortices in stratified non-rotating fluids. Here, we extend this criterion to arbitrary Rossby number Ro. Figure 5.27 shows the growth rate of the shear instability for a columnar vortex as a function of the rescaled vertical wavenumber $kRF_h/|Ro|$. The growth rate is maximum in the 2D limit $k = 0$ and decreases monotonically as $kRF_h/|Ro|$ increases. When F_h is fixed and Ro is varied (figure 5.27a), the upper wavenumber cutoff $kRF_h/|Ro|$ varies. Note

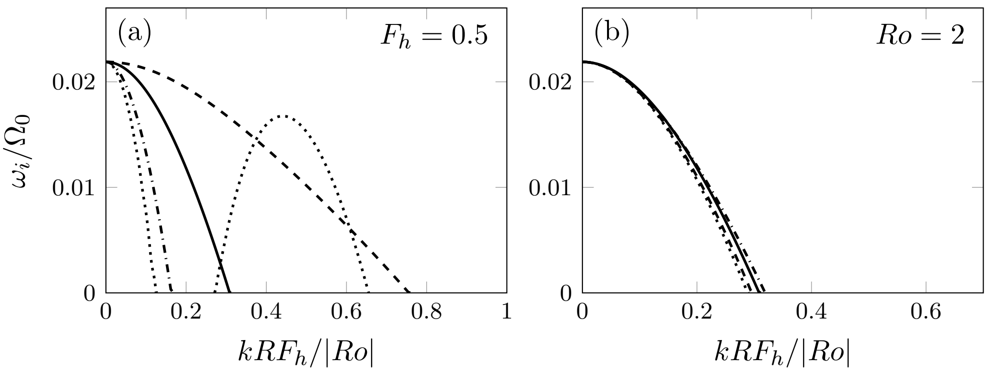

Figure 5.27: Growth rate for $m = 2$ for a columnar vortex as a function of the rescaled axial wavenumber $kRF_h/|Ro|$: (a) for different Rossby numbers Ro at fixed $F_h = 0.5$ and $Re = 10000$: ⋯⋯ $Ro = 20$; - - - $Ro = 7$; —— $Ro = 2$; -·-·- $Ro = -3$ and (b) for different Froude numbers F_h at fixed $Ro = 2$ and $Re = 10000$: ⋯⋯ $F_h = 0.1$;—— $F_h = 0.5$;- - - $F_h = 1$; -·-·- $F_h = 2$.

that the unstable branch near $kRF_h/|Ro| = 0.5$ for $Ro = 20$ corresponds to the centrifugal instability. On the other hand, when F_h is varied between 0.1 and 2 at fixed Ro as in figure 5.27b, all the curves remain similar and stabilizes for $kRF_h/|Ro| \simeq 0.3$. This suggests that the wavenumber cutoff can be written $kF_hR = c(Ro)$ where c is a function of Ro. The growth rate of the shear instability is shown in figure 5.28a as a function of Ro and kRF_h. The wavenumber cutoff kRF_h first increases as Ro decreases from $Ro = \infty$ and then decreases and follow the quasi-geostrophic scaling law $kRF_h/Ro = const$ for small Rossby numbers. For negative Rossby numbers, the cutoff re-increases monotonically as Ro decreases. As discussed in chapter 4, we consider that the thickness of the pancake vortex $2\alpha R$ corresponds to the maximum wavelength (or minimum wavenumber) that can fit along the vertical. This yields the condition $F_h/\alpha \leq c(Ro)/\pi$ for the existence of the shear instability. This critical vertical Froude number is plotted in figure 5.28b. Assuming further that the equivalent vertical wavenumber of the most unstable mode of the shear instability for the pancake vortex is always the smallest fitting along the vertical, i.e. $kR = \pi/\alpha$, one can compare the growth rate of the shear instability for columnar and pancake vortices as done in figure 5.17 for two different Rossby numbers $Ro = 1.25$ and $Ro = -5$. As can be seen, the growth rate for columnar and pancake vortices are in very good agreement for both Ro and vanish around the same value of F_h/α (or equivalently kRF_h/π). For $Ro = 1.25$, the growth rate for the pancake vortex rises again for $F_h/\alpha > 0.5$ owing to the mixed baroclinic-shear instability.

A similar comparison is made in figure 5.30 but now as a function of the Rossby number for the parameters $\alpha = 1.2, F_h = 0.5$ and $Re = 10000$ that have been presented in section 5.3.3. The maximum growth rate of the shear instability for the pancake vortex agrees quite well with the one of the columnar vortex for $kR = \pi/\alpha$. In particular, the shear instability is stabilized in the same range of Rossby number: $-20 \leq Ro \leq 3$. Again, the growth rate for the pancake vortex rises for small Rossby number but under the mixed form of the baroclinic-shear instability. As a conclusion, these results demonstrate that the maximum growth rate of the shear instability in pancake vortices corresponds in good approximation to its growth rate in columnar vortices for the smallest vertical wavenumber $kR = \pi/\alpha$ fitting in the pancake vortex. When this wavenumber is beyond the upper wavenumber cutoff, i.e. $\pi/\alpha > c(Ro)/F_h$, the shear instability is suppressed in pancake vortices.

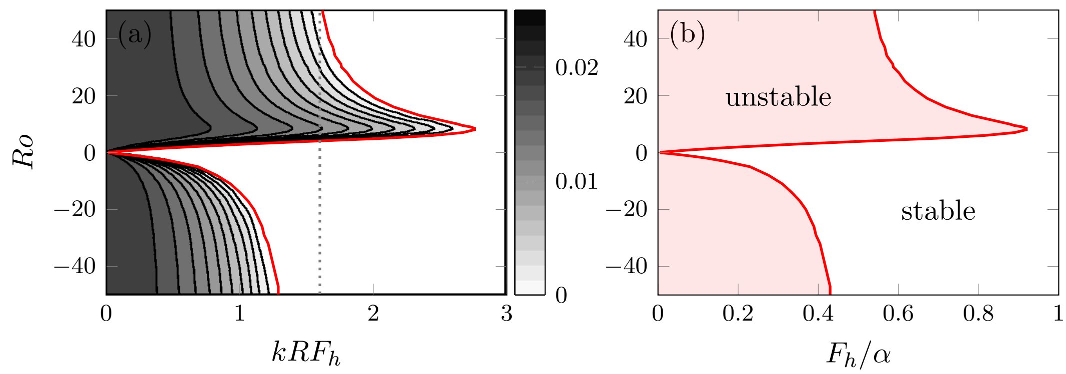

Figure 5.28: (a) Growth rate ω_i/Ω_0 of the shear instability for a columnar vortex as a function of Rossby number Ro and the rescaled vertical wavenumber kRF_h for fixed $F_h = 0.2$ and $Re = 10000$. The vertical dotted line is the wavenumber cutoff $kRF_h = 1.6$ for $Ro = \infty$. (b) Critical vertical Froude number F_h/α for the shear instability as a function of Ro deduced from the wavenumber cutoff for a columnar vortex.

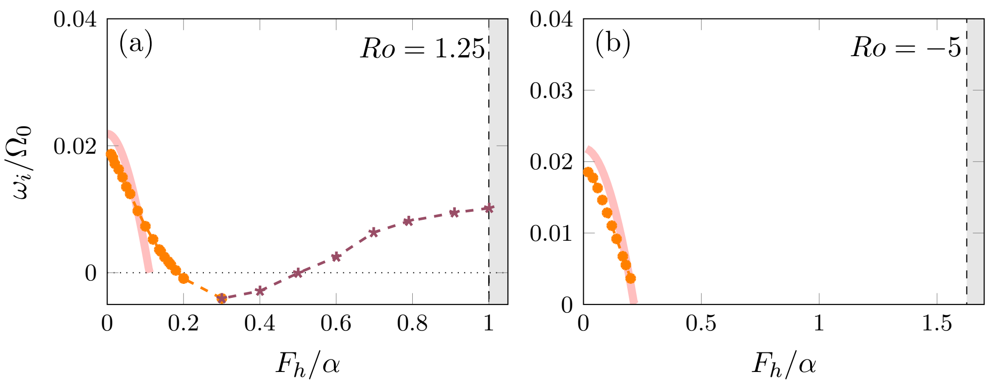

Figure 5.29: Maximum growth rate of the shear instability for columnar (for $kR = \pi/\alpha$) ( ) and pancake ( ) vortices as a function of F_h/α for $m = 2, F_h = 0.3$ and $Re = 10000$ for (a) $Ro = 1.25$ and (b) $Ro = -5$. The vertical shaded region is the gravitationally unstable region. in (a) indicates the baroclinic-shear instability.

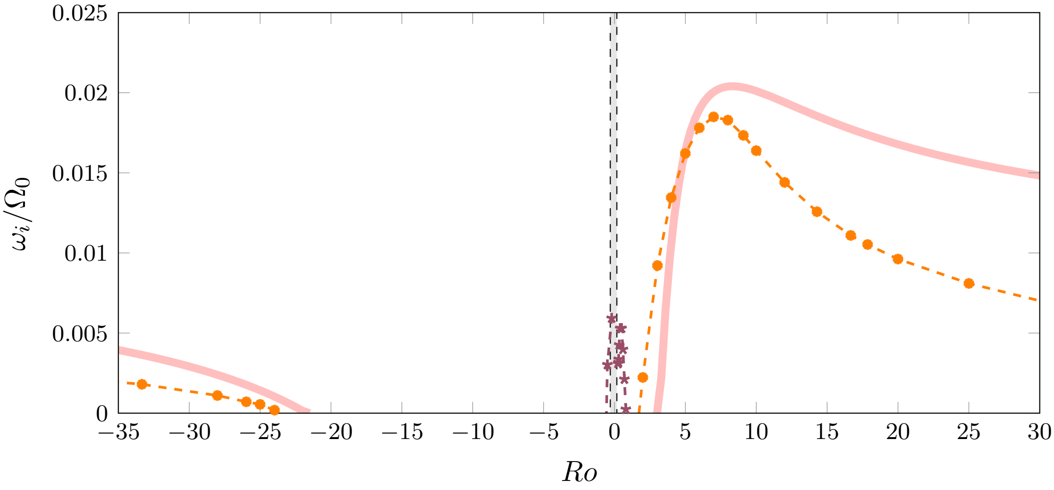

Figure 5.30: Maximum growth rate of the shear instability for columnar (—) and pancake ($\alpha = 1.2$) (-•-) vortices as a function of Ro for $m = 2, F_h = 0.5$ and $Re = 10000$. The vertical shaded region is the gravitationally unstable region. -*- indicates the baroclinic-shear instability.

5.6 Scaling laws for the Gent-McWillliams instability

The fluctuations of the growth rate of the Gent-McWilliams instability as a function of the vertical Froude number F_h/α (figure 5.25) can be also understood by comparison with the columnar case. First, the vertical wavenumber k of the Gent-McWilliams eigenmodes for pancake vortices can be estimated as $k = 2\pi/\lambda$ where λ is twice the vertical distance between contiguous minimum and maximum of the radial velocity perturbation. The growth rate plotted as a function of this wavenumber scaled by F_hR is shown in figure 5.31. The corresponding growth rate for a columnar vortex is shown by the grey continuous line.

Let us first focus on figure 5.31a where the Froude number is fixed while the aspect ratio varies. When α increases from $\alpha = 0.5$ to $\alpha = 3$, the growth rate of the Gent-McWilliams instability for the pancake vortex (dashed line with triangles) increases and then decreases in a fashion similar to the columnar case. In particular, the growth rate is maximum for $kRF_h = 0.6$ near the most amplified wavenumber kRF_h of the columnar vortex. Nevertheless, the growth rate maximum for the pancake vortex is much smaller than for the columnar vortex. Along the curve, the eigenmodes remains similar to the one shown in figure 5.20b, i.e. the mode has a single oscillation along the vertical and occupies the whole pancake vortex. However, when $\alpha = 3$, a secondary mode with a structure similar to the one shown in figure 5.24b starts to have a growth rate as high as the primary mode. The wavenumber of this secondary mode is much higher and its growth rate is shown by the dashed line with diamond in figure 5.31a. When α is further increased, the growth rate of this secondary mode increases rapidly but its estimated wavenumber decreases only slightly toward the most amplified wavenumber of the columnar vortex. Along this curve, the eigenmode has therefore more and more oscillations along the vertical like in figure 5.24c. In other words, the confinement effect due to the pancake shape becomes weaker as the vortex becomes taller. Alternatively, when α is kept constant $\alpha = 0.5$ (figure 5.31b), a similar evolution is first observed when the Froude number is decreased from $F_h = 0.3$ to $F_h = 0.05$ (dashed line with triangles). When $F_h = 0.05$, a secondary mode (dashed line with diamonds) becomes also unstable as the primary mode. This occurs for the same vertical Froude number $F_h/\alpha = 0.1$ as in figure 5.31a. The structure of this secondary mode is shown in figure

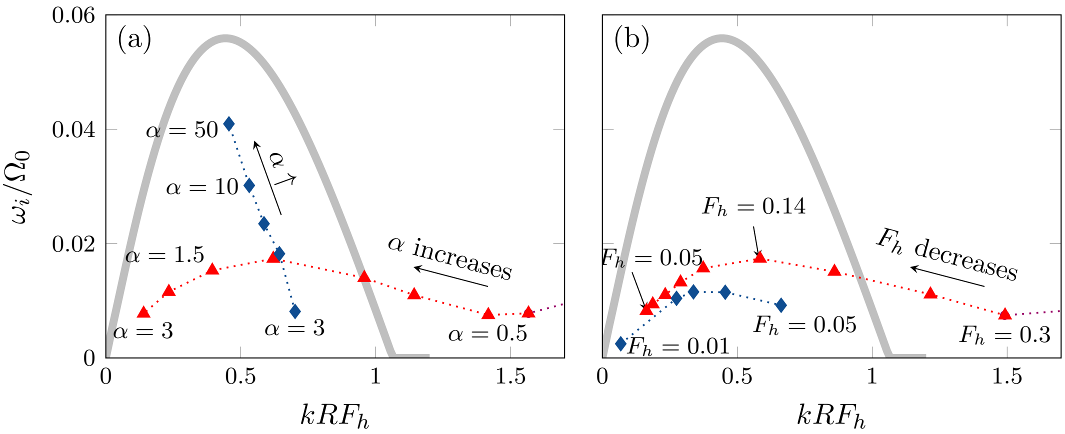

Figure 5.31: Maximum growth rate as a function of the estimated vertical wavenumber kRF_h for $m = 1$, $Ro = 1.25$ and $Re = 10000$. (a) F_h is varied for $\alpha = 0.5$ and (b) α is varied for $F_h = 0.3$. The thick grey line corresponds to the columnar vortex with the same parameters. The symbols are: ···▲··· for $F_h/\alpha > 0.1$ and ···◆··· for $F_h/\alpha < 0.1$ in Figure 5.25.

5.20a. However, the growth rate of the secondary mode first increases slightly as F_h is further decreased and then it decreases toward zero while its wavenumber also decreases.

The difference in behaviour compared to figure 5.31a comes probably from the fact that the buoyancy Reynolds number ReF_h^2 becomes too low when the Froude number F_h is decreased below 0.05. It would be interesting to increase the Reynolds number to test this hypothesis.

5.7 Detailed study of the baroclinic instability

In sections 5.3 and 5.4, the baroclinic instability has been observed for $m = 1$ and $m = 2$ near the threshold for the gravitational instability. Here, we will further study its dependence on the Rossby number Ro and the vertical Froude number F_h/α. In addition, we will show that the baroclinic instability destabilizes also higher azimuthal wavenumbers. A theoretical criterion and scaling laws for the baroclinic instability will be next derived following the approach used in chapter 4 for stratified non-rotating fluid.

5.7.1 A typical example

Figure 5.32 shows the spectra of the baroclinic instability for $\alpha = 0.5, F_h = 0.3, Ro = 0.4$ and $Re = 10000$ for different azimuthal wavenumbers m. These control parameters are very close to the threshold of the gravitational instability which is $F_h = 0.32$ for $\alpha = 0.5$ and $Ro = 0.4$. Among all azimuthal wavenumbers, $m = 2$ is the most unstable. For each m, the most unstable mode is anti-symmetric (black symbol) and the second most unstable mode is symmetric (grey symbol). Nevertheless, the growth rate difference between anti-symmetric and symmetric modes becomes very small as m increases. The displacement mode is also observed for $m = 1$ near the origin and the baroclinic-shear mode for $m = 2$ is located near $\omega_r/\Omega_0 = 0.18$ with a small growth rate compared to the baroclinic instability. No different instability type is found for other azimuthal wavenumbers $m \geq 3$. The characteristic frequency of each azimuthal wavenumber is proportional to m: $\omega_r/\Omega_0 \simeq 0.25m$, i.e. the azimuthal phase velocity is constant. In fact, this corresponds clear to the angular velocity of the base flow $\Omega(r_b, z_b) \simeq 0.25$ at the point $r_b = 0, z_b = 1.17\Lambda$ where the vertical density gradient $\partial\rho_t/\partial z$ is maximum for $\alpha = 0.5, F_h = 0.5$ and $Ro = 0.4$.

5

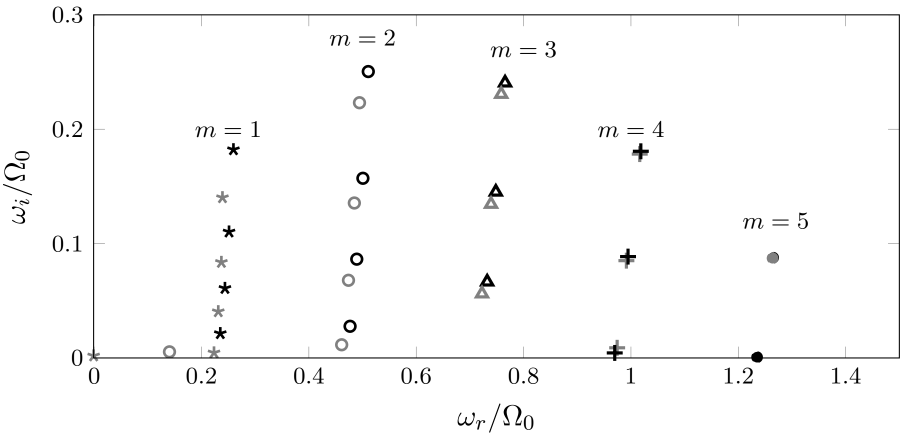

Figure 5.32: Growth rate (ω_i/Ω_0) and frequency (ω_r/Ω_0) spectra of the baroclinic instability for different azimuthal wavenumbers: $m = 1$ ($\star$); $m = 2$ ($\circ$); $m = 3$ ($\triangle$); $m = 4$ ($+$); $m = 5$ ($\bullet$) for $\alpha = 0.5, F_h = 0.3, Ro = 0.4$, and $Re = 10000$. Grey and black symbols indicate symmetric and anti-symmetric modes, respectively.

Figure 5.33 shows the first three anti-symmetric eigenmodes for $m = 3$. As already shown for $m = 1$ and $m = 2$, the number of oscillations in the radial direction increases with the mode number while the vertical structure remains the same. Figure 5.34a shows the growth rate as a function of the radial wavenumber $l = 2\pi/\lambda_r$ where the radial wavelength λ_r has been measured for each eigenmode as illustrated in figure 5.33b. For each azimuthal wavenumber, the growth rate decreases monotonically as l increases. As already visible in figure 5.32, the maximum growth rate exhibits a bell-shape curve as a function of m (figure 5.34b). No instabilities has been found for $m = 0$ and $m \geq 6$. These wavenumber properties are very reminiscent of the baroclinic instability in parallel shear flows (Vallis, 2006).

5.7.2 Parametric study

Figure 5.35 outlines the effect of the Rossby number on the most unstable baroclinic mode for each azimuthal wavenumber for $\alpha = 0.5, F_h = 0.3$ and $Re = 10000$. When Ro increases, the growth rate decreases all the more faster than m is large. Hence, $m = 3$ is the most unstable azimuthal wavenumber when Ro is close to the threshold for the gravitational instability whereas $m = 1$ becomes the most unstable for $Ro \geq 0.5$. In contrast, the frequency of each azimuthal wavenumber is independent of the Rossby number (figure 5.35). Similarly, figure 5.36 shows the effect of the Froude number for $\alpha = 0.5, Ro = 0.4$ and $Re = 10000$. The frequency is again independent of the Froude number (figure 5.36b) whereas the maximum growth rate (figure 5.36a) increases with F_h/α all the mode faster than m is large.

5.7.3 A simple analytical model

In chapter 4, a model consisting in a bounded vortex with an angular velocity varying only in the vertical direction has been considered and shown to account qualitatively for the characteristics of the baroclinic instability in stratified non-rotating fluids. Such model takes into account the main features of the base pancake vortex in the core where the baroclinic instability develops. Its stability can be solved analytically when the vertical variations are weak. Here, this model is extended to take into account a background rotation. The base angular velocity of the vortex is assumed to be

$$\Omega = \tilde{\Omega}_0 - \tilde{\Omega}_1 z, \tag{5.29}$$

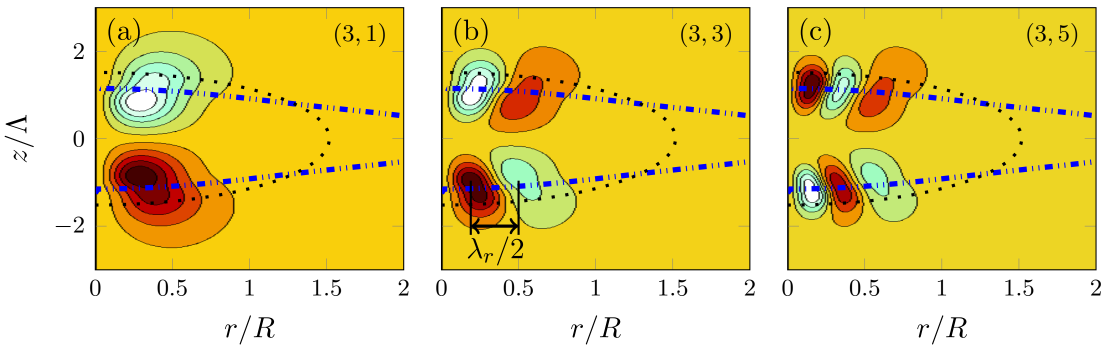

Figure 5.33: Real part of the radial velocity perturbation $\mathrm{Re}(u_r)$ for the three anti-symmetric baroclinic modes for $m = 3$: (a) the most unstable mode $(3, 1)$, (b) $(3, 3)$ and (c) $(3, 5)$ for $\alpha = 0.5$, $F_h = 0.3$, $Ro = 0.4$ and $Re = 10000$. The dotted line indicates the extension of the base flow where $\Omega = 0.1\Omega_0$. The double dotted dashed line ( ) shows where the isopycnal potential vorticity gradient (5.21) changes sign.

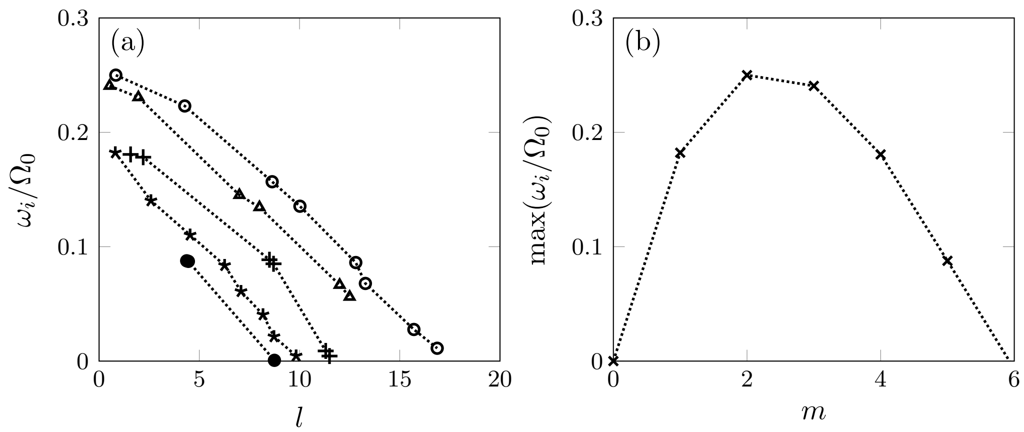

Figure 5.34: (a) Growth rate (ω_i/Ω_0) as a function of the radial wavenumber l for different azimuthal wavenumbers: $m = 1$ ($\star$); $m = 2$ ($\circ$); $m = 3$ ($\triangle$); $m = 4$ ($+$); $m = 5$ ($\bullet$) and (b) maximum growth rate as a function of the azimuthal wavenumber m for $\alpha = 0.5, F_h = 0.3, Ro = 0.4$, and $Re = 10000$.

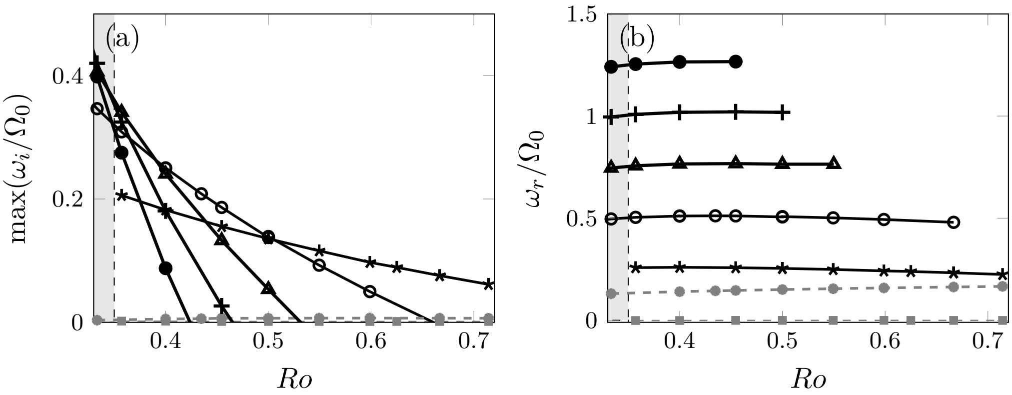

Figure 5.35: (a) Maximum growth rates and (b) corresponding frequencies of the baroclinic instability (dark solid lines) as a function of Ro for different azimuthal wavenumbers: m =1 ($\star$); m =2 ($\circ$); m =3 ($\triangle$); m =4 ($+$); m =5 ($\bullet$) for $\alpha = 0.5, F_h = 0.3$ and $Re = 10000$. Grey symbols indicate other instabilities: baroclinic-shear instability -•- for $m = 2$ and displacement mode -▪- for $m = 1$. The shaded area indicates the gravitationally unstable region.

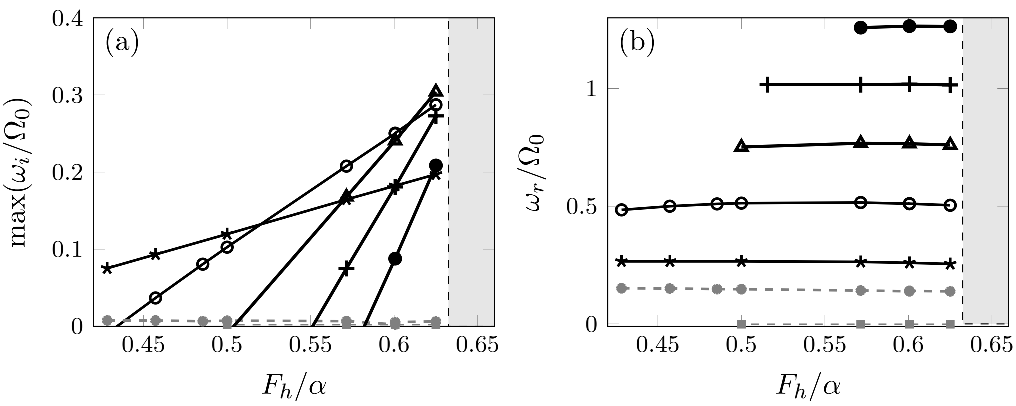

Figure 5.36: (a) Maximum growth rates and (b) corresponding frequencies of the baroclinic instability (dark solid lines) as a function of F_h/α for different azimuthal wavenumbers:m =1 ($\star$); m =2 ($\circ$); m =3 ($\triangle$); m =4 ($+$); m =5 ($\bullet$) for $\alpha = 0.5, Ro = 0.4$, and $Re = 10000$. Grey symbols indicate other instabilities: baroclinic-shear instability -•- for $m = 2$ and displacement mode -▪- for $m = 1$. The shaded area indicates the gravitationally unstable region.

where $\tilde{\Omega}_0$ and $\tilde{\Omega}_1$ are constants. From the thermal-wind relation (5.4), the base density is obtained as

$$\rho_b = \frac{\rho_0}{g}\left[\tilde{\Omega}_0 + \frac{f}{2} - \tilde{\Omega}_1 z\right]\tilde{\Omega}_1 r^2. \tag{5.30}$$

As in chapter 4, we consider that the base flow is contained in a rigid cylinder of radius R and height H between $z = -H/2$ and $z = H/2$. By assuming that the vertical variations are weak, i.e. $\tilde{\Omega}_1 H \ll |\tilde{\Omega}_0 + f/2|$, the equation (5.8)–(5.12) in the inviscid limit can be reduced at leading order in $\tilde{\Omega}_1$ to

$$\frac{1}{r}\frac{\partial}{\partial r}\left(r\frac{\partial p}{\partial r}\right) + \left[-\frac{m^2}{r^2} - C^2\frac{\partial^2}{\partial z^2}\right]p = 0 + O(\tilde{\Omega}_1^2), \tag{5.31}$$

where $C = 2|\tilde{\Omega}_0 + f/2|/N$. Note that the hypothesis $\tilde{\Omega}_1 H \ll |\tilde{\Omega}_0 + f/2|$ is not valid around $\tilde{Ro} \equiv= 2\tilde{\Omega}_0/f = -1$. The only difference in (5.31) with the stratified non-rotating case considered in chapter 4 is contained in the constant C. The general solution of (5.31) is

$$p = \mathrm{J}_m(Ckr)\left(A\cosh kz + B\sinh kz\right), \tag{5.32}$$

where J_m is the Bessel function of order m of the first kind and A and B are constants. Imposing the boundary conditions $u_z(z = \pm H/2) = 0$ and $u_r(r = R) = 0$ yield two relations similar to those for the classical Eady problem (Vallis, 2006)

$$\omega = m\tilde{\Omega}_0 + \frac{m\tilde{\Omega}_1}{k}\sqrt{\left(1 - \frac{kH}{2\tanh(kH/2)}\right)\left(1 - \frac{kH\tanh(kH/2)}{2}\right)}, \tag{5.33}$$

$$CkR = \mu_{m,n}, \tag{5.34}$$

where $\mu_{m,n}$ is the nth root of J_m. Combining the condition for instability $kH < 2.4$ and the fact that $\mu_{m,n} > \mu_{1,1} = 3.83$, yield the instability condition

$$\frac{\tilde{F}_h}{\tilde{\alpha}}\left|1 + \frac{1}{\tilde{Ro}}\right| > 0.8, \tag{5.35}$$

where $\tilde{\alpha} = H/R$ and $\tilde{F}_h = \tilde{\Omega}_0/N$. This condition simply states that the Burger number $Bu = \tilde{\alpha}^2 N^2/(f+2\tilde{\Omega}_0)^2$ based on the absolute angular velocity $\tilde{\Omega}_0 + f/2$ should be below a threshold for instability. When $\tilde{Ro} \ll 1$, (5.35) recovers the classical condition for the baroclinic instability (Eady, 1949; Saunders, 1973; Hide & Mason, 1975). We can also derive scaling laws for the maximum growth rate and the most amplified wavenumber (5.33). For any m, the growth rate is maximum for the first root of the Bessel function $n = 1$. An asymptotic expansion of this root for large m is $\mu_{m,1} = m + 1.856m^{1/3} + O(m^{-1/3})$ (Abramowitz & Stegun, 1972). Taking only the leading order of this expansion, i.e. $\mu_{m,1} \sim m$, (5.34) implies $m/k = CR$. The growth rate is thus maximum when the term inside the square root in (5.33) is minimum, i.e. when $kH = 1.6$. The most amplified azimuthal wavenumber is therefore

$$m_{\max} \simeq 3.2\frac{\tilde{F}_h}{\tilde{\alpha}}\left|1 + \frac{1}{\tilde{Ro}}\right| \tag{5.36}$$

and the maximum growth rate is

$$\omega_{i\,\max} \simeq 0.6\tilde{\Omega}_1 R\frac{\tilde{F}_h}{\tilde{\alpha}}\left|1 + \frac{1}{\tilde{Ro}}\right|, \tag{5.37}$$

5

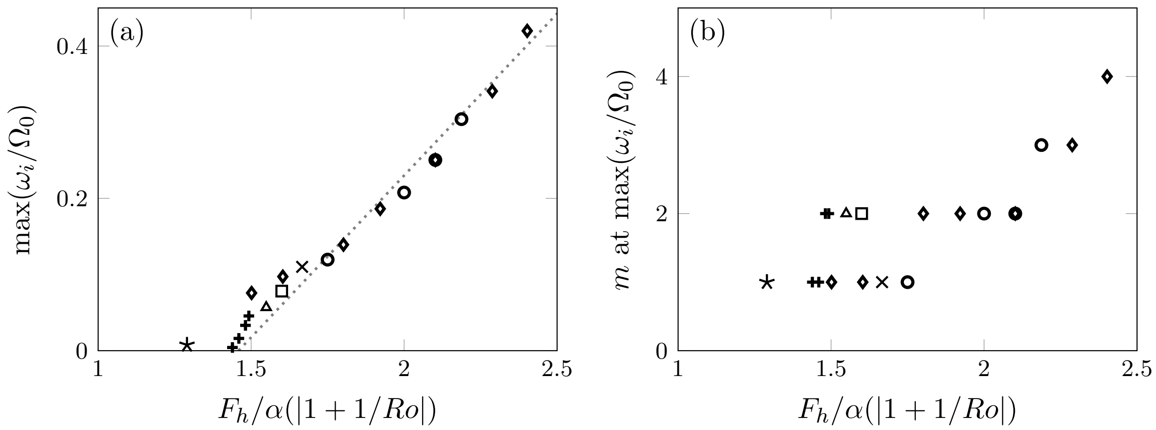

Figure 5.37: (a) Maximum growth rate and (b) most amplified azimuthal wavenumber m of the baroclinic instability for different combinations of Ro and F_h: $Ro = 0.4$, F_h varies ○, $F_h = 0.3$, Ro varies ◇, $Ro = 1$, $F_h = 0.42$ ×, $Ro = 5$, $F_h = 0.67$ □, $Ro = 10$, $F_h = 0.7$ △, $Ro = -5$, $F_h = 0.8$ ⋆ and $Ro = \infty$, F_h varies +. Other parameters are fixed to $\alpha = 0.5$, $Re = 10000$. The dotted line in (a) is a fit.

for large m. These scaling laws are tested in figure 5.37 for the baroclinic instability of the pancake vortex by assuming that $F_h/\alpha|1 + 1/Ro|$ is equivalent to $\tilde{F}_h/\tilde{\alpha}|1 + 1/\tilde{R}o|$. Different combinations of F_h and Ro for $\alpha = 0.5$ and $Re = 10000$. As seen in figure 5.37a, the maximum growth rate align in a straight line when represented as a function of $F_h/\alpha|1 + 1/Ro|$. The baroclinic instability only occurs for $F_h/\alpha|1 + 1/Ro| \geq 1.46$ in qualitative agreement with (5.35). Note that the leftmost (star) in figure 5.37a, which is slightly away from the other points, is for a negative Rossby number $Ro = -5$. Similarly, figure 5.37b shows that the most amplified azimuthal wavenumber increases approximately linearly with $F_h/\alpha|1 + 1/Ro|$.

Figure 5.38 displays a map of the domain of existence of the baroclinic instability in the parameter space $(F_h/\alpha, Ro)$. The dashed line represents the threshold $F_h/\alpha(|1+1/Ro|) = 1.46$ deduced from figure 5.37a. The shaded region delimited by the solid line is gravitationally unstable. The circle symbols indicate the parameter for which the baroclinic instability has been observed for $m = 2$, $Re = 10000$ and $\alpha = 0.5$ while the cross symbols correspond to the parameters stable to the baroclinic instability for $m = 2$. We can see that there is a good agreement between the threshold $F_h/\alpha(|1 + 1/Ro|) = 1.46$ and the numerical results for positive Rossby number. However, the threshold departs from the numerical results for negative Rossby number. This is most likely due to the assumption of the slow vertical variation $\tilde{\Omega}_1 H \ll \tilde{\Omega}_0 + f/2$ used to derive the theoretical scaling laws. This hypothesis indeed breaks down around $\tilde{R}o = -1$. Furthermore, the location where the density gradient is maximum actually varies with the Rossby number implying that $\tilde{\Omega}_0$ also varies with Ro. These variations could be taken into account in a refined analysis.

5.8 Map of the instabilities

Figure 5.39 summarizes the different instabilities observed for each azimuthal wavenumbers $m = 0, 1$ and 2 in the parameter space $(Ro, F_h/\alpha)$ for $Re = 10000$ and various aspect ratios. The symbols indicate the instability type while the lines separate the different semi-theoretical thresholds that have been derived throughout the paper. The solid lines correspond to the thresholds for the centrifugal instability that can be obtained from the asymptotic formula (5.17). For each azimuthal wavenumber, there is a stabilization at

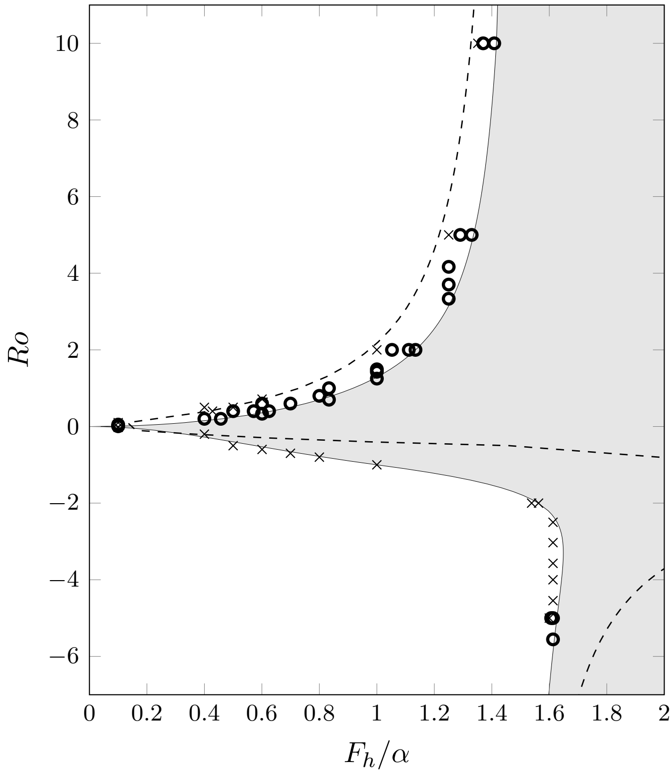

Figure 5.38: Domain of existence of the baroclinic instability for $m = 2$ as a function of F_h/α and Ro for $\alpha = 0.5$ and $Re = 10000$: circles (o) indicate the parameters unstable to baroclinic instability, crosses (×) are for the stable case. The shaded area indicates gravitational instability and the dashed line (- - -) corresponds to the threshold $F_h(|1 + 1/Ro|) = 1.46$.

low Froude numbers because the buoyancy Reynolds number ReF_h^2, which control viscous effects, decreases. The criterion for the baroclinic instability $F_h/\alpha(|1+1/Ro|) = 1.46$ is again shown by a dashed line and the condition derived in section 5.5 for the shear instability is represented by a dotted line. These conditions are generally in good agreement with the numerical results for all the parameters investigated. In summary, the centrifugal instability exists for sufficiently high Rossby and Froude numbers. The shear instability for $m = 2$ is present below a critical vertical Froude number F_h/α depending on the Rossby number. The Gent-McWilliams instability for $m = 1$ is observed over wide ranges of Ro and F_h/α except when it transforms to the baroclinic-Gent-McWilliams and baroclinic instabilities. The baroclinic instability occurs only in a small band close to the threshold for the gravitational instability (shaded region). However, mixed instabilities: baroclinic-shear for $m = 2$ and baroclinic-Gent-McWilliams for $m = 1$ instabilities are also observed beyond the threshold for the classical baroclinic instability where the Rossby number is not too large.

5.9 Conclusions

We have investigated the stability of an axisymmetric pancake vortex with Gaussian angular velocity in both radial and vertical directions in stratified rotating fluids. In stratified non-rotating fluids, chapter 4 and Negretti & Billant (2013) have shown that a pancake vortex can be unstable to centrifugal, shear, baroclinic and gravitational instabilities. The centrifugal instability occurs when the buoyancy Reynolds number ReF_h^2 is sufficiently large while the three other instabilities are mostly governed by the vertical Froude number F_h/α when the Reynolds number is large. The shear instability develops when $F_h/\alpha \leq 0.5$ whereas the baroclinic and gravitational instabilities are active when $F_h/\alpha \geq 1.43$ and $F_h/\alpha \geq 1.5$, respectively. In contrast, in quasi-geostrophic fluids, Nguyen *et al.* (2012) found that, in general, baroclinic instabilities are dominant for small Burger number $Bu = \alpha^2 Ro^2/(4F_h^2) < 1$ while barotropic instabilities are dominant for $Bu > 1$.

In order to link the two limits: stratified non-rotating and quasi-geostrophic, we have first investigated the effect of the Rossby number for fixed aspect ratio α, Froude F_h and Reynolds Re numbers. Then, the effect of the other parameters has been investigated for a fixed Rossby number of order unity. When $|Ro|$ is large, the centrifugal instability is dominant since the generalized Rayleigh discriminant Φ is negative. It is stabilized for small Rossby numbers before that Φ becomes positive everywhere because of viscous effects. The asymptotic formula for the growth rate of the centrifugal instability for columnar vortices for long axial wavenumber (Billant & Gallaire, 2005) works well also for pancake vortices for $m = 0$ and $m = 2$. For $m = 1$, it is in good agreement with the numerical results only for negative Rossby numbers. For moderate positive Rossby numbers, there is a discrepancy both for columnar and pancake vortices because the centrifugal instability merges continuously with the Gent-McWilliams instability. It is therefore not possible to distinguish them when their growth rates are comparable. The Gent-McWilliams instability for $m = 1$ exists over wide ranges of Rossby and vertical Froude numbers. This instability is due to the presence of a critical radius where $\Omega = \omega_r$ in which the vertical vorticity gradient is positive $\zeta' > 0$ (Gent & McWilliams, 1986; Yim & Billant, 2015). For small Burger number $Bu < 1$ and not too large Rossby number, the Gent-McWilliams instability transforms continuously into a mixed baroclinic-Gent-McWilliams instability. Just below the threshold for the gravitational instability, it becomes a pure baroclinic instability with a frequency set by the angular velocity at the point where the base density vertical gradient is maximum. For $m = 1$, the displacement mode which derives from the translational invariance is also weakly unstable. It is destabilized by viscous effects since its growth rate is maximum for a finite Reynolds number and vanishes for $Ro \to \infty$.

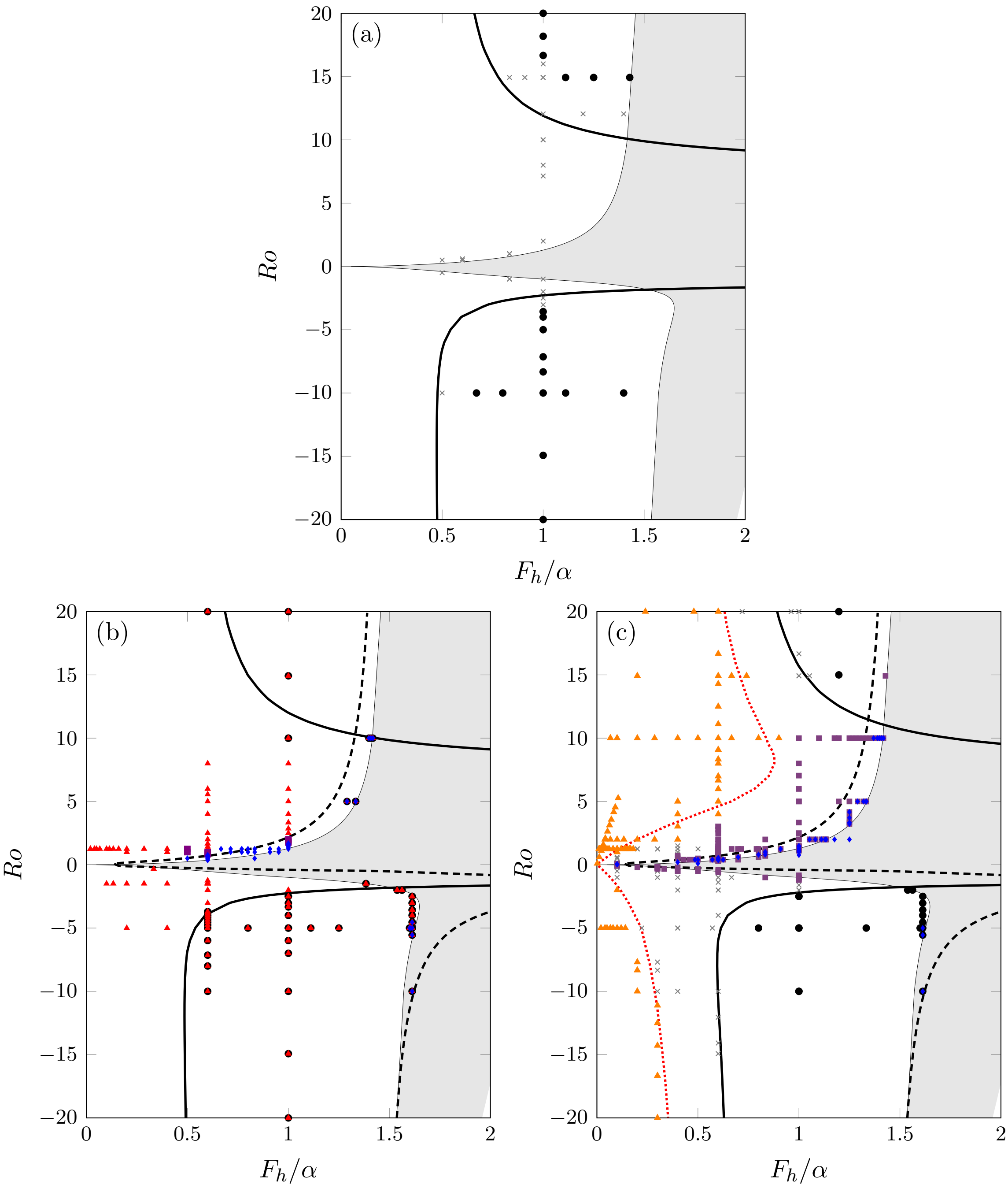

Figure 5.39: Domain of existence of the various instabilities for different azimuthal wavenumbers (a) $m = 0$, (b) $m = 1$ and (c) $m = 2$ as a function of Ro and F_h/α for $Re = 10000$ and various α. The different symbols indicate the different instabilities for each set of parameters investigated: centrifugal (•); Gent-MCWilliams (▴); baroclinic-Gent-McWilliams (▪); baroclinic (⧫); shear (▴) and baroclinic-shear (▪) instabilities, and stable (×). The shaded area indicates the gravitationally unstable region, the thick solid line shows the asymptotic growth rate for the centrifugal instability (5.17) and the dashed line (- - -) is the threshold the baroclinic instability: $F_h(|1 + 1/Ro|) = 1.46$.

5

The shear instability for $m = 2$ exists when $F_h/\alpha \leq c(Ro)/\pi$ where c is a function of Ro. This condition derives directly from the fact that the shear instability for a columnar vortex exists in the vertical wavenumber band $0 \leq kRF_h \leq c(Ro)$. The minimum wavenumber fitting inside the pancake vortex $kR = \pi/\alpha$, is therefore unstable only when $F_h/\alpha \leq c(Ro)/\pi$. In addition, the growth rate of the shear instability for pancake vortices agrees well with the one of columnar vortices for the wavenumber $kR = \pi/\alpha$. When the Burger number is small $Bu < 1$ and the Rossby number is not too large, the shear instability transforms continuously into a mixed baroclinic-shear instability whose eigenmode exhibits deformations along the critical layer $\omega_r = m\Omega$ and at the inflection radius $\zeta' = 0$. Just below the threshold for the gravitational instability, the pure baroclinic instability is triggered and both baroclinic-shear and baroclinic instabilities can co-exist. The baroclinic instability can also destabilize higher wavenumbers $m \geq 3$.

An analytical model consisting in a bounded vortex with an angular velocity only varying slowly in the vertical direction has allowed us to show that the maximum growth rate and the most amplified azimuthal wavenumber of the baroclinic instability should scale as $F_h/\alpha|1 + 1/Ro|$ in good agreement with the numerical results for positive Rossby numbers. The baroclinic instability develops only when $F_h/\alpha|1 + 1/Ro| \geq 1.46$. For negative Rossby numbers around $Ro = -1$, the model breaks down because the hypothesis of small vertical variation of the angular velocity compared to the absolute angular velocity $\Omega_0 + f/2$ no longer holds. Altogether, these results have allowed us to draw the domains of existence of each instability in the parameter space $(F_h/\alpha, Ro)$.

5.A Discussion on the mixed instabilities: baroclinic-Gent-Mcwilliams and baroclinic-shear for small Burger number

In previous sections, when the Burger number Bu is smaller than unity, the Gent-McWilliams instability remains unstable with a frequency larger than the upper cutoff ($\omega_r = \Omega(r_I) = 0.135\Omega_0$) for columnar vortices in the mixed form of the baroclinic-Gent-McWilliams instability. Also, the shear instability re-appears continuously as a baroclinic-shear instability beyond the vertical Froude number cutoff. Then, for smaller $Bu \ll 1$, the (pure) baroclinic instability appears: for $m = 1$, the baroclinic-Gent-McWilliams instability transforms to the baroclinic instability while the baroclinic-shear instability co-exists with the baroclinic instability for $m = 2$. These mixed baroclinic-Gent-McWilliams and baroclinic-shear instabilities are not observed when $|Ro|$ is large although there exist strong density deformations when F_h/α is near the threshold for the gravitational instability. This is different from the pure baroclinic instability because it is observed for all Ro as soon as the isopycnal deformations are strong enough. This suggests that these mixed baroclinic-Gent-McWilliams and baroclinic-shear instabilities are not only controlled by the isopycnal deformations but also need the small Burger and Rossby numbers. Here, we consider the instability conditions in quasi-geostrophic fluids. By assuming $f \gg 1$ and $N \gg 1$ in (5.8)–(5.12), we recover the quasi-geostrophic equation,

$$\frac{\partial \Pi'}{\partial t} + J(\psi', \bar{\Pi}) + J(\bar{\psi}, \Pi') = 0, \tag{5.38}$$

where $\bar{\Pi}$ and $\bar{\psi}$ are the potential vorticity and streamfunction of the base flow

$$\bar{\psi} = -\frac{1}{2}\mathrm{e}^{-r^2 - z^2/\alpha^2}. \tag{5.39}$$

$$\bar{\Pi} = \zeta + f + \frac{f^2}{N^2}\frac{\partial^2 \bar{\psi}}{\partial z^2}, \tag{5.40}$$

where $\zeta = 1/r\partial(r\partial\psi/\partial r)/\partial r$ is the vertical vorticity, while (Π', ψ') are those of the perturbations, $J(a,b) = 1/r(\partial a/\partial r)\partial b/\partial\theta - 1/r(\partial b/\partial r)\partial a\partial/\theta$ is the Jacobian operator

Assuming that the perturbation has the form $\psi' = \psi(r,z)\exp(\mathrm{i}m\theta - \mathrm{i}\omega t)$, (5.38) becomes

$$(m\Omega - \omega)\left[\frac{1}{r}\frac{\partial}{\partial r}\left(r\frac{\partial \psi}{\partial r}\right) - \frac{m^2}{r^2}\psi + \frac{f^2}{N^2}\frac{\partial^2 \psi}{\partial z^2}\right] + \frac{m}{r}\frac{\partial \bar{\Pi}}{\partial r}\psi = 0. \tag{5.41}$$

Multiplying (5.41) with $r\psi^*$ where ψ^* is the complex conjugate of ψ and integrating in radial and vertical directions with boundary conditions that ensure that the perturbation vanishes at $r = \infty$ and $z = \pm\infty$ gives

$$\int_{-\infty}^{\infty}\int_{0}^{\infty}\left(r\left|\frac{\partial \psi}{\partial r}\right|^2 + \frac{f^2}{N^2}r\left|\frac{\partial \psi}{\partial z}\right|^2\right)\mathrm{d}r\mathrm{d}z = -\int_{-\infty}^{\infty}\int_{0}^{\infty}\frac{m}{m\Omega - \omega}\frac{\partial \bar{\Pi}}{\partial r}|\psi|^2\mathrm{d}r\mathrm{d}z. \tag{5.42}$$

The left-hand side of (5.42) is real. Hence, the instability condition, Im(ω)$\neq 0$, is then

$$\frac{\partial \bar{\Pi}}{\partial r} = 0, \tag{5.43}$$

somewhere which corresponds to the Charney-Stern instability condition. For the $m = 1$ Gent-McWilliams instability, the condition that the potential vorticity gradient at the

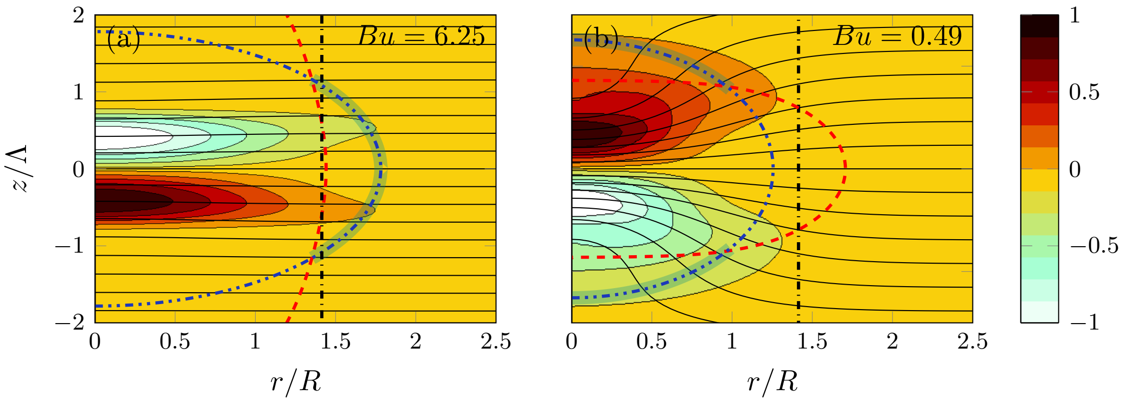

Figure 5.40: Radial velocity perturbation $\mathrm{Re}(u_r)$ for the Gent-McWilliams instability for (a) $Bu = 6.25$ ($F_h = 0.1$) and (b) $Bu = 0.49$ ($F_h = 0.36$) for $\alpha = 0.5, Ro = 1$ and $Re = 10000$. ···· the critical layer $m\Omega(r_c) = \omega$, - - - potential vorticity gradient changes sign, -·-· vertical vorticity gradient changes sign and ▬ where the potential vorticity gradient at critical layer is positive. The horizontal lines are isopycnals.

critical layer should be positive, $\partial\bar{\Pi}/\partial r(r_c) > 0$, gives

$$\frac{\partial\bar{\Pi}}{\partial r} = \frac{\partial\zeta}{\partial r} + \frac{\partial}{\partial r}\underbrace{\left(\frac{4F_h^2}{Ro^2}\frac{\partial^2\bar{\psi}}{\partial z^2}\right)}_{O(Bu^{-1})\times\zeta}, \tag{5.44}$$

For large Bu, the gradient of the vertical vorticity is dominant. However, for small Bu, the second term in (5.44) becomes dominant meaning that there may exist $\bar{\Pi}'(r_c) > 0$ while $\zeta'(r_c) < 0$. Figure 5.40 shows two example of the Gent-McWilliams instability for $Bu = 6.25$ and for $Bu = 0.49$. As can be seen for large Bu, the inflection radius for the vertical vorticity (vertical dash dotted line) and the one for the potential vorticity (dashed line) are close while when Bu is small (figure 5.40b), differ. The thick continuous line indicates when the potential vorticity gradient is positive at the critical radius ($\Omega(r_c) = \omega_r$). When Bu is large, it is located at large r but for small Bu, it is above and beneath the vortex. For a columnar vortex, the stabilization of the Gent-McWilliams instability for a frequency which is larger than the cutoff frequency $\omega = 0.135\Omega_0$ comes from the fact that the vorticity gradient is negative at the critical radius above this frequency. However, for pancake vortices, even though the vertical vorticity gradient is negative at the critical layer, regions exist where the potential vorticity gradient is positive as can be seen in figure 5.40b. Hence, this may explain why the Gent-McWilliams instability continues to exist as a mixed baroclinic-Gent-McWilliams instability for small Bu for frequency over the frequency cutoff of the columnar vortex.

The $m = 2$ baroclinic-shear instability which also occurs when $Bu < 1$ could be explained similarly. Figure 5.41 shows the vertical vorticity perturbation of the shear instability $m = 2$ for different Rossby numbers. When $Ro = 3$ (figure 5.41a,b), the vorticity deforms around the inflection point r_I where $\zeta'(r_I) = 0$ and the sign changes of potential and vertical vorticities occur at similar radii. However, when Ro or Bu decreases, the contour where $\partial\bar{\Pi}/\partial r = 0$ flatten and differs from the inflection radius $\zeta' = 0$. This is likely to be the reason of the reappearance and distortions of the mode of the shear instability above the cutoff vertical Froude number in the form of the mixed baroclinic-shear instability.

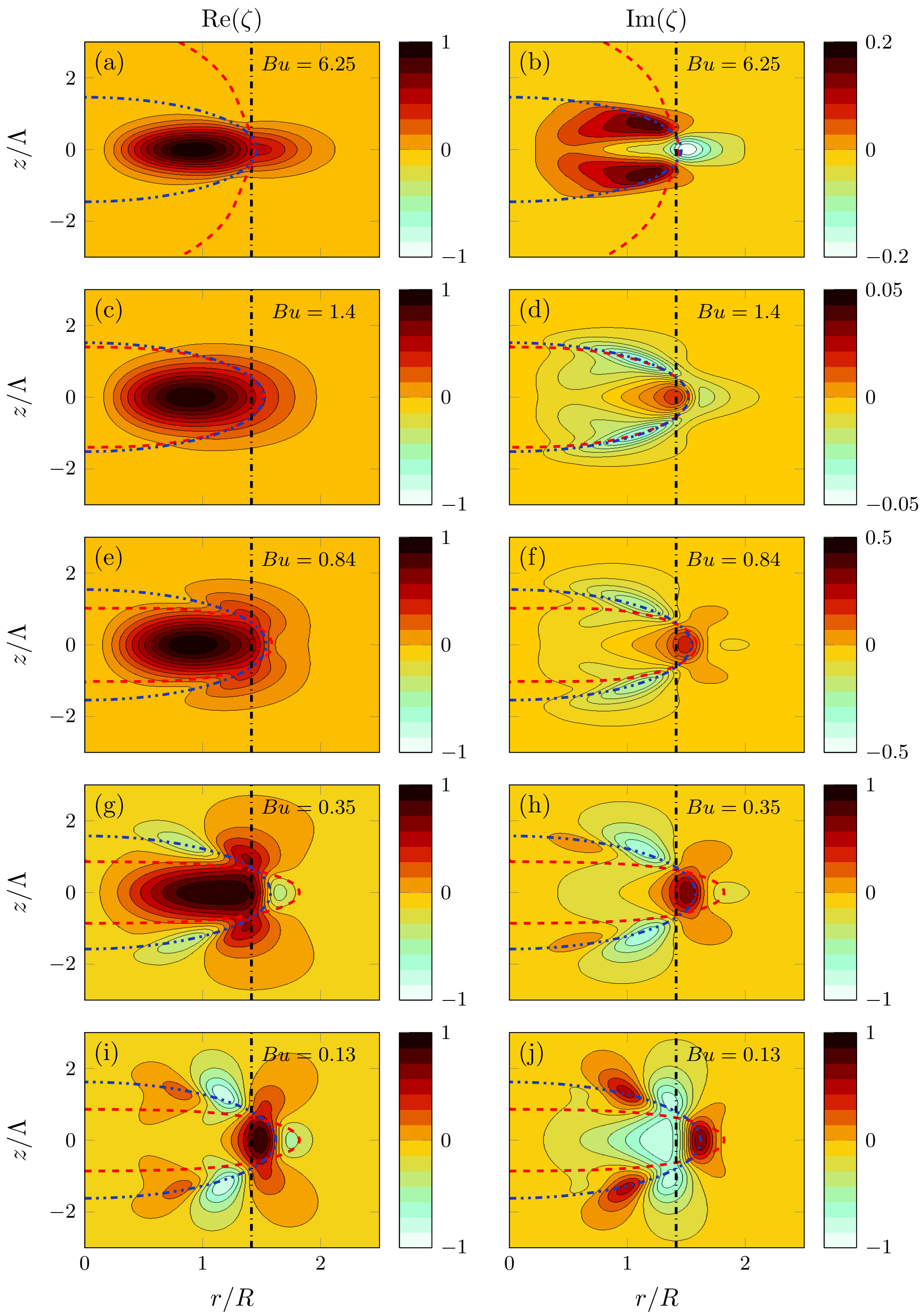

Figure 5.41: Vertical vorticity perturbation (Re(ζ) and Im(ζ)) for different Rossby numbers: the shear instability (a,b) $Bu = 6.25$ ($Ro = 3$) and the mixed baroclinic-shear instability (c,d) $Bu = 1.4$ ($Ro = 1.42$), (e,f) $Bu = 0.84$ ($Ro = 1.1$), (g,h) $Bu = 0.35$ ($Ro = 0.71$) and (i,j) $Bu = 0.13$ ($Ro = 0.43$) for $\alpha = 0.5$, $F_h = 0.3$ and $Re = 10000$. critical layer $m\Omega(r_c) = \omega$, potential vorticity gradient changes sign and vertical vorticity gradient changes sign.

5.B Typical eigenmodes for each instability type

Throughout the thesis, only radial velocity Re(u_r) is shown. Here, we show other typical eigenmodes for each type of instability.

Centrifugal instability

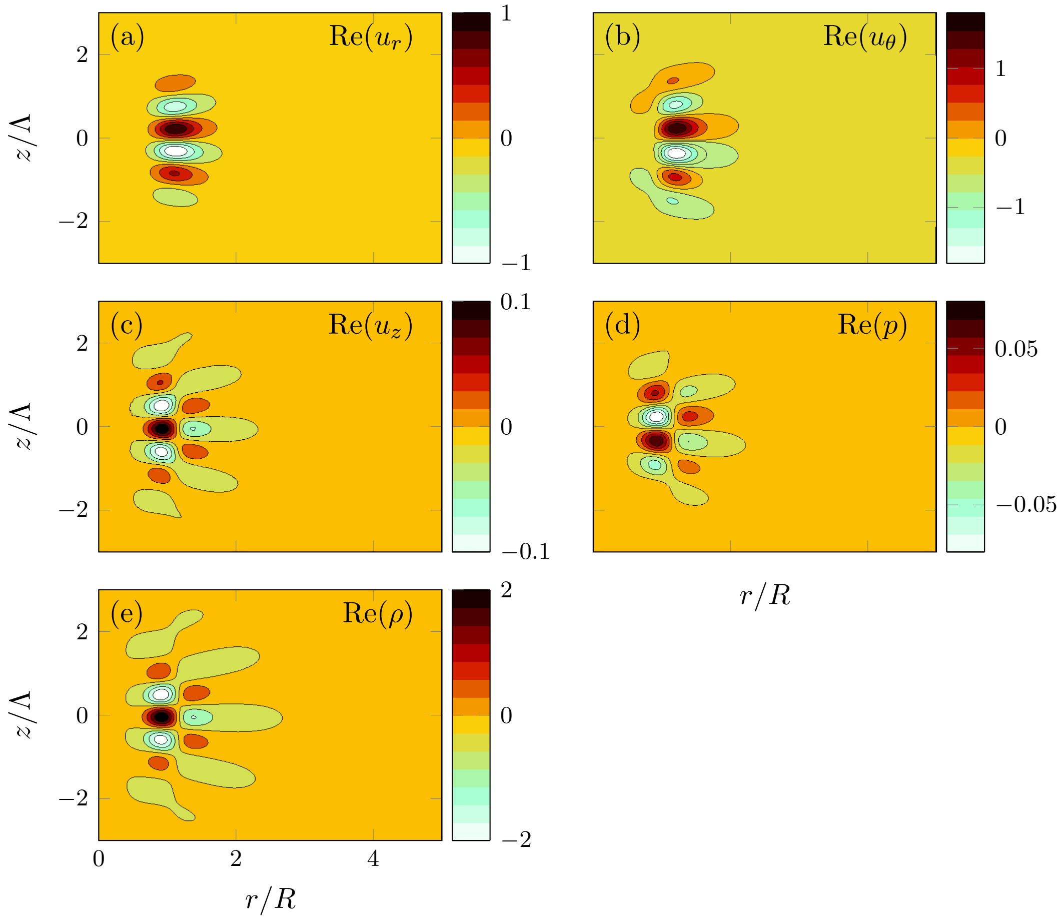

Figure 5.42: Typical eigenmodes for the centrifugal instability (a) u_r, (b) u_θ, (c) u_z, (d) p and (e) ρ for $\alpha = 0.5, m = 0, F_h = 0.5, Ro = -0.1$ and $Re = 10000$.

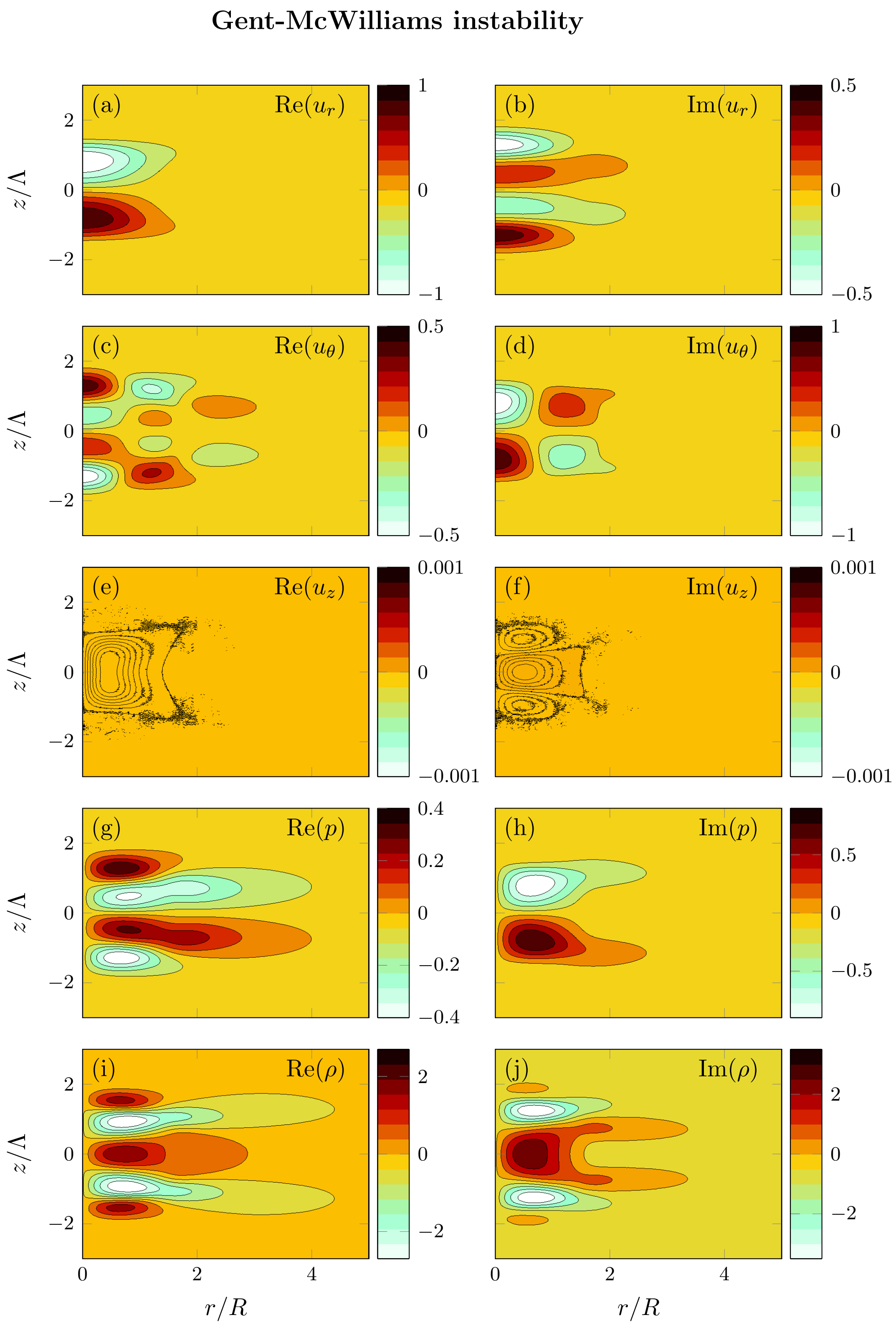

Figure 5.43: Typical eigenmodes for the Gent-McWilliams instability (a,b) u_r, (c,d) u_θ, (e,f) u_z, (g,h) p and (i,j) ρ for $\alpha = 0.5, m = 1, F_h = 0.1, Ro = 1.25$ and $Re = 10000$.

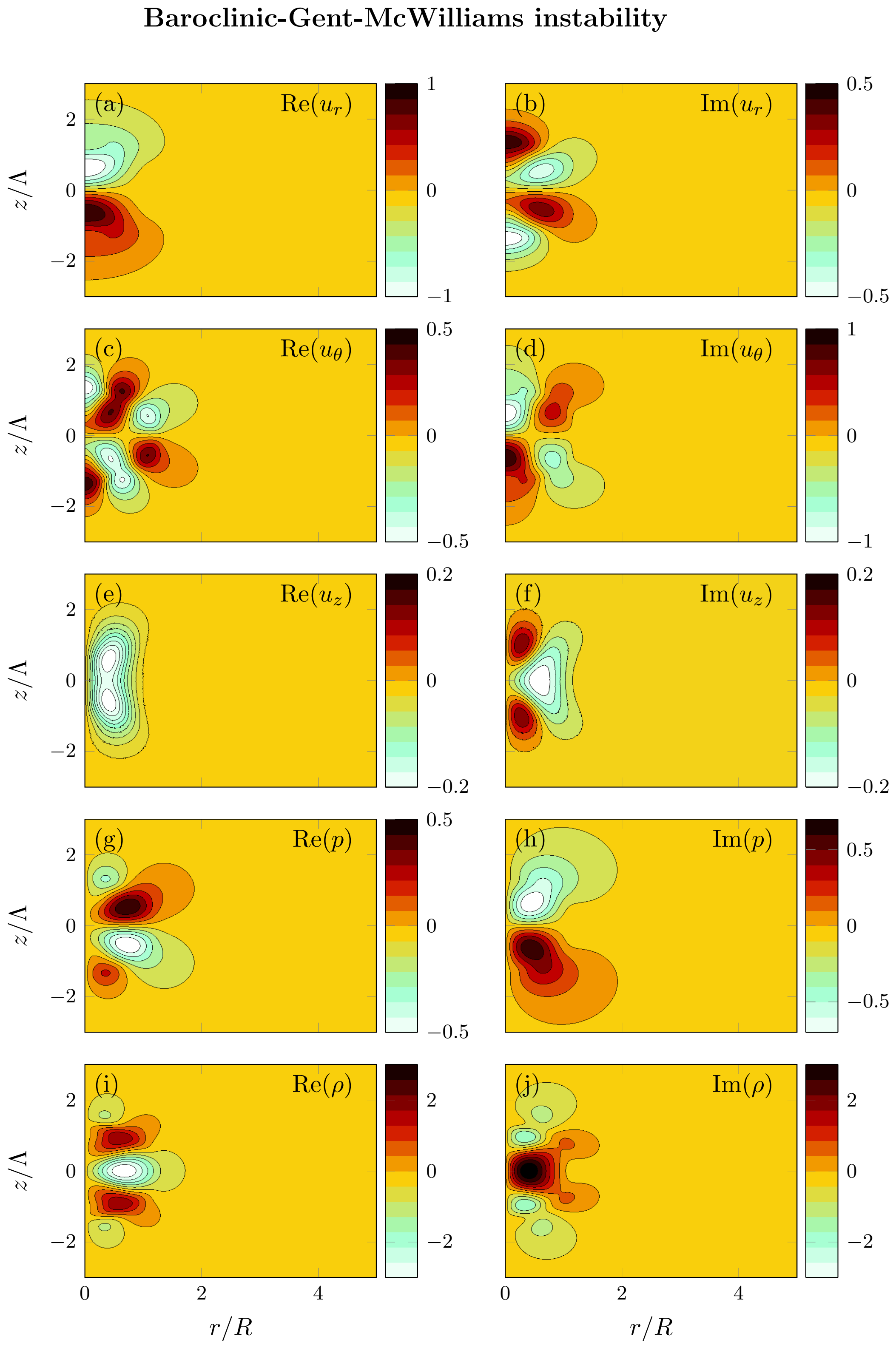

Figure 5.44: Typical eigenmodes for the baroclinic-Gent-McWilliams instability (a,b) u_r, (c,d) u_θ, (e,f) u_z, (g,h) p and (i,j) ρ for $\alpha = 0.5, m = 1, F_h = 0.4, Ro = 1.25$ and $Re = 10000$.

Shear instability

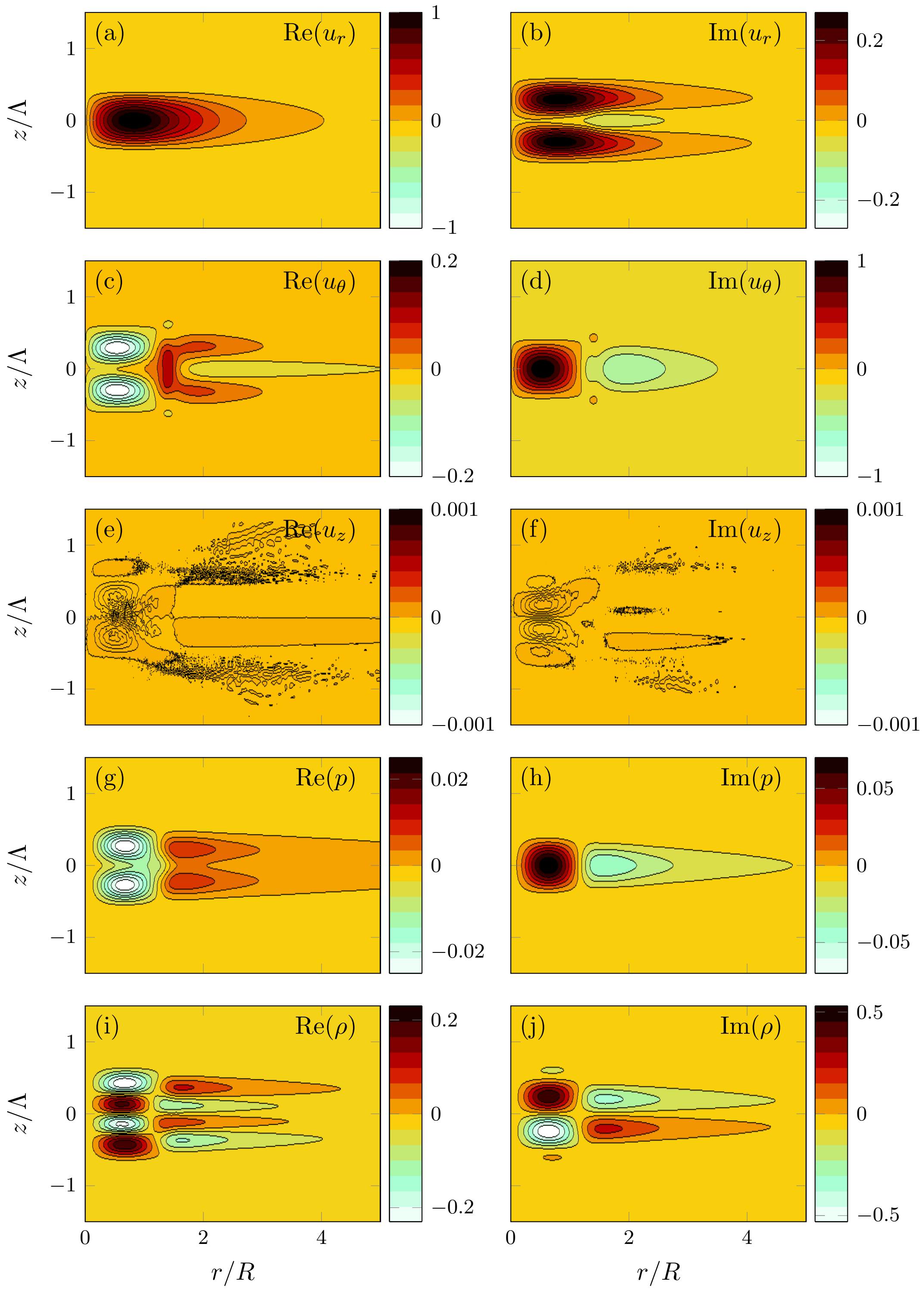

Figure 5.45: Typical eigenmodes for the shear instability (a,b) u_r, (c,d) u_θ, (e,f) u_z, (g,h) p and (i,j) ρ for $\alpha = 0.5, m = 2, F_h = 0.05, Ro = 10$ and $Re = 10000$.

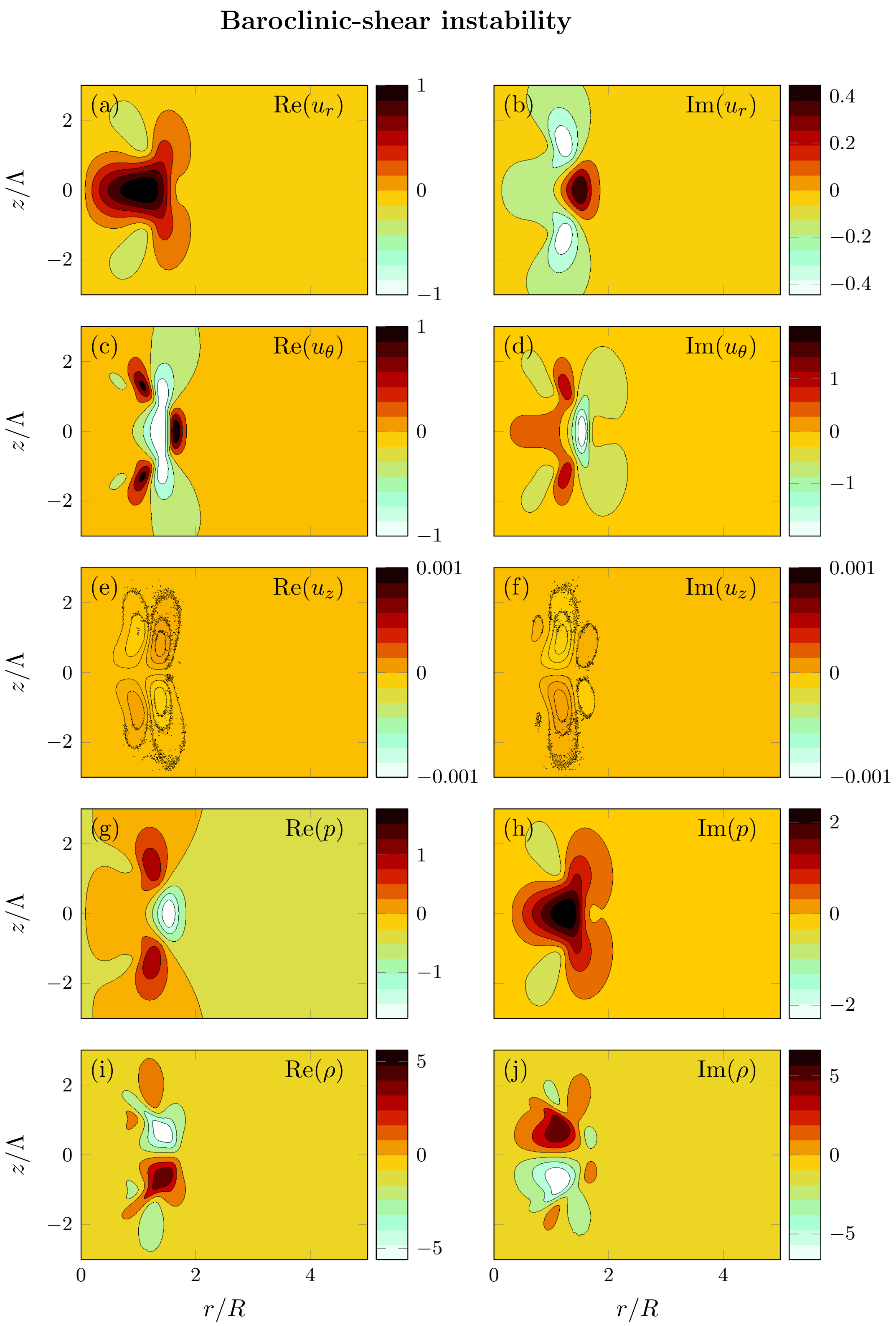

Figure 5.46: Typical eigenmodes for the baroclinic-shear instability (a,b) u_r, (c,d) u_θ, (e,f) u_z, (g,h) p and (i,j) ρ for $\alpha = 0.5, m = 2, F_h = 0.3, Ro = 0.4$ and $Re = 10000$.

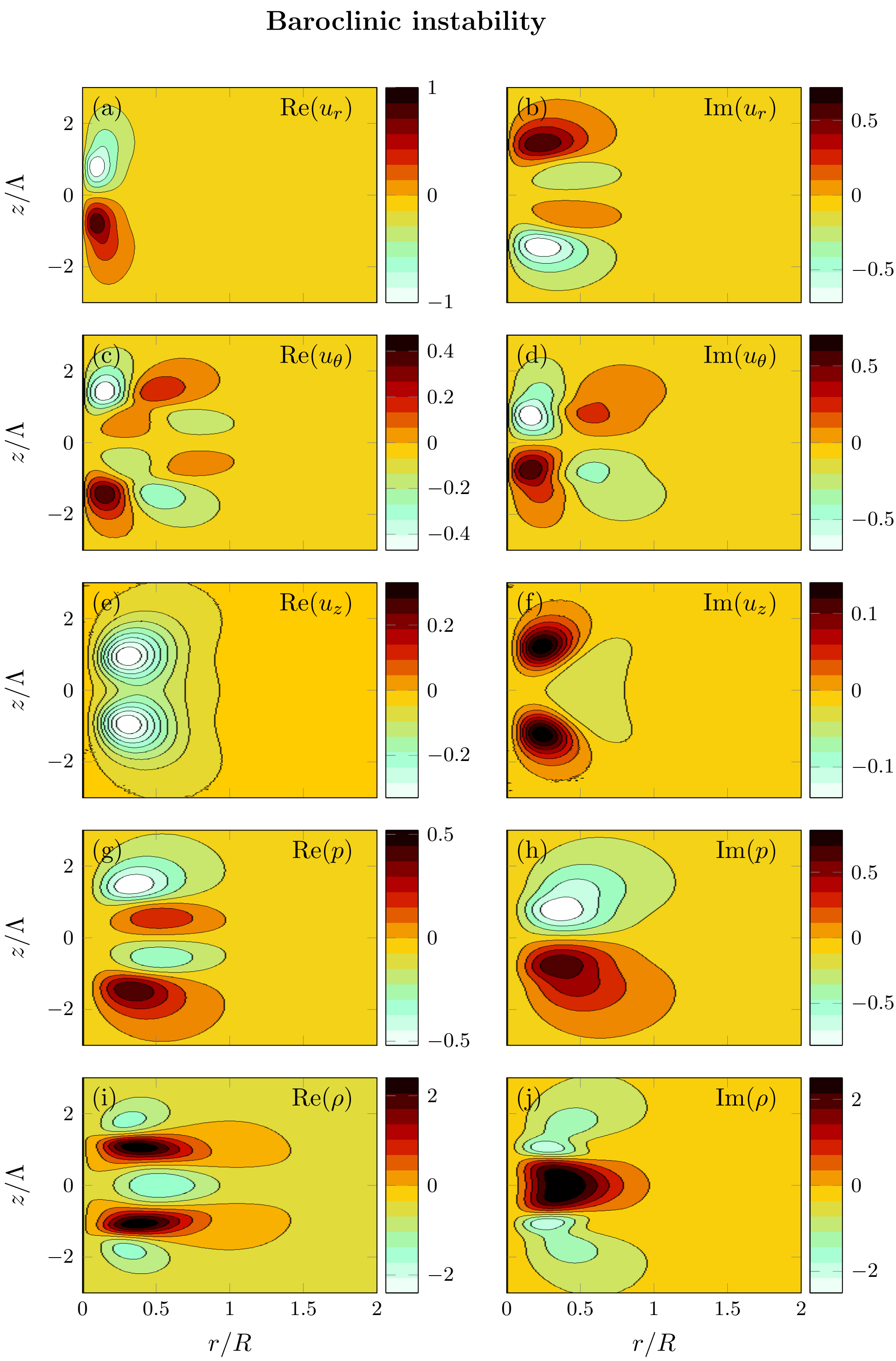

Figure 5.47: Typical eigenmodes for the baroclinic instability (a,b) u_r, (c,d) u_θ, (e,f) u_z, (g,h) p and (i,j) ρ for $\alpha = 0.5, m = 2, F_h = 0.3, Ro = 0.4$ and $Re = 10000$.

6

Conclusions & Perspectives

Contents

6.1 Conclusions

The linear stability of columnar and pancake vortices has been investigated in stratified-rotating fluids. In the first part of the thesis, the stability of the azimuthal wavenumber $m = 1$ of an axisymmetric columnar vortex in a stratified and rotating inviscid fluid has been analysed. As first evidenced by Gent & McWilliams (1986) and further studied by Smyth & McWilliams (1998), the instability of the azimuthal wavenumber $m = 1$ can be the dominant instability which bends and slices the vortex into pancake-shaped vortices in strongly stratified and rapid rotating fluids. This three-dimensional instability, called the "Gent-McWilliams (GMW) instability" herein, can occur in the centrifugally stable regime and in the quasi-geostrophic limit. The criterion for the instability in quasi-geostrophic fluids is that the vorticity gradient ζ' is positive. We have extended this criterion to arbitrary background rotation and stratification by means of numerical and analytical studies. We have shown that the Gent-McWilliams instability with long wavelength disturbances is always unstable as long as the Froude (F_h) and Rossby (Ro) numbers are finite for a vortex with Gaussian angular velocity. When F_h is larger than unity, an attenuation of the instability occurs due to a critical layer where $\Omega(r_{c2}) = 1/F_h$. To generalize the instability condition, we have studied two more vortex profiles: a vortex with an algebraic decay of the angular velocity with exponent n controlling the sign of the vorticity gradient and a vortex with non-zero circulation by combining a Gaussian and a Lamb-Oseen profiles. The vortex with an algebraic decay is unstable to long-wavelength disturbances when the vorticity gradient at the critical radius is positive provided that the Froude and Rossby numbers are finite. Moreover, the condition $\zeta'(r_c) > 0$ is necessary and sufficient for $F_h < 1$. The study of the Lamb-Oseen-Gaussian vortex has shown that the critical radius is very large in the long-wavelength limit. As a result, the vorticity gradient $\zeta'(r_c)$ is exponentially small for long-wavelength. The instability occurs only above a cutoff wavenumber when the critical point is closer to the vortex core where the vorticity gradient is not negligible.

In the second part of the thesis, the stability of an axisymmetric vortex with a pancake shape has been analyzed in a continuously stratified and rotating fluid. The angular velocity is chosen as Gaussian both in radial and vertical directions. Since there exist only few studies on the linear stability of pancake vortices, the identification of unstable modes has been first conducted. This step is done by considering generalized stability criteria for the various instabilities and by comparing the radial profiles of the velocity perturbations to those for columnar vortices. There exist columnar-like instabilities: centrifugal (for $m = 0, 1$, and 2), Gent-McWilliams (for $m = 1$) and shear (for $m = 2$) instabilities as well as specific instabilities to pancake vortices: baroclinic and gravitational instabilities. These types of instability are due to the non-uniform density field inside the vortex. The effect of the aspect ratio α, Froude F_h, Reynolds Re and Rossby Ro numbers have been next investigated. The aspect ratio of the pancake vortex has almost no effect on the spectrum of the centrifugal instability because it is a local instability of short wavelength nature, which is generally much shorter than the thickness of the pancake vortex. The spectra and scaling laws are very close to those for columnar vortices. It stabilizes due to viscous effects which are controlled by the buoyancy Reynolds number ReF_h^2. The Rossby number stabilizes this instability by increasing the minimum of the generalized Rayleigh discriminant $\min(\Phi)$ so that it becomes positive everywhere when $|Ro|$ is $O(10)$. Shear instability exists for small vertical Froude number: $F_h/\alpha < 0.5$ for $Ro = \infty$. This vertical Froude number threshold derives from the maximum wavenumber cutoff for a columnar vortex meaning that the vertical length of the pancake vortex should be large enough to fit at least a vertical wavelength of the shear instability. This holds for all the range of Ro in the form $F_h/\alpha < c(Ro)$ but the constant c varies with Ro and cannot be expressed analytically. When Ro is small and F_h/α is large

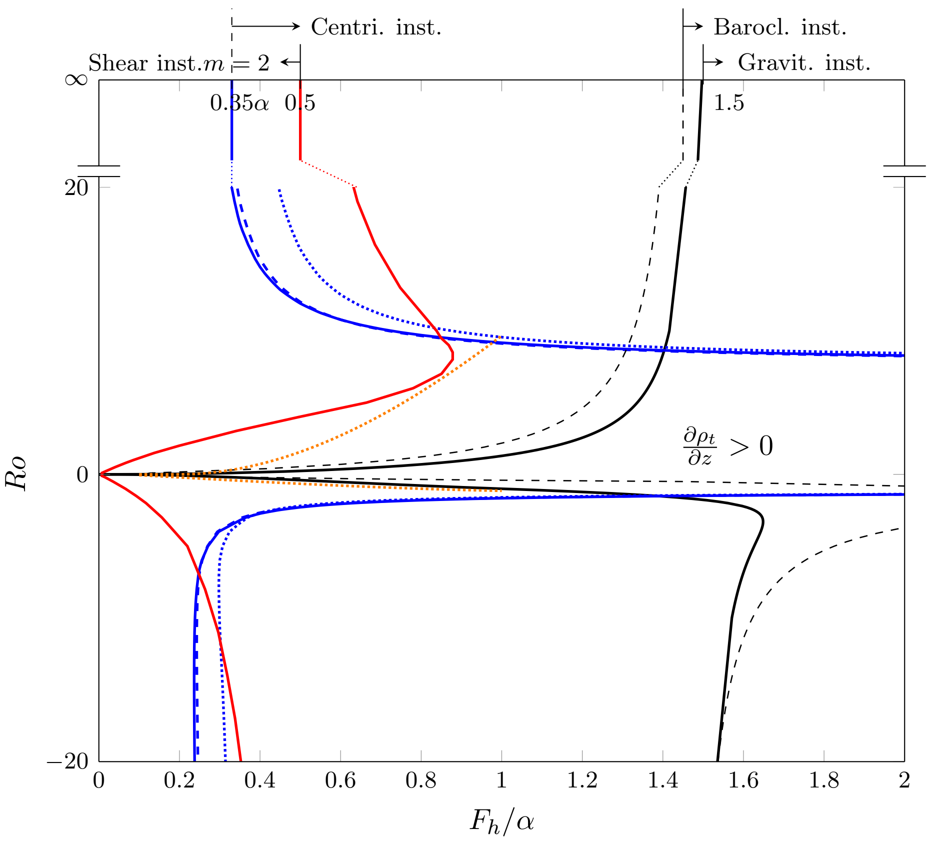

Figure 6.1: Domains of existence of the various instabilities as a function of Ro and F_h/α. The lines indicate the thresholds for the centrifugal instability for $m = 0$ (——), $m = 1$ (- - -) and $m = 2$ (⋯⋯) obtained from the asymptotic formula (3.4) in chapter 5, the shear instability (——), the baroclinic-shear instability (⋯⋯), the baroclinic instability (- - -): $F_h(|1 + 1/Ro|) = 1.46$ and the gravitational instability (——).

(small Bu), the columnar-like shear instability is stabilized but baroclinic-shear instability appears. The eigenmode is similar to the shear eigenmode but is strongly distorted along the critical radius and the inflection point r_I where $\zeta'(r_I) = 0$. The Gent-McWilliams instability for $m = 1$ exists for wide ranges of Ro and F_h/α and becomes the most unstable in the centrifugally stable region. The growth rate behaves as for the columnar vortex when Bu is large, but it also transforms to a baroclinic-Gent-McWilliams instability when Bu is smaller than unity. The displacement mode which exists for $m = 1$ is weakly unstable with generally small growth rate and frequency. This mode resembles the base angular velocity and translates the vortex horizontally. It is a viscous induced instability: it becomes neutral when $Re \to \infty$ and is most unstable when $Re \sim 500$ while it is independent of the other parameters. A pure baroclinic instability appears for $m \geq 1$. This instability is due to the density deformations of the base vortex due to the thermal-wind relation. Hence, the growth rate becomes large near the threshold of the gravitational instability when the isopycnals are strongly inclined in the vortex core. From a simple vortex model, it has been shown that the baroclinic instability exists in the range $F_h/\alpha|1+1/Ro| < 1.43$, i.e. only when the Burger number based on the absolute rotation of the vortex is above a threshold.

Figure 6.1 summarizes the stability conditions as functions of Rossby Ro and vertical Froude number F_h/α. The thresholds for the centrifugal instability has been derived from the generalized centrifugal instability condition in chapter 5 and the one for the baroclinic instability corresponds to $F_h/\alpha|1 + 1/Ro| < 1.43$. The criterion for the shear instability is deduced from the minimum wavelength criteria $F_h/\alpha < c(Ro)$ and the one for the baroclinic-shear instability is a fitted line from the numerical results. The Gent-McWilliams instability exists everywhere except near the baroclinic instability threshold when Ro is not too large. It is then in the form of the mixed baroclinic-Gent-McWilliams instability.

6.2 Perspectives

Here, we propose some perspectives to this work.

6.2.1 DNS and laboratory experiments of the instabilities

It would be interesting to perform DNS and laboratory experiments on the Gent-McWilliams instability. To observe the Gent-McWilliams instability in the laboratory, a stratified rotating tank such that $F_h \leq 1$, $Ro \sim O(1)$ and a single columnar vortex generator would be needed. The angular velocity profile needs further to satisfy the necessary condition for instability. In complement to the linear stability of pancake vortices, the next step would be to simulate the nonlinear dynamics of the instabilities. Experimental observations of these instabilities would be also interesting.

6.2.2 Effect of double diffusion (viscous-diffusive)

Throughout the thesis, we have fixed to unity the Schmidt number $Sc = \nu/\kappa$ which is the ratio between the kinematic viscosity ν and the diffusivity of the stratifying agent κ. However, the typical Schmidt number in the ocean is about 700 for the salt meaning that the momentum diffuses much faster than salt. Hence, it would be interesting to investigate the effect of Sc on the instabilities. Figure 6.2 shows an example of the effect of Sc on the axisymmetric mode of the centrifugal instability studied in chapter 4 for $\alpha = 0.5, F_h = 0.5, Ro = \infty$ and $Re = 10000$. Figure 6.2a is for $Sc = 1$ while figure 6.2b,c are for $Sc = 10$ and $Sc = 500$, respectively. When $Sc = 10$, the frequency of the centrifugal mode is no longer zero and the maximum growth rate decreases. The real part of the radial velocity

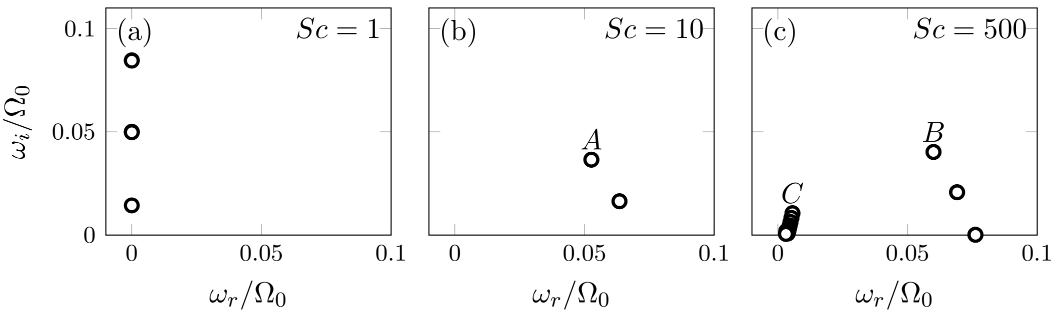

Figure 6.2: Growth rate and frequency spectra for different Schmidt numbers: (a) $Sc = 1$, (b) $Sc = 10$ and (c) $Sc = 500$ for $m = 0, \alpha = 0.5, F_h = 0.5, Ro = \infty$, and $Re = 10000$.

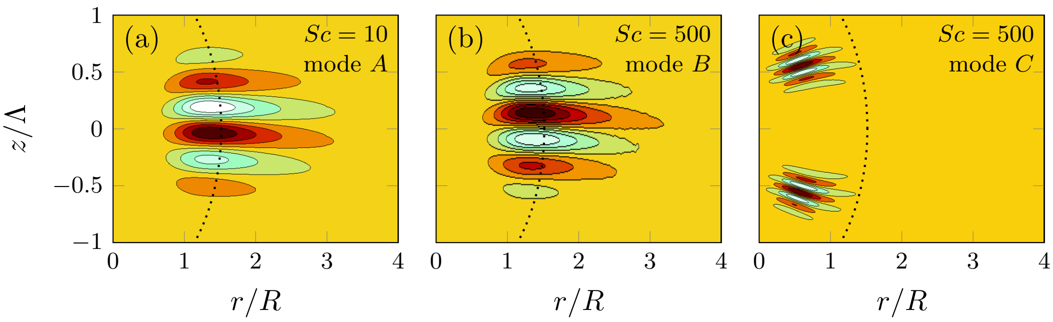

Figure 6.3: Real part of radial velocity perturbations $\mathrm{Re}(u_r)$ for the mode (a) A, (b) B and (c) C in figure 6.2. Dotted lines indicate the limit of the vortex where $\Omega = 0.1\Omega_0$.

$\mathrm{Re}(u_r)$ of the most unstable mode for $Sc = 10$ (figure 6.3a) shows still the same centrifugal mode as for $Sc = 1$. When Sc becomes even larger $Sc = 500$, the frequency increases further and a new branch appears near $\omega_r/\Omega_0 = 0$. The most unstable modes for each branch are shown in figure 6.3b,c. Figure 6.3b shows still the centrifugal modes but figure 6.3c shows a very different mode. The mode has shorter wavelength and is localized above and below the vortex core. It is probably due to the viscous-diffusive McIntyre instability and this mode is similar to the experimental observations of instabilities near a rotating sphere in a stratified fluid by Meunier *et al.* (2014) (figure 6.4). Two instabilities are observed near the equator and above and below the sphere like in figure 6.3b,c. It would be interesting to further study these instabilities for pancake vortices.

6.2.3 Density profiles

Another interesting future work would be to consider different density/velocity profiles of pancake vortices. Here, we have only considered a vortex with Gaussian angular velocity both in radial and vertical directions and the base density is derived from the thermal-wind relation. However, some experiments shows that the angular velocity distribution follows more the profile $\exp(-r^q - z^2/\alpha^2)$ with a steepness parameter q larger than 2. It would be interesting to study the stability of these velocity profiles. Further, the angular velocity of the vortex could be derived from the density data instead of the opposite. Figure 6.5 shows the Brunt-Väisälä frequency inside a Meddy (Hua *et al.*, 2013). The background stratification is represented by a dashed line and the stratification inside the Meddy core is shown by a solid line. As can be seen, the Brunt-Väisälä frequency inside the Meddy is approximately constant. As shown in chapter 2 (2.2), the isopycnals due to the Gaussian

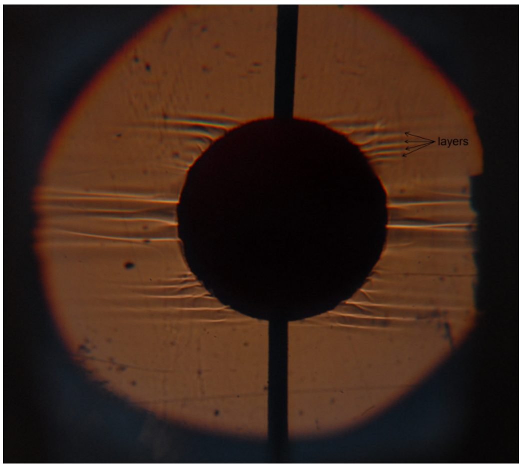

Figure 6.4: Layering observed near a rotating sphere in a stratified fluids ($Sc = 700$). Image from Meunier *et al.* (2014).

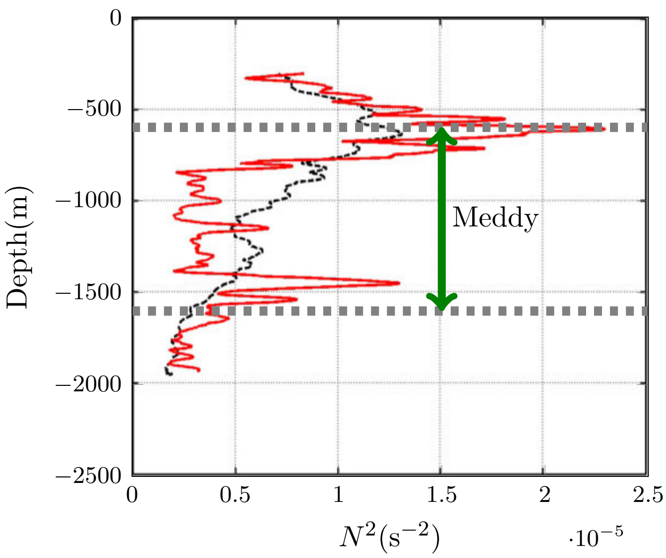

Figure 6.5: Vertical profiles of the Brunt-Väisälä frequency N^2 in the background (black dashed lines) and in the core (red continuous lines) of a Meddy. Image is reproduced from Hua *et al.* (2013).

6

angular velocity are different from those of the Meddy. The angular velocity of such vortex could be then retrieved from an inner constant Brunt-Väisälä frequency.

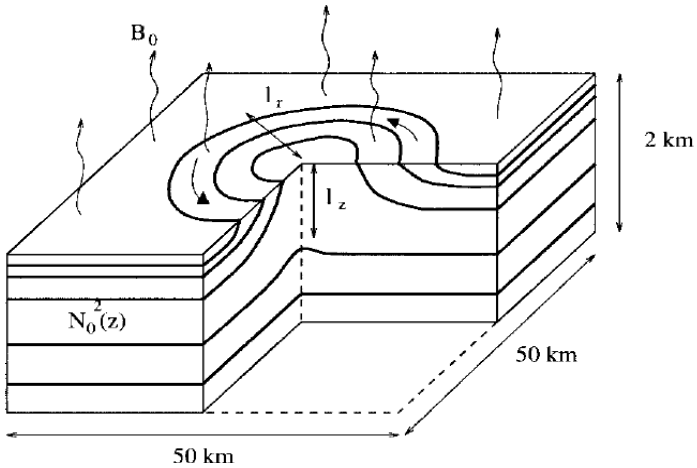

Figure 6.6: A schematic diagram showing a cold core eddy. Image from Legg *et al.* (1998).

6.2.4 Surface vortices

The stability of surface vortices could be also studied. Most of oceanic eddies are formed near the surfaces of the oceans as illustrated in Chapter 1 with the examples of Ulleung and Agulhas eddies. Ulleung eddy is an example of warm core eddy. Now, figure 6.6 shows an example of cold core eddy (Legg *et al.*, 1998). The eddy is formed by a cool current and due to the evaporation, the core is kept cooled. Hence, the isopycnals go upward in the core. Figure 6.7a shows a side view of the isopycnals (Molemaker & Dijkstra, 2000). Due to the density deformation, the baroclinic instability develop as seen in figure 6.5b. This instability mode resembles the one of pancake vortices except that the isopycnals are deformed along the surface (compare figures 6.7 and 6.8). Thus, it would be interesting to further study the stability of warm/cold core surface vortices.

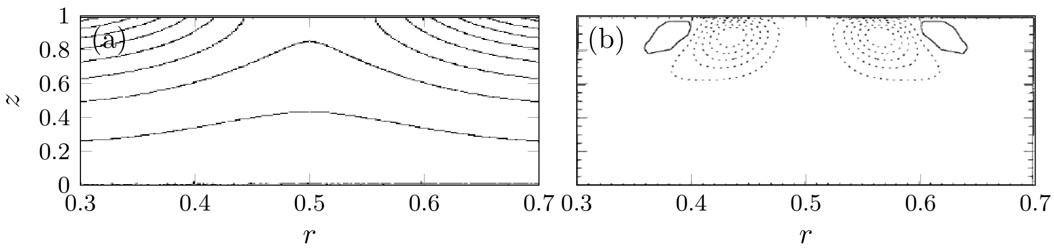

Figure 6.7: (a) Isopycnals of the base flow (b) baroclinic instability eigenmode located near the surface. Image from Molemaker & Dijkstra (2000).

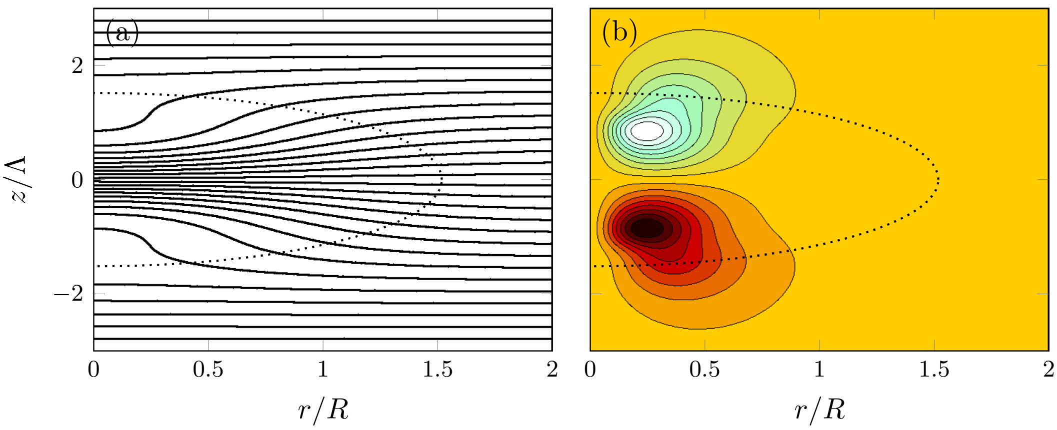

Figure 6.8: (a) Isopycnals and (b) baroclinic instability for pancake vortices. Dotted lines indicate the limit of the vortex where $\Omega = 0.1\Omega_0$.

6

Bibliography

Abramowitz, M. & Stegun, I. A. 1972 *Handbook of Mathematical Functions*. New York: Dover.

Antkowiak, A. & Brancher, P. 2004 Transient energy growth for the lamb-oseen vortex. *Phys. Fluids* **16**, L1–L4.

Armi, L., Hebert, D., Oakey, N., Price, J. F., Richardson, P. L., Rossby, H. T. & Ruddick, B. 1989 Two years in the life of a mediterranean salt lens. *J. Phys. Oceanogr.* **19**, 354–370.

Ash, R. L. & Khorrami, M. R. 1995 Vortex stability. In *Fluid Vortices* (ed. SheldonI. Green), *Fluid Mechanics and Its Applications*, vol. 30, pp. 317–372. Springer Netherlands.

Aubert, O., Le Bars, M., Le Gal, P. & Marcus, P. S. 2012 The universal aspect ratio of vortices in rotating stratified flows: experiments and observations. *J. Fluid Mech.* **706**, 34–45.

Baey, J.-M. & Carton, X. 2002 Vortex multipoles in two-layer rotating shallow-water flows. *J. Fluid Mech.* **460**, 151–175.

Balay, S., Abhyankar, S., Adams, M. F., Brown, J., Brune, P., Buschelman, K., Eijkhout, V., Gropp, W. D., Kaushik, D., Knepley, M. G., McInnes, L. C., Rupp, K., Smith, B. F. & Zhang, H. 2014 PETSc users manual. *Tech. Rep.* ANL-95/11 - Revision 3.5. Argonne National Laboratory.

Balmforth, N. J. 1999 Shear instability in shallow water. *J. Fluid Mech.* **387**, 97–127.

Batchelor, G. K. & Gill, A. E. 1962 Analysis of the stability of axisymmetric jets. *J. Fluid Mech.* **14**, 529–551.

Beckers, M., Clercx, H. J. H., van Heijst, G. J. F. & Verzicco, R. 2003 Evolution and instability of monopolar vortices in a stratified fluid. *Phys. Fluids* **15** (4), 1033–1045.

Beckers, M., Verzicco, R., Clercx, H. J. H. & van Heijst, G. J. F. 2001 Dynamics of pancake-like vortices in a stratified fluid: experiments, model and numerical simulations. *J. Fluid Mech.* **433**, 1–27.

Benilov, E. 2003 Instability of quasi-geostrophic vortices in a two-layer ocean with a thin upper layer. *J. Fluid Mech.* **475**, 303–331.

Billant, P. 2010 Zigzag instability of vortex pairs in stratified and rotating fluids. part 1. general stability equations. *J. Fluid Mech.* **660**, 354–395.

Billant, P. & Chomaz, J.-M. 2000 Experimental evidence for a new instability of a vertical columnar vortex pair in a strongly stratified fluid. *J. Fluid Mech.* **418**, 167–188.

Billant, P. & Chomaz, J.-M. 2001 Self-similary of strongly stratified inviscid flows. *Phys. Fluids* **13**, 1645–1651.

Billant, P., Colette, A. & Chomaz, J.-M. 2004 Instabilities of a vortex pair in a stratified and rotating fluid. *Proceedings of the 21st International Congress of the International Union of Theoretical and Applied Mechanics, Varsovie* pp. 16–20.

Billant, P., Deloncle, A., Chomaz, J.-M. & Otheguy, P. 2010 Zigzag instability of vortex pairs in stratified and rotating fluids. part 2. analytical and numerical analyses. *J. Fluid Mech.* **660**, 396–429.

Billant, P. & Gallaire, F. 2005 Generalized rayleigh criterion for non-axisymmetric centrifugal instabilities. *J. Fluid Mech.* **542**, 365–379.

Billant, P. & Le Dizès, S. 2009 Waves on a columnar vortex in a strongly stratified fluid. *Phys. Fluids* **21**.

Bonnier, M., Eiff, O. & Bonneton, P. 2000 On the density structure of far-wake vortices in a stratified fluid. *Dyn. Atmos. Oceans* **31** (1–4), 117 – 137.

Briggs, R. J., Daugherty, J. D. & Levy, R. H. 1970 Role of landau damping in cross-field electron beams and inviscid shear flow. *Phys. Fluids* **13** (6), 421–432.

Bryden, H. L., Beal, L. M. & Duncan, L. M. 2005 Structure and transport of the agulhas current and its temporal variability. *J. Oceanogr.* **61** (3), 479–492.

Carnevale, G. F. & Kloosterziel, R. C. 1994 Emergence and evolution of triangular vortices. *J. Fluid Mech.* **259**, 305–331.

Carton, X. 2001 Hydrodynamical modeling of oceanic vortices. *Surv. Geophys.* **22** (3), 179–263.

Carton, X., Le Cann, B., Serpette, A. & Dubert, J. 2013 Interactions of surface and deep anticyclonic eddies in the bay of biscay. *J. Marine Syst.* **109–110, Supplement**, S45 – S59, {XII} International Symposium on Oceanography of the Bay of Biscay.

Carton, X. & Legras, B. 1994 The life-cycle of tripoles in two-dimensional incompressible flows. *J. Fluid Mech.* **267**, 53–82.

Carton, X. & McWilliams, J. C. 1989 Barotropic and baroclinic instabilities of axisymmetric vortices in a quasigeostrophic model. In *Mesoscale/Synoptic Coherent structures in Geophysical Turbulence* (ed. J.C.J. Nihoul & B.M. Jamart), *Elsevier Oceanography Series*, vol. 50, pp. 225 – 244. Elsevier.

Chang, K.-I., Teague, W. J., Lyu, S. J., Perkins, H. T., Lee, D.-K., Watts, D. R., Y.-B., Kim., Mitchell, D. A., Lee, C. M. & Kim, K. 2004 Circulation and currents in the southwestern east/japan sea: Overview and review. *Prog. Oceanogr.* **61** (2–4), 105 – 156.

Charney, J. G. 1947 The dynamics of long waves in a baroclinic westerly current. *J. Meteor.* **4** (5), 135–162.

Charney, J. G. & Stern, M. E. 1962 On the stability of internal baroclinic jets in a rotating atmosphere. *J. Atmos. Sci.* **19** (2), 159–172.

Chomaz, J.-M., Bonneton, P., Butet, A. & Hopfinger, E. J. 1993 Vertical diffusion of the far wake of a sphere moving in a stratified fluid. *Phys. Fluids* **5** (11), 2799–2806.

Chomaz, J.-M., Rabaud, M., Basdevant, C. & Couder, Y. 1988 Experimental and numerical investigation of a forced circular shear layer. *J. Fluid Mech.* **187**, 115–140.

Crow, S. C. 1970 Stability theory for a pair of trailing vortices. *AIAA journal* **8** (12), 2172–2179.

De Vuyst, F. 2013 Numerical modeling of transport problems using freefem++ software – with examples in biology, CFD, traffic flow and energy transfer. Lecture.

Deloncle, A., Billant, P. & Chomaz, J.-M. 2011 Three-dimensional stability of vortex arrays in a stratified and rotating fluid. *J. Fluid Mech.* **678**, 482–510.

Deloncle, A., Chomaz, J.-M. & Billant, P. 2007 Three-dimensional stability of a horizontally sheared flow in a stably stratified fluid. *J. Fluid Mech.* **570**, 297–305.

Eady, E. T. 1949 Long waves and cyclone waves. *Tellus* **1** (3), 33–52.

Eliassen, A. 1983 The charney-stern theorem on barotropic-baroclinic instability. *Pure Appl. Geophys.* **121** (3), 563–572.

Eliassen, A. & Kleinschmidt, E. Jr. 1957 Dynamic meteorology. In *Geophysik II / Geophysics II* (ed. Julius Bartels), *Handbuch der Physik / Encyclopedia of Physics*, vol. 10 / 48, pp. 1–154. Springer Berlin Heidelberg.

Fabre, D & Jacquin, L 2004 Viscous instabilities in trailing vortices at large swirl numbers. *J. Fluid Mech.* **500**, 239–262.

Fabre, D., Sipp, D. & Jacquin, L. 2006 The Kelvin waves and the singular modes of the Lamb-Oseen vortex. *J. Fluid Mech.* **551**, 235–274.

Fincham, A.M., Maxworthy, T. & Spedding, G.R. 1996 Energy dissipation and vortex structure in freely decaying, stratified grid turbulence. *Dyn. Atmos. Oceans* **23** (1–4), 155 – 169, stratified flows.

Flierl, G. R. 1988 On the instability of geostrophic vortices. *J. Fluid Mech.* **197**, 349–388.

Flór, J. B. & van Heijst, G. J. F. 1996 Stable and unstable monopolar vortices in a stratified fluid. *J. Fluid Mech.* **311**, 257–287.

Fontane, J. 2002 Etude expérimentale des instabilités 3D d'une paire de tourbillons en milieu tournant. Master's thesis, ENSICA, Toulouse, France.

Garnaud, X. 2012 Modes, transient dynamics and forced response of circular jets. PhD thesis, LadHyX, Ecole Polytechnique X.

Garnaud, X., Lesshafft, L., Schmid, P. J. & Huerre, P. 2013 Modal and transient dynamics of jet flows. *Phys. Fluids* **25** (4).

Gent, P. R. & McWilliams, J. C. 1986 The instability of barotropic circular vortices. *Geophys. Astrophys. Fluid Dyn.* **35** (1-4), 209–233.

Gill, A. E. 1981 Homogeneous intrusions in a rotating stratified fluid. *J. Fluid Mech.* **103**, 275–295.

Godoy-Diana, R. & Chomaz, J.-M. 2003 Effect of the schmidt number on the diffusion of axisymmetric pancake vortices in a stratified fluid. *Phys. Fluids* **15** (4), 1058–1064.

Griffiths, R. W. & Linden, P. F. 1981 The stability of vortices in a rotating, stratified fluid. *J. Fluid Mech.* **105**, 283–316.

Hassanzadeh, P., Marcus, P. S. & Le Gal, P. 2012 The universal aspect ratio of vortices in rotating stratified flows: theory and simulation. *J. Fluid Mech.* **706**, 46–57.

Hecht, F. 2012 New development in freefem++. *J. Numer. Math.* **20** (3-4), 251–265.

Hedstrom, K. & Armi, L. 1988 An experimental study of homogeneous lenses in a stratified rotating fluid. *J. Fluid Mech.* **191**, 535–556.

Hernandez, V., Roman, J. E. & Vidal, V. 2005 SLEPc: A scalable and flexible toolkit for the solution of eigenvalue problems. *ACM Trans. Math. Software* **31** (3), 351–362.

Hide, R. & Mason, P. J. 1975 Sloping convection in a rotating fluid. *Adv. Phys.* **24** (1), 47–100.

Hobbs, R. 2007 Go (geophysical oceanography): a new tool to understand the thermal structure and dynamics of oceans. *European Union Newsletter* **2**.

Hopfinger, E. J. & van Heijst, G. J. F. 1993 Vortices in rotating fluids. *Annu. Rev. Fluid Mech.* **25** (1), 241–289.

Hoskins, B. J. 1974 The role of potential vorticity in symmetric stability and instability. *Quart. J. R. Met. Soc.* **100** (425), 480–482.

Hoskins, B. J., McIntyre, M. E. & Robertson, A. W. 1985 On the use and significance of isentropic potential vorticity maps. *Quart. J. R. Met. Soc.* **111** (470), 877–946.

Howard, L. N. & Gupta, A. S. 1962 On the hydrodynamic and hydromagnetic stability of swirling flows. *J. Fluid Mech.* **14** (3), 463–476.

Hua, B. L. 1998 The internal barotropic instability of surface-intensified eddies. part i: Generalized theory for isolated eddies. *J. Phys. Oceanogr.* **18**, 40–55.

Hua, B. L., Ménesguen, C., Le Gentil, S., Schopp, R., Marsset, B. & Aiki, H. 2013 Layering and turbulence surrounding an anticyclonic oceanic vortex: in situ observations and quasi-geostrophic numerical simulations. *J. Fluid Mech.* **731**, 418–442.

Jimenez, J. 1975 Stability of a pair of co-rotating vortices. *Phys. Fluids* **18** (11), 1580–1581.

Kantha, L. H. & Clayson, C. A. 2000 *Numerical Models of Oceans and Oceanic Processes*, *International Geophysics*, vol. 66. Elsevier Science.

Kelvin, Lord 1880 Vibrations of a columnar vortex. *Phil. Mag.* **10**, 155–168.

Kerswell, R. R. 2002 Elliptical instability. *Annu. Rev. Fluid Mech.* **34** (1), 83–113.

Kim, D., Yang, E., Kim, K., Shin, C., Park, J., Yoo, S. & Hyun, J. 2012 Impact of an anticyclonic eddy on the summer nutrient and chlorophyll a distributions in the ulleung basin, east sea (japan sea). *J. Marine Syst.* **69** (1), 23–29.

Klein, R., Majda, A. J & Damodaran, K. 1995 Simplified equations for the interaction of nearly parallel vortex filaments. *J. Fluid Mech.* **288**, 201–248.

Kloosterziel, R. C. & van Heijst, G. J. F 1991 An experimental study of unstable barotropic vortices in a rotating fluid. *J. Fluid Mech.* **223**, 1–24.

Lahaye, N. & Zeitlin, V. 2015 Centrifugal, barotropic and baroclinic instabilities of isolated ageostrophic anticyclones in the two-layer rotating shallow water model and their nonlinear saturation. *J. Fluid Mech.* **762**, 5–34.

Lazar, A., Stegner, A., Caldeira, R., Dong, C., Didelle, H. & Viboud, S. 2013*a* Inertial instability of intense stratified anticyclones. part 2. laboratory experiments. *J. Fluid Mech.* **732**, 485–509.

Lazar, A., Stegner, A. & Heifetz, E. 2013*b* Inertial instability of intense stratified anticyclones. part 1. generalized stability criterion. *J. Fluid Mech.* **732**, 457–484.

Le Dizès, S. 2000 Non-axisymmetric vortices in two-dimensional flows. *J. Fluid Mech.* **406**, 175–198.

Le Dizès, S. 2004 Viscous critical-layer analysis of vortex normal modes. *Stud. Appl. Math.* **112** (4), 315–332.

Le Dizès, S. & Billant, P. 2009 Radiative instability in stratified vortices. *Phys. Fluids* **21** (9).

Le Dizès, S. & Laporte, F. 2002 Theoretical predictions for the elliptical instability in a two-vortex flow. *J. Fluid Mech.* **471**, 169–201.

Legg, S., McWilliams, J. & Gao, J. 1998 Localization of deep ocean convection by a mesoscale eddy. *J. Phys. Oceanogr.* **28**, 944–970.

Lehahn, Y., d'Ovidio, F., Lévy, M., Amitai, Y. & Heifetz, E. 2011 Long range transport of a quasi isolated chlorophyll patch by an agulhas ring. *Geophys. Res. Lett.* **38** (16), L16610–L16616, l16610.

Leweke, T., Le Dizès, S. & Williamson, C. H. K. 2016 Dynamics and instabilities of vortex pairs. *Annu. Rev. Fluid Mech.* **48**, 1–35.

Leweke, T. & Williamson, C. H. K. 1998 Cooperative elliptic instability of a vortex pair. *J. Fluid Mech.* **360**, 85–119.

Leweke, T. & Williamson, C. H. K. 2011 Experiments on long-wavelength instability and reconnection of a vortex pair. *Phys. Fluids* **23** (2), 0241011–02410114.

Lin, C. C. 1955 *The theory of hydrodynamics stability*. Cambridge University Press.

Lin, Q., Boyer, D. L. & Fernando, H. J. S. 1992 Turbulent wakes of linearly stratified flow past a sphere. *Phys. Fluids* A **4** (48), 1687–1696.

McGillicuddy, D. J., Anderson, L. A., Bates, N. R., Bibby, T., Buesseler, K. O., Carlson, C. A., Davis, C. S., Ewart, C., Falkowski, P. G., Goldthwait, S. A., Hansell, Dennis A., Jenkins, W. J., Johnson, R., Kosnyrev, V. K., Ledwell, J. R., Li, Q. P., Siegel, D. A. & Steinberg, D. K. 2007 Eddy/wind interactions stimulate extraordinary mid-ocean plankton blooms. *Science* **316** (5827), 1021–1026.

McIntyre, M. E. 1970 Diffusive destabilization of the baroclinic circular vortex. *Geophys. Fluid Dyn.* **1**, 19–57.

Ménesguen, C., McWilliams, J. C. & Molemaker, M. J. 2012 Ageostrophic instability in a rotating stratified interior jet. *J. Fluid Mech.* **711**, 599–619.

Meschanov, S.L. & Shapiro, G.I. 1998 A young lens of red sea water in the arabian sea. *Deep-Sea Res. Pt. I* **45** (1), 1 – 13.

Meunier, P. & Leweke, T. 2001 Three-dimensional instability during vortex merging. *Phys. Fluids* **13** (10), 2747–2750.

Meunier, P. & Leweke, T. 2005 Elliptic instability of a co-rotating vortex pair. *J. Fluid Mech.* **533**, 125–159.

Meunier, P., Miquel, B. & Le Dizès, S. 2014 Instabilities around a rotating ellipsoid in a stratified rotating flow. In *19th Australasian Fluid Mechanics Conference*.

Michalke, A. & Timme, A. 1967 On inviscid instability of certain 2-dimensional vortex-type flows. *J. Fluid Mech.* **29** (4), 647–666.

Molemaker, M. J. & Dijkstra, H. A. 2000 Stability of a cold core eddy in the presence of convection: hydrostatic versus nonhydrostatic modeling. *J. Phys. Oceanogr.* **30**, 475–494.

Montgomery, M. T. & Shapiro, L. J. 1995 Generalized charney-stern and fjortoft theorems for rapidly rotating vortices. *J. Atmos. Sci.* **52** (16), 1829–1833.

Moore, D. W. & Saffman, P. G. 1975 The instability of a straight vortex filament in a strain field. In *Proceedings of the Royal Society of London A: Mathematical, Physical and Engineering Sciences*, , vol. 346, pp. 413–425. The Royal Society.

Negretti, M. E. & Billant, P. 2013 Stability of a gaussian pancake vortex in a stratified fluid. *J. Fluid Mech.* **718**, 457–480.

Nguyen, H. Y., Hua, B. L., Schopp, R. & Carton, X. 2012 Slow quasigeostrophic unstable modes of a lens vortex in a continuously stratified flow. *Geophys. Astrophys. Fluid Dyn.* **106** (3), 305–319.

Orlandi, P. & Carnevale, G. F. 1999 Evolution of isolated vortices in a rotating fluid of finite depth. *J. Fluid Mech.* **381**, 239–269.

Otheguy, P., Chomaz, J.-M. & Billant, P. 2006 Elliptic and zigzag instabilities on co-rotating vertical vortices in a stratified fluid. *J. Fluid Mech.* **553**, 253–272.

Park, J. 2012 Waves and instabilities on vortices in stratified and rotating fluids. PhD thesis, LadHyX, Ecole Polytechnique X.

Park, J. & Billant, P. 2012 Radiative instability of an anticyclonic vortex in a stratified rotating fluid. *J. Fluid Mech.* **707**, 381–392.

Park, J. & Billant, P. 2013 Instabilities and waves on a columnar vortex in a strongly stratified and rotating fluid. *Phys. Fluids* **25** (8).

Pedlosky, J. 1992 *Geophysical Fluid Dynamics*. *Springer study edition* 2. Springer New York.

Phillips, N. A. 1954 Energy transformations and meridional circulations associated with simple baroclinic waves in a two-level, quasi-geostrophic model1. *Tellus* **6** (3), 273–286.

Pingree, R. D. & Le Cann, B. 1992 Anticyclonic eddy x91 in the southern bay of biscay, may 1991 to february 1992. *J. Geophys. Res.* **97** (C9), 14353–14367.

Plougonven, R. & Zeitlin, V. 2002 Internal gravity wave emission from a pancake vortex: An example of wave–vortex interaction in strongly stratified flows. *Phys. Fluids* **14** (3), 1259–1268.

Rayleigh, Lord 1880 On the stability, or instability, of certain fluid motions. *Proc. London Math. Soc.* **11**, 57–70.

Rayleigh, Lord 1917 On the dynamics of revolving fluids. *Proc. R. Soc. A* **93** (648), 148–154.

Reasor, P. D. & Montgomery, M. T. 2001 Three-dimensional alignment and corotation of weak, tc-like vortices via linear vortex rossby waves. *J. Atmos. Sci.* **58** (16), 2306–2330.

Reasor, P. D., Montgomery, M. T. & Grasso, L. D. 2004 A new look at the problem of tropical cyclones in vertical shear flow: Vortex resiliency. *J. Atmos. Sci.* **61** (1), 3–22.

Richardson, P. L., Bower, A. S. & Zenk, W. 2000 A census of meddies tracked by floats. *Prog. Oceanogr.* **45**, 209–250.

Riedinger, X. & Gilbert, A. D. 2014 Critical layer and radiative instabilities in shallow-water shear flows. *J. Fluid Mech.* **751**, 539–569.

Riedinger, X., Le Dizès, S. & Meunier, P. 2010 Viscous stability properties of a lamb-oseen vortex in a stratified fluid. *J. Fluid Mech.* **645**, 255–278.

Riedinger, X., Le Dizès, S. & Meunier, P. 2011 Radiative instability of the flow around a rotating cylinder in a stratified fluid. *J. Fluid Mech.* **672**, 130–146.

Roman, J.E., Campos, C., Romero, E. & Tomas, A. 2015 SLEPc users manual. *Tech. Rep.* DSIC-II/24/02 - Revision 3.6. D. Sistemes Informàtics i Computació, Universitat Politècnica de València.

Saffman, P. G. 1992 *Vortex Dynamics*. Cambridge University Press.

Saunders, P. M. 1973 The instability of a baroclinic vortex. *J. Phys. Oceanogr.* **3**, 61–65.

Schecter, D. A., Dubin, D. H. E., Cass, A. C., Driscoll, C. F., Lansky, I. M. & O'Neil, T. M. 2000 Inviscid damping of asymmetries on a two-dimensional vortex. *Phys. Fluids* **12** (10), 2397–2412.

Schecter, D. A. & Montgomery, M. T. 2003 On the symmetrization rate of an intense geophysical vortex. *Dyn. Atmos. Oceans* **37**, 55–88.

Schecter, D. A. & Montgomery, M. T. 2004 Damping and pumping of a vortex Rossby wave in a monotonic cyclone: Critical layer stirring versus inertia—buoyancy wave emission. *Phys. Fluids* **16**, 1334–48.

Schecter, D. A. & Montgomery, M. T. 2006 Conditions that inhibit the spontaneous radiation of spiral inertia–gravity waves from an intense mesoscale cyclone. *J. Atmos. Sci.* **63**, 435–456.

Schecter, D. A., Montgomery, M. T. & Reasor, P. D. 2002 A theory for the vertical alignment of a quasigeostrophic vortex. *J. Atmos. Sci.* **59** (2), 150–168.

Shin, H.-R., Shin, C.-W., Kim, C., Byun, S.-K. & Hwang, S.-C 2005 Movement and structural variation of warm eddy {WE92} for three years in the western east/japan sea. *Deep-Sea Res. Pt. II* **52** (11–13), 1742 – 1762, the Circulation of the Japan-East Sea.

Smyth, W. D. & McWilliams, J. C. 1998 Instability of an axisymmetric vortex in a stably stratified, rotating environment. *Theor. Comp. Fluid Dyn.* **11** (3-4), 305–322.

Solberg, H. 1936 Le mouvement d'inertie de l'atmosphere stable et son role dans la theorie des cyclones. In *Meteor. Assoc. U.G.G.I.* (ed. vol. 1 (ed. Lisbon)), pp. 66 – 82. Dupont.

Spedding, G. R., Browand, F. K. & Fincham, A. M. 1996 Turbulence, similarity scaling and vortex geometry in the wake of a towed sphere in a stably stratified fluid. *J. Fluid Mech.* **314**, 53–103.

Takehiro, S.-I. & Hayashi, Y.-Y. 1992 Over-reflection and shear instability in a shallow-water model. *J. Fluid Mech.* **236**, 259–279.

Thivolle-Cazat, J., Sommeria, J. & Galmiche, M. 2005 Baroclinic instability of two-layer vortices in laboratory experiments. *J. Fluid Mech.* **544**, 69–97.

Tsai, C.-Y. & Widnall, S. E. 1976 The stability of short waves on a straight vortex filament in a weak externally imposed strain field. *J. Fluid Mech.* **73** (04), 721–733.

Vallis, G.K. 2006 *Atmospheric and Oceanic Fluid Dynamics: Fundamentals and Large-scale Circulation*. Cambridge University Press.

Verzicco, R., Lalli, F. & Campana, E. 1997 Dynamics of baroclinic vortices in a rotating, stratified fluid: A numerical study. *Phys. Fluids* **9** (2), 419–432.

Widnall, S. E., Bliss, D. B. & Zalay, A. 1971 Theoretical and experimental study of the stability of a vortex pair. In *Aircraft Wake Turbulence and Its Detection* (ed. A. Olsen, J. H. Goldburg & Rogers M.), pp. 305 – 338. Springer US.

Yim, E. & Billant, P. 2015 On the mechanism of the gent-mcwilliams instability of a columnar vortex in stratified rotating fluids. *J. Fluid Mech.* **780**, 5–44.

Zienkiewicz, O. C. & Taylor, R. L. 2000 *The Finite Element Method: The basis*. *Referex Engineering* 2. Butterworth-Heinemann.

bib

Abstract

The stability of vortices in a stratified and rotating fluid is studied numerically and theoretically in order to better understand the dynamics of vortices in the oceans and atmosphere. In the first part, the stability of a columnar vertical axisymmetric vortex is analysed. For strong stratification and rapid background rotation and some vortex profiles such as a Gaussian angular velocity, the dominant instability is a special instability, called "Gent-McWilliams instability", which bends and slices the vortex into pancake-shaped vortices. Numerical and asymptotic stability analyses for long-wavelength show that this instability originates from a destabilization of the long-wavelength bending mode by a critical layer at the radius where the frequency of the mode is equal to the angular velocity of the vortex. A necessary condition for instability is that the base vorticity gradient is positive at the critical radius. In the second part, the stability of an axisymmetric pancake-shape vortex with a Gaussian angular velocity in both radial and vertical directions is analyzed depending on the intensity of the stratification, the rotation of the fluid, the aspect ratio α of the vortex and the Reynolds number Re. In the case of a strongly stratified non-rotating fluid, centrifugal and shear instabilities are shown to have similar characteristics as for columnar vortices. The centrifugal instability occurs when the buoyancy Reynolds number ReF_h^2 (where F_h is the Froude number) is above a threshold and can be non-axisymmetric close to the threshold. The shear instability develops only when the vertical Froude number F_h/α is low such that the vortex thickness is larger than the cutoff wavelength for a columnar vortex for the same parameters. Gravitational and baroclinic instabilities are also observed, respectively, above and just below the threshold $F_h/\alpha = 1.5$ which corresponds to a zero maximum total density gradient. A simple model predicts the characteristics of the baroclinic instability. Strongly stratified rotating fluids are next considered. The centrifugal instability becomes stabilized for small Rossby number Ro, in agreement with the generalized Rayleigh criterion. An instability similar to the Gent-McWilliams instability of a columnar vortex occurs for small Froude and Rossby numbers. The occurrence of the shear instability continues to be governed by confinement effects. Mixed shear-baroclinic and baroclinic-Gent-McWilliams instabilities are also observed when the isopycnals are strongly deformed in the vortex core. The baroclinic instability develops when $F_h/\alpha(1 + 1/|Ro|) > 1.46$, i.e. when the Burger number based on the absolute angular velocity is below a threshold.

Keywords: instability, columnar vortex, pancake vortex, stratified fluid, rotating fluid

Résumé

La stabilité de tourbillons dans un fluide stratifié en rotation est étudiée numériquement et théoriquement afin de mieux comprendre la dynamique des tourbillons dans les océans et l'atmosphère. Dans la première partie, la stabilité d'un tourbillon colonnaire vertical est analysée. Pour des fortes stratifications et des rotations rapides, certains tourbillons comme ceux ayant une vitesse angulaire gaussienne présente une instabilité particulière, appelée "instabilité de Gent-McWilliams", qui courbe et découpe le tourbillon en couches. Des analyses numériques et asymptotiques pour de grandes longueurs d'onde montrent que cette instabilité provient d'une déstabilisation du mode de déplacement de grande longueur d'onde par une couche critique au niveau du rayon où la fréquence du mode est égale à la vitesse angulaire du tourbillon. Une condition nécessaire d'instabilité est que le gradient de vorticité de base soit positif au niveau du rayon critique. Dans la deuxième partie, la stabilité d'un tourbillon axisymétrique en forme de crêpe avec une vitesse angulaire gaussienne dans les directions radiale et verticale est analysée en fonction de l'intensité de la stratification, de la rotation du fluide, du rapport d'aspect α du tourbillon et du nombre de Reynolds Re. Dans le cas d'un fluide fortement stratifié non-tournant, les instabilités centrifuges et de cisaillement ont les mêmes caractéristiques que celles des tourbillons colonnaires. L'instabilité centrifuge se produit lorsque le nombre de Reynolds de flottabilité ReF_h^2 (où F_h est le nombre de Froude) est supérieur à un seuil et est non-axisymétrique près du seuil. L'instabilité de cisaillement ne se développe que lorsque le nombre de Froude vertical F_h/α est faible de sorte que l'épaisseur du tourbillon est plus grande que la longueur d'onde de coupure d'un vortex colonnaire pour les mêmes paramètres. Des instabilités gravitationnelles et baroclines sont également observées, respectivement, au dessus et juste en dessous du seuil $F_h/\alpha = 1.5$ qui correspond à un gradient de densité total maximum nul. Un modèle simplifié prédit les caractéristiques de l'instabilité barocline. Le cas des fluides fortement stratifiés-tournants est ensuite considéré. L'instabilité centrifuge disparaît pour les nombres de Rossby Ro petits, en accord avec le critère de Rayleigh généralisé. Une instabilité semblable à l'instabilité de Gent-McWilliams d'un tourbillon colonnaire se produit pour les faibles nombres de Froude et Rossby. L'existence de l'instabilité de cisaillement continue d'être régie par des effets de confinement. Des instabilités mixtes, Gent-McWilliams-barocline et cisaillement-barocline, sont également observées quand les iso-densités sont fortement déformées dans le coeur du tourbillon. L'instabilité barocline se développe lorsque $F_h/\alpha(1 + 1/|Ro|) > 1.46$, c'est à dire lorsque le nombre de Burger basé sur la vitesse angulaire absolue est inférieure à un seuil.

Mots clés: instabilité, tourbillon colonnaire, tourbillon crêpe ou lenticulaire, fluide stratifié, fluide tournant